

**High-Resolution Characterization
of Nitrogen-Doped Carbon Support
Materials Decorated with Noble
Metal Atom Catalysts**

HIGH-RESOLUTION CHARACTERIZATION OF N-DOPED CARBON
SUPPORT MATERIALS DECORATED WITH NOBLE METAL ATOM
CATALYSTS

by

SAMANTHA STAMBULA, B.A.Sc.

A Thesis
Submitted to the School of Graduate Studies
in Partial Fulfilment of the Requirements for the degree of
Doctor of Philosophy

McMaster University © Copyright by Samantha Stambula, March 2018

DOCTOR OF PHILOSOPHY (2018)

Materials Engineering

McMaster University, Hamilton, Ontario, Canada

TITLE: High-Resolution Characterization of N-doped Carbon Support
Materials Decorated with Noble Metal Atom Catalysts

AUTHOR: Samantha Stambula, B.A.Sc. (University of Waterloo)

SUPERVISOR: Professor Gianluigi A. Botton

NUMBER OF PAGES: xviii, 276

Abstract

Graphene and its functionalized derivatives, such as nitrogen-doped graphene, have recently become a popular substrate material for the proton exchange membrane fuel cell (PEMFC) due to its enhanced electrical conductivity, electrochemical stability, and increased surface area when compared to the conventional, carbon black. In order to further develop the alternative fuel industry, the Pt catalyst within the PEMFC must also be considered. Single Pt atoms have a higher surface area to volume ratio when compared to nanoparticles, thus offering the potential to create a more affordable and efficient PEMFC. In this thesis, electrode materials comprising single Pt atoms and clusters, produced using atomic layer deposition (ALD) on various C derivatives, including graphene, N-doped graphene, carbon nanotubes (CNTs), and N-doped CNTs (NCNTs) are investigated through the utilization of aberration corrected transmission electron microscopy.

Structural and chemical analysis was performed on thermally exfoliated N-doped graphene and CVD-produced graphene that was exposed to N^+ ion sources. It was determined that the thermally exfoliated N-doped graphene maintained the short-range order of the graphene lattice; however, local inhomogeneities existed for the total N concentration, and the specific N-dopants within and between graphene sheets. More importantly, Pt atoms and clusters were observed and determined to be primarily stabilized at the edge of the N-doped graphene sheets. The stabilization of the Pt atoms and clusters resulted in a significantly higher mass and specific activity for the hydrogen evolution reaction, when compared to the use of a graphene substrate and Pt nanoparticles on C black. The N^+ ion implantation in the CVD graphene showed the incorporation of N-dopants; however, electron energy loss spectroscopy revealed structural damage to thin sheets.

NCNTs were also characterized in this thesis as possible gas containers, and as a substrate material to examine the effects of varying ALD conditions. It was determined that the NCNTs were an effective N_2 gas conduit, wherein a decreasing pressure was observed with an increase to the inner diameter of the nanotubes. Using similar NCNTs,

the effect of dosing time, temperature, and substrate on the Pt size were analyzed using ALD. While no singular condition resulted in the sole production of single Pt atoms, modifying both the substrate and dosing time were shown to provide the greatest potential for producing individual Pt atom catalysts.

Acknowledgements

I would like to take this opportunity to thank all the individuals who have contributed to the completion of my thesis. Whether it was acting as a mentor, being a person to bounce ideas off or helping me understand the theory behind the microscope, to just being someone who got my mind off work when I desperately needed a break. Without all of you, I would not have finished my thesis, or my Ph.D.; this is not just my accomplishment, but yours as well.

The first person I would like to thank is my supervisor, Prof. Gianluigi Botton, for all your guidance and care. You answered all my theory based questions and encouraged my exploration with the microscope through specific training sessions with experts in different fields. Unlike other supervisors, you also acted as a nurturer when I would approach you with my panicky questions during exam time and throughout my thesis writing. I am truly grateful for having you as my supervisor. While this may not be appropriate for a thesis, I know you will understand; thanks, dog.

I would also like to thank my committee members Prof. Adam Hitchcock and Prof. Joey Kish. I have greatly appreciated the comments and suggestions you have provided regarding my work during our numerous committee meetings, and meetings outside those. These comments have improved my understanding of this work and improved the quality of my thesis. Furthermore, I would like to thank Prof. Hitchcock for voluntarily running experiments on my samples to help confirm results.

I owe a lot to my collaborators, Prof. Andy Sun and various past and present members of his research group at Western University, in particular, Shuhui Sun, Naincai Cheng, and Andrew Lushington. Thank you for providing me with such interesting materials to examine, and the opportunity to learn so much about carbon based materials and the PEMFC, both of which may have very bright futures in the academic community.

I also want to acknowledge the CCEM staff. I am grateful to Andreas Korinek and Andy Duft for maintaining the microscopes in good operating condition and for knowing

the answers to my trouble-shooting questions. I owe a lot to Andy, without his help many of my experiments would not have been possible. Thank you for modifying equipment to suit my needs, and being willing to help design and machine new parts to make my work possible. I'm also thankful for Travis Casagrande, who performed all the Auger quantification and SEM imaging in this thesis, and became a good friend. I look forward to future game nights.

My group members have contributed greatly to my knowledge in the microscopy field, but also in maintaining my sanity throughout the years. I have been lucky to work with an amazing group of individuals. All of them have taught me so much and encouraged many of my ideas. While everyone played a role in the completion of my thesis, there are a few specific individuals I would like to thank. To begin, I would like to thank Nicolas Gauquelin for introducing me to the microscope and acquiring many of my first images and spectra. Next, I would like to thank both Nicolas and Matthieu Bugnet for taking the time to painstakingly train me on various aspects of the microscope; not to mention the many late nights and weekends you stayed with me on the microscope just so I could finish acquiring that one last (or ten last) spectra. Not to be forgotten are David Rossouw, Alex Pofelski, Isobel Bicket, Andrew Scullion, Lidia Chinchilla, Michael Chatzidakis, and Kevin Villegas for your contribution to the work listed in this thesis. Lastly, a big thank you to Mickey Chan, Steffi Woo, Matthieu Bugnet, Sagar Prabhudev, Alex Pofelski, Isobel Bicket, Viktor Kapetanovic, and Eric Daigle for always being there when I need someone to hang out with and especially for listening to me vent while completing my thesis writing.

A special thank you is necessary to Kelly Leighton and Matthieu, for both volunteering to edit my thesis for its grammatical and technical content. I greatly appreciate the hard work and the improvements you made to my thesis.

Last but certainly not least, I would like to express my gratitude for my family and friends. While you may not have helped me scientifically, you helped me mentally. Every time I thought I had enough, you were there with your encouragement and loving words. Jeff, I know you took the brunt of my stress, and for that I am very sorry, but know that I

appreciate your patience and am blessed to have you by my side. Your strength and ability to make me smile kept me going in those difficult moments. I would also like to thank my grandparents for all their encouragement and pride in the work that I do. My only regret is that I wasn't able to finish my Ph.D. before my Dredi's passing; however, I know he would be very happy to see me finish, as he was a great supporter of my academic endeavours. To my brother, Dan, thank you for making me laugh, whether it is from my memories of you as a kid, or just being yourself now. Master Alvey, Master Hance, and Ms. Jolanta Oko, thank you for taking me as a student, your training provided me with a creativity and strength that I carried throughout my Ph.D. process. Pooper, you were the best furry study buddy I could have asked for, and you will be missed; for you I have included my "carbon zoo" in my thesis. Lastly, I would like to thank my parents, Deb Stambula and Nick Stambula. Together you have always provided me with patience, nurturing, and when needed, tough love. With your guidance and encouragement, I have gained confidence, courage, and a work ethic required to finish this thesis.

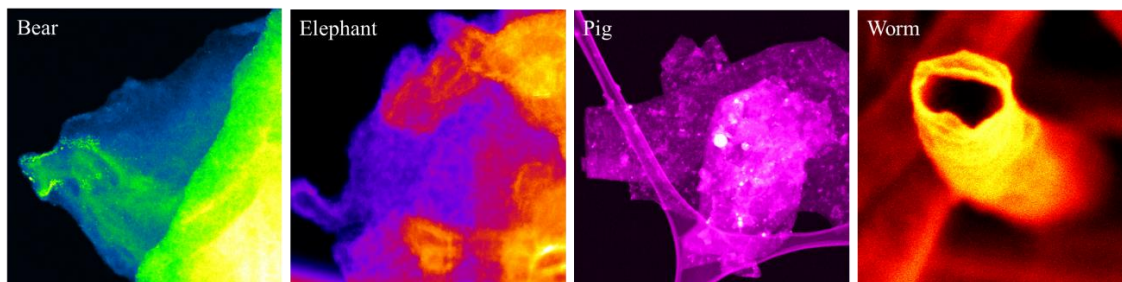


Figure 1 My love for animals and my creative side led to find animals in graphene sheets and carbon nanotubes (colouring applied with ImageJ). Welcome to the carbon zoo!

To my parents, with love.

Table of Contents

Abstract	iii
Acknowledgements	v
Table of Contents	viii
List of Figures	xiv
List of Tables	xvii
List of Abbreviations and Symbols	xviii
Declaration of Academic Achievement	xix
Chapter One	1
Introduction	1
1.1 Fuel Cells: A Quick Introduction	2
1.1.1 PEMFC	3
1.1.1.1 Challenges and Solutions	5
1.1.2 Hydrogen Evolution Reaction	6
1.2 Material Selection	7
1.2.1 Catalyst Operation and Selection	8
1.2.1.1 Pt Deposition	10
1.2.1.2 Atomic Layer Deposition	11
1.2.1.3 Catalyst: Pt Atoms and Clusters	13
1.3 Electrode Support	15
1.3.1 Graphene	16
1.3.1.1 Nitrogen-Doped Graphene	19
1.3.1.2 Advantages and Limitations	20

1.4 Summary.....	24
Chapter Two	26
Electron Microscopy	26
2.1 Electron Interactions with Matter.....	27
2.2 Using TEM to Study Graphene and Heavy Atoms	29
2.2.1 High Resolution TEM	32
2.2.1.1 Increasing the Temporal Coherence	35
2.2.1.2 Electron Source Selection	36
2.2.1.3 Monochromator Excitation.....	36
2.2.1.4 Electron Source Acceleration Voltage	37
2.2.1.5 Examples of HRTEM Imaging of Graphene.....	38
2.2.2 High Resolution STEM.....	40
2.2.2.1 STEM Image Formation.....	40
2.2.2.2 Examples of HRSTEM Imaging of Metal-Graphene Interactions....	43
2.2.3 EELS	44
2.2.3.1 Elemental Quantification using EELS	46
2.2.3.2 Signal Processing: Independent Component Analysis	47
2.2.3.3 Examples of EELS Characterization of Metal Atoms on N-Doped Graphene and CNTS	47
2.2.4 Special Techniques: Identical Location Transmission Electron Microscopy (ILTEM)	49
2.3 Auger Photoelectron Spectroscopy	49
2.3.1 Elemental Quantification using Auger Spectroscopy	51
2.4 Summary.....	52

Chapter Three.....	53
Structural and Chemical Characterization of Graphene with Pt Atoms and Clusters	53
3.1 Experimental Conditions	54
3.1.1 Material Preparation	54
3.1.2 TEM Sample Preparation	54
3.1.3 Microscope Settings	54
3.1.4 Quantification of HAADF Images and EEL Spectra	56
3.2 Results and Discussion	57
3.2.1 Graphene	57
3.2.2 Nitrogen-Doping	62
3.2.2.1 Density Functional Theory (DFT) ELNES Calculations	66
3.2.3 Pt Catalyst.....	77
3.2.4 Electrochemical Activity of Pt Atoms and Clusters on N-Doped Graphene	85
3.2.4.1 HER Electrocatalyst Selection	88
3.2.4.2 ALD Pt Catalysts on N-Doped Graphene and Graphene Nanosheet Supports for the HER	89
3.2.5 ILTEM of Pt on Graphene and N-doped Graphene	94
3.2.5.1 Experimental Conditions.....	95
3.2.5.2 ILSTEM of Pt on Graphene and N-Doped Graphene	98
3.3 Summary	102
Chapter Four.....	105
Production and Characterization of Single Sheet N-Doped Graphene	105
4.1 Nitrogen Quantification on TEM Grids Using Auger Spectroscopy	107

4.1.1 Experimental Conditions and Design.....	108
4.1.2 Results and Discussion.....	112
4.2 Production of N-Doped Graphene TEM Grids Using In-House Techniques	117
4.2.1 Characterization of N-Doped Graphene Using High Resolution STEM	118
4.2.2 NanoMill®: Nitrogen Ion Source.....	119
4.2.2.1 Experimental Conditions.....	119
4.2.2.2 Results and Discussion.....	122
4.3 Pd Deposition on Pristine Graphene TEM grids	129
4.4 Summary.....	133
Chapter Five.....	135
NCNT Characterization and ALD Fine Tuning	135
5.1 Gas Filled NCNTs with ALD Pd	136
5.1.1 Experimental Conditions.....	137
5.1.1.1 Material Preparation.....	137
5.1.1.2 High Resolution Imaging	137
5.1.1.3 Auger Quantification.....	138
5.1.1.4 EELS Quantification and ICA Conditions	138
5.1.2 Identification of Gas and Elemental Components.....	143
5.1.3 Pressure Quantification	153
5.2 ALD Fine Tuning to Consistently Produce Single Atom Catalysts with NCNTs	160
5.2.1 Experimental Conditions.....	164
5.2.1.1 Material Preparation.....	164
5.2.1.2 HAADF Imaging.....	164
5.2.1.3 Image Quantification.....	165

5.2.1.4 Error Analysis and Histogram Formation	168
5.2.1.5 EELS Analysis	172
5.2.1.6 Auger Analysis	173
5.2.2 Elemental Quantification and Examination of NCNTs.....	173
5.2.3 Effect of ALD Conditions	182
5.2.3.1 Effect of Dosing Time	183
5.2.3.2 Effect of Temperature	187
5.2.3.3 Effect of Substrate	190
5.3 Summary	192
Chapter Six.....	195
Synopsis and Future Work.....	195
6.1 Future Work and Considerations	199
References	203
Appendix	239
Appendix 1: N-doping Graphene TEM Grids using a Plasma Cleaner and Gentle Mill™	239
Appendix 1.1 Plasma Cleaner: Nitrogen Plasma Source	239
Appendix 1.1.1 Experimental Conditions	239
Appendix 1.1.2 Results and Discussion	241
Appendix 1.2 Gentle Mill: Nitrogen Ion Source	246
Appendix 4.2.1 Experimental Conditions	246
Appendix 4.2.2 Results and Discussion	248
Appendix 2: N-K Edge Reference Spectra	252
Appendix 3: N-K EELS Maps Gas Filled NCNTs	253
Appendix 4: Images Used for ALD Pt Quantification	254
Appendix 5: Individual Histograms from Each Tube Analyzed in Appendix 4.....	262

Appendix 6: STEM Image Simulation.....	268
Appendix 7: Copyright Permissions	271

List of Figures

Figure 1.1 PEMFC electronic assembly commonly known as a membrane electrode assembly	4
Figure 1.2 PEM water splitting electronic assembly.	7
Figure 1.3 <i>d</i> -band theory for transition metals.	10
Figure 1.4 Pt ALD reaction mechanism for ALD	12
Figure 1.5 The growth rate of Pt nanoparticles as a function of the number of ALD cycles of Pt ALD on acid treated carbon paper	13
Figure 1.6 Catalytic activity of Pt atoms and clusters, as a function of <i>d</i> -band center.	15
Figure 1.7 Two-dimensional graphene crystal structure of sp^2 bonded C	17
Figure 1.8 Pt chemically reduced on few-layer graphene sheets	19
Figure 1.9 Possible dopants in N-doped graphene.	20
Figure 1.10 Pt atom locations on N-doped graphene.	23
Figure 2.1 Simplistic schematic of the electron interactions with matter.....	28
Figure 2.2 HRTEM image formation.	34
Figure 2.3 HRTEM images and computed diffractogram from a single sheet of graphene.	39
Figure 2.4 Simplified schematic of STEM image formation and the relative detector positions.	40
Figure 2.5 HAADF micrographs of graphene with deposited metals.	44
Figure 2.6 Schematic of EELS total spectrum and ELNES.....	45
Figure 2.7 Simplified schematic of a KLL Auger electron excitation.	51
Figure 3.1 HAADF and HRTEM images of N-doped FLG and commercially available graphene.	58
Figure 3.2 Diffraction pattern of N-doped graphene with 50 ALD Pt cycles.....	59
Figure 3.3 C-K ELNES from various C sources.	61
Figure 3.4 EELS of C-K, N-K, and O-K edges acquired from N-doped graphene with 50 ALD Pt cycles. 62	
Figure 3.5 Normalized EEL spectra of C-K and N-K edges acquired from three N-doped graphene sheets with 50 ALD Pt cycles and two separate areas on sheet 1.	64
Figure 3.6 Relaxed and optimized structures used for DFT calculations.....	68
Figure 3.7 Convergence of the basis set of the graphene structure using the total DOS.....	69
Figure 3.8 Converged DOS for the five structures outline in Figure 3.6	71
Figure 3.9 N-dopant PDOS for the total N contribution and N-p states.....	73
Figure 3.10 Calculated N-K ELNES for each N-dopant	76
Figure 3.11 HAADF images of 50, 100, and 150 ALD Pt cycles on N-doped FLG.	79
Figure 3.12 HRTEM image of N-doped graphene with 50 ALD Pt cycles at two separate locations.....	80
Figure 3.13 EDX spectra from a refence area and the sample.	81
Figure 3.14 Calculation of Pt atoms (purple) located at an edge site bonded to C atoms (brown) adjacent to a pyridinic-dopant (green).....	83
Figure 3.15 ADF images and respective HER activity of N-doped graphene with 50 and 100 ALD cycles.	92
Figure 3.16 Catalytic activity comparison of N-doped graphene to graphene with 50 ALD Pt cycles.	94
Figure 3.17 IL-TEM microscopy set-up and notes for easy identification of sample positions.	96
Figure 3.18 Electrochemical ILTEM experimental set-up and results.....	97
Figure 3.19 ILTEM results of the graphene substrate with 50 Pt ALD cycles	99
Figure 3.20 ILTEM results of the N-doped graphene substrate with 50 Pt ALD cycles	101
Figure 4.1 TEM holder adaptation for Auger quantitation	109

Figure 4.2 Auger quantification experimental set-up with TEMH.	110
Figure 4.3 Auger quantification TEMH configurations.....	112
Figure 4.4 Effect of tilt angle and aperture arrangement when operating at 10 kV on a holey C TEM grid.	114
Figure 4.5 Effect of accelerating voltage, tilt angle, and aperture size on the PD from a holey C TEM grid.	115
Figure 4.6 SEM image of a hole in the C film with various tilt angles and the comparison of the Auger spectra acquired over a hole and over an aperture.	116
Figure 4.7 HR-STEM images of Graphene Supermarket© TEM grids	119
Figure 4.8 NanoMill® experimental set-up.....	120
Figure 4.9 Auger quantification of various NanoMill® experiment configurations	124
Figure 4.10 SEM SE images comparing N-doped graphene to N-doped graphene with O ₂ /H ₂ plasma exposure.....	125
Figure 4.11 HRTEM and EELS analysis of NanoMill® N-doped graphene sample.	128
Figure 4.12 ALD Pd on Graphene Supermarket© TEM grid	130
Figure 4.13 EELS spectrum images acquired from ALD Pd on a Graphene Supermarket grid.	132
Figure 5.1 Various steps used in the quantification of the N ₂ pressure within the NCNT.	141
Figure 5.2 Experimental measurement of the diameter of the NCNTs.	142
Figure 5.3 NCNT images acquired by (a) SEM (b,c) ADF, and (d,e) HRTEM.....	144
Figure 5.4 EELS N-K maps and edges from NCNTs.	146
Figure 5.5 Higher energy NCNT ICA results showing different spectral components	149
Figure 5.6 NCNT ICA C-K results showing different spectral components.....	150
Figure 5.7 ICA results from Figure 5.4	152
Figure 5.8 EELS N ₂ gas quantification results.	156
Figure 5.9 Quantitative analysis of the N density (atoms/nm ³) for each compartment within the NCNTs containing N ₂ as a function of the NCNTs' compartment volume.	160
Figure 5.10 Experimental steps used for the quantification of the Pt equivalent diameter.	167
Figure 5.11 Error analysis for the Pt quantification process.	169
Figure 5.12 Error analysis results from five days of study on a single HAADF image with bins showing the experimental error.	170
Figure 5.13 EELS analysis of NCNT before Pt deposition.	176
Figure 5.14 EELS analysis of Pt deposited on NCNTs for 30 minutes at a temperature of 250°C.	177
Figure 5.15 Second and third, EELS analysis of Pt deposited on NCNTs for 30 minutes at a temperature of 250°C.....	179
Figure 5.16 EELS analysis of Pt deposited on NCNTs for 60 minutes at a temperature of 250°C	180
Figure 5.17 High energy EELS analysis of Pt deposited on NCNTs for 60 minutes at a temperature of 250°C.....	181
Figure 5.18 Effect of dosing time on the equivalent diameter of Pt with NCNTs and a temperature of 250°C.....	185
Figure 5.19 Effect of dosing time on the equivalent diameter of Pt with PCNTs and a temperature of 250°C.....	186

Figure 5.20 Effect of dosing time on the equivalent diameter of Pt with NCNTs and a temperature of 100°C.....	187
Figure 5.21 Effect of temperature on the equivalent diameter of Pt with NCNTs and a constant dosing time of 1 minute	188
Figure 5.22 Effect of temperature on the equivalent diameter of Pt with NCNTs and a constant dosing time of 30 minutes	190
Figure 5.23 Effect of substrate on the equivalent diameter of Pt with a constant dosing time of 1 minute and a temperature of 250°C.....	192
Figure A.1.1 N ₂ /H ₂ plasma activated in the Solarus 950 Gatan Advanced Plasma System. The central window shows the pink colour of the plasma inside the chamber.	240
Figure A.1.2 Quantification results from N plasma exposure.	243
Figure A.1.3 STEM images and EELS analysis from N-doped graphene after exposure to the Solarus plasma cleaner at 30 W for 20 minutes with direct N plasma exposure and Pt deposited using 50 ALD cycles.	245
Figure A.1.4 Gentle Mill experimental set-up.	247
Figure A.1.5 Average N % (normalized to C and N) in Graphene Supermarket© TEM grids, as characterized by Auger spectroscopy	249
Figure A.1.6 STEM images and EELS analysis of Gentle Mill sample acquired at 50 V for three minutes using a current of nine to ten µA.	250
Figure A.2.1 EELS N-K reference spectra acquired from gaseous species.....	252
Figure A.3.1 N-K areal density maps normalized to the maximum areal density for each individual NCNT.	253
Figure A.4.1 250°C NCNT 1minute.....	254
Figure A.4.2 250°C NCNT 30 minutes	255
Figure A.4.3 250°C NCNT 60 minutes	256
Figure A.4.4 100°C NCNT 1 minute.....	257
Figure A.4.5 100°C NCNT 30 minutes	258
Figure A.4.6 175°C NCNT 1 minute.....	259
Figure A.4.7 250°C PCNT 1 minute	260
Figure A.4.8 250°C PCNT 30 minutes	261
Figure A.6.1 JEMS multislice ADF image simulations of six graphene layers	268
Figure A.6.2 Line profiles acquired from averaged intensities in the yellow rectangle in Figure A.6.1. ...	269
Figure A.6.3 JEMS multislice ADF image simulations from 21 nm thick graphene sheet.....	270

List of Tables

Table 1.1 Electron mobility in various C support materials.....	24
Table 2.1 Equations to calculate optimized C_1 and C_3 coefficients.	35
Table 3.1 Atomic N fraction deduced from quantification of the EELS N-K edges	65
Table 3.2 LAPW basis set and ELNES convergence values.	69
Table 5.1 Auger quantification of NCNTs after Pd deposition.....	145
Table 5.2 Number of images analyzed, and the number of Pt entities counted per image.	172
Table 5.3 Auger Spectroscopy elemental quantification of NCNTs.	175
Table 5.4 Average measurement values from various deposition parameters of the first ALD cycle for Pt on NCNTs and PCNTs.....	183

List of Abbreviations and Symbols

ADF	annular dark field	LAPW	linear augmented plane wave
ADT	accelerated degradation test	LDA	linear density approximation
ALD	atomic layer deposition	MAADF	medium angle annular dark field
at. %	atomic percent	MD	molecular dynamics
BF	bright field	MeCpPtMe ₃	(methylcyclopentadienyl) trimethyl platinum
C ₁	defocus	MLLS	multiple linear least square
C ₃	third-order spherical aberration	MO	molecular orbital
C ₅	fifth-order spherical aberration	MWCNT	multi-walled carbon nanotube
C _c	chromatic aberration	NCNT	nitrogen-doped carbon nanotube
CVD	chemical vapour deposition	ICE	internal combustion engine
CNT	carbon nanotube	PCNT	pristine carbon nanotube
DF	dark field	PCTF	phase contrast transfer function
DOS	density of states	PD	percent difference of Auger C-KLL signal for a hole and C film
DFT	density functional theory	PD10kV	percent difference of Auger C-KLL signal measured at 10 kV for a hole and C film
ECSA	electrochemically active surface area	PDOS	partial density of states
EDXS	energy dispersive X-ray spectroscopy	PEMFC	proton exchange membrane fuel cell
EELS	electron energy loss spectroscopy	PSD	particle size distribution
EPW	exit plane wave	ORR	oxygen reduction reaction
ETEM	environmental transmission electron microscopy	OTF	optical transfer function
FC	fuel cell	RK _{max}	number of basis set functions
FEG	field emission gun	ROI	region of interest
FLG	few layer graphene	sccm	standard cubic centimeter per minute
FWHM	full width at half maximum	SCF	self consistent field
GDL	gas diffusion layer	SE	secondary electrons
GDP	gross domestic product	SEM	scanning electron microscopy
GHG	green house gas	SWCNT	single-walled carbon nanotube
GIF	GATAN image filter	STEM	scanning transmission electron microscopy
HAADF	high angle annular dark field	STM	scanning tunnelling microscopy
HOPG	highly oriented pyrolytic graphite	STXM	scanning transmission X-ray microscopy
HPLC	high performance liquid-chromatography	TEM	transmission electron microscopy
HRTEM	high resolution transmission electron microscopy	TEMH	transmission electron microscope grid holder for Auger spectroscopy
ICP-AES	inductively coupled plasma-atomic emission spectroscopy	VASP	Vienna Ab initio software package
ILTEM	identical location transmission electron microscopy	wt. %	weight percent
ILSTEM	identical location scanning transmission electron microscopy	XANES	X-ray absorption near edge structure
k-mesh	number of k-points in reciprocal space	XPS	X-ray photoelectron spectroscopy
LaB ₆	lanthanum hexaboride	Z	atomic number

Declaration of Academic Achievement

Peer-reviewed publications:

S. Stambula, N. Gauquelin, M. Bugnet, S. Gorantla, S. Turner, S. Sun, J. Liu, G. Zhang, X. Sun, G.A. Botton, Chemical Structure of Nitrogen-Doped Graphene with Single Platinum Atoms and Atomic Clusters as a Platform for the PEMFC Electrode, *The Journal of Physical Chemistry C*, 118 (8), 3890-3900, 2014.

N. Cheng¹, **S. Stambula**¹, D. Wang, M. Norouzi Banis, J. Liu, A. Riese, B. Xiao, R. Li, T-K. Sham, L-M. Liu, G.A. Botton, X. Sun, Platinum single-atom and cluster catalysis of the hydrogen evolution reaction, *Nature Communications*, 7, 13638, 2016.

E.T. Bjerglund, M.E.P. Kristensen, **S. Stambula**, G.A. Botton, S.U. Pedersen, K. Daasbjerg, Efficient Graphene Production by Combined Bipolar Electrochemical Intercalation and High-Shear Exfoliation, *ACS Omega*, 2 (10), 6492-6499, 2017.

¹ Contributing first authors.

Chapter One

Introduction

There is an international consensus that climate change is occurring and can be attributed to greenhouse gas (GHG) emissions, with the transportation sector being one of the top contributors to GHG emissions in Canada [1]. Short term emission trends show a decrease in GHG emissions since 2005 in all sectors with the exception of transportation [2], where the common internal combustion engine (ICE) of road vehicles is responsible for 81 percent of fuel use in the transportation sector [2], [3]. Not only are natural disasters expected due to climate change, as seen by increased extreme weather activity in recent years, but more importantly the cost and risk can amount to five percent of the global gross domestic product (GDP) by 2050 [4]. This suggests that climate change mitigation is required to reduce costs associated with natural disaster occurrences and risk management.

In an effort to decrease or remove GHG emissions from road transportation, modifications to industry and personal attitudes are essential [3]. As vehicles are becoming more economically viable, a global increase in car ownership has been observed. With more vehicles at the disposal to individuals, road congestion has increased, and general trends show individual motor travel rather than public transportation or zero-emission modes of transportation (i.e. walking or cycling) have been preferred [3]. In order to maintain the convenience and preference of personal vehicles and still decrease GHG emissions, low- or zero-emission vehicles must become the norm.

Global adoption of a new technology for the masses requires that the performance matches or exceeds current technology. Within the transportation industry this includes vehicle power, speed, travel distance, and refueling time. A variety of technologies are available with reduced GHG emissions for personal use vehicles, with batteries and fuel cells (FCs) primarily competing as the new industry favourite. Each option has reduced GHG emissions in comparison to the ICE; however, neither option is zero-emission due to the required processes to produce the fuels [3]. In regards to performance, batteries lag behind the ICE and FCs due to their weight; generally causing the vehicles to operate at lower speeds or travel less distance on a single charge [3], [5]. Furthermore, battery-operated vehicles can take hours to refuel [3]. Accordingly, to increase the desirability and probability of adopting a new clean technology to replace the ICE, it is recommended that FC vehicles be considered as the key candidate [6].

1.1 Fuel Cells: A Quick Introduction

FCs were first realized by Sir W. Groves in 1842, where he demonstrated that the connection of a circuit consisting of separate catalysts in O₂ and H₂ rich environments produced an electrical current [7]. This particular construction is known today as the proton exchange membrane FC (PEMFC); however, it is only one of six main classes of FCs. Each class of FC is determined by the reacting gases, and the operating temperature [8]. Generally, low temperature FCs have lower reaction kinetics and require more complex catalyst and electrode designs to facilitate the electrochemical reactions [8]. Further, the reacting gases control the power of the FC, as determined by the number of electrons delivered to the load, and complexity of a single reaction scheme. The variations in the FC

classes impart each FC to a specific application [8], such as personal power sources for houses or cars, or scaling to power grid energy production [9].

The FC compatibility with a specific application requires the delivery of a suitable quantity of power. The PEMFC lends itself to the automotive industry, where it can be utilized to replace the ICE [8]. The PEMFC offers the benefits of low CO₂ emissions [10], a higher energy conversion efficiency in comparison to the ICE [10], and the simplicity of the PEMFC design suggests that less mechanical damage will occur during operation [8]. The low operating temperature also offers a fast start-up, as the FC does not require an initial heating, therefore instantaneous operation is possible as desired in automobiles [11].

1.1.1 PEMFC

The PEMFC makes use of a spontaneous reaction between protons and O ions to produce water. Separation of the chemical reactions by isolating the electrodes results in a potential drop that can be utilized as a power source when applied to a load. The anode yields protons and electrons from H₂ in the presence of a catalyst, as expressed by



The protons react with O atoms through a reduction reaction to form water,



where a theoretical potential drop of 1.229 V is generated [10]. A membrane is placed between the electrodes for electrical isolation to ensure the electrons are delivered to the load; however, the membrane must conduct protons to facilitate (1.2), thus it is referred to as an electrolyte (Figure 1.1). The membrane is composed of a hydrophobic backbone with hydrophilic side-chains [8], therefore in the presence of water the polymer phase separates into a porous system where the morphology and pore size are controlled by the relative lengths of the backbone and side-chains. Secondly, the side-chain must contain a negative charge to facilitate the transportation of the proton to the cathode, whilst preventing the

transportation of O^{2-} ions to the anode. Water is required in the membrane to create the porous system and create a medium for free movement of the proton. The conductivity of the electrolyte is controlled by the water content; typically, 20 water molecules per one side chain is ideal to prevent swelling or incomplete phase separation of the porous system [8].

The entire PEMFC contains various components to aid in the delivery of the reactant gases and manage the water content in the membrane (Figure 1.1). Following the electrodes, a gas diffusion layer (GDL) is fabricated, consisting of a series of macroporous to microporous C paper coated with a hydrophobic polymer (generally polytetrafluoroethylene) [12], [11]. The GDL controls the diffusion of the reacting gasses to the electrode to ensure an even distribution is obtained across all catalysts [11]. Further, the polytetrafluoroethylene prevents excess water produced by (1.2) from clogging the membrane. Lastly, a current collector plate is placed at the end of each assembly to collect the generated current, introduce the reacting gases, separate the coolant and FC components, and isolate individual FCs when arranged in a stack for increased power production [12].

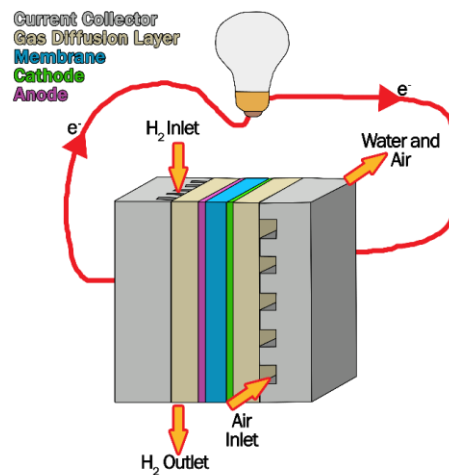


Figure 1.1 PEMFC electronic assembly commonly known as a membrane electrode assembly (adapted from [13]).

1.1.1.1 Challenges and Solutions

The theoretical potential drop imposed by the electrochemical reactions in the PEMFC is never achieved due to the most prevalent energy-losses that occur during the chemical reaction and transport of the electrons to the load, leading to a potential drop as low as approximately 0.6 V [14]. These losses are a result of poor kinetics at the electrode where the oxygen reduction reaction (ORR) is rate limiting, permeation of reactants and electrons through the membrane, and ohmic losses caused by electrical resistance in the electrode material [10], [8]. The poor kinetics and ohmic losses are a direct result of the catalyst selection and the electrode support conductivity, respectively. Selecting an electrode support of higher electrical conductivity than C black will increase the efficiency of the PEMFC by ensuring all electrons produced at the catalyst are delivered to the load. Further, selection of a catalyst with a proficiency in performing the ORR and many active sites will decrease the potential loss, as the reaction rate and number of reaction sites will increase, respectively. It has been shown that Pt operates most efficiently as a homocatalyst for both the hydrogen oxidation reaction and the ORR [8]. The number of active sites can be increased by increasing the surface area of the catalyst, as catalysts facilitate surface reactions. A method to increase the surface area of a material while utilizing the same load can be achieved by decreasing the size, thereby moving from bulk Pt catalysts to nanoparticles.

A major challenge for economical mass-production of the PEMFC is introduced through the high cost of the precious metal, Pt. Possible solutions include further downsizing the Pt catalyst into clusters or atoms [15]. This suggests that a method of producing Pt clusters must be developed. An additional issue plaguing the FC industry results in decreased efficiency over time due to catalyst degradation. Generally, nanoparticles will grow from dissolution of small particles followed by redeposition on larger particles (Ostwald Ripening), random particle movement on the support material

resulting in agglomeration, or small clusters depositing on large particles to reduce the Gibb's free energy by increasing the atomic coordination [12]. Degradation can be prevented by increasing the catalyst to support bond energy, thus further stabilizing the catalyst and decreasing the opportunity for diffusion and dissolution.

The US Department of Energy has set targets and measurement standards for FC light-duty vehicles with a standard production rate of 500,000 vehicles manufactured per year [9]. Within the 2015 and 2020 year targets the start-up time, specific power (650 W/kg), and power density (650 W/L) have thus far been met; however, the vehicles are still lacking durability (5,000 hours with less than a 10% loss), and cost (\$40/kW) [9]. The electrocatalyst and support material are major contributors to the targets not met hitherto, due to the high cost of the Pt catalysts, and degradation of the Pt catalysts and membrane support [9].

1.1.2 Hydrogen Evolution Reaction

Within the renewable energy sector, hydrogen production is critical to ensure pure H₂ gas is widely available for the PEMFCs in the automotive industry. Commonly, steam reforming of hydrocarbon gases is utilized; however, this results in GHG emissions and the reduction of individual country's autonomy of power production [16], [17]. Preferably, a clean production method would be utilized, such as an electrolysis method that uses electricity for the water splitting reaction. The greenness of this method can be argued depending on the nation's individual electricity production method, but in certain circumstances such as hydroelectricity, the water splitting method can be made clean through electrolysis [17].

Using a similar set-up to the PEMFC, PEM water splitting makes use of proton conduction through a water-soluble membrane. A potential greater than 1.229 V must be

applied to drive the reverse reactions of the PEMFC [10], in which hydrogen gas is produced at the cathode (hydrogen evolution reaction (HER)),



and oxygen is produced at the anode



as described in Figure 1.2. Similar challenges associated with the PEMFC, as outlined in *Chapter 1.1.1.1 Challenges and Solutions*, also apply to the PEM water splitting reaction, thus leading to the overall reduction in the efficiency and a need for a higher applied potential than 1.229 V. The material selection, as discussed in the following sections, also apply to the HER reaction, but the specific electrocatalysts used for the HER will be discussed in *Chapter 3.2.4.1 HER Electrocatalyst Selection*.

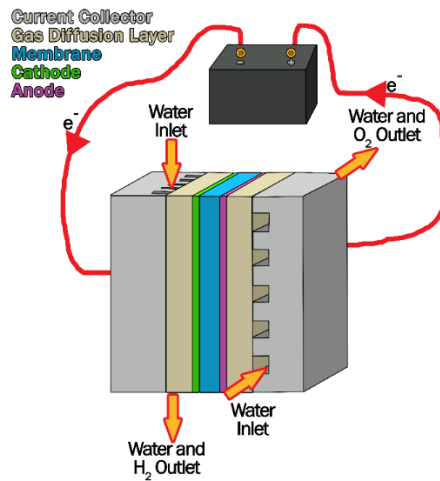


Figure 1.2 PEM water splitting electronic assembly.

1.2 Material Selection

Before economical mass production can be considered for the PEMFC, the efficiency must be increased by addressing the loss mechanisms and cost. Specifically, the support material

must have high electrical conductivity to decrease the ohmic losses, high surface area to increase catalyst loading, and it must have the ability to form strong covalent bonds with the catalyst to prevent Pt agglomeration during deposition and cycling [18], [19]. Further, the support material must be thermally and electrochemically stable to prevent degradation of the support during FC operation [18], [19].

The selection of the catalyst must also be addressed, such that it is desired to decrease the Pt loading while maintaining or increasing the electrochemically active surface area (ECSA). The process of decreasing the catalyst size to increase the surface area to volume ratio suggests the use of nanoparticles, or Pt clusters and atoms. Moreover, the use of a secondary catalyst for the ORR, such as a dopant in the support material would benefit the PEMFC as this could increase the number of active catalytic sites.

1.2.1 Catalyst Operation and Selection

The sole purpose of a catalyst is to facilitate chemical reactions by increasing the proximity and changing the electron distribution within reactants. The ORR can occur through three different mechanisms that can produce four or two-electrons [20]. The adsorption of O₂ in a side-on manner results in the consumption of four-electrons; however, the adsorption of O₂ end-on can proceed in the two or four-electron pathways, producing hydrogen peroxide and water, respectively [20]. The mechanism is further complicated by the fact that the proton can react with O through surface adsorption or by direct bonding to an O atom [21]. Ideally, the four-electron process will be followed, as this enhances the total current per single surface reaction.

Norskov proposed a method to predict the activity of a catalyst by the position of the *d*-band center for the transition metals, which is summarized herein [22]. The *d*-band is formed from the overlapping density of states (DOS) of the valence *d*-orbital electrons. When an adsorbate approaches the surface of a metal, the presence of a metallic band at

the same energy as a molecular orbital (MO) causes the formation of an interaction state between the electrons originating from the metal and molecule. The interaction state is broadened in comparison to the MO (Pauli Exclusion Principle), and forms a bonding and antibonding orbital when the *d*-band is narrow. The activity of the catalyst can be predicted by the center of the *d*-band, as this determines the position of the interaction state with respect to the Fermi level. The Fermi level is located at the highest filled electron orbital energy at absolute zero, where all energy states below are populated by electrons, and all states above are empty. As the *d*-band center shifts towards the Fermi level, the antibonding orbital of the interaction state shifts above the Fermi level and is no longer populated, thus strong chemisorption occurs between the metal and adsorbate (Figure 1.3 (a)). Conversely, when the *d*-band center shifts away from the Fermi level, the antibonding orbital is filled and adsorption is unstable, therefore leading to a lack of adsorption or enhanced desorption kinetics due to the instability in the chemisorption bond. When considering catalysis, the chemisorption process should not be too strong, as all active sites will be filled by the molecular adsorbates, and the dissociative process for the ORR will be prevented. Further, the binding energy of the adsorbate cannot be too weak, such that adsorption will not occur, or the desorption rate will surpass the dissociation rate. Figure 1.3 (b) compares the binding strength or *d*-band energy to the activity of varying catalysts for the ORR [22]. This suggests that Pt has the optimum binding energy for the ORR kinetics, thus providing its highest activity and dictating its conventional use in the PEMFC [22].

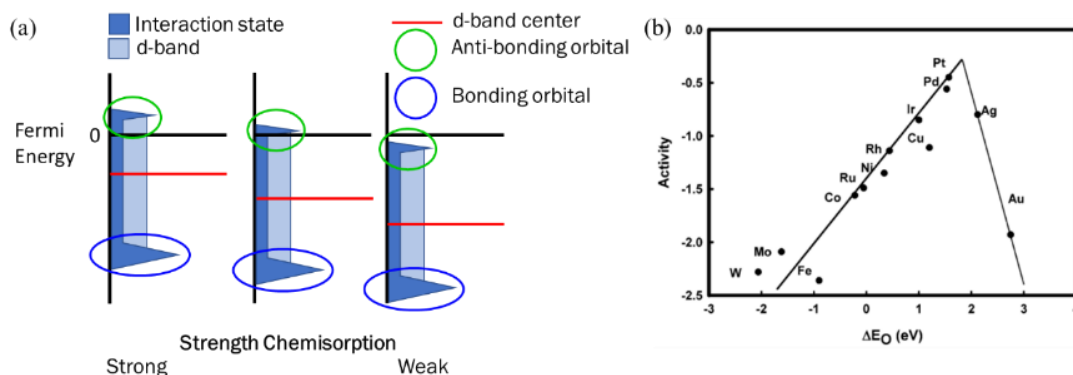


Figure 1.3 *d*-band theory for transition metals. (a) Schematic of DOS illustrating the chemisorption strength as a function of *d*-band metal position and adsorbate molecule interactions (adapted from [22]). (b) Volcano plot for the ORR as a function of O binding energy (ΔE_0). Reprinted with permission from ref. [23]. Copyright 2004 American Chemical Society.

The O_2 dissociation to form the adsorbed hydroxide species is rate limiting in the ORR. Therefore, increasing the *d*-band center of Pt would hinder the catalytic process, as the adsorbed molecular O_2 would remove active sites for dissociation [24], [25]. The catalyst-adsorbate interaction is further complicated when you move from well-defined surfaces of nanoparticles to metallic clusters of 2 to 20 nm, as the substrate-catalyst bond energy will affect the energy states of the catalyst [22], [26] and the geometric structure of the nanoparticle will affect the interaction strength with the adsorbate [27].

1.2.1.1 Pt Deposition

Conventionally Pt nanoparticles are deposited by chemical and heat reduction, sputtering, and electrodeposition [28]. Typically, these deposition techniques on graphene and C nanotubes (CNTs), result in nanoparticle diameters ranging from 2 to 9 nm [28]. The geometry and size of Pt nanoparticles have been extensively studied to investigate their effect on the catalytic activity for particles of 3 nm and greater [27]. Upon reducing the size of Pt nanoparticles, three effects are hypothesized to cause a modification in the ORR

rate: increased surface area, increased density of edge and kink sites to enhance adsorption, and varying crystal face ratios [29].

Ideally, the particle size will continue to decrease in an effort to decrease the loading and cost induced by the use of the Pt catalysts; eventually resulting in the employment of ultra-small Pt clusters (<1 nm). Unfortunately, the production of Pt clusters with a narrow size distribution is extremely difficult, due to agglomeration in an effort to reduce Pt surface energy through increased coordination. Experimentally, little is understood about the ORR on Pt clusters as trends concerning regular crystal structures do not apply due to the decreased coordination and lack of structure in the clusters. Moreover, the ORR is further complicated by the enhanced kink sites from the low coordination, and surface-bonding effects as the electron-distribution is modified from the Pt-substrate binding energy [30]. Additionally, the understanding of Pt cluster catalysts is not certain, as there is a debate in literature concerning whether clusters or nanoparticles are more electrocatalytically active for the ORR (discussed in detail in *Chapter 3.2.4 Electrochemical Activity of Pt Atoms and Clusters on N-Doped Graphene*). The need for a method to produce Pt clusters of consistent size and distribution is required to experimentally determine the ORR when downsizing Pt nanoparticles to clusters.

1.2.1.2 Atomic Layer Deposition

A method to produce conformal and homogenous thin films has been developed through a self-limiting process. Atomic layer deposition (ALD) utilizes a single gas phase reaction of chemical vapour deposition (CVD) and separates them into discrete surface reactions. In the case of Pt ALD, the substrate is first purged with a Pt precursor ((methylcyclopentadienyl) trimethyl platinum (MeCpPtMe₃)), followed by a purge gas to remove the reactant from the chamber. The O₂ precursors are then introduced into the chamber to form Pt-O on the surface and hydrocarbon by-products. The subsequent cycle

of Pt gas forms a Pt thin film or Pt nanoparticles on the surface of the substrate (Figure 1.4). One entire cycle includes the Pt gas precursor, purge gas, O₂ precursor, and final chamber purge [31]. The thickness of the thin film can be controlled by the number of ALD cycles, gas pressures, temperatures, and substrate material (discussed in detail in *Chapter 5.2 ALD Fine Tuning to Consistently Produce Single Atom Catalysts with NCNTs*).

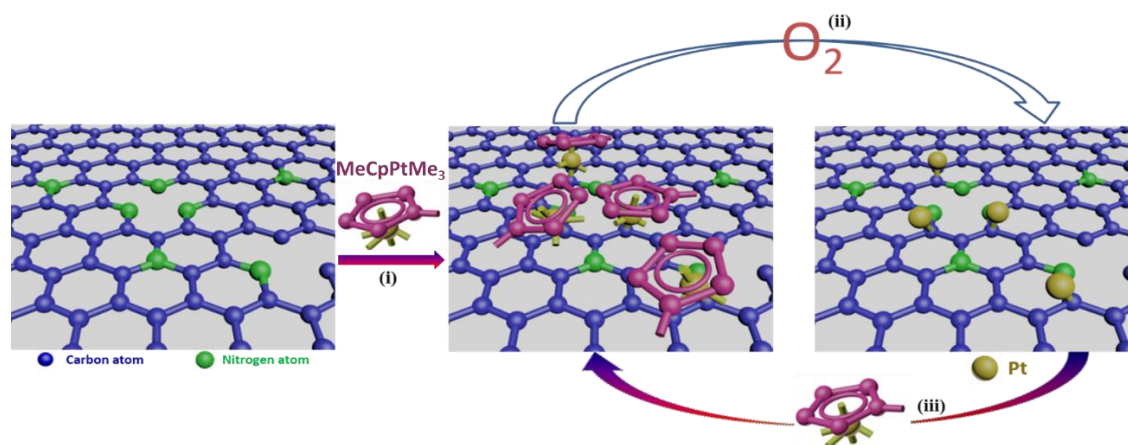


Figure 1.4 Pt ALD reaction mechanism for ALD. (i) In the first cycle the Pt precursor is introduced into the chamber. After the chamber is purged, (ii) O₂ gas is introduced into the chamber, causing the oxidation of the hydrocarbons. After a final purge the cycle begins again with (iii) the introduction of the Pt precursor (from [32]).

ALD on an inert surface, such as graphene, results in the formation of nanoparticles rather than thin films, as the entire surface is not ideal for chemisorption [33]. Consequently, the size of the nanoparticles depends on the number of ALD cycles and defects in the graphene lattice [34]. It has been experimentally demonstrated that ALD produces Pt particles of 2 to 3 nm when grown on varying substrates and with altering deposition parameters (i.e. temperature, gas concentration, pressure) [35], [34], [36], [37], [38]. Liu *et al.* reported on ALD of Pt on acid treated C paper [38]. Figure 1.5 demonstrates an initial substrate-enhanced growth rate attributed to the nucleation of Pt on functional groups (<20 ALD cycles), which created Pt atoms and clusters, followed by a linear growth in Pt loading through the production of Pt nanoparticles as a function of ALD cycles [38],

[39], [34]. This suggests that by operating in the initial regime, in which only Pt atoms and clusters are deposited, it may be possible to stabilize single Pt atoms and clusters on graphene.

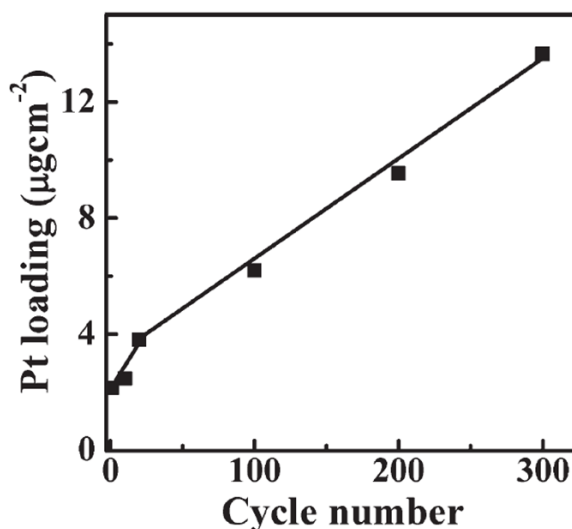


Figure 1.5 The growth rate of Pt nanoparticles as a function of the number of ALD cycles of Pt ALD on acid treated carbon paper. Reprinted with permission from ref. [38]. Copyright 2009 John Wiley and Sons.

1.2.1.3 Catalyst: Pt Atoms and Clusters

Theoretical and experimental studies have been conducted to understand the mechanism of catalysis on Pt clusters and atoms, specifically concerning H_2 oxidation and O_2 reduction. St. John *et al.* designed a layer-by-layer deposition technique to examine the ORR on substrate-free Pt clusters [29]. It was determined that the adsorption strength of OH after O_2 dissociation limited the ORR, as less free sites for adsorption were available and progression of the reaction reduced in comparison to nanoparticles. On the other hand, Zhou *et al.*, through density functional theory (DFT) calculations, showed that small Pt clusters (Pt_2) resulted in increased H_2 dissociative chemisorption and H desorption energy

in comparison to bulk crystalline Pt surfaces, due to the strong overlap of the Pt 5d orbitals with the H 1s orbital [40]. It was illustrated by Toyoda *et al.*, that the substrate affects the activity of the Pt cluster for the ORR, where the bond strength between the catalyst and substrate determines the available electronic states in the Pt cluster [30]. Figure 1.6 (a) illustrates the shift in *d*-band center for Pt clusters of varying size on different substrates. The binding energy increase in defective graphene (Pt/G(d)), compared to pure graphene (Pt/G), results in a decreased *d*-band energy for small clusters due to the enhanced Pt coordination with the substrate [30]. The decreased *d*-band energy of Pt on glassy C for larger nanoparticle diameters results in an increased ORR activity (Figure 1.6 (b)) from the decreased O₂ adsorption energy [30]. This suggests that small Pt clusters on defective graphene from vacancies or N-doping can possibly result in an enhanced ORR activity, as a wide range of *d*-band centers can be achieved through controlling the number of atoms in the Pt cluster. Holme *et al.* confirmed that the N-dopants decrease the *d*-band center of Pt clusters (Pt₄); however, a direct correlation of adsorption energy and *d*-band center does not form the volcano plot introduced from Norskov [41]. Because Pt clusters do not resemble classic bulk surfaces, the *d*-band center and the adsorption energy are not expected to be correlated, but the work-function illustrates a means of determining the correlation between the graphene defects and the ORR activity [41]. This suggests that NH bonds, interstitial N, and double vacancies may result in the highest ORR activity. Holme *et al.* also suggested that the ORR activity is increased, as the two-electron pathway is not stable on Pt clusters (Pt₄) on N-doped graphene, as was experimentally corroborated by Bai *et al.*, thus the four-electron pathway is favoured [41], [42]. Lastly, single Pt atoms were experimentally examined by Qiao *et al.* as a possible Pt catalyst, thus resulting in the ultimate surface area to volume ratio [43]. It was determined that single Pt atoms on an Fe₂O₃ substrate resulted in an increased CO oxidation activity in comparison to Pt clusters, as the Pt atoms transferred electrons to the substrate upon chemisorption which increased the availability of 5*d* states for molecular adsorption. This suggests that the positive charge induced on C atoms from N-doping can result in catalytically active single Pt atoms. Recent

review papers have outlined other single atom catalysts for the use in both the ORR and HER [44], [45], [46]; however, specific details will be discussed in *Chapter 3.2.4 Electrochemical Activity of Pt Atoms and Clusters on N-Doped Graphene*.

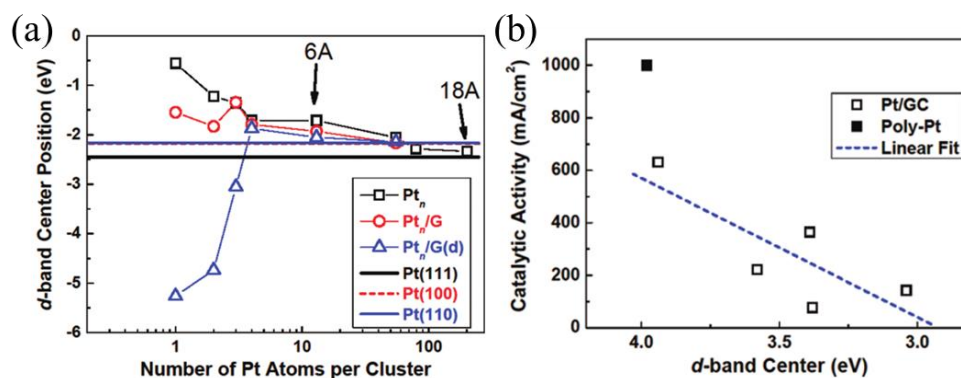


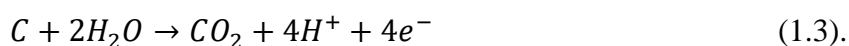
Figure 1.6 Catalytic activity of Pt atoms and clusters, as a function of d -band center. (a) d -band center position as a function of the number of Pt atoms per cluster for various Pt surfaces and substrates with (b) the respective experimental ORR activity for Pt on glassy C (Pt_n/G from (a)). Reprinted with permission from ref. [30]. Copyright 2011 American Chemical Society.

1.3 Electrode Support

In the 19th century, Grove's FC consisted of a porous Pt support to increase the ECSA for catalytic interaction, while also facilitating the diffusion of the gaseous species [47]. It was later realized that powdered materials increase the surface area to volume ratio compared to bulk materials, thus a transition to Pt black was utilized as the electrode material and the first FC was employed in space by NASA. A loading of 2-4 mg·cm⁻² was observed to be limiting the cost of the FC, therefore the Pt was distributed on C black, resulting in a reduced Pt loading of 0.35 mg·cm⁻² with a similar performance [48]. The operation rate

was maintained by increasing the surface area of Pt and the conductivity of the support through the use of C black, thus decreasing the ohmic loss in the FC.

Although C black enhanced the Pt loading by introducing a high surface area support, it is highly susceptible to degradation. Shao *et al.* reviewed potential degradation mechanisms of C black and illustrated that both electrochemical and chemical reactions can degrade the C support [18]. C corrosion occurs at a standard half-cell potential with reference to H of 0.207 V and can be written as:



According to Wu *et al.* the kinetics of the reaction are slow and corrosion is negligible below a potential of 1.1 V [12]. Nevertheless, the corrosion rate is enhanced in an environment lacking H₂, therefore corrosion is generally a product of FC start-up [12]. Further, the C support can undergo degradation through reaction with water:



Unfortunately, both degradation mechanisms are enhanced by the presence of Pt, thus promoting the decomposition of C at Pt sites which results in the loss of Pt during FC cycling [12], [18]. Another deterring mechanism is the production of CO in (1.4), as it acts as a poison to Pt catalysts, thus promoting the decrease of active sites available for the ORR [18]. Stevens *et al.* determined that a higher degree of graphitization produces a C support that is less susceptible to degradation due to the enhanced chemical stability [49].

1.3.1 Graphene

Two-dimensional crystals have been theorized for many years; however, it was not physically produced and experimentally examined until 2004, resulting in Geim and Novoselov being awarded the Nobel Prize for Physics in 2010 [50]. Graphene is a two-dimensional crystal composed of sp² bonded C, which is the basis material for zero-dimensional fullerenes, one-dimensional CNTs, and three-dimensional graphite (Figure

1.7). Because the entire volume of graphene is essentially a surface, a large surface area to volume ratio is available for Pt deposition. Further, electrons and holes undergo ballistic transport in graphene, thus resulting in an enhanced electrical conductivity as scattering centers are separated by $0.3 \mu\text{m}$ even in the presence of a 10^{12}cm^{-2} dopant concentration [51]. It should be noted that to maintain the electrical conductivity of graphene the material cannot exceed 10 layers [52]. The increased surface area and electrical conductivity suggests that the use of graphene as an electrode support will greatly increase the FC efficiency through possible increased Pt loading and decreased ohmic losses.

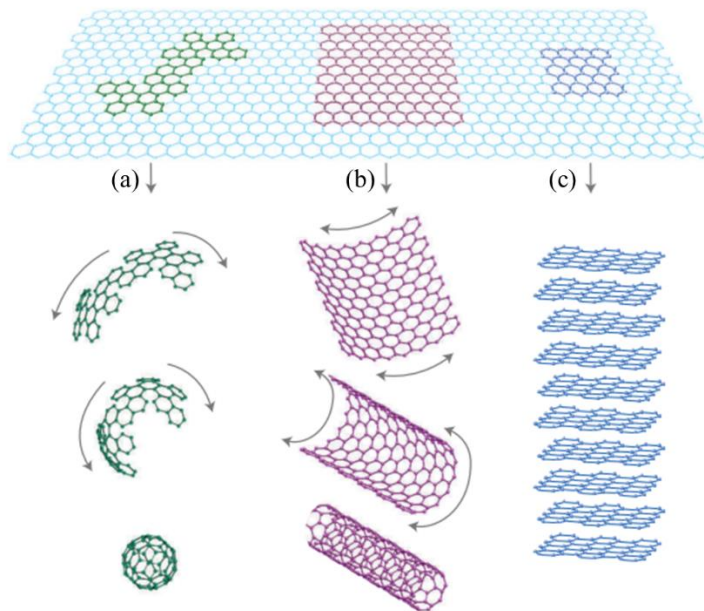


Figure 1.7 Two-dimensional graphene crystal structure of sp^2 bonded C used to form (a) zero-dimensional fullerenes, one-dimensional CNTs, and (c) three-dimensional graphite. Reprinted by permission from Macmillan Publishers Ltd: Nature Materials (ref. [51]), copyright (2007).

Graphene can be produced through mechanical exfoliation of graphite [51], [53], [54], CVD [55], [56], [57], and chemical/thermal exfoliation of graphite oxide [58], [59], [60]. Mechanical exfoliation of graphite using the scotch-tape method and CVD produce pristine graphene; however, the process of removing and transferring the sheets from the growth medium to the device is time consuming and a single sheet is produced in a single

process. Thermal exfoliation uses the intrinsic CO₂ gas produced when heating graphite oxide to create a large pressure between the graphite layers for separation [58], [59], [60]. This facile process is fast and can be applied to a substantial amount of graphite powder, thus producing a large yield of graphene. Unfortunately, the elimination of the gas in the process of separation is destructive and produces vacancies in the graphene lattice. Additionally, if the process is incomplete, the graphene can consist of many layers and contain O-species. For the purpose of mass-production of non-pristine graphene sheets, thermal exfoliation is preferred compared to CVD, as it offers a fast and inexpensive method to create a large yield of product.

The strong sp² bonding in pristine graphene precludes the availability of dangling bonds for chemisorption with exception to edges and defects within the structure, thus it is chemically and electrochemically stable. The increased stability proves useful to prevent the support degradation; however, it can result in large Pt nanoparticles, as the entire surface area cannot be utilized for Pt deposition (Figure 1.8) [61]. It has been theoretically determined through DFT calculations [62], [63], and experimentally [61], [64] confirmed that Pt atoms experience a larger binding energy when located at a defect- or edge-site on the graphene sheet, due to increased coordination and the ability to chemisorb through dangling bonds. The diffusion across graphene sheets to defects and edges will promote Pt agglomeration, therefore decreasing the surface area to volume ratio of the electrocatalysts. Shao *et al.* showed that the incorporation of defective multi-sheet graphene as the electrode support for FCs results in a comparable activity to C black; however, the durability of the support was increased [65]. Defect sites in graphene occur from vacancies or edges in the hexagonal C lattice, and from incomplete oxidation reduction, thus leaving O-containing species on the surface of the graphene sheets. The specific O-species are debated in scientific literature; however, it is suggested that the surface contains hydroxyl, epoxy, carbonyl, and carboxyl groups [66], [67], [68]. Unfortunately, graphene oxide is an insulator, thus it is desirable to decrease the oxide species [67].

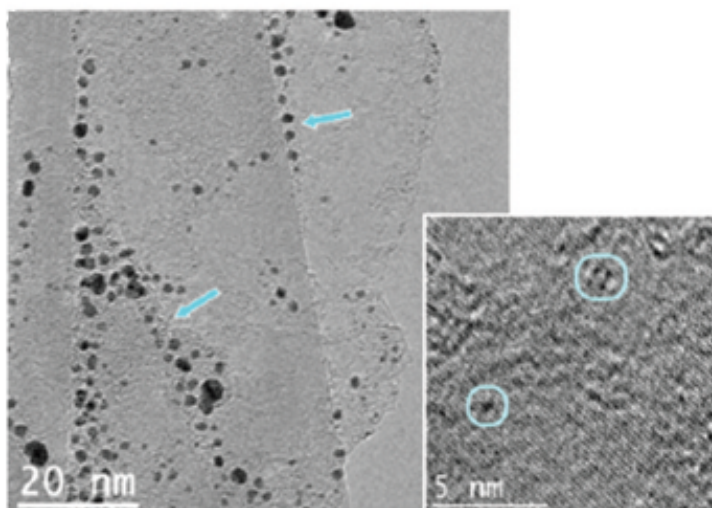


Figure 1.8 Pt chemically reduced on few-layer graphene sheets with arrows pointing to graphene edges, where large nanoparticles and a high density of Pt are observed. The inset shows Pt clusters located at defects in the graphene sheet. Reprinted with permission from ref. [61]. Copyright © 2012 American Chemical Society.

1.3.1.1 Nitrogen-Doped Graphene

Functionalization is utilized to introduce dopants into the graphene lattice to enhance the number of available binding sites in graphene. A common dopant used is N, where a range of dopant-types are available to offer advantages, such as participation in the ORR, and increased Pt binding energy. The possible N-dopants include amino, pyridinic, pyrrolic, and graphitic, as illustrated in Figure 1.9 [69], [70], [71]. Benefits of the N-doping include an increased Pt dispersion [35], Pt agglomeration prevention [41], and an increase in the number of ORR active sites [72], [73].

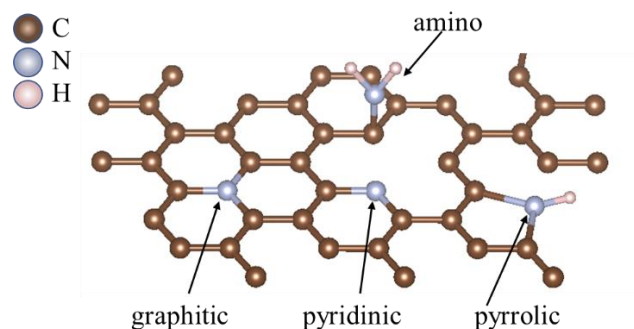


Figure 1.9 Possible dopants in N-doped graphene. Schematic produced using Vesta software [74].

A common method of N-doping can be accomplished by introducing the graphene powder into an N-rich environment at elevated temperatures [35] or in the case of single sheet graphene, performing the CVD in an ammonia/methane rich environment [75]. The high temperature provides energy to break the existing C bonds, while forming bonds between the N and C atoms. It has been experimentally shown that as the temperature is increased the predominant dopants move from amino, pyridinic/pyrrolic, followed by graphitic, as the increased energy permits increased coordination between the N-dopant and C lattice [35]. It should be noted that the pyrrolic-dopant only forms in the presence of a five-member ring defect in the graphene lattice [76]. Further, the specific gas used to introduce the N-dopant determines the sigma bonded N-dopant; where ammonia introduces an amino bond, and urea introduces a urea and amino bond [77].

1.3.1.2 Advantages and Limitations

Experimental and theoretical evidence suggests that N-doped graphene acts as an ORR catalyst. The specific dopant responsible for this effect is still controversial in the scientific literature, as the reaction cannot be directly observed with current microscopy techniques. Multiple sources attribute the induced positive charge on the adjacent C atoms in the case

of graphitic, pyridinic, and pyrrolic dopants to facilitate molecular adsorption for the ORR [41], [76]. Deng *et al.* state that the additional electron in the N atom can donate electrons to the adjacent C atom for the backdonation process of the rate limiting O₂ dissociation [78]. Further, in the case of pyridinic and pyrrolic dopants, the O₂ can directly bond to the N atom, where the lone electron pair will participate in backdonation [78]. Xing *et al.* experimentally corroborated that the pyridinic dopant is the most active site for the ORR process, but suggested that the C atom adjacent to the pyridinic dopant is the active species [79]. According to Ni *et al.* the graphitic dopant aids in increasing the ORR rate as it decreases the energy barrier for O₂ dissociation, accredited to impurity levels in the band gap as the graphene is transformed from a zero-bandgap semi-metal into an n-type semiconductor [80]. Wang *et al.* expanded on this point, suggesting that the electronic states in the band gap of N-doped graphene will approximately align with the empty antibonding orbitals of O₂, thus facilitating the electron backdonation process for O₂ dissociation [72]. Alternatively, it has been reported that pyridinic dopants produce a higher activity for the ORR; however, the relative strength of the pyridinic dopant versus the edge location has not been determined, as the four-electron process is also favoured at graphene edges [81]. Kim *et al.* further examined the ORR process using DFT, and ascertained that the majority of electron transfer prefers the two-electron process, as determined by the lower energy barrier for end-on adsorption [24]. They also concluded that the graphitic N atom located adjacent to a zig-zag edge had the highest selectivity for the four-electron process and lowest activation energy for the rate limiting step of O₂ dissociation. The reaction scheme proposed by Kim *et al.* resulted in the breaking of the C to N bond during the ORR, creating a pyridinic N-dopant from the original graphitic-type dopant. The paper suggests that this reaction scheme may address the controversy in the scientific literature, as the N could be measured as a graphitic- or pyridinic-type dopant depending on detection before or after ORR cycling [24]. Experimental results disagree with theoretical calculations in the case of ORR in acidic media for N-doped graphene, where the less efficient two-electron process dominates [72], [73], [42]. Although the N-

doped graphene participates in the ORR, an additional catalyst is still required to maintain an efficiency equivalent to Pt on C black.

Other than participating in the ORR, the act of N-doping graphene increases the Pt binding energy to the graphene lattice. Kong *et al.* [62] and Groves *et al.* [82] determined that Pt prefers to bind to bridge locations of graphene in the absence of a defect or dopant. The process of chemisorption leads to a covalent bond between the C atoms and Pt through the process of double bond breaking with Pt donating electrons to the π^* orbital of the C atoms in graphene, and the C atoms donating electrons to the d -band orbital in Pt [82]. A defect in the graphene lattice results in an increased binding energy by the presence of three binding sites, where the existence of dangling bonds at graphene edges further increases the binding energy of C and Pt [62]. This results in anisotropic diffusion, as the enhanced binding energy results in a larger activation barrier along graphene edges than on graphene surfaces [62]. The incorporation of N-dopants in graphene is another method to increase the binding energy of Pt to C, where the C atom adjacent to the N atom forms the chemisorption bond (Figure 1.10) [62], [41], [82]. It is suggested by Holme *et al.* that the positive charge invoked by the N-dopant on the C atom attracts Pt, as the Pt will transfer charge during the formation of a covalent bond [41]. The increased binding energy from N results in a decreased particle size and improved distribution, as Pt ripening and agglomeration is reduced and nucleation at the defect sites is encouraged [41]. It is suggested that Pt will nucleate at N-dopants and vacancies before binding to the pure graphene surface [41]. Zhang *et al.* experimentally observed the effect of the increased Pt nucleation energy on N-doped graphene, as an improved Pt distribution and decreased Pt catalyst size was observed in comparison to pure graphene [69]. It was suggested that the pyridinic N is responsible for the improved catalyst distribution [69]. Calculations performed by my own collaborators also confirm these results [32]. It was shown that the bonding of a Pt atom to two C atoms and one N atom at a pyridinic/single vacancy defect (pyridinic dopant) resulted in the transfer of electrons from the Pt atoms to the N atom, and

in a stronger bond to the pyridinic dopant than to a graphene lattice [32]. The electron transfer was observed experimentally using XANES, wherein samples comprising small Pt clusters and atoms resulted in a higher total unoccupied DOS for the $5d$ character when compared to Pt nanoparticles [32]. In contrast, Lin *et al.* experimentally determined with electron energy loss spectroscopy (EELS), that during the production of Cr -N bonds at a divacancy (pyridinic dopant), the N atoms donate electrons to the metal's $3d$ state, causing a reduction of the metal [83]. These differing results suggests that the specific catalyst and defect site can influence the bonding characteristics and the filling of the metal's catalytically active energy state. This further complicates the understanding of how the atoms/clusters contribute to the ORR, and the role the dopant plays due to its defect configuration within the graphene lattice.

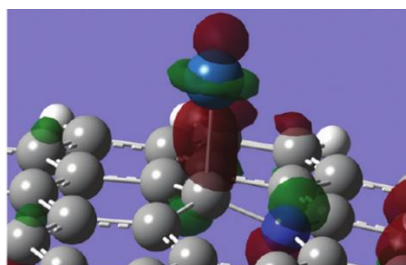


Figure 1.10 Pt atom locations on N-doped graphene. N-doped graphene (N is blue atom in the graphene lattice) with blue Pt adatom bonded to C adjacent to a graphitic N dopant. Reprint with permission from ref. [82]. Copyright © American Chemical Society.

These calculations suggest that the N-dopant is responsible for an increased Pt-C binding energy, which is confirmed through experimental observation on N-doped hollow C spheres from Galeano *et al.* [84]. Smaller particle sizes were observed on the N-doped substrate in comparison to the non-N-doped samples, resulting in better Pt dispersions and a higher ECSA. This resulted in an initial high mass activity for the ORR on the N-doped samples in acidic media compared to the other samples, but a lower specific activity comparable with conventional catalysts [84]. Unfortunately, it was determined that between 360 and 1080 ORR cycles, the ECSA drastically decreased from the loss of the

smaller, less stable Pt clusters, resulting in a decrease in the catalytic activity [84]. This suggests that more studies are required to examine the Pt degradation mechanisms with respect to N-doped samples.

Although N-doped graphene facilitates the ORR and increases the Pt-C binding energy, it limits the electrical conductivity of graphene by introducing scattering centers from defects into the lattice. Further, the incorporation of graphitic-type dopants creates an n-type semiconductor, thus decreasing the electrical conductivity from the intrinsic semi-metal zero band-gap graphene [70], [85]. Electron mobility in graphene, N-doped graphene, and C black can be observed in Table 1.1. The direct correlation of conductivity and mobility suggests that the conductivity of the N-doped graphene will be less than pure graphene; however, the value is much larger than C black. This implies that N-doped graphene will enhance the conductivity of the electrode support in comparison to the conventional material, thus increasing the overall efficiency of the FC.

Table 1.1 Electron mobility in various C support materials.

Source	Mobility ($\text{cm}^2\text{V}^{-1}\text{S}^{-1}$)
Pure Graphene [70], [57]	300-1200
N-doped Graphene (8.9 atomic %) [70]	200-450
Carbon Black [86]	3.6-6.3

1.4 Summary

In order to address the current state of GHG emissions and its contribution to climate change, the automotive industry should be targeted by moving away from the traditional ICE to new cleaner technology, such as PEMFCs. The current state of the PEMFC technology still requires improvements in effort to reach the targets set by the US Department of Energy, wherein the primary concern is the electrode support degradation

and catalyst selection related to the cost and efficiency. Within this thesis, the use of higher electrically conductive and increased corrosion resistant support material will be analyzed through the use of graphene and CNTs. In effort to further decrease the degradation mechanism, due to Pt dissolution, N-doped substrates will be examined. Furthermore, the cost of the catalyst will be addressed through the production of ultra-small Pt clusters and Pt atoms by utilizing the ALD technique. This suggests that the material must be characterized at the atomic scale, to observe the small Pt catalysts and the graphene support, which will be completed using electron microscopy techniques. This thesis is focused on the material characterization of a real electrode support material, followed by the in-house production of single-sheet N-doped graphene for theoretical investigations of the N-dopants and Pt catalysts. Lastly, N-doped CNTs (NCNTs) will be used as a platform to understand the effects of different ALD conditions on the Pt size and density, to fine-tune the sole production of Pt atoms. Full characterization of the NCNTs will also be completed using electron microscopy techniques.

Chapter Two

Electron Microscopy

A variety of characterization techniques are utilized to analyze the quality of graphene and functionalized graphene to understand the defect density and chemical bonding. The defect density is commonly analyzed with Raman spectroscopy through comparison of the D and G bands; however, this gives a relative percent without the qualification of the specific defects and distribution through observation [66]. Further, the chemical bonding can be determined through X-ray absorption near edge spectroscopy (XANES), and X-ray photoelectron spectroscopy (XPS), but the distribution and specific locations of the defects with respect to the graphene lattice is not possible [87]. Scanning transmission X-ray microscopy (STXM) can be used, as it collects the transmitted X-rays with the XANES techniques while scanning the X-ray beam over a desired area of the sample. STXM allows the mapping of each XANES spectra with respect to the position on the graphene lattice; however, the best achievable spatial resolution is 10 nm with a more general value of 25 nm [88]. Lastly, the material has been characterized on the atomic scale using scanning tunneling microscopy (STM) for the purpose of locating dopants and analyzing defects. Unfortunately, the process of obtaining STM maps is time consuming and the resolution concerning chemical bonding is restricted to the tip sensitivity [87].

Ideally, structural and chemical bonding information can be derived on the atomic scale with the possibility of directly relating the spectroscopic results to specific atoms

within the graphene structure. It would be beneficial to have each characterization tool located within one instrument to allow for multiple examination techniques on a single location of the graphene lattice. Transmission electron microscopy (TEM) has proven ideal for the characterization of graphene, as atomic resolution is possible with the option of mapping chemical components and bonding information with respect to structural information, as will be discussed below.

2.1 Electron Interactions with Matter

The source of the electron signals must be understood to determine the appropriate imaging and spectroscopy techniques to gather the desired information from the sample of interest. A simplistic schematic diagram of the signals generated when high energy electrons interact with a thin specimen (<100 nm) can be seen in Figure 2.1 (a). Within this figure, only the signals that pertain to this thesis are labelled and briefly discussed herein, as many more signals can be produced from the interaction of electrons with the sample, but are outside the scope of this report. The characteristic peaks from the X-ray signal, inelastically scattered electrons, and Auger electrons are labelled K, L, and M, based on the respective principle quantum numbers labelled in Figure 2.1 (b).

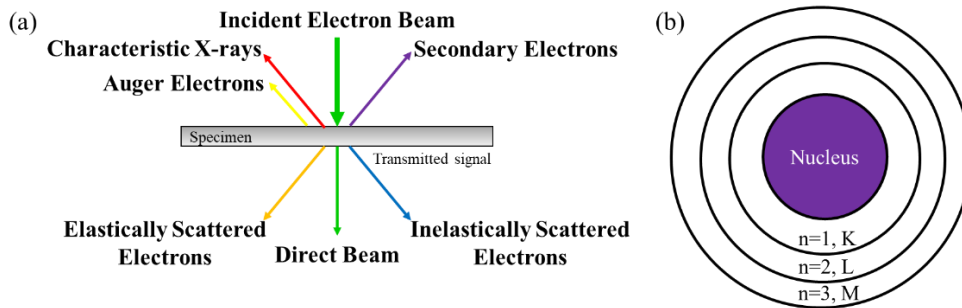


Figure 2.1 Simplistic schematic of the electron interactions with matter. (a) Interaction of a fast electron with a thin specimen and the produced signals analyzed in this thesis, and (b) the atomic model with the corresponding principle quantum number (n) and characteristic peak labels for X-rays, EELS, and Auger electrons.

Using a scanning electron microscope (SEM) secondary electrons (SEs) can be detected. During the incident electron interaction with a thick specimen the electrons can lose energy through inelastic scattering with electrons in the sample. Secondary electrons are generated through these inelastic scattering events, such that the outer shell electrons from the atoms within the sample, or conduction band electrons, are excited with enough energy to escape the surface of the sample [89]. While travelling through the sample the SEs will lose energy, thus only those close to the surface can escape before the kinetic energy is completely attenuated [89]. These electrons provide topographical information about the sample and were used to analyze features of NCNTs [89].

The SEM can also be used in conjunction with an Auger detector to chemically map surface elements by examining the Auger electrons and SEs. Auger electrons are created during the de-excitation of a core electron to its ground state from an excited state, due to an ionization process through inelastic scattering with the incident beam. This technique will be discussed in more detail below, but in brief, during the de-excitation process the internal energy of the electronic transition is converted to the excitation and release of another electron. The kinetic energy of this electron can be detected, which is sensitive to the elemental identity in which the electron originally resided. Due to the secondary nature of the excitation event for the Auger electrons, they are of low energy and can only escape the sample surface from a few nanometers, thus this is a surface

sensitive characterization technique. Auger electrons were used in this report to quantify the N concentration within N-doped graphene and NCNTs.

Similar to Auger electrons, X-rays are produced during the de-excitation of a core electron to its ground state after being ionized to an empty energy state from an inelastic excitation with the incident electron. During the de-excitation, energy related to the difference in the energy of the empty and core states causes the release of a photon (X-ray). The X-rays are characteristic of each element, as each element has unique energy states, thus the characteristic X-rays can be used for elemental identification and quantification. The X-rays can be detected in both SEM and TEM through a detector located above the sample. Through the use of X-ray detection in TEM the presence of Pt was found on the N-doped graphene samples.

The transmitted elastic electron signal is used in TEM and has many practical applications for analyzing the sample structure, and chemical composition, simply by examining the different signals generated from the transmitted electrons. Additionally, the transmitted inelastic electron signal can be inspected using EELS, wherein the chemical composition, and bonding can be determined. Each signal will be discussed in more depth based on the techniques used in the remaining chapters of this thesis.

2.2 Using TEM to Study Graphene and Heavy Atoms

The TEM was invented in 1931 by Ernst Ruska and Max Knoll, where electron sources and spherical electromagnetic lenses were used to produce the transmitted image of elastically scattered electrons to provide structural information of the material under examination. Theoretically, the use of electrons for imaging can produce a spatial resolution on the sub-angstrom scale, due to the inverse relation between wavelength and energy. Elastically and inelastically scattered electrons from sample interactions can be detected with a camera or an energy filter spectrometer, thus supplying information

concerning material structure, elemental distribution, chemical bonding, and elemental composition.

Two key electron imaging techniques include the broad beam based TEM, where all scattered electrons are collected over a large illumination area on the specimen, and scanning TEM (STEM) which utilizes a raster scanning probe source on the specimen to examine elastically scattered electrons from the sample with respect to position. Physically the instrument contains an electron source, which under ideal conditions acts as a point source. In reality the electrons are emitted from a tip with a small but measurable radius and varying electron energies, thus resulting in partial spatial and temporal coherence of electrons interacting with the sample [90]. Further, aberrations in the primary imaging and probe forming lens (objective and condenser lenses) distort the information transfer to the back-focal plane, which limits the image resolution for both TEM and STEM.

The resolution of the microscope can be enhanced through aberration correction with multipole lens and by increasing the electron energy; however, when examining fragile samples, low energies are required to prevent knock-on damage. Knock-on damage occurs when the energy of the incident electron exceeds the displacement energy of the sample, therefore damaging the sample by causing the elimination of atoms [91]. Particularly, graphene's composition of a single layer of light atoms makes the material inherently susceptible to knock-on damage above electron excitation voltages of 86 kV [92], [93], [94]. Meyer *et al.* reported that at enhanced doses of $10^{10} \text{ e}^- \text{ nm}^{-2}$ (dose rate $3.5 \times 10^5 \text{ e}^- \text{ nm}^{-2} \text{ s}^{-1}$) at 80 kV in TEM can instigate knock-on damage in graphene when operating in TEM mode [93]. On the other hand, Robertson *et al.* determined that at higher dose rates in TEM ($10^8 \text{ e}^- \text{ nm}^{-2} \text{ s}^{-1}$) it was possible to induce damage with a lower electron dose, wherein a dose of $3 \times 10^9 \text{ e}^- \text{ nm}^{-2}$ at 80 kV caused an average of 0.1 atoms per nm^2 to be lost from the graphene lattice [94]. The increased defect rate determined by Robertson *et al.* was suggested to be caused by knock-on damage from phonon excitation due to local heating from the electron source and enhanced vibrations in the z-direction, which increased the electron momentum and sputtering rate [94].

Alternatively, a dose rate of $2.54 \times 10^{10} \text{ e}^- \text{ nm}^{-2} \text{ s}^{-1}$ did not result in a sputtering event of pristine graphene when operating in STEM mode at 80 kV and situating the beam on a single C atom for five minutes (assumed dose of $7.6 \times 10^{12} \text{ e}^- \text{ nm}^{-2}$). Nevertheless, large holes were observed approximately 5 to 20 nm away from the electron beam after a 30 minute continuous STEM exposure, due to chemical etching from Fe catalysts and indirect beam exposure [94]. Furthermore, it should be noted that areas containing contamination and edge sites are more inherently susceptible to knock-on damage due to the reduced stability as compared to the pristine graphene lattice, thus edge atoms can be displaced at energies as low as 20 kV [95], [93], [96]. Lowering the energy of the electron source reduces induced beam damage; however, the overall achievable resolution of the image is limited [93]. This was confirmed by Suenaga *et al.*, where it was determined that imaging edge structures required a large decrease of excitation voltage to prevent damage originating from the decreased atomic coordination [95]. Additionally, Suenaga *et al.* validated the ability to atomically examine the electronic structure of single C atoms in the graphene lattice, resulting in local electronic variations depending on its location along the edge or within the bulk structure with an electron source of 30 kV [97]. In this experiment damage was still induced on the sample when acquiring spectrum images, thus the dose was reduced by using line scans [97]. To reduce knock-on damage, most graphene experiments in literature are completed with the use of a 60 kV electron source, with an aberration-corrector, and a reduced current.

Based on the microscopes available at the CCEM, high resolution images were performed with an 80 kV electron source. Using the pixel size as reference for the probe size, an over estimation for the approximate upper dose used during STEM image acquisition in the experiments of this report is $1.4 \times 10^7 \text{ e}^- \text{ nm}^{-2}$ and a dose rate of $1.4 \times 10^{12} \text{ e}^- \text{ nm}^{-2} \text{ s}^{-1}$. A more reasonable estimation of the dose and dose rate is acquired when considering a probe size of 0.06 nm for annular dark field (ADF) imaging conditions (measured from the full width half maximum (FWHM)), as measured from a single C atom in *Chapter 4.2.1 Characterization of N-Doped Graphene Using High Resolution STEM*

which results in a dose of $6.9 \times 10^6 \text{ e}^- \text{nm}^{-2}$ and a dose rate of $2.3 \times 10^{11} \text{ e}^- \text{nm}^{-2} \text{s}^{-1}$. When operating in high angle ADF (HAADF) imaging conditions, a probe size of 0.2 nm (as measured by Pt atoms in *Chapter 5.2 ALD Fine Tuning to Consistently Produce Single Atom Catalysts with NCNTs*) was used, resulting in a maximum dose and dose rate of $9.6 \times 10^5 \text{ e}^- \text{nm}^{-2}$ and $1.9 \times 10^{10} \text{ e}^- \text{nm}^{-2} \text{s}^{-1}$.

2.2.1 High Resolution TEM

This section is summarized from Rolf Erni's book "Aberration-corrected imaging in transmission electron microscopy" [90]. For more comprehensive details on the exit plane wave (EPW) of the electron beam, aberrations in the objective lens, and the operation of the image corrector, consult this easily readable and very detailed textbook. The first step in high-resolution TEM (HRTEM) micrograph image formation occurs when the initial plane electron wave travels down the TEM column with its wave vector (k_0) parallel to the optical axis. When the beam reaches the sample, it diffracts at angles determined through Bragg's law (Figure 2.2 (a)), where the diffracted beams are focused on the back focal plane of the objective lens, forming a diffraction pattern [90]. The partial beams (k_g) generating the diffraction spots then interfere to produce an HRTEM micrograph in the image plane [90]. The HRTEM micrograph contains structural information of the specimen described by the phase shift experienced by the incident electron wave when interacting with the sample. This information is contained in the wave function of the electron plane wave (EPW) exiting the specimen. Modifications to the EPW function can be introduced through aberrations in the objective lens dictated by the phase contrast transfer function (PCTF) (Figure 2.2 (b)), which are transferred to the final HRTEM image. Therefore, the contrast

comprising the HRTEM image contains information about the specimen's atomic potential and the lens aberrations.

Generally, the PCTF is an oscillating function with respect to spatial frequency, thus resulting in varying contrasts for different spatial frequencies within the HRTEM image. The pass-band is the range of spatial frequencies that fall within a single PCTF value, and ensures that the image intensity can be directly interpreted as the sample's atomic potential [90]. The pass-band and point resolution (spatial frequency with the first zero crossing of the PCTF) can be enhanced by adjusting lower order aberrations (defocus (C_1)) to compensate for the intrinsic third-order spherical aberration (C_3), which is known as the Scherzer defocus [98]. Ideally, the PCTF will have a large pass-band and the point resolution will exceed the information limit (maximum spatial frequency contributing intensity to the image), therefore producing an image wherein contrast reversal does not occur for different spatial frequencies [90]. Very specific conditions are required to expand the pass-band, thus most HRTEM images require image simulations to accurately interpret the contrast of the image. Furthermore, the effect of the partial spatial and temporal coherence of the electron source can be seen in Figure 2.2 (b), as envelopes which reduce the contrast in the image and restricts the information limit of the TEM image. In the case of conventional TEM, the limiting C_3 aberration of the objective lens causes the spatial coherence envelope to damp the PCTF, thus causing a low frequency information limit.

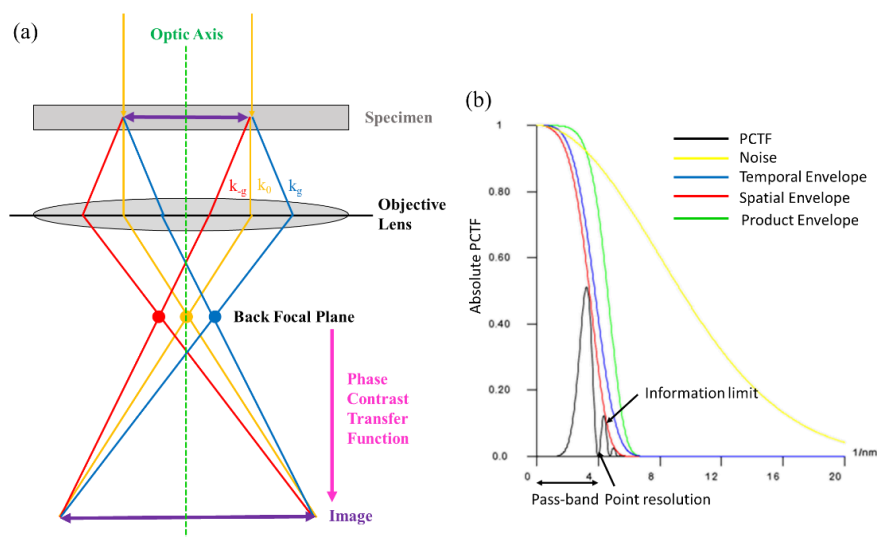


Figure 2.2 HRTEM image formation. (a) Ray diagram schematic of the interaction of the electron with the specimen and the focusing power of the objective lens. (b) The objective lens influences the contrast in the HRTEM image, as dictated by the PCTF. The PCTF (intensity) was generated in JEMS [99] to illustrate the effect of the aberrations on the HRTEM image contrast.

Multipole lens (image corrector) are utilized to correct for intrinsic and parasitic geometrical aberrations up to the third-order [100], [101], which limit the resolution and spatial coherence of the source [90], [100], [101]. By minimizing the lens aberrations, the transfer function approaches finite values for a broad range of spatial frequencies and the spatial coherence no longer damps the image intensity. However, aberrations of an order greater than three now limit the resolution. Similar to the conventional TEM, in TEMs containing image correctors, optimized conditions must be utilized by setting lower order aberrations to compensate for higher-order aberrations. When the intrinsic C_3 is controlled, the fifth-order spherical aberration (C_5) limits the resolution. The C_5 is considered a fixed positive finite aberration due to the geometry of the objective lens. An optimized C_1 and C_3 can be derived when the C_5 is limiting the resolution through different numerical and analytical approaches (Table 2.1) [90]. It is apparent in Table 2.1 that a negative C_3 is required to compensate for the positive fifth-order spherical aberration C_5 , thus this condition is called negative spherical aberration imaging. Upon optimization of the lens aberrations, the pass-band and point resolution of the PCTF can be expanded, thus allowing

for the direct interpretation of the HRTEM images. It should still be noted that when working with crystalline samples contrast can arise from crystallographic features, thickness, and atomic potentials, therefore even when working in optimized TEM conditions, care must still be taken when examining the contrast of images.

Table 2.1 Equations to calculate optimized C_1 and C_3 coefficients. These are used to compensate for the intrinsic limiting C_5 when using an image corrector, where q_{max} is the maximum spatial frequency transferred and λ is the wavelength of the electron source [102], [103].

	Scherzer (2.1)	Chang (2.2)	Lentzen (2.3)
Defocus C_1	$C_{1\ Scherzer,corr}$ $= 2^3\sqrt{\lambda^2 C_5}$	$C_{1\ Chang,corr}$ $= 1.56^3\sqrt{\lambda^2 C_5}$	$C_{1\ Lentzen,corr}$ $= \frac{2}{\lambda q_{max}^2}$ $+ \frac{2}{15} C_5 \lambda^4 q_{max}^4$
Third-order spherical aberration C_3	$C_{3\ Scherzer,corr}$ $= -3.2^3\sqrt{\lambda C_5^2}$	$C_{3\ Chang,corr}$ $= -2.88^3\sqrt{\lambda C_5^2}$	$C_{3\ Lentzen,corr}$ $= -\frac{10}{3\lambda^3 q_{max}^2}$ $-\frac{8}{9} C_5 \lambda^2 q_{max}^2$

2.2.1.1 Increasing the Temporal Coherence

The microscope configuration for negative spherical aberration imaging results in bright atomic contrast on a dark background when operating with a required negative C_3 and a positive C_1 . Unfortunately, now the partial temporal coherence limits the information transfer. Also, the introduction of the image corrector causes an increase in the source of current instabilities in the post-objective lens, thus inherently increasing the chromatic aberration (C_C) from approximately 1.2 mm to 1.4 mm [104]. Currently, chromatic aberration correctors are available that can correct the C_C from the source instabilities and the objective lens [105]; however, only a few exist in the world which are dedicated to very specific uses, therefore a different approach to decrease the energy spread of the imaging

electrons is required until the development of the chromatic aberration correctors have advanced. Three methods to improve the temporal coherence include the selection of the electron source, the use of a monochromator, and the selected incident electron acceleration voltage.

2.2.1.2 Electron Source Selection

A common method used to enhance both the spatial and temporal coherence is the operation of a field emission gun (FEG) rather than a thermionic source, such as Lanthanum hexaboride (LaB_6) [104]. A consequence of the weakening of both the spatial and temporal coherence envelopes for the FEG is an increase in the information limit. These effects are due to the fact that the FEG offers a smaller tip radius, higher brightness, and lower energy spread of the electron beam [106]. This suggests that the use of a FEG is necessary for HRTEM imaging; however, an inherent energy spread of approximately 0.8 eV still exists [106].

2.2.1.3 Monochromator Excitation

Further improvement of the temporal coherence requires a decrease in the electron energy spread of the source, which can be completed with a monochromator. Various monochromator designs have been created which comprise electromagnetic lenses, electrostatic lenses, and an energy selecting slit [107]. The specific selection of a monochromator design will determine the energy spread and electron current of the source [108]. The monochromator disperses the electrons into a line ranging from high to low energy, where a slit can be used to select a single electron energy, thus creating a monochromatic source and decreasing the energy spread (0.1 eV) and temporal coherence

envelope [108], [109]. An increasing excitation voltage of the monochromator results in a stronger dispersion and a lower energy spread, as the relative energies of the electron source are more readily separated [110]. However, the use of a monochromator also reduces the electron current, especially with high dispersions as the electrons of varying energies are no longer focused to a single point (excitation = 0.0). The decreased current leads to a reduction in the signal to noise ratio of the image and limits the maximum magnification that can be achieved before the contrast in the image diminishes [110]. The selection of a moderate excitation voltage will ensure that the electron source has a low energy spread, while also maintaining a beam current that can reach high magnifications. Omission of a selection slit (rainbow mode) will also increase the current used to acquire the image; however, a slightly higher energy spread is obtained [110]. To optimize the energy spread of the monochromator, the lenses can be tuned without the slit. Further, the beam must be condensed to the dispersion line to maintain the monochromatic source, therefore strengthening the spatial coherence envelope. When the monochromator is used in combination with an image corrector the spatial coherence envelope will not limit the PCTF as the low spherical aberration offsets the increased beam divergence semi-angle.

2.2.1.4 Electron Source Acceleration Voltage

Lastly, the information limit of the microscope can be enhanced by increasing the electron energy; however, as previously mentioned, when examining fragile samples low energies are required to prevent knock-on damage. This puts an emphasis on the requirement for an image corrector, FEG electron source, and a monochromator to increase the spatial frequency of the information limit [107]. Freitag *et al.* [107] compares the PCTF for a conventional TEM, spherical aberration correction, and spherical aberration correction with the application of a monochromator. They indicate that the pass-band increases with each subsequent change in the imaging system; first due to the decrease of the axial

aberrations and weakening of the spatial coherence envelope, and second to the weakening of the temporal coherence envelope, respectively [107].

The information limit and point resolution of a microscope should be determined for specific imaging conditions to determine if an HRTEM micrograph can be directly interpreted. If the information limit exceeds the point resolution, the micrographs should be compared to HRTEM simulations using equivalent microscope conditions.

2.2.1.5 Examples of HRTEM Imaging of Graphene

Although, there is a means to directly interpret the structural information from the HRTEM micrographs, atomic distinction is not strong. The small scattering angle collected when performing HRTEM indicates that the detected electrons interact with atomic valence electrons of the sample. This interaction allows for the extraction of the structural information; however, there is not a direct correlation of valence electrons in chemical bonds with atomic charge [111]. Using negative spherical aberration imaging with an aberration corrected microscope, Meyer *et al.* showed that the graphene lattice can be directly extracted (Figure 2.3 (a)) when spatial frequencies reached the 1.23 Å reflection in the characteristic hexagonal pattern of the computed diffractograms (Figure 2.3 (b)) [103]. Care must still be taken when interpreting the image as indicated by Warner *et al.*, as multilayered graphene sheets at varying defocus may have a similar lattice in HRTEM micrographs to a single layer sheet [52]. Further, the computed diffractogram from Figure 2.3 (b) does not elucidate the number of layers in the graphene structure as each graphene sheet contains an identical lattice. Upon tilting a monolayer of graphene, the intensity of the diffraction spots remains constant; however, an isotropic broadening will occur due to 1 nm corrugations in the graphene lattice used to maintain the stability of the sheet and two-dimensional structure [112]. Anisotropic broadening of diffraction spots can be attributed to misorientations between multilayered graphene sheets and grain boundaries

within graphene sheets, as a range of misorientation angles will produce a set of hexagonal spots at varying rotation angles [113], [114], [115], [116]. Alternatively, multilayered graphene results in a decreased intensity of the diffraction spots as a function of specimen tilt, but isotropic broadening is not observed as a function of the tilt-angle as the two-dimensional structure is no longer maintained [112]. The fact that the intensity of the diffraction spots change for multilayered graphene, suggests that small specimen tilts from imperfections in the graphene lattice will result in brightness variations across a multilayered graphene sheet in a HRTEM micrograph [112]. To fully interpret the structure and number of sheets within graphene, the sample should undergo a tilt series to examine the effect on the intensity of the diffraction spots, followed by HRTEM simulations using multislice theory introduced by Kirkland [111].

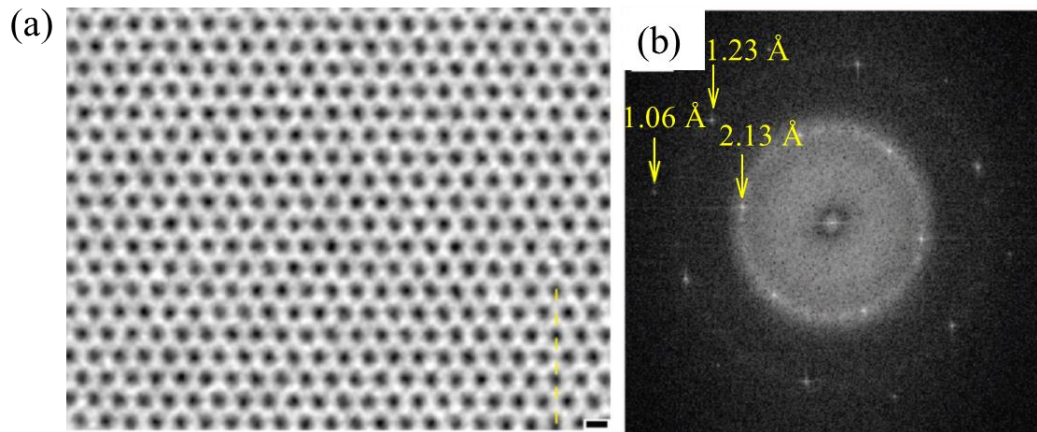


Figure 2.3 HRTEM images and computed diffractogram from a single sheet of graphene. (a) HRTEM micrograph of graphene lattice using negative spherical aberration imaging (scale bar is 2 Å) and (b) the computed diffractogram with labelled reflections. Reprinted (adapted) with permission from ref. [103]. Copyright 2008 American Chemical Society.

2.2.2 High Resolution STEM

Similar to HRTEM, STEM examines elastically scattered electrons from the interaction of the incident electron source with the atomic potential of the sample. The uniqueness of STEM originates from the use of a probe rather than a broad beam to examine the specimen. The probe is formed on the sample by placing the specimen in the back focal plane of the objective lens, where the electron beam is focused to a point on the sample (Figure 2.4). Raster scanning is employed to move the probe across the surface of the sample, where a convergent beam diffraction pattern is formed in the detector plane from each scanned location.

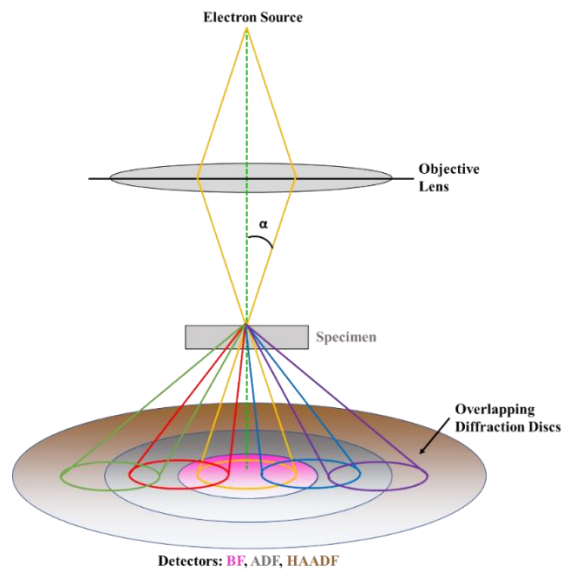


Figure 2.4 Simplified schematic of STEM image formation and the relative detector positions.

2.2.2.1 STEM Image Formation

Diffraction pattern overlap is necessary to produce lattice fringes when using the STEM imaging technique, which can be accomplished by utilizing a larger limiting aperture.

Moreover, the annular shape and angular position of the STEM detectors determines the intensity of the image, as low to high scattering angles can be collected with an annular detector. When operating in STEM a bright field (BF) and annular dark field ADF detector can be utilized simultaneously, due to the hole in the ADF detector. Similar to HRTEM, the intensity function of the BF detector relies on the coherence of the scattered wavefunction and forms an image with an intensity that is a convolution of the sample's atomic potential and the PCTF [117].

On the other hand, the ADF detector can be used to collect elastically scattered electrons at much higher angles. Simplistically, when moving to higher collection angles and assuming the reciprocity theory between STEM and TEM, it can be understood that incoherent imaging conditions are satisfied as the collection angle increases [117]. Mathematically this is shown when examining the intensity function for ADF imaging conditions, which is a convolution of the object's atomic potential with the probe shape [117]. This can be understood as applying an optical transfer function (OTF) to the samples atomic potential when transferring from reciprocal space (specimen) to real space (detector) [117]. Unlike the PCTF in HRTEM, the OTF is a monotonically decaying function with respect to the spatial frequency and does not oscillate like the PCTF, thus the contrast in ADF images can be directly interpreted as the object's atomic potential [117]. It should be remembered that the incoherence of the electrons forming the image will depend on the inner angle of the ADF detector, as small inner angles will lead to more coherent wavefunctions, thus moving towards a PCTF [117].

The intensity of an ADF image can be further controlled to collect specific signals through adjustment of the inner semi-collection angle of the detector. In the literature, medium angle ADF (MAADF) imaging has an inner angle of approximately 50-60 mrad, and HAADF has an inner angle of approximately 80-90 mrad [118]. The inner angle can be controlled based on the camera length selected during the experiments. In this thesis, the MAADF imaging conditions are referred to ADF. The higher collection angles achieved when using the ADF detector, as opposed to the BF detector, indicate that they

collect Rutherford scattered electrons, thus these images contain elemental information through nuclear interactions of the incident electrons with the sample. This suggests that HAADF images of atoms with a high atomic number (Z) are of higher intensity, as these atoms can scatter electrons to higher angles than low Z material. The contrast of the HAADF imaging technique is proportional to $Z^{1.6}$, therefore a sample of constant thickness has an intensity variation corresponding to the elemental composition [90]. The exponent of Z depends on the collection angles, where larger collection angles lead to the approximation of Z^2 . Furthermore, the mass of the sample can be imaged with HAADF, such that a linear increase in the signal exists for stacked atoms in a column [117], but this increase is no longer linear when working in MAADF conditions [118]. Generally, HAADF conditions are acquired to directly observe the Z - and mass-contrast in the image, due to the combination of the incoherent imaging conditions with the Rutherford scattering, thus image interpretation is more direct when compared to HRTEM imaging. MAADF is used when imaging light elements in effort to increase the signal, as lower Rutherford scattering angles are experienced when the atomic number is decreased.

In STEM imaging, the probe size dictates the image resolution, therefore methods to increase the resolution through decreasing the probe size must be considered. Generally, a condenser aperture is used to limit the introduction of aberrations in the probe from the objective lens, thus increasing the resolution of the OTF. This aperture will control the convergence semi-angle of the probe (α in Figure 2.4), therefore influencing the diffraction limit [118]. It should be noted that the diameter of the probe is affected by the diffraction limit and the source size, which is directly related to the probe current to brightness ratio, and inversely related to the semi-convergence angle [118]. This suggests that the largest aperture that removes the probe aberrations should be utilized in effort to increase the semi-convergence angle, or in other words, to decrease both the diffraction limit and the source size. Similar to HRTEM, an aberration-corrector can be used for the probe forming lens, thus decreasing the aberrations in the probe and allowing a larger semi-convergence angle to be used. When working at low acceleration voltages with an aberration-corrector, it has

been determined that above approximately 50 kV the beam is limited by the C_5 when the C_3 has been corrected. Additionally, when operating below 50 kV the beam is limited by C_C , therefore similar strategies discussed above to increase the temporal coherence should be utilized for these operating conditions [118]. In this thesis, a probe size of 0.2 nm was achieved with a limiting aperture of 50 μm and spot 9 (19 mrad, as measured by FEI), and 0.06 nm with an aperture of 70 μm and spot 10 (26 mrad, as measured by FEI), respectively.

2.2.2.2 Examples of HRSTEM Imaging of Metal-Graphene Interactions

ADF has proven invaluable in examination of metal-graphene interactions, as the difference of the atomic number between the C lattice and metal atoms results in large contrast variations in the image, thus allowing easy identification of atomic positions and distributions. Ramasse *et al.* demonstrated the observation of various metal atoms on a graphene lattice through HAADF, as observed in Figure 2.5 [119]. The bright intensity in the images is due to the high electron scattering of the metallic atoms and the low intensity results from individual C atoms. It was also confirmed by Zan *et al.*, using HAADF that Pt binds at bridge sites on the graphene lattice; however, adsorption will first occur on hydrocarbon contamination [120]. In Figure 2.5 beam excitation is visible through streaking of the metallic atoms, as they diffuse of the graphene and hydrocarbon surface. Interestingly, it was observed that contact between the metal atoms and graphene lattice under beam irradiation resulted in enlarged hole formation for non-gold metals [120]. They attributed this to local heating of the graphene lattice, thus lower dose rates should be considered when examining metal-graphene interactions [120]. Many other researches have published STEM images of the individual C lattice of graphene and CNTs with interacting metal atoms [121], [122].

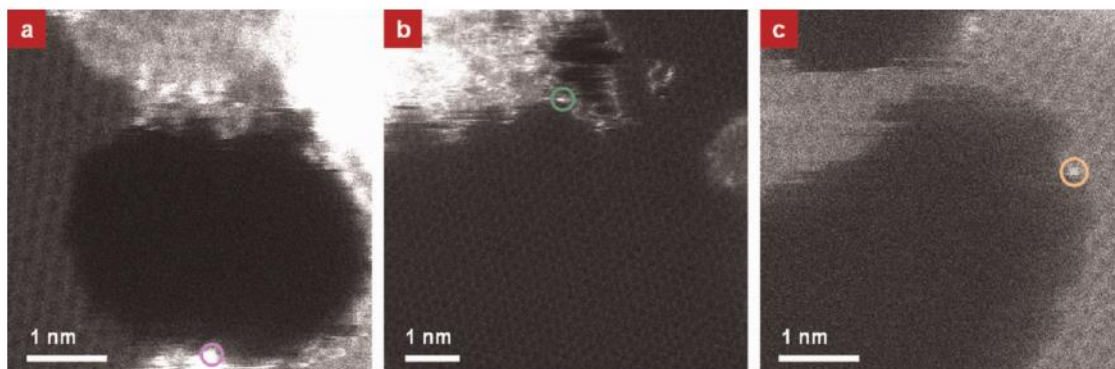


Figure 2.5 HAADF micrographs of graphene with deposited metals. (a) Pd, (b) Ti, and (c) Al. Reprint with permission from ref. [119]. Copyright © 2012 American Chemical Society.

2.2.3 EELS

Detection of inelastically scattered electrons proves useful for analytical measurements of elemental composition and chemical bonding within a material. Interaction of the incident electrons with the specimen can result in a loss of energy due to excitation of atomic electrons. Detection of the incident electron energy-loss, when exciting a bound electron to the conduction band from the sample, with use of a spectrometer results in an intensity graph with peaks corresponding to energy levels within the material (Figure 2.6 (a)). Specific regions in the EEL spectrum are outlined in Figure 2.6 (a), where the transmission of electrons that are elastically scattered comprise the “zero-loss” peak, excitation of electrons from the valence band to the conduction band contributes to the “low-loss” region (50-100 eV), and excitation from the core energy level electrons to the conduction band forms “core-loss” states [123]. Core-loss states can be used for elemental identification, as each element has unique energy levels and binding energies. The core-loss states are labelled based on the ground state of the excited core-electron (K implies an excitation from a $1s$ state). More importantly the core-loss states contain information concerning the chemical bonding within a material through the examination of the first 10-20 eV of a core-loss edge, known as electron energy-loss near edge structure (ELNES) (Figure 2.6 (b))

[123]. Within crystalline material the conduction band will contain empty electronic states, where the specific number of states per energy are not equivalent and can be described through the DOS of the material. ELNES is an approximate image of the empty DOS of a material, which is sensitive to the chemical state and the bonding environment [123]. Botton illustrated the DOS for graphite, where a large number of available states occur at the π^* and σ^* energy levels, thus suggesting an increased probability of core excitation into these states compared to the other available empty states [123]. This is observed in the ELNES as two strong peaks with other oscillations occurring from available states in the continuum. The simultaneous acquisition of the HAADF image and EEL signal through the removal of the BF detector results in the acquisition of a data cube with the x and y positions corresponding to the Rutherford scattered electron HAADF image, and the z-axis to the EELS spectrum [124]. The data cube allows for elemental mapping, thus providing identification of elements within an HAADF image to be used to determine elemental distribution and chemical bonding [123].

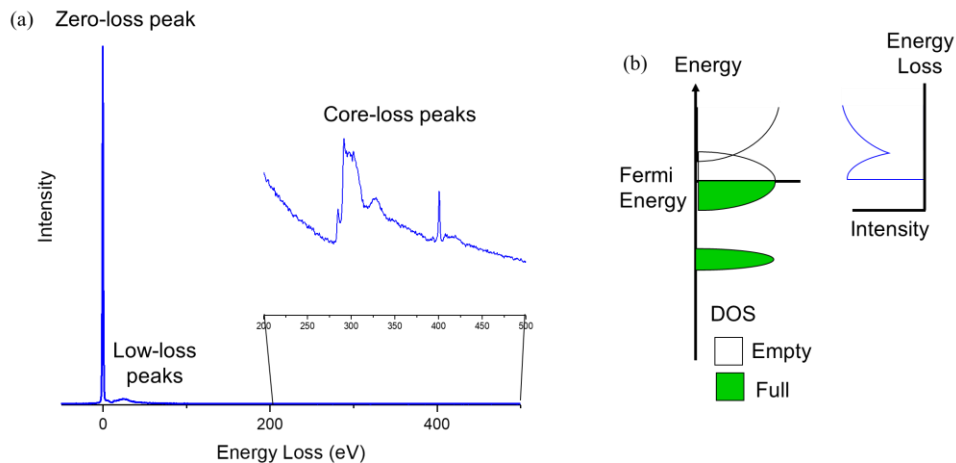


Figure 2.6 Schematic of EELS total spectrum and ELNES. (a) EEL spectrum produced from the inelastic interaction of an incident electron with N_2 gas filled NCNT with respective labelled regions, and (b) schematic of ELNES produced from the empty DOS of the material under investigation.

2.2.3.1 Elemental Quantification using EELS

Other than simply identifying elemental composition and bonding environments, EELS can be used for elemental quantification, such that the edge intensity depends on the inelastic cross-section for the specific ionization process, and elemental concentration. Details on EELS quantification can be found in “Electron Energy-Loss in the Electron Microscope” by Egerton [125], but a brief explanation will be discussed herein. Commonly the integration method is used to determine the areal density (atoms/nm²) and/or atomic ratios. During quantification, the background signal is first removed by modeling the pre-edge region with a power law. Secondly, a partial inelastic scattering cross-section ($\sigma_k(\beta, \Delta)$) is modelled based on the element of interest, EELS collection angle, and the energy range under consideration. When calculating the areal density (N), the integrated intensity of the zero-loss peak (I_0) and the core-loss edge (I_k^1), must both be collected, such that when performing deconvolution to remove the effects of plural scattering,

$$N = \frac{I_k^1(\beta, \Delta)}{I_0 \sigma_k(\beta, \Delta)} \quad (2.4) [125].$$

Atomic ratios are calculated using a similar method; however, due to the nature of the calculation, the zero-loss peak is not required, thus the calculation can be more versatile when considering experimental conditions. When different elements are quantified, and a deconvolution is not performed to remove the plural scattering, energy windows of the same size should be used. The atomic ratio of element A (N_a) and element B (N_b) can be completed by employing the integrated intensity of each element ($I_{ka}(\beta, \Delta)$ and $I_{jb}(\beta, \Delta)$) and their respective scattering cross-sections ($\sigma_{ka}(\beta, \Delta)$ and $\sigma_{jb}(\beta, \Delta)$, respectively),

$$\frac{N_A}{N_B} = \frac{I_{ka}(\beta, \Delta) \sigma_{jb}(\beta, \Delta)}{I_{jb}(\beta, \Delta) \sigma_{ka}(\beta, \Delta)} \quad (2.5) [125].$$

Both equations (2.4) and (2.5) have been implemented in this thesis to determine the absolute and relative atomic fraction of N within various samples.

2.2.3.2 Signal Processing: Independent Component Analysis

Often when extracting EELS elemental maps, signal processing can be quite difficult due to overlapping EELS edges. Within this thesis issues from overlapping edges have resulted in poor background subtractions or the inability to spectrally separate the overlap of a broad edge (Pd-M) with a sharp well-defined excitation (N-K). Furthermore, when performing atomic resolution EELS, noise often dominates the signal due to the requirement of fast spectral acquisition, in effort to reduce beam damage. In these cases, signal processing routines can be used to extract the individual signals from the spectrum image. Independent component analysis (ICA) has been used in this thesis to separate overlapping spectral features in order to observe the origin of σ^* and π^* C-K peaks within NCNTs, to separate overlapping edges, such as the Pd-M and N-K edges, and to extract mixed signals such as FeOx catalysts from only Fe catalysts. ICA separates statistically independent components from a mixed source by considering a linear combination of independent sources [126]. When using the ICA algorithm each component is considered of equal importance, therefore component one is of no more importance than the other components. Hyperspy [127] has been used to implement the ICA on spectrum images found within this report.

2.2.3.3 Examples of EELS Characterization of Metal Atoms on N-Doped Graphene and CNTS

The detection of the N-K edge through XANES is strongly prevalent in scientific literature. XANES detects the disappearance of X-rays through an absorption process from a core level electron excitation within the material under study. The intensities of the XANES and EELS peaks are related to the excitation cross-sections for each element and concentration. Because each N-dopant has a different bonding environment, each has a separate peak in the N-K edge. Specific values for these peaks have been measured with XANES, XPS, and

calculations based on the DOS of N-doped graphene; however, the peaks and chemical species vary between papers with an energy range of 396-403 eV with a consistent arrangement of species from low to high energy of pyridinic, pyrrolic, amino, cyanic, and graphitic [69], [128], [77], [129], [130], [131], [132]. Zhang *et al.* determined the relative change in N-species concentration as a function of temperature through XANES detection [69]. An increase in temperature resulted in the N-dopant species transforming from primarily amino to pyridinic, and finally to graphitic-type dopants. Unfortunately, the local variations of N-dopants within graphene sheets cannot be observed in XPS and XANES, as they examine the average dopant presence over a large area due to the lower spatial resolution of the technique with respect to TEM. Li *et al.* used EELS to map the N-K edge through simultaneous acquisition of HAADF and EELS for a N-doped CNT with Fe catalysts [133]. It was determined that Fe predominately binds next to N; however, the specific N-species and the C-Fe bond could not be resolved through enhanced noise levels associated with low atomic concentrations. Lin *et al.* [132], later used atomically resolved EELS to determine that multiple metallic atoms (Cr, Mg, Al, Mn, Ca, Fe, Ti) prefer to bind to pyridinic-N sites, wherein bonds are formed with the C and N atoms in vacancies to stabilize the metallic species. They later went on to examine the effect of the N-species on the spin state of Cr atoms and determined that as the Cr formed bonds with more N atoms the *d*-band became filled from the lone N electron pairs [83]. The *d*-band filling suggests that a method exists to control the spin state of the adsorbed atom through N-defect manipulation. These experiments demonstrate the benefit of EELS versus XANES, through the ability to atomically resolve binding species from the higher spatial resolution offered by the electron probe when STEM is utilized.

2.2.4 Special Techniques: Identical Location Transmission Electron Microscopy (ILTEM)

Generally, catalyst sizes and distributions are compared before and after *ex situ* electrochemical cycling. Unfortunately, there often exists inhomogeneities between the support structures on a single TEM grid, thus the catalysts analyzed are not being directly observed and compared, but an average picture of the sample is being collected. It would be beneficial to directly image the same area before and after cycling, in order to observe the explicit effects of the electrochemical reactions on the catalysts. This can be accomplished through the direct cycling of the TEM grid containing the support and catalyst material. ILTEM has been developed such that TEM grids are cycled in conventional rotating disk electrode experiments, and the exact catalysts are imaged before and after cycling [134]. Through detailed image analysis, a change in particle size can be measured similar to *ex situ* results, but more importantly, the direct change of individual catalysts can be observed [134]. Moreover, other than examining the structures in 2D projections, this quasi *in situ* technique can be coupled with tomography to examine the volume changes and nearest-neighbour distances in the catalysts before and after cycling [135]. Also, rather than only probing structural changes through imaging techniques, ILTEM can be paired with EELS to observe chemical and morphological changes in the support and catalyst material [136].

2.3 Auger Photoelectron Spectroscopy

Similar to EELS, Auger photoelectron spectroscopy examines an inelastic scattering event; however, the incident electron beam is not detected in this case, rather the released Auger electron is analyzed. After the ionization of an atom from inelastic scattering from ground

state W (Figure 2.7 (a) and (b)), the atom will undergo a de-excitation process (Figure 2.7 (c)), wherein an electron from a higher energy state X will move to state W , thereby releasing energy. This energy can result in the production of a characteristic X-ray or it can cause the emission of an electron (Auger electron) from state Y (Figure 2.7 (d)). The Auger electron generated is characteristic to the specific element and the energy states involved in its production. Commonly, the Auger electron peak is labelled with each of the energy states (WXY), related to Figure 2.1, and common transitions include KLL, MNN, and LVV [137]. Through the detection of the kinetic energy of the Auger electron the elemental composition can be determined [137]. Generally, Auger electrons will be released with kinetic energies below 2,000 eV, otherwise the fluorescent yield takes over and X-rays are subsequently produced [137]. Due to the low energy of the Auger electrons they have a small attenuation length, thus they are extremely surface sensitive, resulting in sample emission from thicknesses varying from 0.3 to 3 nm [137]. Furthermore, the Auger peak is small in comparison to the background, therefore the derivative of the peak is utilized for more precise measurements, such as elemental quantification or bonding examination.

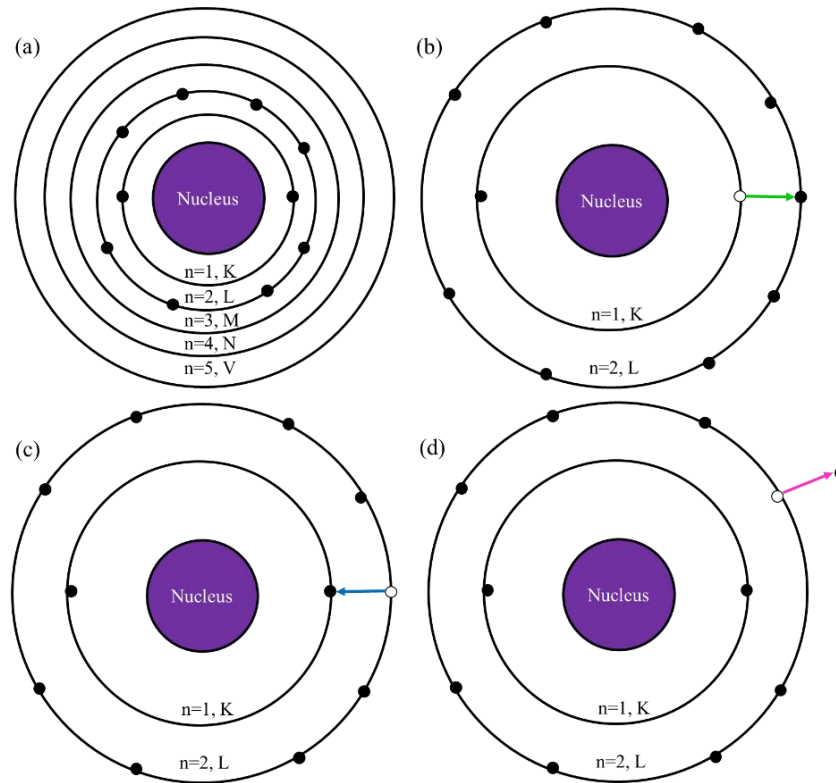


Figure 2.7 Simplified schematic of a KLL Auger electron excitation. (a) Ground state of an atom illustrating the labels of the energy levels, as related to the principle quantum number. (b) The atom is ionized from an inelastic scattering event with an electron source, (c) the excited electron moves back to the ground state, and (d) an Auger electron is released due to the de-excitation process.

2.3.1 Elemental Quantification using Auger Spectroscopy

Identification of the characteristic Auger electron energies through spectral analysis indicates the elements present in the sample. Through intensity examination the relative atomic ratio of these elements can be quantified, such that the intensity depends on the elemental concentration, ionization cross-section, and the fluorescent yield [137]. Quantification is usually completed through the comparison of the experimental intensity of the peak-to-peak height from the derivative of the signal to a pure elemental reference

acquired using the same experimental conditions (spectra resolution, current, voltage, and the emission angle) [137]. When the Auger peaks are separated, and the signals do not overlap, a single reference spectrum can be used to determine the mole fraction (X_A) of the element (A) under consideration,

$$X_A = \frac{I_A}{I_A^0} \quad (2.6) [137],$$

where I_A is the peak-to-peak intensity of the experimental data, and I_A^0 is the peak-to-peak intensity of the reference spectra. Once the mole fractions of all the individual elements are determined, the relative atomic percent of each element can then be quantified. Using this method, the Auger peaks were quantified in this thesis with specific conditions outlined in each individual section.

2.4 Summary

In effort to fully understand the material produced and potentially engineer the most efficient electrode for the ORR and HER the electrode material must be characterized on the atomic scale. Using electron microscopy techniques, the structure of the N-doped graphene and NCNT supports will be analyzed using HRTEM and ELNES examination with EELS. HAADF and ADF will be used to examine the heavy metal structures with respect to the support material. Furthermore, quantification of N concentration and specific N-dopants within the support material will be performed using Auger electron spectroscopy and EELS, respectively. Lastly, using quantification techniques in combination with HAADF imaging, the ALD technique will be fine-tuned to understand the effects of the temperature, dosing time, and the nature of the substrate on the size of the Pt catalysts.

Chapter Three

Structural and Chemical Characterization of Graphene with Pt Atoms and Clusters

In order to understand and optimize the production of Pt atoms and clusters in the absence of nanoparticles, it is crucial to determine the preferred binding locations of the Pt atoms. Additionally, the effect of the graphene structure, specific N-dopants, and the Pt size (atomic to sub-nanometer clusters) on the catalytic activity can only be understood and optimized through detailed characterization of the material's structure at the atomic scale. Through the use of TEM, the N-doped graphene and Pt catalyst were fully characterized. It is demonstrated that the combination of N-doped graphene with ALD Pt generates clusters and single atoms, resulting in a catalyst with a high surface area to volume ratio for the PEMFC. Specifically, HRTEM and HAADF imaging were utilized to determine the structural information of the graphene lattice and the Pt distribution. Electron diffraction and EELS were used to investigate the quality of the N-doped graphene, local variation of N content, and the site preference of N in the lattice. These techniques ultimately provide a full understanding of the material structure, deeming them invaluable tools and techniques for material optimization. DFT was used to examine the origins of the N-dopants within the EELS N-K edge, and ILTEM was utilized to observe the presence of

Pt atoms before and after electrocatalyst cycling. A mix of Pt atoms, clusters, and nanoparticles were also examined for their efficiency as catalysts for the HER.

3.1 Experimental Conditions

3.1.1 Material Preparation

All material preparation was performed by collaborators in Dr. Andy Sun's group at Western University and the specific details can be found in reference [138].

3.1.2 TEM Sample Preparation

The N-doped graphene powders were transferred to a 200-mesh copper grid with a lacey amorphous C support via the dry-press method. Samples with hydrocarbon contamination were baked in a TEM holder overnight at 100°C to minimize electron beam induced contamination.

3.1.3 Microscope Settings

The samples were examined with an 80 kV electron beam to reduce knock-on damage to the graphene [92], [93]. In addition, the high electrical conductivity of N-doped graphene inherently reduces the possibility of ionization damage to the sample [139]. HRTEM and HAADF experiments were performed with an FEI Titan 80-300 Cubed TEM equipped

with a monochromator, hexapole-based aberration correctors (Corrected Electron Optical Systems GmbH) for the image and probe lenses, and a high brightness field emission gun (*XFEG*). For HRTEM, the spherical-aberration correction of the objective lens was set to a negative spherical aberration imaging configuration [139] and a monochromated beam. Similarly, HAADF-STEM was performed with the aberration-corrector tuned to minimize spherical aberration in the probe lens.

EELS and nanoprobe diffraction experiments were carried out with an FEI 80-300 Cryo-Twin TEM equipped with a monochromator, and a Schottky field emission gun (*SFEG*). Specifically, the ELNES from the EEL spectra was extracted to understand the bonding environment of the C, N, and O atoms. The EELS acquisition for the N-K edge was performed in STEM mode with the spectrum imaging technique implemented by the GATAN Digital Micrograph software. The monochromator was used to achieve an energy resolution of 0.08 eV as measured from the FWHM of the zero-loss peak. The low N concentration in the graphene and small cross-section of the N-K edge increases the difficulty in collecting the ELNES [140]. Long acquisition times ranging from 3.0 to 4.0 seconds/pixel were utilized to acquire the N-K edge with a high signal to noise ratio to ensure the fine structure corresponding to each N-dopant was resolved. A dispersion of 0.1 eV/pixel was used for the EELS acquisition of the C-K and the N-K edges, with the areas carefully monitored before and after acquisition of the spectra to ensure contamination from surface hydrocarbons did not influence the fine structures. The EEL spectra containing the O-K edge were acquired on the FEI Titan 80-300 Cubed with a dispersion of 0.2 eV/pixel for simultaneous acquisition of C-K, N-K, and O-K edges. The background of the EEL spectra was removed using a power-law fit [141]. Lastly, the energy dispersive X-ray spectroscopy (EDXS) data was acquired with an FEI Tecnai-Osiris microscope equipped with a *Super-EDX* spectrometer and a single aligned excitation voltage of 200 kV².

² Special thank you to Dr. Feihong Nan for performing EDX analysis at CANMET Materials Technology Laboratory, a facility supported by Natural Resources Canada.

3.1.4 Quantification of HAADF Images and EEL Spectra

The quantification and processing of the HAADF images to determine the location of Pt with respect to the graphene edges were carried out as follows. A band-pass filter was first applied to the HAADF images in order to determine the Pt atom locations. Images were then smoothed with a Gaussian blur, and the local gradients (Sobel filter) were examined to determine the position of the edges of the graphene sheets. Lastly, the Pt atoms and graphene edge outlines were then superimposed on the original image. All images were personally visually inspected to ensure the Pt locations were correct; manual addition and removal of Pt atom locations was performed when it was apparent that the routine failed with comparison to the original image. The coding utilized for the HAADF analysis and Pt location was written with Andrew Scullion using MATLAB. Coding for Pt filled circles was completed using a publicly available code by Sadik Hava produced in 2010, which makes use of code from Zhenhai Wang generated in 2002. These codes are available through MATLAB's online forum, MATLAB central file exchange³.

Quantification of the sample composition was determined using EELS edges. The concentration of the N and O atoms were calculated using the quantification routine in the GATAN Digital Micrograph software with the Hartree-Slater cross-section model and the extraction of the signals of the N-K and O-K edges relative to the C-K edge.

³ Code was found at <http://www.mathworks.com/matlabcentral/fileexchange/27703-draw-a-filled-circle/content/filledCircle.m>

3.2 Results and Discussion

3.2.1 Graphene

Graphene obtained from thermal exfoliation of graphite oxide [142] is susceptible to incomplete exfoliation at reduced temperature and time, thus producing few-layer graphene (FLG), as observed by the fringes induced by folding in Figure 3.1 (a) (orange arrows indicating fringe locations) and the overview of the N-doped FLG sheet in the bottom inset of Figure 3.1 (c). The defects inflicted on the graphene lattice by the thermal exfoliation [143] and the incorporation of N-dopants can be visualized with HRTEM images in single-layer graphene, as illustrated by Gómez-Navarro *et al.* [144] and Meyer *et al.* [103], [145]. For the use of qualitative analysis and comparison, Figure 3.1 (b) of commercially-produced CVD graphene illustrates the characteristic hexagonal lattice of graphene with slight contamination from hydrocarbons floating on the surface as islands (encircled in blue in Figure 3.1 (b)). While the CVD-grown graphene is not defect-free (defects may be intrinsic or beam induced), in qualitative comparison, the N-doped graphene is highly defective on the long-range, as suggested by the multitude of grain boundaries and layers from the edges of the N-doped graphene sheets in the HRTEM image (Figure 3.1 (c)) with confirmation from the computed diffractograms (Figure 3.1 (c) and (d) top inset). In the short range, the complex hexagonal lattice of the N-doped FLG is visible in the thin regions of the N-doped graphene edge (Figure 3.1 (c)), where the computed diffractogram of the bulk area image (Figure 3.1 (d) top inset) confirms the presence of the hexagonal lattice of graphene. Two sets of hexagonal elongated spots in the diffractogram (encircled in blue and green) indicate that the N-doped graphene in this area contains two main grain orientations. An isotropic broadening of the diffraction spots can be observed in the diffractograms originating from the N-doped graphene, while distinct diffraction spots are observed for the CVD-grown graphene. The angular broadening is attributed to multiple

low and high angle misorientations, likely due to the defects present in the lattice, lattice folding, and the presence of misoriented sheets within and between graphene layers [113], [114].

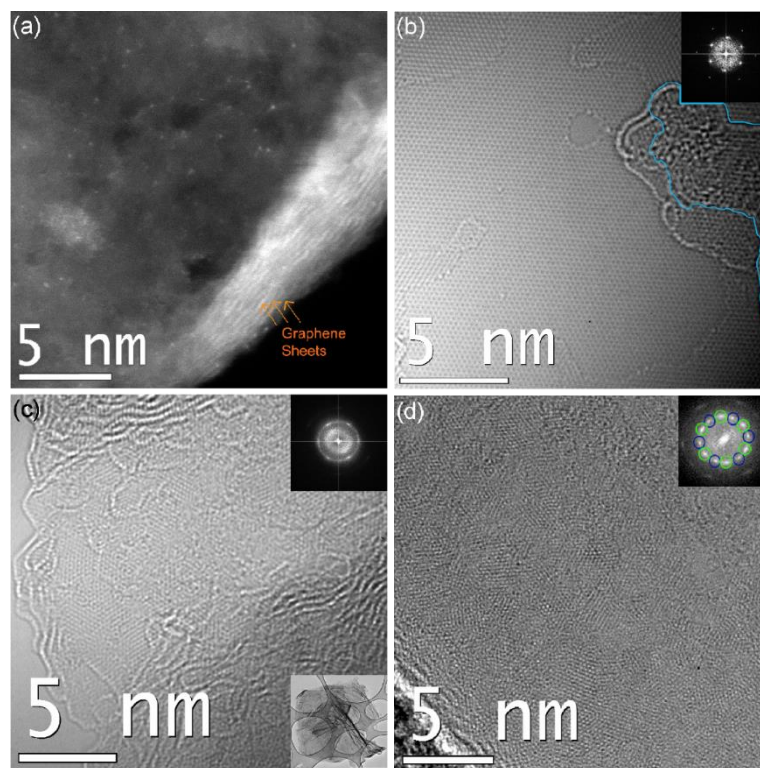


Figure 3.1 HAADF and HRTEM images of N-doped FLG and commercially available graphene. HAADF image after 150 Pt ALD cycles on N-doped graphene. The edges of the graphene sheets are labeled in (a) in orange, indicating that the thermally exfoliated graphene does not consist of single sheets. HRTEM micrographs were acquired from (b) commercially obtained graphene, (c) the edge of an N-doped graphene sheet (C_3 -40 μm), and (d) the bulk area of N-doped graphene after 50 ALD cycles (C_3 -15 μm). The commercial graphene contains floating hydrocarbons encircled in blue. The lower inset in (c) shows a general overview of the N-doped graphene sheets (scale bar 1 μm). Fourier transform diffractograms are displayed in the top insets of (b), (c) and (d) and illustrate the characteristic hexagonal structure of graphene. The 12 elongated diffraction spots highlighted with circles (green and blue) in (d) are a result of two main grain orientations, while the broadening of the diffraction spots can be attributed to stacking misorientations, defects in the graphene lattice, and lattice folding within the field of analysis. The top inset in (d) suggests that the short-range order of the hexagonal lattice is maintained. Reprinted with permission from ref. [138] (S. Stambula *et al.* 2014). Copyright © 2014 American Chemical Society.

The quality of the graphene is further examined using nanoprobe diffraction as observed in Figure 3.2. A graphitic diffraction pattern is obvious through the hexagonal pattern, thus suggesting that the area examined was thick and not pure single sheet graphene. Additionally, the diffraction spots are anisotropically broadened in a similar fashion to the computed diffractogram. Most importantly, the obvious hexagonal arrangement of the computed diffraction pattern reveals that the short-range graphene structure is maintained after N-doping. Because the graphene sheet is multilayered, and the broadening is anisotropic, corrugations are not responsible for the broadening [112]. This indicates that the broadening is due to the fact that the sheets are multilayered and highly defective.

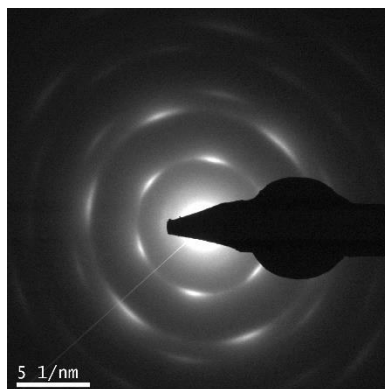


Figure 3.2 Diffraction pattern of N-doped graphene with 50 ALD Pt cycles. The diffraction pattern shows elongated spots from grain and stacking misorientations, lattice folding, and defects within the lattice in the field of analysis, where a single main grain was analyzed (gamma adjusted). Reprinted with permission from ref. [138] (S. Stambula *et al.* 2014). Copyright © 2014 American Chemical Society.

The nature of the local environment of the C atoms in the FLG was studied through a comparison of the C-K edge ELNES of the N-doped graphene (Figure 3.3 (a) green plot) to the amorphous C support on the TEM grid (Figure 3.3 (a) red plot) and commercial graphene (Figure 3.3 (a) black plot)⁴. While a first inspection reveals similarities in the

⁴ The graphene EELS spectrum was acquired by Dr. David Rossouw using commercial graphene obtained from Graphene Supermarket©.

overall shape of the three spectra, the sharp π^* peak (labeled as C1) and σ^* peak (C2) of the C-K edge of the N-doped graphene bears strong similarities to the pure graphene EEL spectrum, as opposed to the weak π^* and broad σ^* peak of the amorphous C, where C is in the sp^2 configuration. The excitonic peak at approximately 292 eV in C2 is present in both the pure graphene and N-doped graphene, while it is absent in the amorphous C-K edge. This suggests that defects introduced from the N-doping process do not affect the very short-range order (i.e. the C is still mostly in trigonal coordination) and the hybridization of the C atoms in a detectable way, which is likely due to the small concentration of dopants. The slight broadening of the σ^* peak (C2) of the N-doped graphene in comparison to the commercial graphene indicates longer-range distortions and is consistent with the disorder observed from the computed diffractograms in Figure 3.1 (d). In particular, the loss of some fine-structure features occurring in the C-K edge after the excitonic peak (e.g. at 296, 302 and 306 eV) and a broadening of the π^* peak (C1) in the N-doped graphene EEL spectrum, as compared to the reference graphene, suggests the highly defective nature of the N-doped graphene.

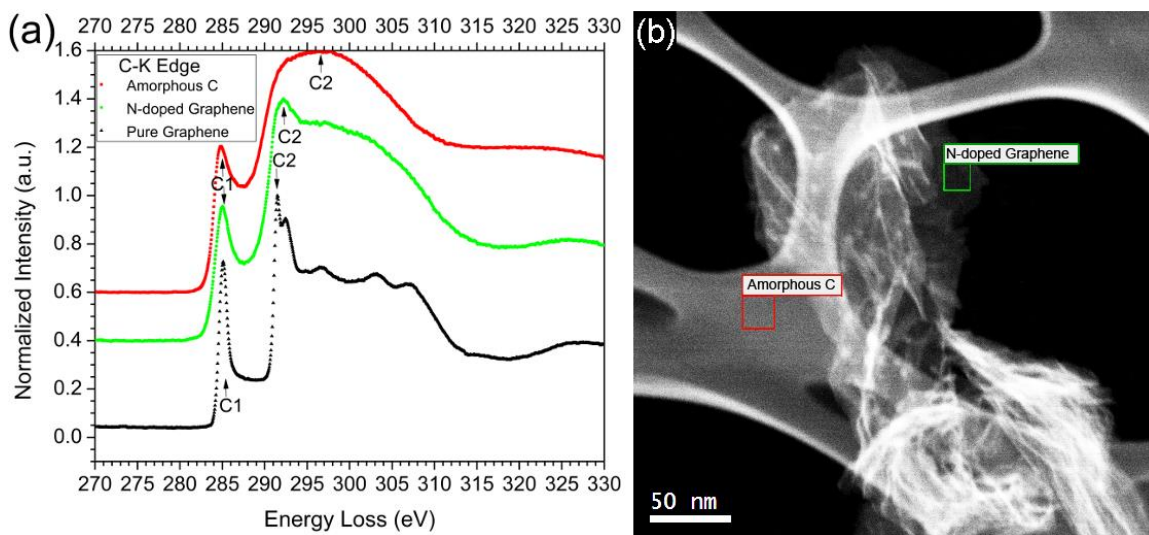


Figure 3.3 C-K ELNES from various C sources. (a) C-K edge ELNES spectra from amorphous C (red), N-doped graphene with 50 ALD Pt cycles (green), and pure graphene (black). The C-K edge π^* and σ^* peaks are labeled as C1 and C2, respectively. The N-doped graphene and amorphous C EEL spectra in (a) were acquired from the corresponding coloured outlined areas in (b) and the EEL spectrum of pure graphene in (a) was acquired from a standard commercial reference sample. Reprinted with permission from ref. [138] (S. Stambula *et al.* 2014). Copyright © 2014 American Chemical Society.

Defects in the structure of the N-doped graphene lattice can be attributed to the graphene production method and the N-dopants. Direct visualization of the N-dopant atoms is not realistically possible due to the multilayered nature of the sample and the similarity in electron scattering of the C and N atoms that gives rise to contrast in imaging techniques in TEM [69]. Consequently, the site location of specific dopants in images such as Figure 3.1 (c) and (d) cannot be taken further in this work. An additional defect source is due to the incorporation of O-species from the incomplete reduction of the graphite oxide, resulting in hydroxyl, epoxy, carbonyl, and carboxyl groups on the surface of the graphene lattice [66], [67]. These moieties can give rise to the broader onset of the σ^* peak (C1) of the N-doped graphene edge in Figure 3.3 (a), but no single peak attributed to any of the O groups appear to dominate this well-resolved region [146], [147]. O-containing defects contribute to the structural defects observed in Figure 3.1 (d), as EELS analysis of the O-K edge indicates a 9.08 ± 1.19 at. % (atomic percent, normalized to C, N, and O) O within

the sample (Figure 3.4). This suggests that the defects in the graphene arise from the thermal exfoliation production method, incomplete reduction, and N-species; however, as suggested by the various characterization techniques the overall short-range graphene quality is preserved. Moreover, Ca contaminants were found on the N-doped graphene samples, which occasionally correlated with Pt catalysts.

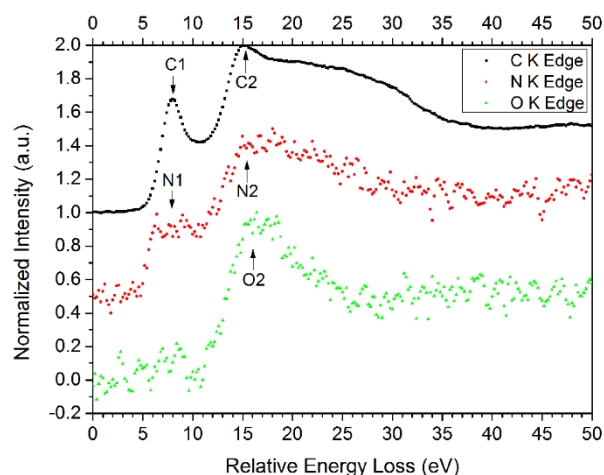


Figure 3.4 EELS of C-K, N-K, and O-K edges acquired from N-doped graphene with 50 ALD Pt cycles. The π^* and σ^* components of the C-K edge are labeled as C1 and C2, respectively.

Furthermore, the N-K edge is also divided by the π^* (N1) and σ^* (N2) regions, where the O-K edge contains only a σ^* (O2) component. Reprinted with permission from ref. [138] (S. Stambula *et al.* 2014). Copyright © 2014 American Chemical Society.

3.2.2 Nitrogen-Doping

Various experimental results report the incorporation of specific N-species in the graphene lattice through XANES of the N-K edge, [69], [77], [128], [129] XPS binding energies, [71], [148], EELS [131], [149], [132], and DFT calculations [150], [130], [131], [149], [132]. The N-dopant atoms were detected here with EELS through examination of the N-K edge, as shown in Figure 3.5. Through quantification of the spectra, relative to the C-K edge, the local concentration of the N atoms in different areas was determined (Table 3.1).

The noise associated with the N-K edge is a result of the low atomic N concentration, as reported in Table 3.1. In addition, from inspection of the near edge structure, the presence of strong features in the N-K edge from 397-400 eV associated with a π^* hybridization (P1-P3), and the feature at 405 eV (P4) associated with a σ^* hybridization can be observed. Each N-dopant species has a specific bonding environment that represents a characteristic peak in the N-K edge fine-structure appearing in the energy range from 397 to 400 eV. The identification of the peaks is not entirely straight forward, due to discrepancies in literature and the uncertainty in the absolute energy in EELS measurements; however, it can be suggested that the peaks can be identified with increasing energy as pyridinic/pyrrolic (P1), amino/cyanic (P3), and graphitic (P3) (recognized in Figure 3.5) [69], [128], [77], [129], [130], [131], [132], [151]. Unlike Nicholls *et al.* [140], an additional well-resolved feature attributed to the N atoms is not observed in the C-K edge, as the EEL spectra were averaged over hundreds of nanometers in an effort to extract the N-K edge rather than acquiring atomically resolved spectra from surrounding C atoms. However, when comparing the C-K and N-K edge on a relative energy scale (Figure 3.5) the similar covalent bonding between the C and N atoms is evident.

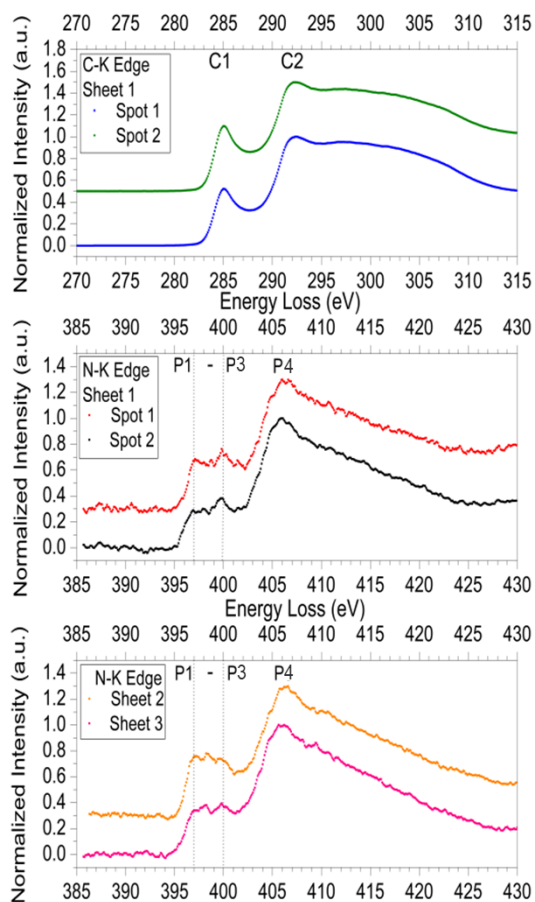


Figure 3.5 Normalized EEL spectra of C-K and N-K edges acquired from three N-doped graphene sheets with 50 ALD Pt cycles and two separate areas on sheet 1. The π^* and σ^* components of the C-K edge are labeled as C1 and C2, respectively. Furthermore, the N-K edge is also divided by the π^* (P1-P3) and σ^* (P4) regions, where P1 to P3 are attributed to the individual N-dopants of pyridinic/pyrrolic-, amino-/cyanic-, and graphitic-type, respectively. Energy scale is within ± 2 eV. Adapted with permission from ref. [138] (S. Stambula *et al.* 2014). Copyright © 2014 American Chemical Society.

Although we cannot be quantitative in the absolute N-species concentration because reference spectra of individual species are not available, changes in the relative contributions of N atoms in various bonding environments can be shown. It is possible to infer, from the N-K near edge structure (Figure 3.5), that there are local variations in the relative proportions of different N-species between N-doped FLG sheets, and even possibly within a single sheet, as the relative intensity of the P1 to P3 peaks (hence the weight of

pyridinic/pyrrolic, amino/cyanic, and graphitic moieties, respectively) vary locally. The N concentration, as determined by EELS analysis, is within the same compositional range between each examined sheet in Figure 3.5 (Table 3.1); however, local variations in the distribution and concentration of the individual N-species exist among the graphene sheets. This is specifically evident through the presence of three peaks in sheet 2 (P1, P2, and P3), whereas only two peaks (P1, and P3) are observed in the other N-doped graphene sheets. P2 is not visible in the π^* region due to the possible overlap from the strong P3 peak.

Table 3.1 Atomic N fraction deduced from quantification of the EELS N-K edges from Figure 3.5 (error acquired from EELS quantification routine in Digital Micrograph). Reprinted with permission from ref. [138] (S. Stambula *et al.* 2014). Copyright © 2014 American Chemical Society.

graphene sheet number (area number)	Percent N (normalized to C and N)
1 (1)	7.3 ± 1.0
1 (2)	6.6 ± 0.9
2	6.9 ± 0.9
3	6.0 ± 0.8

From spatially resolved EELS measurements of several FLG flakes, it is also clear that N is not present in every sheet, or its concentration is below the practical detection limit of EELS of approximately 0.5% in our experimental conditions. It can be proposed that the variation in the relative overall concentration between sheets may be an effect of the location of the sheet within the bulk powder during the doping process. The ammonia gas would likely be more readily available to sheets directly exposed to the flow of the gas rather than within regions of the batch powder where doping would be limited by diffusion. N-doped graphene sheets in Table 3.1 were likely located near the surface of the batch powder during the doping process, while the sheets without a detectable N-K edge were likely located deeper within the powder.

The N-K near edge structures of the electrode material presented here suggests that each of the dopant sites (pyridinic/pyrrolic (P1), amino/cyanic (P2), and graphitic (P3)) are present in the samples under consideration. It is thus possible to infer that an enhanced

ORR activity is expected when these materials are tested for their electrochemical performance. Nevertheless, the N-dopants are not homogeneously distributed across the graphene sheets or within the FLG sample, thus possibly resulting in local variations of the ORR. Our results also suggest that local measurements such as the ones reported in the present work, rather than average measurements with broad-beam methods, need to be carried out in order to optimize the synthesis and thus ensure full utilization of the electrode support for the ORR.

3.2.2.1 Density Functional Theory (DFT) ELNES Calculations

In order to better understand the origins of the peaks in the π^* region of the N-K edge, DFT was used to model the ELNES structure using WIEN2k [152].⁵ WIEN2k is an *ab initio* based software package used to calculate electronic structure of ground state material through the implementation of DFT using a full potential basis set. The choice of a full potential basis set makes this software package unique, as it includes all electrons in its calculation rather than employing pseudo-potentials, where the core-states and nuclei are combined into a single potential [153]. This program is commonly used to calculate ELNES spectra [131], [154], as the calculated total DOS is very precise from the full potential code. Unfortunately, this can lead to lengthy calculations, thus WIEN2k is not recommended for large unit cells. For more information on WIEN2k and its implementation, the following references can be consulted [155], [156], [157].

In order to complete the calculations, graphene crystal structures were produced following a simulation from Warner *et al.* [154]. Two main considerations were applied as follows: (1) a large (25 Å) c-spacing was used to prevent the interaction of graphene sheets, and (2) the sub-units for the N-doped graphene sheets were increased to a 3x3x1 super-cell

⁵ I would like to thank Dr. Matthieu Bugnet and Dr. Stefan Löffler for discussions concerning DFT implementation, WIEN2k code, and WIEN2k downfalls for graphene modelling.

to prevent the interaction of the dopants [154]. Each graphene structure was produced by Dr. Ali Malek, wherein they were relaxed using the Vienna Ab initio simulation package (VASP) before their use in WIEN2k. Using the “.cif” files of the relaxed structures, five different graphene structures were examined (Figure 3.6): graphene, graphitic N-dopant, pyridinic N-dopant at a zig-zag edge, amino N-dopant, and a Pt adatom with a graphitic N-dopant. Based on in-depth analysis of DFT parameters on ELNES calculations from single sheet graphene [149] and single-walled carbon nanotubes [131], the core-hole was excluded from the calculation. While a core-hole best replicates the physical electron excitation during the EELS process, when included in the DFT calculation the ELNES results in a poor spectral match; however, the agreement with the experimental spectrum is better when the core-hole is omitted. A possible explanation for the poor spectral match when adding the core-hole is that it is added into an arbitrary conduction state without the consideration of electron rearrangement after excitation. In reality, the ground state electronic structure will be modified from the introduction of an electron into the conduction band, which will affect the ELNES spectra and could result in the poor agreement observed by others.

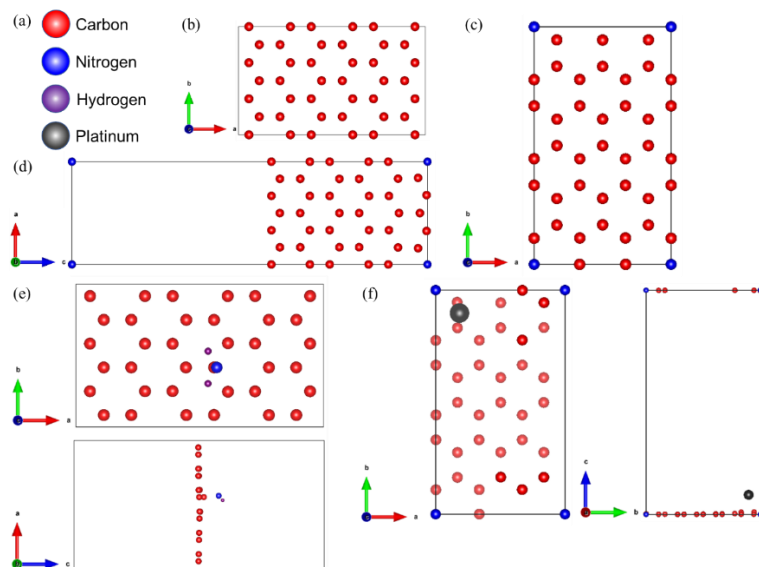


Figure 3.6 Relaxed and optimized structures used for DFT calculations (a) legend, (b) graphene, (c) graphitic N-dopant, (d) pyridinic N-dopant, (e) amino N-dopant, (f) graphitic N-dopant with Pt adatom. All structures were constructed using Vesta software [74].

Following the construction of each structure, the symmetry was optimized using WIEN2k, and the DOS were produced with the *TETRA* program [158], [159]. The self-consistent field (SCF) calculation was used to converge the basis set by examining the total DOS with varying number of basis set functions (RK_{\max}) and the number of k-points in reciprocal space (k-mesh) for each structure (Figure 3.7). A linear augmented plane wave (LAPW) basis set was selected, and the linear density approximation (LDA) was used for the calculation of the exchange-correlation energy based on ref. [131]. For the structures containing the single Pt adatom, the calculations were performed with spin polarization. Following the convergence of the DOS, the ELNES structures for the atoms of interest were produced using the *TELNES3* program [157]. The k-mesh was gradually increased for each structure until convergence was achieved. The convergence and collection semi-angles for the ELNES calculation were selected to be a median value of 20 mrad. Additionally, the spectra were selected to be sampled in all directions to remove the anisotropic effects of the graphene structure. It was believed that this would better represent

the nanosheets observed in Figure 3.5, due to the fact that the graphene sheets were randomly oriented from the defects found within the graphene lattice. Further, a spectrometer Gaussian broadening of 0.4 eV was added to each spectrum based on experimental conditions. For more accurate spectra simulations, a Lorentzian with a linear energy broadening should be applied to the converged spectra to resemble the lifetime of the excited state. Unfortunately, this broadening in WIEN2k is too strongly implemented, and therefore was not utilized, and an external code should be written at a later date. Convergence values for the LAPW basis set and ELNES for each structure can be found in Table 3.2.

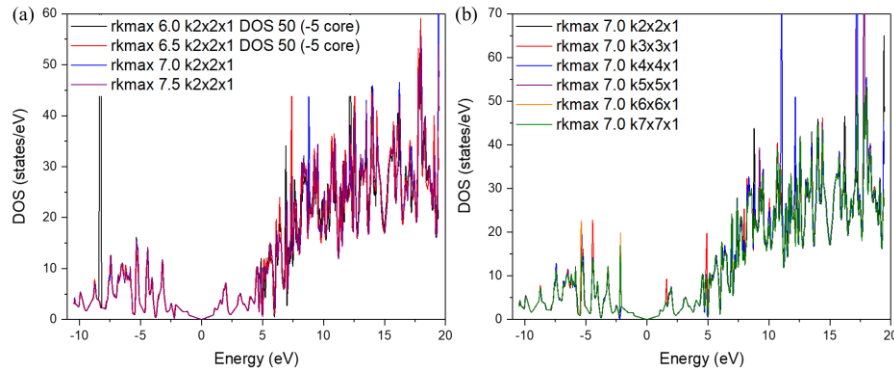


Figure 3.7 Convergence of the basis set of the graphene structure using the total DOS by first converging the (a) RK_{\max} , followed by the convergence of the (b) k-mesh. Spectra were acquired with 50 k-points and broadened by 0.003 Rydbergs.

Table 3.2 LAPW basis set and ELNES convergence values.

Structure	LAPW Basis Set		ELNES
	RK_{\max}	k-points	k-points
Graphene	7.0	4 x 4 x 1	12,000
Graphitic	6.5	4 x 4 x 1	6,000
Pyridinic	6.5	12 x 12 x 1	8,000
Amino	5	13 x 13 x 1	1,000
Graphitic-Pt	6.5	6 x 6 x 1	2,000

The DOS from the total crystal structure, an isolated C atom, and the N-dopant can be found in Figure 3.8 with a broadening of 0.03 Rydbergs applied to the spectra. It is expected that the incorporation of various defects and N species within the graphene lattice will affect the DOS, as the electronic properties are being modified through a doping process. It has been suggested that the graphitic N-dopant acts as an n-type electronic dopant to the graphene crystal structure, as an additional electron is added into the lattice [87]. Alternatively, it has been theorized in literature that the amino- and pyridinic- type dopants result in a p-type doping [87]. From Figure 3.8 (a) the effects of the doping can be observed through relative shifts to the total DOS with respect to the Fermi energy (0 eV) of the graphene structure. Graphene behaves as a semi-metal with a zero-band gap, which is observed at the Fermi energy. When examining the total DOS of the graphitic dopant with respect to the pure graphene structure, a shift towards lower energy appears with respect to the Fermi energy, thus filling the conduction band and illustrating the n-type doping. Interestingly, the Pt atom on the graphitic-type dopant seems to have weakened the n-type behaviour from the total DOS, thus indicating that the additional N atom incorporated into the graphene lattice is acting in the chemisorption bond with the Pt atom. The p-type characteristic of the other dopants is not as obvious; however, there are electron states that appear at the Fermi level which is an indication of the doping process, and a potential shift in the valence bands towards a higher energy. It can be noted from Figure 3.8 (b) that the N atoms affect the total partial DOS (PDOS) of an individual isolated atom that is located ~5 C atoms away from the dopant. This indicates that the N atoms are not effectively isolated from each other and are interacting. Based on the atomic models, the N concentration are set to 2.8 at. % for the graphitic and pyridinic dopants, and 2.6 at. % for the amino dopant. This is not ideal, as it does not replicate a single N-dopant, thus interaction of the N-dopants will occur within the computation. Li *et al.* suggested that a change in the dopant concentration with the size of the crystal structure can modify the nature of the N-K ELNES, as seen through intensity variations and fading of the higher energy oscillations [130]. Lastly, the total PDOS of the N-dopants can be observed in

Figure 3.8 (c). Here, the contribution of the changes in the total DOS observed in Figure 3.8 (a) can be isolated to the N-dopants, such that the n-type behavior from the graphitic dopant is observed in Figure 3.8 (c) as a shift of the conduction band to energies below the fermi energy, and the p-type behavior of the amino and pyridinic dopant is observed as a shift in the valence band towards higher energies. As a final note, the graphitic-Pt dopant has a nearly overlapping DOS for the spin-up and spin-down calculations, suggesting that spin polarization calculations are not necessary in this structure.

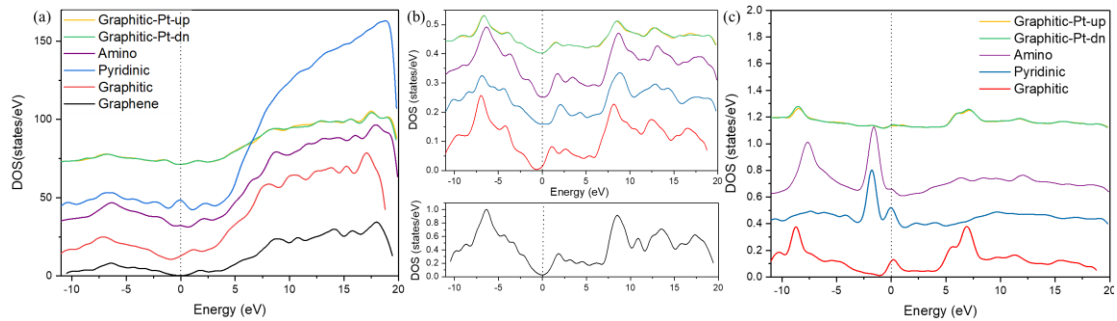


Figure 3.8 Converged DOS for the five structures outline in Figure 3.6 showing the (a) total DOS, (b) total C PDOS from an isolated C atom (same legend as (a)), and (c) the total PDOS from the N-dopant. Spectra were acquired with 50 k-points and broadened by 0.03 Rydbergs to smooth the noise.

When probing the ELNES structure in graphene, we are observing the $1s \rightarrow 2p$ transition of the core electron, and in doing so, we are examining the π^* and σ^* unoccupied states from the p_z , and p_x and p_y orbitals, respectively. With this being said, the total PDOS of the N atoms and their p-orbitals are plotted in Figure 3.9. Simply by examining the total N-PDOS, it is apparent that local changes with the band structure occurs based on the incorporated N-dopant, indicating the origins of the sensitivity of the N-K edge for fingerprinting the type of dopant present in the sample. Based on the N-p states, the approximate shape of the N-K edge can be resolved, such that it contains the sharp π^* peak at lower energy and broader σ^* peak at higher energy with respect to the Fermi energy. Interestingly, of the four structures examined, the peaks in the pyridinic type dopant were

more spread out. It should be noted that in the case of the pyridinic-type dopant, the p_y orbital is out of plane due to the optimized orientation introduced by WIEN2k, thus the p_y orbital is related to the π^* state and the p_z and p_x orbital are related to the σ^* state. The broadening of the N-PDOS for the pyridinic-type dopant differs from Schiros *et al.* [87], Lie *et al.* [130], and Lin *et al.* [132], in which sharp π^* peaks were observed. This could be an effect of the doping concentration, as suggested by Li *et al.* [130], or due to the fact that the pyridinic dopant was set at a zig-zag versus a vacancy configuration commonly used in literature.

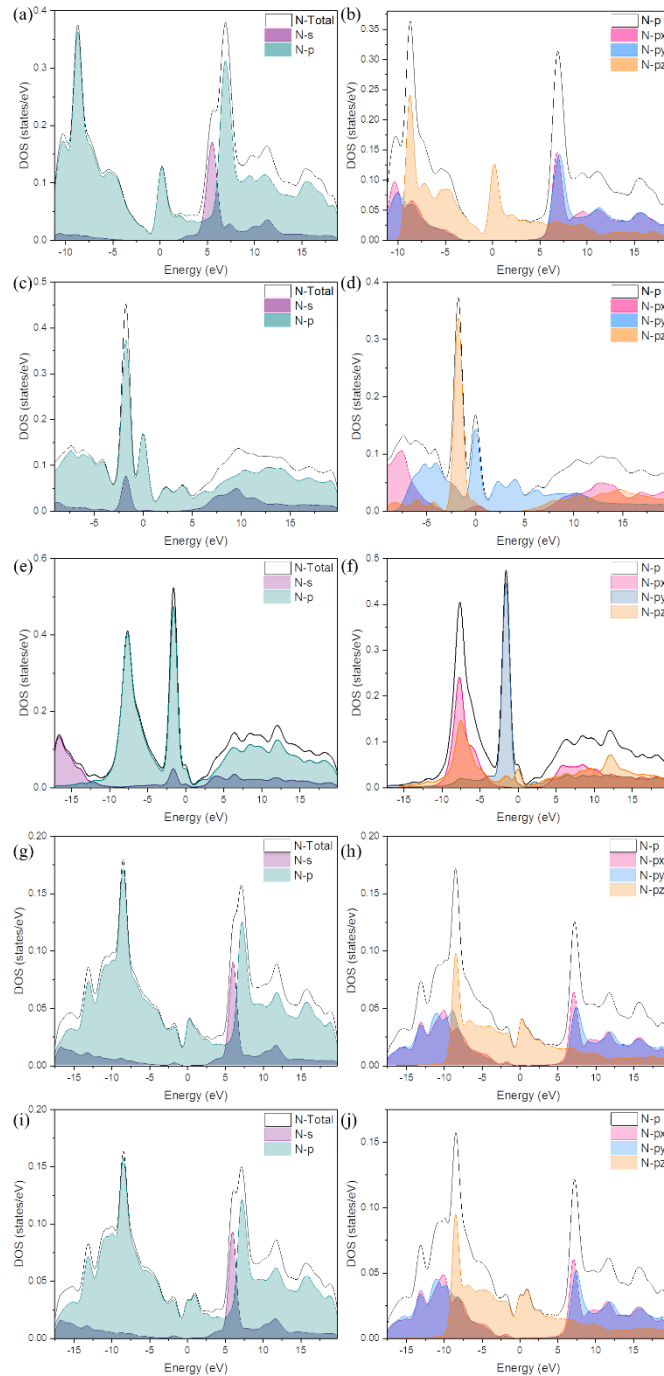


Figure 3.9 N-dopant PDOS for the total N contribution and N-p states. PDOS of (a,c,e,g,i) the total N contribution as constructed from the N-s and N-p states and of (b,d,f,h,j) the N-p state as constructed by the p_x , p_y , and p_z states. The specific dopants examined are (a,b) graphitic, (c,d) pyridinic, (e,f) amino, (g,h) graphitic-Pt-spin down, and (i,j) graphitic-Pt-spin up.

Using the converged DOS and the *TELNES3* program, the N-K edge ELNES from each N-dopant was calculated, as shown in Figure 3.10. Through comparison of the calculated ELNES to the N-p PDOS in Figure 3.9 (d), the origins of the peaks in the N-K edge can be determined. As expected, the amino and pyridinic structures resulted in broad π^* and σ^* peaks, which differ from those found in literature [87], [130], [132]. However, the graphitic-dopant results in a sharper π^* (~ 0 eV) and σ^* (~ 7 eV) peak, which more closely resembles literature structures [131], [149], [154], [132]. The comparison with the experimentally obtained N-K edge from Figure 3.5 to the computed structures in Figure 3.10 is the most important aspect for examining the validity of the calculation, as these structures would ideally be used to characterize the specific peaks associated with the N-dopants in the graphene N-K edge. Unfortunately, the three peaks observed in the experimental N-K edge were not replicated from the calculation, except for the graphitic dopant. Initially, optimism for this calculation was quite high, based on the successful modelling in literature of C-K ELNES from graphene using WIEN2k and other DFT based codes. Unfortunately, the structure in which we are trying to characterize is quite complex, thus leading to a higher degree of complications when attempting to model the system. First, the graphene used to obtain the N-K in Figure 3.5 is multilayered, and has a total doping concentration of ~ 7 at. % (normalized to C and N) or less with varying concentrations of individual dopants. It has been suggested by Li *et al.* that the concentration of the dopants will affect the DOS and hence the ELNES structure [130]. This suggests that a model structure that better represents the experimental conditions should be used. In an effort to obtain a more representative distribution of the N-dopants, X-ray spectroscopy can be used to gather the relative at. % for each dopant on an average scale. Furthermore, the presence of different defects in the graphene lattice have been shown to greatly affect the ELNES of the C-K edge, thus it can be suggested that the selection of the N-dopants and the defects with their relative proximity to the N-dopant under examination, may also affect the overall N-K edge [160]. Through inspection of the HRTEM images in Figure 3.1 (c) and (d), possible defects may range from point defects to

graphene edges and folding. Therefore, the effect of defects on the N-K should be also be examined. Lastly, Arenal *et al.* [131] noted that the presence of N in an amorphous C layer resulted in a significant change in the N-K edge with respect to the graphitic-dopant, resulting in a broadening and overlapping of the π^* and σ^* peaks. As they suggested, this amorphous layer may not be visible at low magnifications or spatial resolution, thus it would not be accounted for in the proposed N-K edge structures. The N-K edge acquired experimentally here was collected at a low magnification, to increase the signal to noise ratio, thus an amorphous layer may have gone unnoticed, therefore possibly resulting in the discrepancies between the experimental and computed N-K ELNES. Overall, it is suggested that the individual dopants modeled using WIEN2k do not represent the configuration of the N-dopants in this system. It is possible that the spectral signatures found in literature match the experimental data with more precision than the results found here, due to the fact that single sheet graphene and CNTs were examined with specific dopant configurations imaged with STEM.

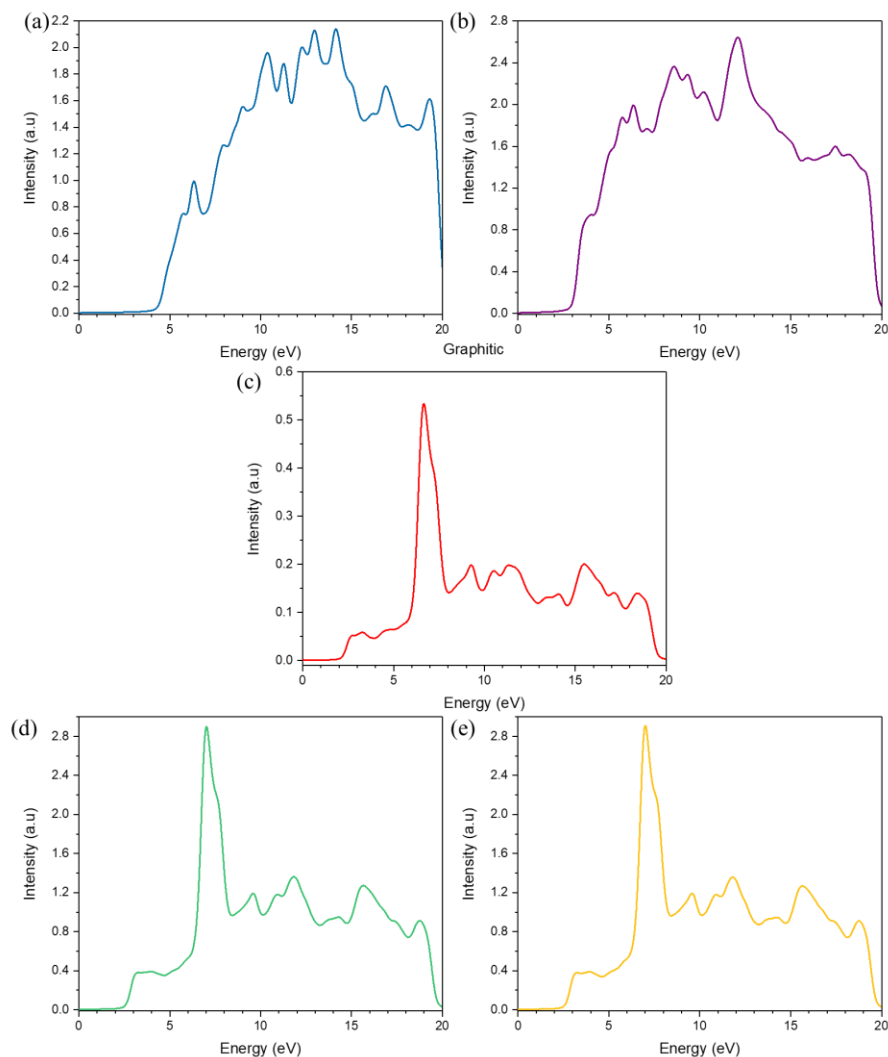


Figure 3.10 Calculated N-K ELNES for each N-dopant, (a) pyridinic, (b) amino, (c) graphitic, (d) graphitic-Pt-spin down, and (e) graphitic-Pt-spin up.

Comparison of the WIEN2k data to calculations and experiments in literature suggests that WIEN2k can effectively calculate the N-K edge of the graphitic-type dopant. Other than the potential causes for the disagreement between the ELNES calculated in Figure 3.10, and the experimental data in Figure 3.5 discussed above, additional causes of inconsistencies may be due to the method in which the ELNES calculation is implemented. First, the calculation only considers single atom inelastic scattering, and excludes all other

scattering events that will physically occur between the incident electron and the crystal (i.e. elastic scattering, multiple scattering, and channeling). Because graphene is a single layer, this effect should bear little influence on the accuracy of the simulation to produce the same structure as the ELNES spectra. However, in the case of the experimental data which is from a multilayered graphene sheet, this may have a small effect. Secondly, the existence of an excitonic state between the core-hole and excited electron is poorly described by DFT. With the complexity of the structure to be calculated, and the shortcomings of the code, the possibility of achieving a direct spectral match between the experimental and computed ELNES is unlikely without the direct characterization of the Pt bonding location with respect to the specific N-dopants and lattice defects.

3.2.3 Pt Catalyst

The Pt atoms and clusters deposited on N-doped graphene through ALD are visible in Figure 3.11 (a,b,c) using HAADF imaging, where they appear as bright dots over a darker background, corresponding to the graphene support and vacuum. In each image, the N-doped graphene has localized small regions with fewer layers (examples encircled in orange) and folds, resulting in intensity variations in the support material through the mass-contrast contribution in the HAADF signal. The graphene and N-doping production method consistently yields multilayered, and folded sheets, as determined through HRTEM (Figure 3.1 (c)). Due to the multilayered nature of the N-doped FLG and sheet misorientations observed from the computed diffractogram (Figure 3.1 (d)), the graphene lattice cannot be resolved using the experimental conditions for our HAADF imaging. Similarly, the exact location of the Pt atoms with respect to the graphene hexagonal lattice and the N-dopants, as done previously by other researchers with other elements on single layer graphene, cannot be retrieved [140], [120], [161]. However, through quantitative analysis of the HAADF signals in our images, we can retrieve the location of the edges

(yellow lines) composing the N-doped FLG and Pt atom and cluster locations (pink dots) (Figure 3.11 (d,e,f)). From this analysis, it is clear that the Pt atoms are primarily located along the edges of the graphene stacked nanosheets, with few Pt atoms situated in the central part of the sheets (indicated by green arrows). Remarkably, in each set of ALD cycles (50, 100, and 150), Pt atoms and few-atom clusters are observed on the N-doped graphene support, rather than nanoparticles. According to Sun *et al.* [162], increased ALD cycling results in increased Pt loading, and the formation and growth of nanoparticles on pure graphene nanosheets. Instead, our work shows that the growth of nanoparticles did not occur within the N-doped graphene samples, as the atoms and clusters appear to be stabilized, and thus rendered immobile by the defects within the graphene lattice and the N-dopants. Also, a decreased nominal Pt loading in comparison to the graphene nanosheets reported by Sun *et al.* [162] may be responsible for the lack of nanoparticles in the N-doped samples. Furthermore, our measurements show that the specific Pt density in the N-doped samples varied amongst locations on the graphene sheets, likely due to local variations in defects in the graphene lattice, N-dopant concentration, dopant site distribution, and variations in Pt loading. It is expected, as suggested by Hsueh *et al.* [34], that increasing the number of ALD cycles and therefore the Pt loading, will eventually form nanoparticles as the N-dopant and edge nucleation sites are filled by Pt atoms; however, this was not observed up to the 150 ALD cycles in our work.

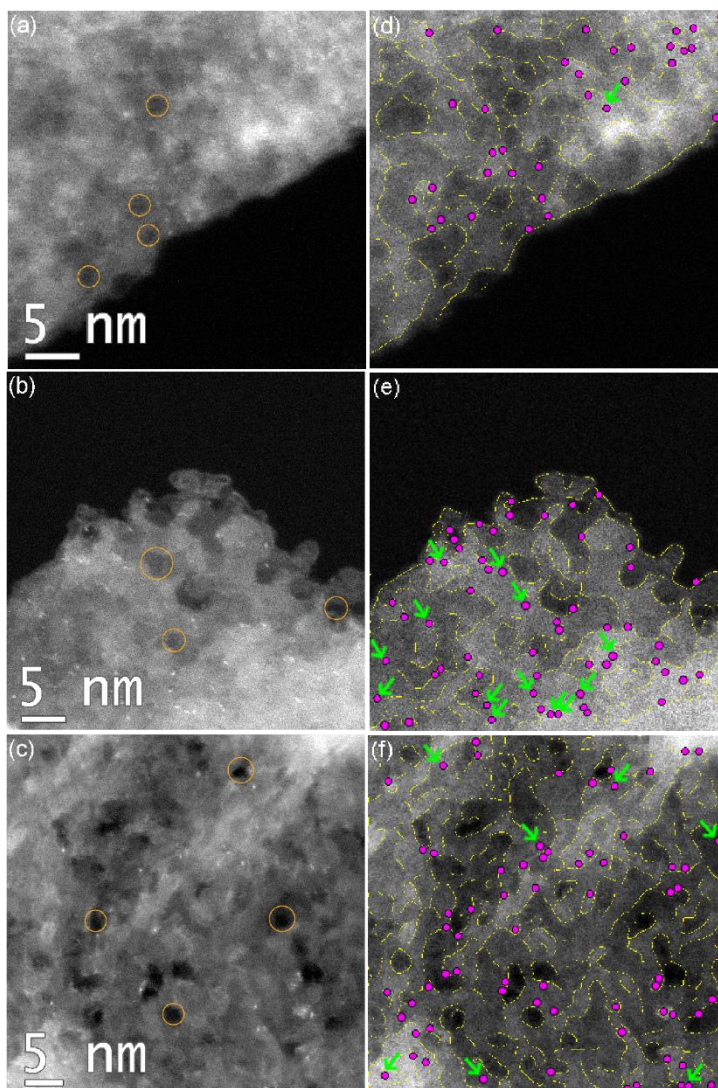


Figure 3.11 HAADF images of 50, 100, and 150 ALD Pt cycles on N-doped FLG. Raw (left) and processed (right) HAADF images of (a,d) 50, (b,e) 100, and (c,f) 150 ALD Pt cycles on N-doped graphene, respectively. The orange circles in the raw images locate the specific areas with fewer layers in the graphene lattice from the destructive thermal exfoliation process. The processed images outline the edges of the graphene nanosheets with yellow lines, and the Pt atoms and clusters are distinguished with pink dots. These are simply overlaid on the original raw image. Green arrows highlight atoms that are not located on the edges of the graphene sheets. Specific details of the processed images can be found in the experimental section. Reprinted with permission from ref. [138] (S. Stambula *et al.* 2014). Copyright © 2014 American Chemical Society.

HRTEM, using negative spherical aberration imaging conditions (Figure 3.12), can be used to provide complementary information to the HAADF images in Figure 3.11. The Pt atoms are observed as sharp dots in the HRTEM images [163], [164] and the amorphous C contamination is encircled in blue, where the contrast of the image is dependent on the microscope imaging parameters. However, the unambiguous identification of Pt atoms and clusters is difficult in the HRTEM images, due to the multiple-layered nature of the graphene. To more precisely observe the location of the Pt with respect to local graphene defects and N-dopants, experiments with single sheet graphene would need to be conducted.

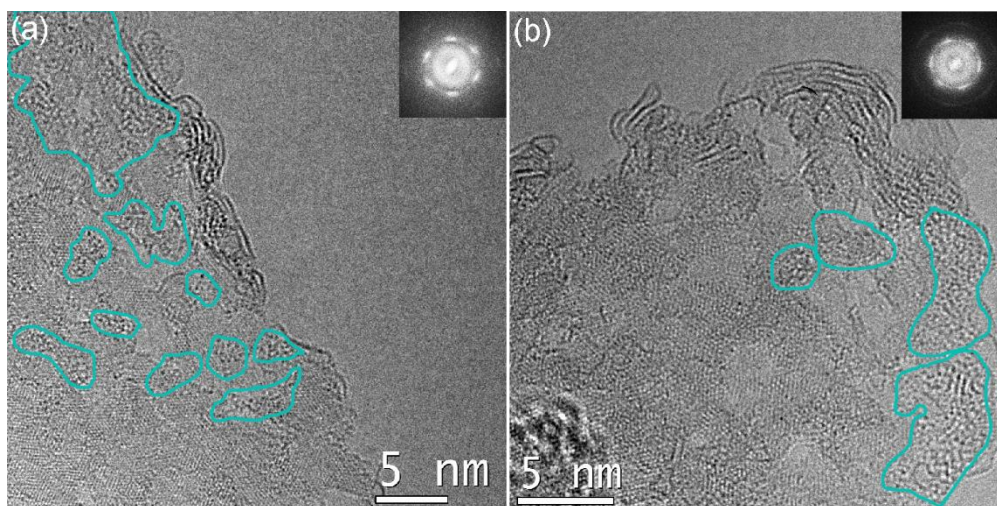


Figure 3.12 HRTEM image of N-doped graphene with 50 ALD Pt cycles at two separate locations (a) and (b) (C_3 -15 μm for each image). The amorphous C contamination is encircled in blue. The Pt atoms and clusters can be identified as sharp dots; however, the multilayered nature of the samples makes the precise location of Pt ambiguous. Reprinted with permission from ref. [138] (S. Stambula *et al.* 2014). Copyright © 2014 American Chemical Society.

Further, the presence of Pt on the N-doped FLG is confirmed with EDXS on a similar sample to Figure 3.11 with 100 ALD Pt cycles on N-doped graphene (Figure 3.13). Small Pt peaks are present in the EDX spectrum of the sample (Figure 3.13), while no such peaks are observed in the reference spectrum acquired over vacuum. The Cu, and C in the

reference spectrum are due to the lacey C support on the Cu TEM grid, while the Mo and Mn are likely originating from the sample holder, apertures, and instrumental contributions. Both the sample and the reference spectrum contain Si, which could be a contaminant originating from the lacey C support. The spectrum from the N-doped FLG and the comparison of the in-vacuum spectrum confirm that the Pt signal is arising from the sample rather than instrumental effects or contamination. Further, the O in both the reference and sample spectra is related to the oxidized Si that contaminated the lacey C support, and an incomplete reduction of the graphite oxide, respectively.

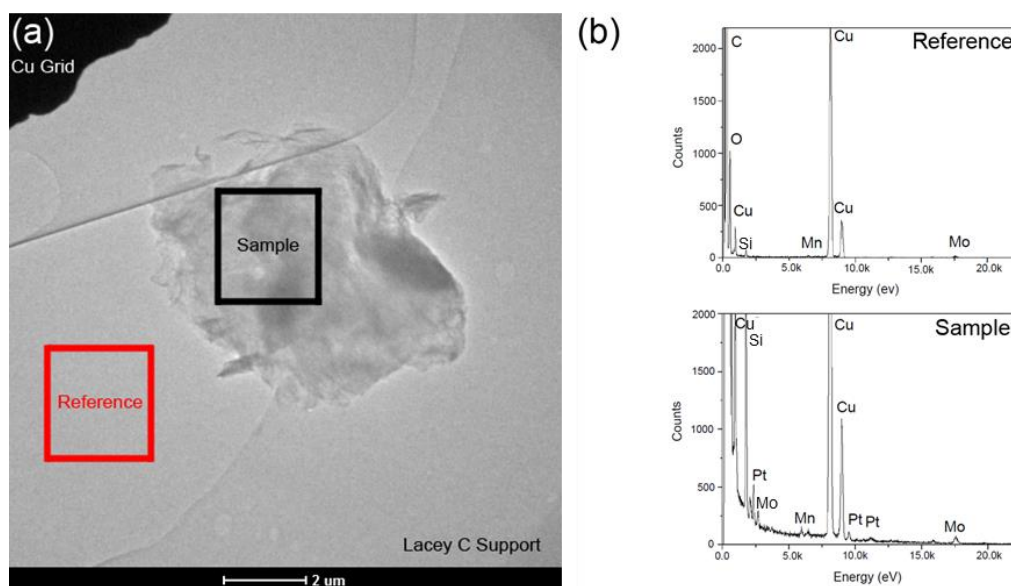


Figure 3.13 EDX spectra from a reference area and the sample. (a) TEM image of respective areas utilized to acquire (b) the reference and sample EDX spectra (similar sample to those in Figure 3.11 with 100 ALD Pt cycles on N-doped graphene). Reprinted with permission from ref. [138] (S. Stambula *et al.* 2014). Copyright © 2014 American Chemical Society.

The relationship between the Pt observation and the detection of N in different bonding configurations can now be considered. Through various calculations [41], [76] in literature, it has been shown that Pt is expected to bind to the C atoms adjacent to N-dopants due to the imposed positive charge. Indeed, Holmes *et al.* [41] showed that N incorporation increases Pt nucleation and that Pt ripening is unfavorable over pyridinic sites. This creates

an ideal situation for Pt catalyst deposition as it results in an increased Pt loading without Pt agglomeration, as shown in Figure 3.11 and Figure 3.12, through the production of Pt atoms and clusters. The predominant location of Pt at N-doped graphene edges (Figure 3.11), and the lack of Pt ripening is consistent with calculations [62], suggesting that the adsorption energy of Pt on graphene is enhanced at edge locations due to dangling bonds and the presence of pyridinic-type dopants at the FLG edge, thus allowing for the stable formation of atoms and clusters. Additionally, Kong *et al.* [62] calculated that the diffusion rate of Pt on the surface of graphene is greater than the diffusion at edge sites, which is consistent with the experimental data found here with the location of Pt on graphene edges. An additional contribution to the observation is due to Groves *et al.* [82], who concluded that N-doping enhances the adsorption energy of Pt on C. Thus, the presence of Pt atoms and clusters located on the terraces of the graphene nanosheets (labeled with green arrows in Figure 3.11), and not as Pt nanoparticles, is likely linked to N-dopants increasing the Pt-C bond energy, or to vacancies in the graphene lattice [41]. This possibly suggests that the Pt remains in atomic and atomic-cluster form on the N-doped graphene due to the incorporation of vacancies and edge defects, and the increased binding energy between Pt and C from N-dopants; thereby reducing the mobility of Pt on the surface of the FLG, and preventing the growth into larger nanoparticles. The EEL spectra in Figure 3.5 indicate that pyridinic-N (peak P1) is contained in each examined graphene nanosheet, which can influence the preferential position of Pt atoms and clusters at the edge of these sheets. According to calculations performed by Holmes *et al.* [41], Pt nucleation is more favorable on pyridinic-type dopants rather than graphitic-type, while Pt ripening is unfavorable on pyridinic-type in comparison to graphitic-type. Our study agrees with these calculations [41], as the EEL spectra in Figure 3.5 indicate that both pyridinic (P1)- and graphitic (P3)-type dopants moderate the effect of both ripening and nucleation in the sample. In collaboration with Dr. Ali Malek (Simon Fraser University), calculations were performed to determine the binding energy of Pt on different N-dopants in single sheet graphene. It was determined that the Pt binding energy was greatest when located in binding spots 1

and 5 (or 6) in Figure 3.14 on pyridinic-type dopants, as compared to graphene and graphitic N-dopants. The schematic diagram in Figure 3.14 illustrates the bonding configuration of the stabilized Pt atoms at the edge location adjacent to the pyridinic-type dopant. One should note, however, that the binding energy of Pt to a pyridinic-type dopant at a vacancy or the vacancy on its own were not calculated, thus it cannot be completely ruled out that the highest Pt binding energy occurs at the edge location of the pyridinic-type dopant. Nevertheless, it is clear from Figure 3.11, and the calculations performed to produce Figure 3.14, that Pt prefers to nucleate at edge sites, thus resulting in the formation of atoms and clusters at edges rather than a continued growth to nanoparticles from the increased binding energy of available dangling bonds, and the decreased ripening from N-dopants.

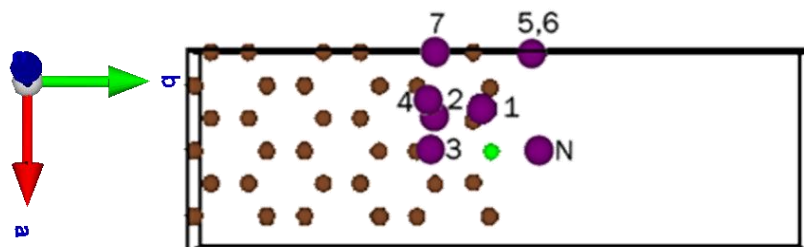


Figure 3.14 Calculation of Pt atoms (purple) located at an edge site bonded to C atoms (brown) adjacent to a pyridinic-dopant (green). Based on energy calculations performed by Dr. Ali Malek the most stable configuration of Pt on N-doped graphene occurs at locations 1 and 5 (or 6). Structure was constructed using Vesta software [74].

It is still unclear if the sheer volume of graphene defects and edges within the N-doped FLG effect the preferred bind spots, and hence the size of the Pt examined. It can be argued that the Pt atom will prefer to bind to edge locations or defects, whether or not an N-dopant is present. Other than calculations, this would require an in-depth experiment ensuring the ALD is performed with identical experimental set-up on graphene and N-doped graphene samples that contain the FLG sheets with the same ratio of the

circumference of the edges to the surface area of the basal plane. This experiment could be completed in the future; however, a high difficulty level is expected due to estimating the total edge area with respect to the surface area of the basal plane. Only ratios that are relatively similar should be examined and compared for the Pt size on graphene and N-doped graphene substrates to ensure the edge effects are removed from the experimental results. Further complications with this study could result from observations of Pt on graphene from Zan *et al.* [165], [120]. They found that metal atoms can be mobile under the electron beam and divide small clusters into atoms, which inevitably leads to the distribution of atoms along the graphene edges, wherein catalytic hole growth and repair can ensue. Wang *et al.* also determined that Si atoms are mobile and can also act as catalysts for graphene hole growth under electron beam exposure [166]. With this understanding it is possible to propose that the Pt atoms were dragged to the edge of the N-doped graphene sheets with the help of the electron beam. In the specific conditions used in the experiments discussed earlier, the movement of the Pt atoms with the beam cannot be conclusively omitted. It can be suggested that if the Pt atoms did move under the influence of the electron beam, then this movement would inevitably result in the Pt atoms finding the most stable sites, thus suggesting that the edge location is the preferred nucleation sites when the atoms are provided conditions for diffusion.

The role of N-dopant sites on the ALD growth mechanism can also be discussed. Literature on C nanotubes indicates that a substrate-enhanced growth rate of ALD Pt occurs when defects are introduced by O plasma treatment [34], [167]. That work showed that Pt atoms initially attach at defect sites, and then linearly grow into nanoparticles with subsequent ALD cycles once the defect sites were filled [34]. This suggests that preferential formation of Pt atoms and clusters can be controlled through the number of successive ALD cycles, where Pt atoms and clusters will form when nucleation sites remain available by ensuring the Pt atomic density does not exceed the lattice defect density. The literature discussed here, and the results shown in Figure 3.11, suggest that in order to ensure Pt atoms and clusters are consistently formed, both defective N-doped

graphene and ALD are required to increase the binding energy from dangling bonds at defect sites and N-dopants, and to control the Pt density with deposition cycles, respectively. Because the N-dopant species and overall N concentration are not consistent between and among graphene nanosheets as shown here, the Pt distribution is varied. Unfortunately, with more ALD cycles this could result in low N concentration graphene nanosheets containing Pt nanoparticles, while other areas with high N concentration will still maintain atoms and clusters. In an effort to homogenize the Pt distribution, and potentially the Pt size (assuming more ALD cycles are performed) and specific activity, the N-dopant distribution and concentration must be made consistent.

3.2.4 Electrochemical Activity of Pt Atoms and Clusters on N-Doped Graphene

Taking an industrial perspective, the production of stable single Pt atom catalysts is important when considering the potential for the overall reduction in the cost to the PEMFC, but the real figure of merit is the catalytic activity of the single atoms. The literature predicts, through DFT calculations, the potential for single atoms to behave as efficient ORR catalysts through the optimization of the electronic structure when bonded to a defective graphene lattice [30]. Conversely, it is generally believed, within the FC community, that the catalytic properties of Pt are limited to particles with a diameter of 2 to 3 nm [168], [169]. This belief potentially originates from the examination of clusters and particles consisting of the “magic number” of Pt atoms to form stable icosahedron structures [168]. When comparing non-symmetrical structures to the icosahedron Pt₁₃ cluster, which have similar electronic properties, it was determined that the less symmetrical Pt₁₂ had a catalytic activity greater than 2-fold when compared to Pt₁₃ [168], and Pt₁₉ had a greater than 3-fold catalytic activity [170]. This suggests that when dealing with Pt clusters, as opposed to nanoparticles, the surface geometry can greatly change the

catalytic activity. Thus, the pure electronic model predicted by Hammer and Norskov [22] may no longer hold. It was determined through DFT that the sharp edges of the non-symmetrical clusters were responsible for the enhanced ORR catalytic activity [170]. This finding was contradicted by Aarons *et al.* through a detailed electron microscopy analysis accompanied by DFT calculations, in which the O binding energy of real catalysts was calculated through atom counting in nanoparticles ranging in size from approximately 2 to 5 nm [27]. It was determined that the reduced atomic coordination induced from the surface roughness of the real particles, in comparison to the commonly examined cube-octahedron particles, increased the O binding energy for small Pt nanoparticles [27]. These calculations showed a steep decrease in the potential for catalytic activity for particles less than 3.5 nm.

It can be suggested that the binding energy of O to the Pt catalysts cannot be directly compared for nanoparticles to real non-symmetrical Pt clusters, due to the drastic change in atomic coordination and shape. Under these circumstances more calculations and experiments are required for the ORR of small clusters and single atoms. More specifically in the case of clusters and single atoms, the electronic structure of the substrate and atom must be considered as one entity, as the electron exchange during the bonding process can result in a general modification in the electronic structure of the catalyst. It has been observed through experimentation and predicted from DFT calculations that there is a reduction in the number of electrons in the d-orbital for single Pt atoms when adsorbed on N-doped graphene [32]. Unfortunately, the work performed through our collaborators, showed that the single atom Pt catalysts were not effective for the ORR. X. Zhang *et al.* determined that single atom Nb catalysts embedded in graphitic sheets had a higher kinetic-limiting current density than commercially available Pt catalysts (in a basic medium), which they attributed to the promotion of the four-electron pathway [171]. Additionally, Zhang *et al.* [172] reported that the combination of single Ru atoms with N-doped graphene produce a higher mass activity of the ORR reaction in an acidic medium similar to the PEMFC. Through DFT calculations they proposed that a Ru=O-N₄ species contributed to the enhanced catalytic activity [172]. Similarly, Fe atoms in C/N macromolecules have

been seen to be active for the ORR, which has been ascribed to a transition in oxidation state at different applied potentials [173], and a $\text{FeN}_4\text{C}_{12}$ moiety [174]. More examples of successful single atom catalysts for the ORR are reviewed by Zhang *et al.* [44], wherein Co atoms were shown to have an ORR activity greater than commercially available Pt nanoparticles on C black [175]. The specific cause for the poor ORR activity observed for the samples presented in this work is not completely understood, but can be hypothesized to be related to the effect of the substrate [41], the particle sizes [30], or potentially the presence of the organic component of the Pt precursor due to incomplete reduction during ALD. Choi *et al.* demonstrated that the ORR on Pt atoms on S-doped C zeolites undergo the two-electron pathway, which is less prevalent on larger clusters and Pt nanoparticles, wherein the four-electron pathway dominated [176]. This suggests the Pt atoms may be kinetically sluggish for the ORR, thus resulting in the poor activity observed for the ALD samples.

In later experiments, it was determined that the production of only single Pt atoms and clusters using the ALD technique as shown in Figure 3.11 was an irregularity. It was more commonly found that the size of the Pt entities could vary from single atoms to nanoparticles when operating at as low as 50 ALD cycles. Qualitative variations in Pt size and density were observed on N-doped graphene and graphene nanosheets within individual and between multiple experimental runs, thus it should be noted that the Pt cluster size during ALD is not as easily controlled as previously discussed. The Pt size can be affected by many contributing factors such as the number of cycles, deposition temperature, O_2 pressure and exposure time, Pt precursor exposure time, and the substrate [177], [178], [34], [179]. Furthermore, these values can be system dependent, thus a detailed analysis is required to understand the preferred deposition conditions for each individual ALD system. With these considerations, the direct reason for the low catalytic performance of the Pt atoms, clusters, and nanoparticles for the ORR is complicated, such that a range of Pt sizes exist in a single electrocatalytic experiment. The system is then further obscured by the fact that the Pt may be adsorbed to different locations on the N-

doped graphene lattice, including various N-dopants, graphene defects, edge locations, and surface hydrocarbon contamination. According to Holme *et al.* the specific binding location of the Pt on the N-doped graphene can vary the *d*-band center of the Pt cluster, thus resulting in individual changes in the activity [41]. Moreover, the electronic structure of the Pt cluster or particle will also vary with Pt size [168], [169], [170]. Through the combined electronic and geometrical effects from the substrate and cluster size, an ideal system may be constructed; however, this will require in-depth DFT analysis and a better controlled production method for both the N-doped graphene and Pt deposition. Examination of controlled Pt deposition will be analyzed in *Chapter Five*.

Unexpectedly, it was experimentally determined that the Pt atoms, clusters, and nanoparticles are electrochemically active for the HER. It can be proposed that the faster kinetics of the HER contribute to the enhanced electrochemical activity for the HER opposed to the ORR, thus the reaction may be less affected by changes in the electronic and geometrical variations of the Pt entities on different N-dopants and defect sites. The following section will outline potential HER catalysts, and the experimentally achieved activity for the ALD Pt on N-doped graphene and graphene nanosheets, in comparison to conventional Pt nanoparticles on C black.

3.2.4.1 HER Electrocatalyst Selection

Utilizing the same *d*-band theory as the ORR reaction, preferred electrocatalysts for the HER reaction can be assigned based on the individual electronic system. Once again Norskov *et al.* performed detailed DFT analysis on the HER reaction to determine the free energy of adsorption of H on bulk catalyst surfaces, and compared these to experimental values in the literature [180]. Similar to the ORR, Pt homocatalysts are the most active for the HER, as the adsorbed H atom does not bind too weakly or strongly based on the *d*-band center [180]. As is the case with the ORR reaction, alternative catalysts are being

investigated to reduce the use of Pt, thus allowing the reduction in cost for the HER. As outlined in numerous review papers, other catalysts include: Pt/non-precious metal alloys (Ni-Mo), transition metal chalcogenides (MoS_2), and non-metallic materials with carbides/nitrides/borides/phosphides [181], [182], [183], [184], [185]. Examination and comparison of various electrocatalysts to Pt for the HER indicates that work is still required to further increase the catalytic activity of the new potential catalysts in order for them to be competitive with Pt. Within the following section, Pt atoms and clusters will be examined as potential electrocatalysts to examine the effect of the size reduction and substrate on the efficiency for the HER.

3.2.4.2 ALD Pt Catalysts on N-Doped Graphene and Graphene Nanosheet Supports for the HER

During these experiments the material preparation, ALD, and electrochemical characterization were completed by Dr. Sun's group as described in ref. [32]. STEM analysis was performed with an FEI Titan 80-300 Cubed TEM using ADF imaging conditions and an XFEG operating at an 80 kV accelerating voltage. The hexapole based probe corrector was utilized to minimize the aberrations in the probe forming lens. Prior to imaging, the samples were baked at 100°C in vacuum to prevent beam-induced contamination.

Qualitative image analysis was completed for the N-doped graphene nanosheets for both 50 and 100 ALD cycles before and after accelerated degradation tests (ADT) (Figure 3.15 (a-d)) for 1,000 electrochemical cycles. Prior to electrochemical cycling the N-doped graphene samples were examined and determined to have a range of Pt sizes from atoms, clusters, and nanoparticles. It should be noted that for both 50 and 100 ALD cycles the Pt size ranged from atoms to nanoparticles with inhomogeneous distributions between N-doped nanosheets from the same production batch. It is possible that this inhomogeneous

distribution of Pt sizes could be a result from the observed inhomogeneity in the N-doping described in *Chapter 3.2.2 Nitrogen-Doping*. The Pt loading⁶ was measured using inductively coupled plasma-atomic emission spectroscopy (ICP-AES), which showed a lower Pt loading (2.1 weight % (wt. %)) on the 50 ALD cycled sample compared to 100 ALD cycles (7.6 wt. %). Based on the loading it is expected that the 100 ALD samples should contain a higher quantity of Pt nanoparticles.

While physical characterization is important, the real figure of merit is the activity of the catalysts. Linear sweep voltammetry was used to determine the catalyst mass (normalized to Pt loading) and specific (normalized to geometric area of electrode) activity at an overpotential of -0.05 V (Figure 3.15 (e)), as compared to conventional Pt nanoparticles (4.2 nm)⁷ on C black supports. Examination of the activities before electrochemical cycling indicate that the ALD samples performed significantly better than the conventional Pt catalysts. While the ALD samples showed inhomogeneity between the N-doped sheets, it can be proposed that the presence of the Pt atoms and clusters resulted in the increased catalytic activity observed for those samples. Moreover, a significant improvement in the activity can be observed in the 50 ALD sample when comparing both the specific and mass activity before and after ADTs (Figure 3.15). Qualitative analysis was performed for the ALD samples after the ADT test (Figure 3.15 (c) and (d)), which did not reveal a drastic increase in particle size with cycling; however, due to the inhomogeneity in the Pt size on the N-doped nanosheets, this statement is not conclusive. Cases in which inhomogeneous sizes exist within a single experimental batch require a more detailed analysis when comparing catalysts before and after cycling, which was outside of the scope of this investigation, but is outlined in *Chapter 3.2.5 ILTEM of Pt on Graphene and N-doped Graphene* of this thesis. While the exact cause for the increased activity of the ALD N-doped samples compared to the Pt/C sample cannot be specific, due

⁶ ICP-AES was measured by Dr. Sun's group.

⁷ Size of nanoparticles were measured by Dr. Sun's group from HRTEM images acquired at the CCEM with an FEI Titan 80-300 Cryo-Twin TEM with an SFEG and a 300 kV source.

to the inhomogeneous nature of the Pt deposition, it can be suggested that the Pt atoms and clusters are responsible for this occurrence. This agrees with Bulushev *et al.* [186], who determined that single Pt atoms on N-doped C nanofibers increased the turnover frequency for the HER in formic acid when compared to samples containing larger nanoparticles. In the future, better control of the ALD process is desired, such that a more precise size range can be achieved, thereby resolving the dispute in literature related to the particle size versus catalytic activity through firm and conclusive evidence.

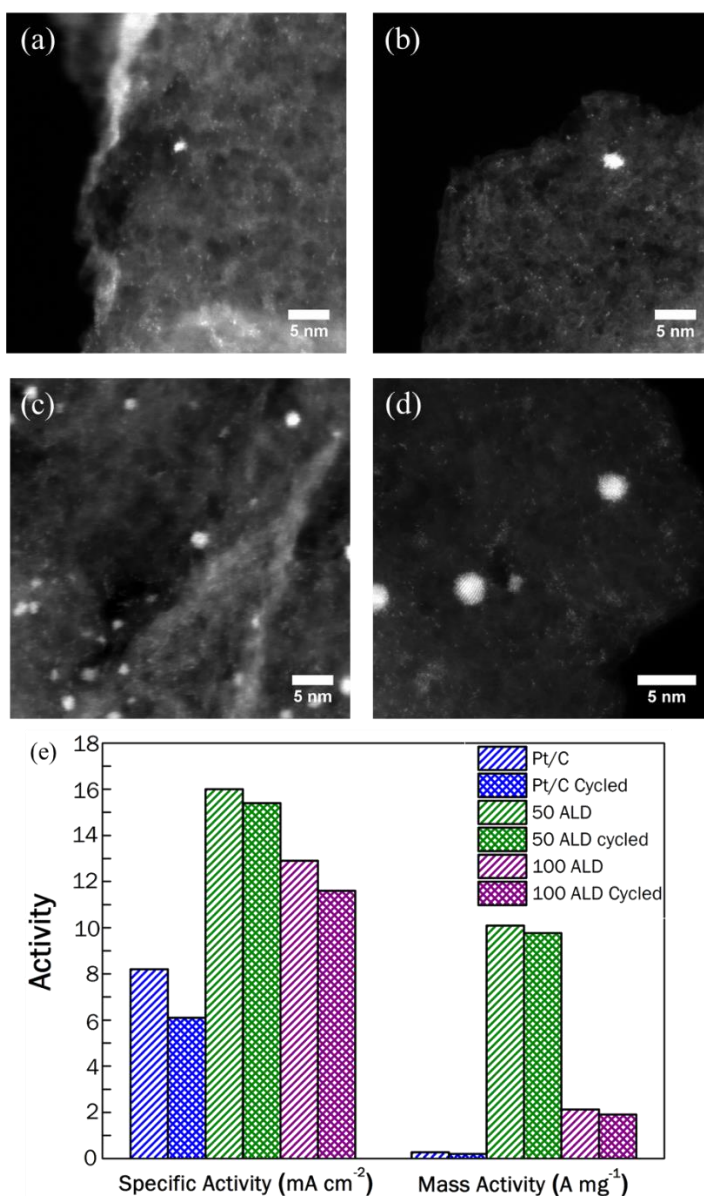


Figure 3.15 ADF images and respective HER activity of N-doped graphene with 50 and 100 ALD cycles. ADF images of (a) 50ALD Pt cycles on N-doped graphene nanosheets, (b) 50 ALD Pt cycles on N-doped graphene nanosheets after ADT, (c) 100 ALD Pt cycles on N-doped graphene nanosheets, and (d) 100 ALD Pt cycles on N-doped graphene nanosheets after ADT [32] (N. Cheng, S.Stambula *et al.* 2016). (e) The electrochemical activity of the species in (a)-(d) and for conventional Pt nanoparticles on C black electrodes, as measured by Dr. Sun's group at an overpotential of -0.05V. Adapted from [32] (N. Cheng, S.Stambula *et al.* 2016).

In an attempt to better understand the system, the effect of the substrate was also examined, in which ALD was used to deposit Pt on graphene nanosheets (Figure 3.16 (a)). Similar to the N-doped graphene, the graphene nanosheets exhibited a range of Pt sizes from atoms to nanoparticles, which could vary locally and between multiple graphene nanosheets. Through comparison of the catalytic activity of the N-doped graphene to the graphene nanosheets, it can be observed that there is a slight reduction in the activity when comparing samples with 50 ALD cycles. The reduction in the Pt activity on the graphene substrate versus the N-doped graphene substrate could originate from the substrate effect, due to the different bonding nature of Pt on different defects or dopants. These results are similar to Bulushev *et al.* [186], wherein they found that the Pt atoms have an improved turnover frequency on N-doped C nanofibers in comparison to non-doped C fibers. Fei *et al.* [187] also established that Co atoms performed more efficiently for the HER when deposited on N-doped graphene, as opposed to graphene; however, the Co atoms on the N-doped graphene did not out-perform the Pt/C sample. Importantly, the catalytic activity of the 50 ALD graphene nanosheet sample is higher than the Pt/C sample. This further supports the fact that the Pt atoms and clusters present on the ALD samples (N-doped and pristine graphene) are responsible for the increased catalytic activity as compared to the Pt nanoparticles found on the C black substrate. This result also illustrates that the electronic structure of the catalyst atoms/clusters still dictates the activity of the HER, thus, as predicted by Norskov *et al.* [180], Pt is the most efficient homocatalyst for the HER. Furthermore, as apparent in Figure 3.16 (c), the activity observed after the ADTs on the graphene sample caused a greater decrease in the specific activity compared to the N-doped graphene support. This may suggest that the stronger Pt adsorption energy [32] on the N-doped substrate is responsible for the decreased reduction in the catalytic activity with cycling, when comparing the N-doped graphene to graphene substrate, thus resulting in more stable Pt atoms and clusters with electrocatalytic cycling. STEM images were also acquired after ADT of the graphene samples, but quantitative analysis was not performed. From the images shown in Figure 3.16 (b) a slight increase in the Pt size is plausible;

however, the inhomogeneous nature of the deposition method must be considered, therefore a fair comparison between the Pt size before and after cycling is not possible when associating individual nanosheets.

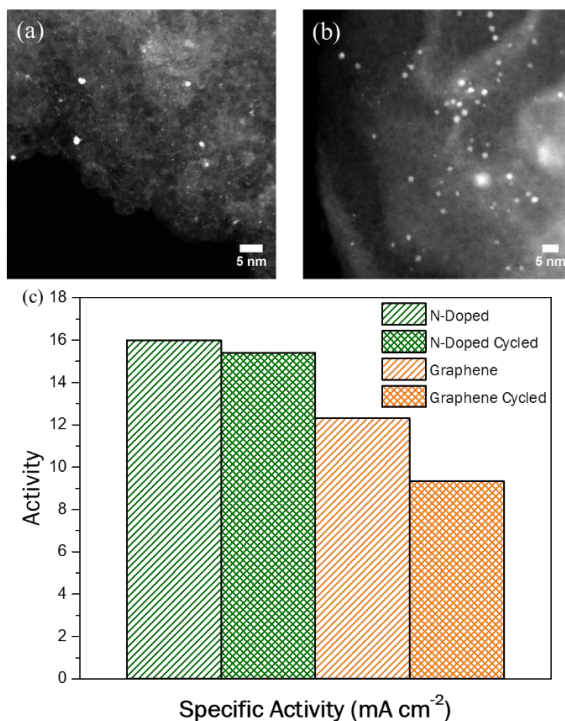


Figure 3.16 Catalytic activity comparison of N-doped graphene to graphene with 50 ALD Pt cycles. ADF images of (a) 50 ALD Pt graphene nanosheets and (b) 50 ALD Pt graphene nanosheets after ADT [32] (N. Cheng, S.Stambula *et al.* 2016). The specific activity of species in (a) and (b) compared to 50 ALD Pt on N-doped graphene nanosheets. Adapted from [32] (N. Cheng, S.Stambula *et al.* 2016).

3.2.5 ILTEM of Pt on Graphene and N-doped Graphene

In order to account for the effects of the inhomogeneities of the Pt catalysts on the graphene support material, identical location STEM (ILSTEM) imaging needs to be used to examine

the stability of the Pt atoms and clusters for the HER. This method is used to study both graphene and N-doped graphene support material for a sample prepared with 50 Pt ALD cycles. The initial experimental design and results will be discussed in the following sections with possible improvements and considerations for future experiments.

3.2.5.1 Experimental Conditions

The experimental set-up (with exclusion to the microscope settings) and sample preparation was completed through consultation with a post-doctoral fellow in the group with IL-STEM experience, Dr. Lidia Chinchilla. Au Quantifoil® holey C TEM grids from Ted Pella Inc with a 300 mesh and 2 μm holes were used to support the graphene substrate. A dilute graphene (and N-doped graphene) powder (light grey in colour) was suspended and ultrasonicated in high performance liquid chromatography (HPLC) grade methanol. One drop was applied to the TEM grid using a glass pipette. The sample was baked in vacuum at 100°C overnight, prior to TEM examination. High resolution HAADF imaging was completed using the Titan 80-300 Cubed with the spherical aberrations in the probe lens minimized. A dose and dose rate of approximately $2.0 \times 10^5 \text{ e}^- \text{nm}^{-2}$ and $7.8 \times 10^9 \text{ e}^- \text{nm}^{-2} \text{s}^{-1}$ were used, respectively. A series of images with increasing magnification were acquired and mapped such that the exact location of the graphene sheets could be found after cycling (Figure 3.17).

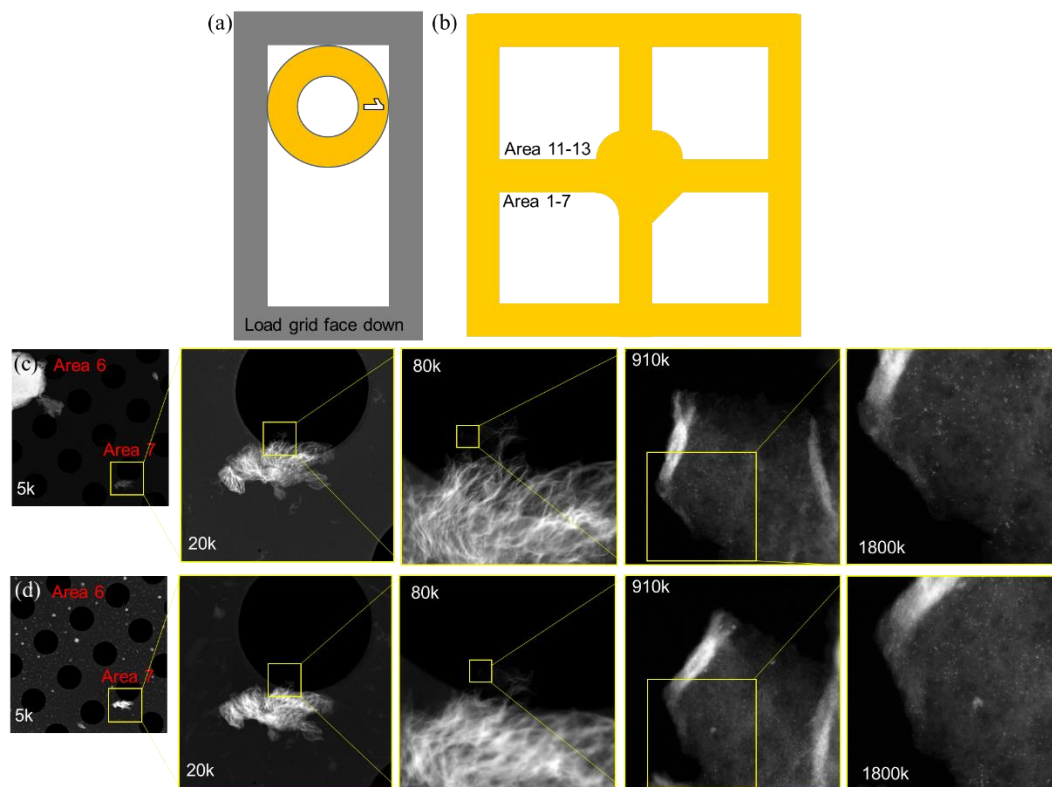


Figure 3.17 IL-TEM microscopy set-up and notes for easy identification of sample positions. (a) The direction that the TEM grid was placed into holder was noted to ensure a mirror image was not obtained if inserted upside down after cycling, and (b) the location of the sample within the TEM mesh was noted with respect to the center of the grid. A series of images ((c) and (d)) with increasing magnifications were acquired while noting the location of each subsequent image. The number of holes in the Quantifoil holey C was used as a reference to find the sample (c) before and (d) after cycling.

The TEM grids were then sent to Western University, where Dr. Niancai Cheng performed the electrochemical cycling for the HER. In order to cycle the TEM grid, it was held in contact with the glassy carbon electrode using gold wire and scotch tape (Figure 3.18 (a) and (b)). The polarization curves for the graphene and N-doped graphene substrates with 50 Pt ALD cycles are compared in Figure 3.18 (c), in which different curves are observed for each substrate. It is possible that the difference in the polarization curves originate from the substrates/catalyst, such that the N-doped substrate results in catalysts that are more efficient for the HER reaction, as determined in *Chapter 3.2.4*

Electrochemical Activity of Pt Atoms and Clusters on N-Doped Graphene. A reference grid without a sample was not examined; however, the difference observed in the polarization curves from the two substrates suggests the individual substrates were involved in the cycling process. Furthermore, the polarization curves before and after 1,000 cycles can be seen for the graphene (Figure 3.18 (d)) and N-doped graphene (Figure 3.18 (e)) substrates. It is evident in the curves that the initial catalyst was more efficient than the cycled samples, wherein the graphene sample saw a larger decrease in activity after 1,000 cycles. These results resemble those observed in *Chapter 3.2.4 Electrochemical Activity of Pt Atoms and Clusters on N-Doped Graphene.* After the electrochemical cycling was completed, the TEM grids were used for imaging. The samples were stored in air at room temperature and were baked at 100°C overnight in vacuum before HAADF imaging.

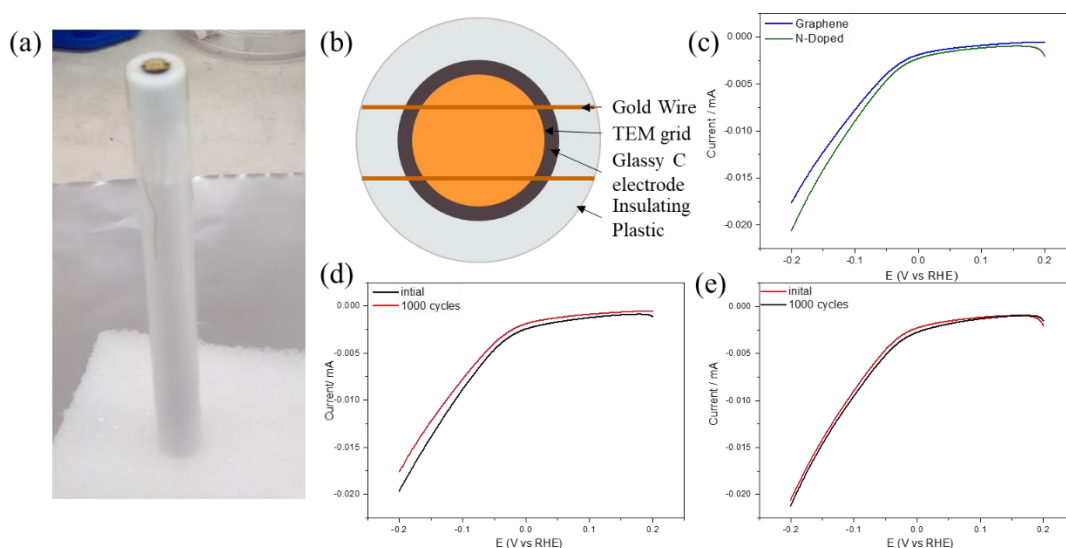


Figure 3.18 Electrochemical ILTEM experimental set-up and results. (a) RDE electrode holding a TEM grid in contact with the glassy carbon electrode using gold wire and scotch tape and (b) a schematic of the electrode contact. Initial polarization curves from (c) TEM grids with graphene and N-doped graphene with 50 Pt ALD cycles, and (d) and (e) of graphene and N-doped with 50 ALD Pt cycles, respectively, before and after electrochemical cycling for the HER.

3.2.5.2 *ILSTEM of Pt on Graphene and N-Doped Graphene*

Two different graphene nanosheets can be observed in Figure 3.19 (a) and (d) before cycling. From the image it is evident that variability exists between the two graphene sheets concerning not only the Pt loading but also the average Pt size. The Pt loading in Figure 3.19 (a) is qualitatively significantly higher, thus resulting in the formation of larger Pt sizes likely due to the increase growth regime during the ALD cycles. The HAADF images demonstrate that the graphene substrate results in the production of single Pt atoms, Pt clusters, and Pt nanoparticles, with an inhomogeneous distribution across the graphene sheets. The inhomogeneous distribution could be an effect of the substrate, or an intrinsic effect of the ALD disposition on powders, based on its location within the ALD chamber. Other than noting the inhomogeneity of the Pt catalyst on the graphene support, Figure 3.19 (a) and (c) can be compared to (d) and (e), respectively, to observe the difference in the individual catalysts before and after cycling. Within Figure 3.19 red arrows were used to point to locations of Pt growth after cycling, and the yellow arrows point to Pt atoms/clusters that underwent dissolution, whether through complete Pt loss or a size decrease. While not all Pt entities were examined, the arrows indicate that both Pt growth and dissolution are occurring simultaneously on the graphene sample. It can be suggested that the growth mechanism appears to be occurring through coalescence of the Pt atoms/particles in close proximity to each other, while the dissolution mechanism may be caused by the loss of the Pt atoms to the electrolyte. In an effort to provide a better image of the comparison of the “before” and “after” conditions, an overlay was produced in Figure 3.19 (c) and (f). It is clear there were significant changes to the substrate material preventing the direct overlap of the images before and after HER cycling. It is unclear if these changes were due to the sample handling, electrochemical changes to the substrate, or potential beam effects through interaction with the catalyst or the edges of the sample. Nevertheless, from these figures it can be inferred that Pt undergoes growth and dissolution with cycling, but most importantly, atoms still appear after cycling. More cycles should be

completed to determine the point in which the particle growth and dissolution are detrimental to the catalyst surface area, thus leading to a poor catalytic performance. This can potentially be used to understand the life-time of the Pt catalyst, and to devise methods in which the life time can be improved.

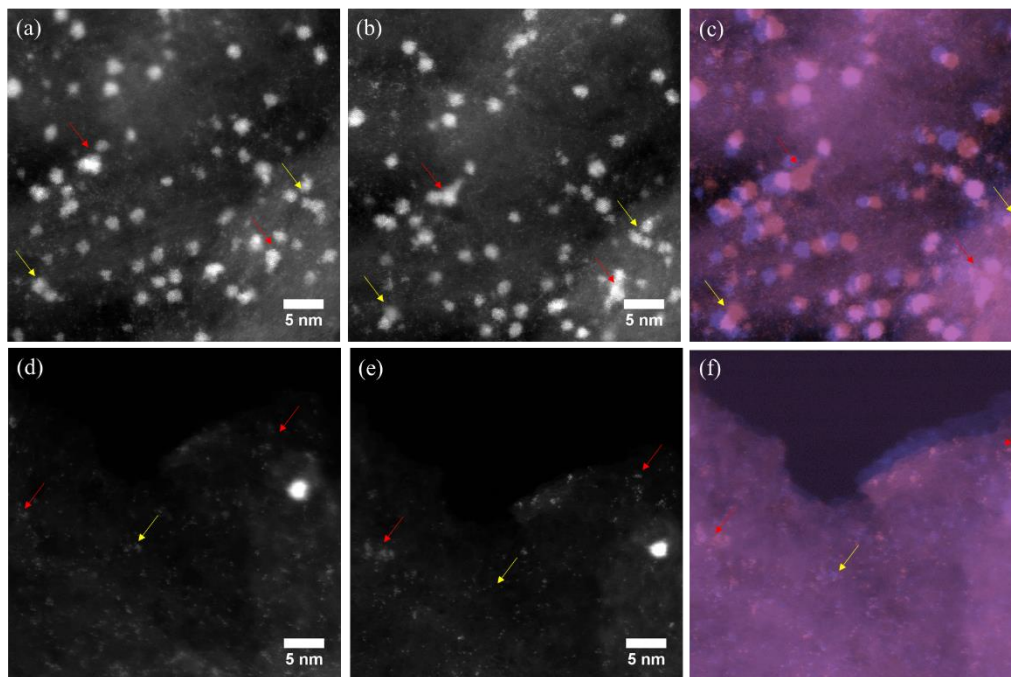


Figure 3.19 ILTEM results of the graphene substrate with 50 Pt ALD cycles (a) and (d) before, and (b) and (e) after cycling, respectively. Overlay images were produced ((c) (brightness and contrast adjusted) and (f) (gamma, brightness, and contrast adjusted) for the two different graphene sheets analyzed, wherein arrows were used to show Pt catalyst growth (red) and dissolution (yellow). The colour coding of the overlay images is such that the blue image was acquired from before cycling ((a) and (c)) and the red image after cycling ((b) and (e)).

The N-doped graphene nanosheets were also examined before (Figure 3.20 (a) and (d)) and after (Figure 3.20 (b) and (e)) 1,000 HER cycles. These images are quite representative of the 10 areas analyzed, such that they are composed primarily of Pt atoms and clusters with some nanoparticles. Similarly, to the graphene substrate, arrows were used to indicate Pt growth (red) and dissolution (yellow). Interestingly, while likely a coincidence, each nanosheet seemed to have Pt undergo either growth or dissolution. Yet,

in Figure 3.20 (b) a nanoparticle formed in a location without a clear presence of a cluster or nanoparticle before cycling. This growth process could have originated from single Pt atoms in an effort to minimize the overall surface energy of the system, or it may indicate re-deposition from dissolved Pt in the electrolyte solution during cycling. This dissolution could have taken place from any number of other N-doped graphene sheets that are simultaneously cycled on the TEM grid, such as that observed in Figure 3.20 (e). Furthermore, modifications to the N-doped graphene substrate can be observed in the overlay images (Figure 3.20 (c) and (f)). Again, the exact reason for the change in the substrate is unknown, but can be potentially attributed to sample handling, electrochemical changes to the substrate, or potential beam effects through interaction with the catalyst or the edges of the sample. Similar to the graphene sample, Pt atoms and clusters are clearly observed to be stable on the N-doped graphene sheets after HER cycling, likely accounting for the increased activity observed after cycling from the N-doped samples in *Chapter 3.2.4 Electrochemical Activity of Pt Atoms and Clusters on N-Doped Graphene*. Direct quantitative analysis and comparison of the ILSTEM images before and after cycling are required to directly determine the change in the number of Pt atoms and clusters on the different substrates after cycling.

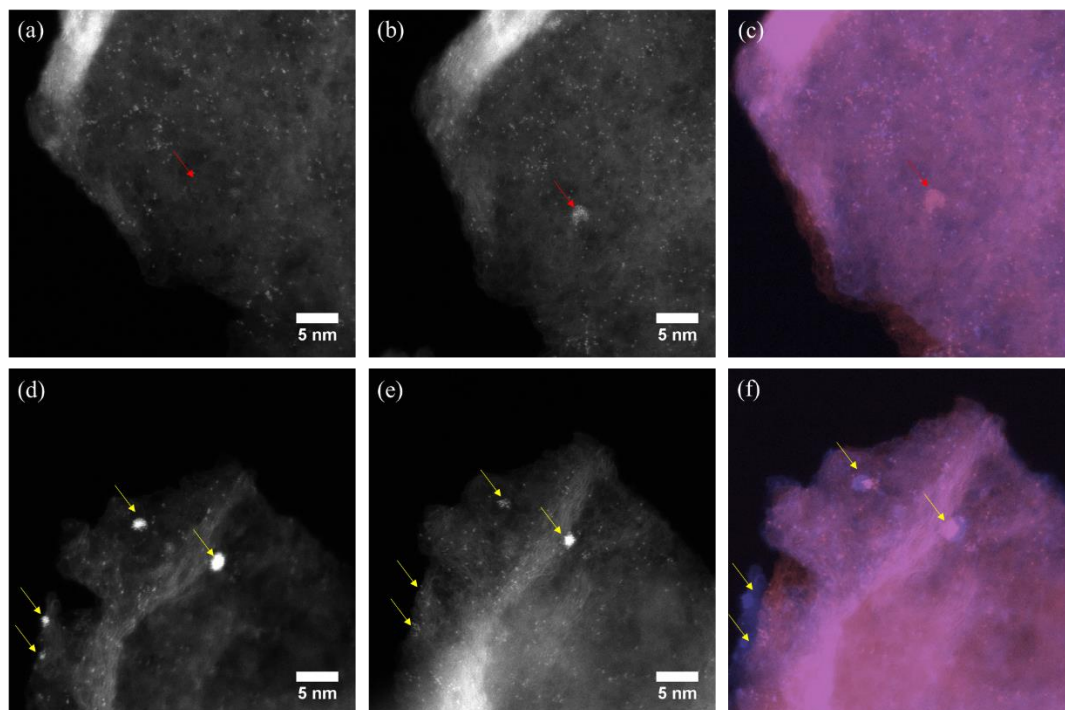


Figure 3.20 ILTEM results of the N-doped graphene substrate with 50 Pt ALD cycles (a) and (d) before, and (b) and (e) after cycling, respectively. Overlay images were produced ((c) (brightness and contrast adjusted) and (f) (gamma, brightness, and contrast adjusted) for the two different graphene sheets analyzed, wherein arrows were used to show Pt catalyst growth (red) and dissolution (yellow). The colour coding of the overlay images is such that the blue image was acquired from before cycling ((a) and (c)) and the red image after cycling ((b) and (e)).

While the results for ILSTEM of Pt in the form of single atoms and clusters seems promising based on Figure 3.19 and Figure 3.20, some potential issues with this measurement technique should be addressed before future measurements and quantitative results are performed. It was previously mentioned that the beam can interact with Pt atoms, causing them to move on the substrate, wherein it has been observed that they tend to edge locations [120]. Furthermore, the beam has also been observed to break apart Pt clusters into Pt atoms in high-beam current conditions [120]. Thus, for techniques such as ILSTEM, in which it is desired to determine the direct effect of electrochemical cycling on the Pt catalysts, the effect of the beam would ideally be removed, or at the very least understood for particular experimental conditions. It is recommended that a quantitative

analysis be completed on the Pt mobility with the desired imaging conditions, such that the mobility is minimized. In order to accomplish reduced Pt motion, it may require utilizing a lower beam energy [188] with a lower dose rate and/or dose. Once the Pt motion is determined through fast sequential STEM image analysis, quantitative data can be collected from the ILSTEM images, such that the exact location of the Pt atoms and sizes can be better trusted, and the effect from the beam and electrochemical cycling can be separated.

Additionally, experiments should be completed to ensure the transferring and storing of the TEM grids is not responsible for changes to the Pt catalysts or the substrate. As suggested by Mayrhofer *et al.* [134], a sample with known Pt sizes should be analyzed via *ex situ* and using ILSTEM. Two electrochemical conditions can be chosen from the *ex situ* experiments, such that one is known to induce change in the Pt size and the other has no effect on the Pt. The same sample batch and electrochemical cycling conditions can then be applied on the ILSTEM grids. The Pt size and change in substrate can be monitored after cycling and compared to the *ex situ* results. If a change in the Pt was observed in the control sample, where the cycling conditions should have little to no effect on the Pt, it would suggest that the grid transfer and cycling is inducing an unwanted modification and should be identified before further detailed experiments are performed. This is an important aspect of the study, as bright spots which were not initially present, can be seen decorating the Quantifoil C after electrochemical cycling (Figure 3.18).

3.3 Summary

In summary, a detailed chemical and structural investigation of N-doped FLG graphene derived from graphite oxide on which Pt was deposited by ALD has been presented. From HRTEM and computed diffractograms, it has been shown that the short-range hexagonal characteristic lattice of graphene was largely preserved after N-doping, but a high density

of defects was present. Detailed high-resolution spectroscopic analysis through ELNES of the C-K edge showed that the nature of the graphene sp^2 hybridization, consistent with strong π^* and σ^* peaks, was maintained after N-doping. The dopant-site locations of the N-species were probed through detailed analysis of the N-K edge, which showed strong features consistent with pyridinic/pyrrolic, amino/cyanic, and graphitic sites. Based on the literature that has been discussed, the features present in the near edge structures promote an increase in the Pt-C binding energy. It has been demonstrated that the dopant concentration varies among and within the graphene sheets and that local probing techniques, rather than bulk average methods, must be used to assess the effectiveness of the doping process. Most importantly, the effects of the reduced Pt particle size achieved through ALD and the prevention of the Pt agglomeration from N-doping and dangling bonds were apparent through HAADF and HRTEM imaging, where only single Pt atoms and atomic clusters were observed. These are sustained primarily at graphene edges with few atoms and clusters stable on terrace sites. This effect was maintained up to 150 ALD cycles without the formation of nanoparticles.

ALD cycled samples were also analyzed for the HER catalytic activity in comparison to conventional Pt/C catalysts. It was determined that both the 50 and 100 ALD cycled samples resulted in higher specific and mass activities than the conventional Pt nanoparticles on C black. Upon STEM examination of the ALD samples it was determined that a range of Pt sizes existed: from atoms and clusters to nanoparticles. Because all samples produced with ALD, independent of the substrate, resulted in higher activities for the HER in comparison to the conventional nanoparticles, it is feasible that the Pt atoms and clusters are responsible for the observed enhanced catalytic activity. Furthermore, upon comparing the N-doped graphene substrate to the graphene substrate, it was determined that the specific activity of the Pt was more stable after ADTs on the N-doped support, which can potentially be attributed to the enhanced Pt binding energy to N-doped graphene. Further examination of this material is required to fully understand the mechanism behind the enhanced catalytic activity, such as the Pt size, and specific dopant/defect effects.

Before these effects can be fully understood, the control of the Pt deposition and the substrate dopants must be enhanced. Nevertheless, the enhanced HER activity of the ALD Pt on the N-doped graphene is a great step forward for the hydrogen FC industry.

Lastly, steps towards ILSTEM imaging were performed on N-doped graphene and graphene substrates with 50 ALD Pt cycles. This method is preferred over *ex situ* cycling such that it allows for the direct observation of the same Pt catalysts before and after cycling, thus removing any ambiguities associated with inhomogeneous distributions of Pt. Both Pt growth and dissolution were observed on the N-doped graphene and graphene substrates, but most importantly the Pt atoms and clusters were stable on individual sheets after electrochemical cycling. While this experiment was promising, in order to rule out effects of the beam and sample handling on the Pt atom location, control experiments are required for the future.

Chapter Four

Production and Characterization of Single Sheet N-Doped Graphene

Multilayer N-doped graphene produced through thermal reduction and exfoliation prevents the physical and spectroscopic identification of individual N-dopants due to the projection effect of the overlapping graphene sheets. Thus, the production of single sheet graphene for the more fundamental examination of N-dopants is highly desirable. This limits production and doping methods to CVD growth and/or post-processing of supported or freely suspended graphene sheets. For the ease of TEM characterization, it is preferred to N-dope suspended graphene TEM grids, thus taking advantage of commercially available mass produced single-sheet graphene grids and the removal of a potential processing step.

Doping graphene through plasma or ion implantation, which are well established methods from the semiconductor industry, has been investigated in literature. By using an N₂ plasma source, it has been reported that approximately 1% [189] to 8.5% N [190] can be doped into the graphene lattice depending on the power of the plasma source and exposure time; resulting in the production of pyridinic, pyrrolic, graphitic and nitrogen oxide dopants. Unfortunately, plasma doping results in the introduction of oxygen as high as approximately 13% [189], which is undesirable as graphene oxide behaves as an insulator [67]. It was suggested that defects created during plasma doping resulted in the

increased O content in the graphene lattice due to oxidation when exposing the sample to air. Lin *et al.* suggests that the N content cannot exceed a few atomic percent for graphitic-type dopants; however, higher concentration levels may exist for other N-dopants [132].

In an effort to decrease the O content in the N-doped graphene, N⁺ ion beams have been examined as a N-doping post-processing procedure. Initially, energies as high as 30 keV at varying fluences (10^{12} to 10^{14} ions·cm⁻²) were utilized to damage the graphene sheets, which were then post-annealed in ammonia to create the N-dopants, at a doping level of approximately 1% [191]. Using high-resolution microscopy and a He source of 30 keV, it was determined that a single sheet of graphene could withstand fluences up to 3×10^{15} ions·cm⁻² before inducing major structural changes [192]. However, it was determined that surface contamination had become an issue at low beam exposures and greatly increased with exposure time [192]. Rather than using such large beam energies, Åhlgren *et al.* determined, through molecular dynamic (MD) studies and DFT calculations, that the efficiency of N-doping reaches a maximum probability of 55% at an energy of 50 eV when using only an N⁺ ion source [193]. Experiments then followed using energies of 2 eV to 150 eV, in which doping occurred solely from the ion beam [194], [195], [196], and from the amalgamation of ion beam exposure and a post-annealing step [197], [198], [199]. Generalizations from these studies concerning the experimental conditions indicate that, as the ion beam energy is increased, the N concentration increases, defect density increases to the point of irreversibility with annealing after 150 eV, and a preferential pyridinic-dopant appears [199]. Furthermore, Bangert *et al.* observed that at an energy of 25 eV the N concentration reaches an average value of 1%; however, this value can have local variability [196]. The ion fluence has also been seen to affect the defect density in the graphene lattice, where a fluence greater than 10^{15} ions·cm⁻² could result in the formation of amorphous C even when operating at low ion beam energies (20 eV) [191], [195]. In addition, the exposure time of the ion beam not only increased the N concentration, but also resulted in the preferred formation of pyridinic-type dopants due to damage induced in the graphene lattice after long exposure times [194], [199]. Lastly, annealing has been

used to recover the graphene lattice from the defects formed during ion bombardment, which resulted in the increased formation of graphitic-type dopants and a decrease in N₂ captured in the multilayered graphene sheets [197], [199].

This chapter will outline investigations regarding in-house doping methods using modified electron microscopy sample preparation instruments to produce N plasma sources and low energy N⁺ ion beams. Additionally, a quantification method of the N content was optimized for TEM grids using Auger spectroscopy to detect N with a concentration up to approximately 1%.

4.1 Nitrogen Quantification on TEM Grids Using Auger Spectroscopy

Auger spectroscopy⁸ is a surface analysis technique, in which electrons can be detected from an escape depth of 0.3 to 3 nm from the surface of the sample [200]. Under typical Auger operating conditions, graphene is examined only after it has been transferred to or grown on a solid substrate [201]. Therefore, to examine a free-standing graphene film on a TEM grid, care must be taken to reduce the instrumental source of electrons from below the sample. Graphene Supermarket© produces graphene TEM grids consisting of one to six layers or 0.3 to 2 nm in thickness, respectively, thus Auger electrons can originate from beyond the graphene source. When examining the free-standing graphene films, electron sources may emanate from within the spectrometer chamber, resulting in an increased background and unexpected elemental sources during Auger detection. The following section will discuss methods devised to reduce the detection of electrons originating from

⁸ All Auger spectroscopy and quantification was performed by the CCEM operator, Travis Casagrande.

below the sample, and perform Auger quantification from free-standing graphene TEM grids.

4.1.1 Experimental Conditions and Design

A new holder for the Auger quantification of a TEM grid was designed after discussing the potential issues with an expert in the field⁹. It was suggested to produce a holder in which the TEM grid could be suspended over a small hole with a large aspect ratio to prevent the detection of the material below the TEM grid, while simultaneously reducing any background electrons from interacting with the sample. Other than the geometry of the holder, the material selection was also of importance to reduce the background signal generated from SE and backscattered electrons. Therefore, a material with a low backscatter electron yield and non-overlapping Auger peaks with the N-doped graphene was of primary interest. Considering these conditions, the holder was composed of Al and machined to the specifications shown in Figure 4.1 (a).¹⁰ During the design of the schematic, it was determined that the TEM grid would be held in the Technoorg Linda™ Model IV5 Gentle Mill holder, as it securely holds TEM grids while suspending the samples in air. The measurements of the schematic in Figure 4.1 (a) were set based on measurements from the Gentle Mill holder, resulting in the final holder displayed in Figure 4.1 (b). The Gentle Mill holder is composed of Ti, which unfortunately slightly overlaps the N-KLL edge; however, the background signal will be minimized through our experimental design and should have little effect on the final N quantification. Thus, for the proof of concept of N-doping the graphene TEM grids, the Gentle Mill holder will be used to reduce the cost of creating a specialty holder for the TEM grid. In the future, for

⁹ I would like to thank Dr. Nestor J. Zaluzec for discussing this point with me during the 2014 CCEM summer school.

¹⁰ Special thank you to Andy Duft for helping in the schematic measurements and performing the machining of the holder.

best quantification results, a holder with a design similar to the Gentle Mill holder can be machined from Al to reduce the Auger peak overlap. If elemental quantification is to be performed on other materials suspended on TEM grids, the material selection should be re-examined.

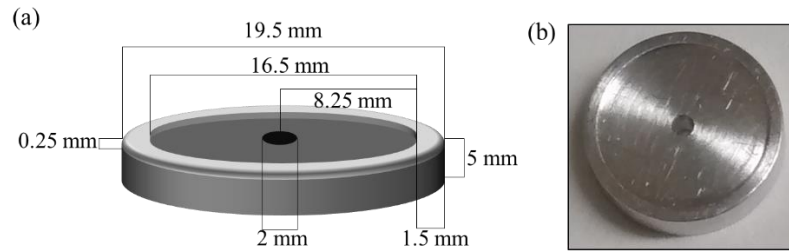


Figure 4.1 TEM holder adaptation for Auger quantitation (a) schematic and (b) machined product.

The JEOL JAMP-9500F field emission Auger in the CCEM was used for the quantification of N content. Typically, the Auger microscope is operated at an energy of 10 kV, a current of 20 nA, and a tilt of 30° with respect to the electron gun (Figure 4.2 (a)). In order to determine the best experimental design for the TEM grid using the new holder (TEMH) the effect of the voltage, tilt angle, and use/placement of an aperture were examined. This was accomplished with the utilization of a holey C TEM grid. During the examination, a spot analysis was acquired from the film of the holey C TEM grid and a neighbouring hole, which were each suspended over the hole in the TEMH, producing the representative spectra in Figure 4.2 (b). Full spectra were initially acquired to observe the elements detected by the spectrometer when using the TEMH and a TEM grid. It is apparent that an Al peak does not exist, suggesting that Auger electrons were not detected from the TEMH. C, O, and Si peaks were found on the holey C film and over the hole, which originate from the TEM grid.

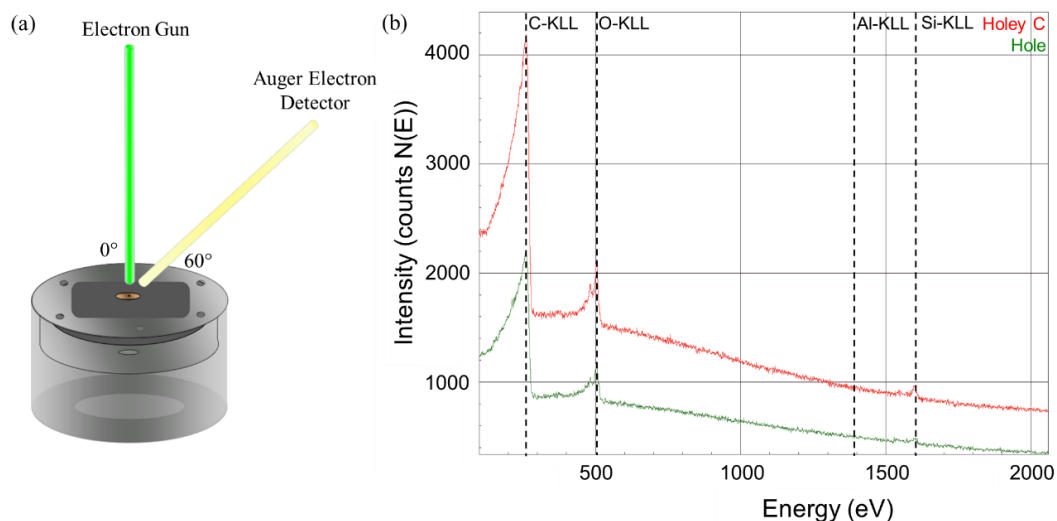


Figure 4.2 Auger quantification experimental set-up with TEMH. (a) Schematic of the Auger arrangement. (b) Spectra acquired from the TEMH when looking at a holey C TEM grid with spectra collected from the C film and a hole, respectively. The spectra were acquired with an energy of 10 kV, tilt angle of 0°, and a beam current of 40 nA.

Ideally, Auger electrons should not be detected from the hole in the C film. However, this background signal can occur from the excitation of Auger electrons from the nearby C film, due to the interaction with the primary electron beam or from backscattered electrons and/or SEs that are excited from the holder and/or the sample chamber. Three experimental designs were used to minimize the signal acquired over the hole in the C film: utilizing only the TEMH (Figure 4.3 (a)), inserting a Pt aperture on top of the TEM grid when using the TEMH (Figure 4.3 (b)), and placing the aperture below the TEM grid when using the TEMH (Figure 4.3 (c)). The effect of varying the aperture size from 300 μm to 800 μm was investigated to reduce the background Auger signal. For each analysis, a spectrum was acquired on the C film and compared to the spectrum obtained from an adjacent hole (Figure 4.3 (d)). The background signal was quantified by comparing the relative difference in the C-KLL signals attained from the C film and hole, respectively. During examination of the tilt angle for a single voltage at 10 kV with the

different geometrical arrangements outlined in Figure 4.3 (a), (b), and (c), the difference between the highest C-KLL peak intensities (I_{peak} in Figure 4.3 (e)) was analyzed:

$$\text{Percent Difference (PD}_{10\text{kV}}) = \frac{(I_{\text{peak-film}} - I_{\text{peak-hole}})}{I_{\text{peak-film}}} \times 100\% \quad (4.1).$$

In addition, a more generic version of equation (4.1) was used when comparing experiments completed at different voltages, such that the relative C-KLL peak heights were examined by comparing the difference between the highest peak intensity (I_{peak}) and the lowest peak intensity ($I_{\text{background}}$) (Figure 4.3 (e)),

$$\text{Percent Difference (PD)} = \frac{((I_{\text{peak-film}} - I_{\text{background-film}}) - (I_{\text{peak-hole}} - I_{\text{background-hole}}))}{(I_{\text{peak-film}} - I_{\text{background-film}})} \times 100\% \quad (4.2).$$

A PD of 100% would indicate that no signal was detected over the hole, which would result in the ideal experimental scheme without a background signal. The following section will use equation (4.1) and (4.2) to examine the effect of the proposed experimental design, the primary electron beam energy, and tilt angle (Figure 4.2 (a)) on the removal of the background Auger electrons when examining a TEM grid.

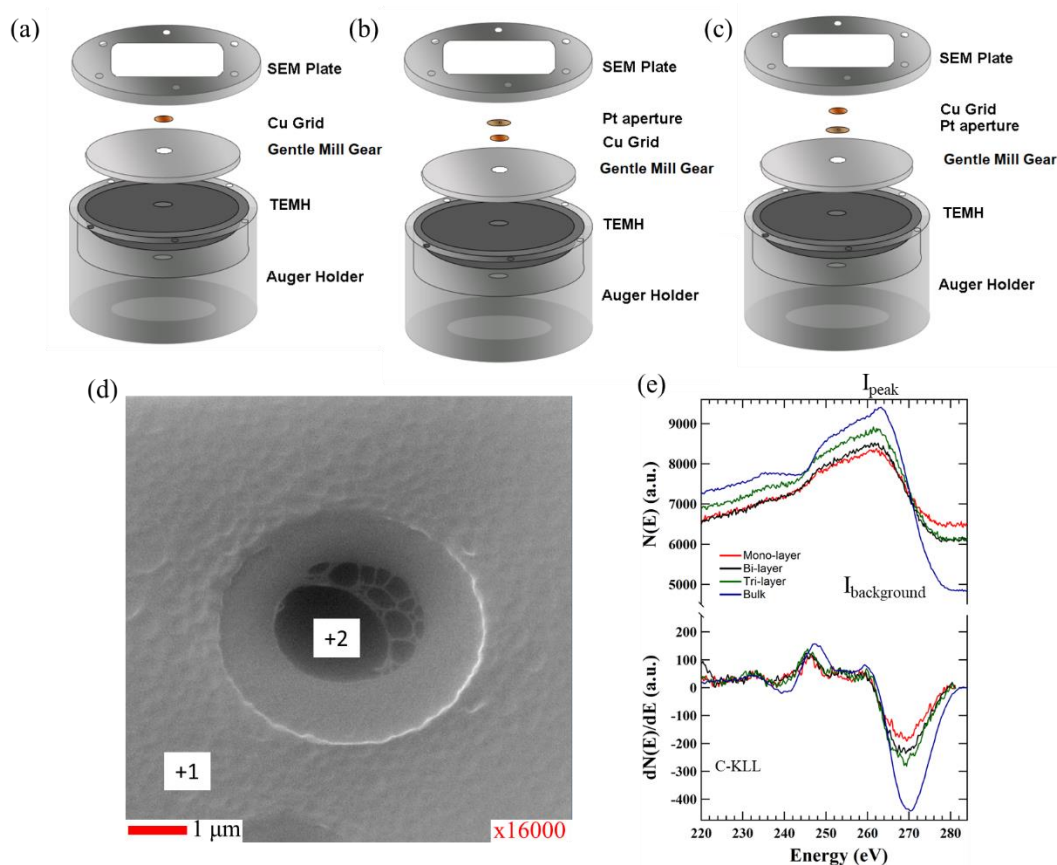


Figure 4.3 Auger quantification TEMH configurations with (a) no aperture, (b) Pt aperture above the TEM grid, and (c) the Pt aperture below the TEM grid. Each measurement was completed with a spectrum acquired from (d) the C film (+1) and the hole (+2) producing a (e) C-KLL Auger peak¹¹.

4.1.2 Results and Discussion

The C-KLL peak was examined for the holey C TEM grids using the TEMH (Figure 4.1) and equation (4.1). First, the effect of the TEMH tilt angle with respect to the electron gun was examined when operating under typical Auger conditions with an accelerating voltage

¹¹ Figure 4.3 (e) produced by Kevin A. Villegas (summer student) for varying thicknesses of graphene on SiO₂. The thicknesses were determined using light microscopy.

of 10 kV. Initially the TEMH with the tilt angle varying from 0° to 50° at intervals of 5° (Figure 4.4) was examined. At each tilt angle the PD10kV from equation (4.1) was used to determine the decrease in the background signal. Without the use of an aperture (Figure 4.4 purple), it was observed that as the tilt angle increased the PD10kV decreased, thus resulting in a higher background with an increasing tilt angle. It is possible that as the holder was tilted the primary electron beam was potentially striking the side of the high aspect ratio hole in the TEMH, resulting in the production of SEs and/or backscattered electrons that were possibly resulting in the excitation of Auger electrons of the C film around the hole. It was hypothesized that the background signal could be reduced by decreasing the hole size in the TEMH, as less primary electrons would enter the high aspect ratio hole in the TEMH. Rather than completely re-machining the holder, as a quick test, an Al film with a small hole (size unknown) was placed on top of the TEM grid and an increase in the PD10kV (Figure 4.4 green) was observed with respect to the purple curve (no aperture). Having success with this make-shift Al aperture, a Pt aperture of $300\ \mu\text{m}$ was placed above (Figure 4.4 orange) and below (Figure 4.4 blue) the TEM grid within the Gentle Mill holder as outlined in Figure 4.3 (b) and Figure 4.3 (c), respectively. Overall, an increase in the PD10kV was observed for both positions of the aperture, with the greatest value being obtained when the aperture was placed below the TEM grid. Simulations were not performed to determine the specific reasoning behind the difference in the PD10kV value with the position of the aperture. It can be speculated that when the aperture is above the TEM grid the background electrons generated from the TEMH have an opportunity to interact with the C film and through scattering mechanisms could result in the production of Auger electrons in the area free from the aperture.

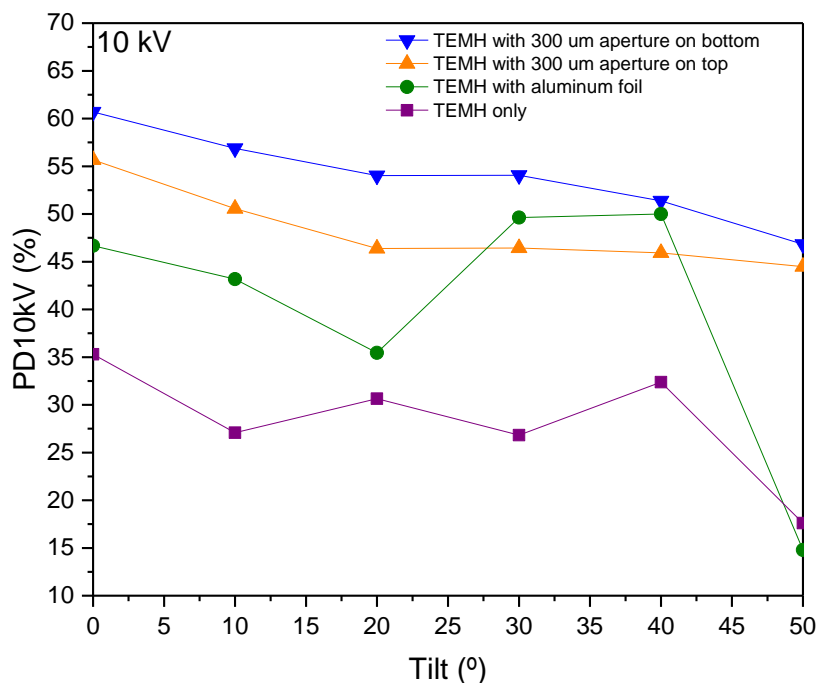


Figure 4.4 Effect of tilt angle and aperture arrangement when operating at 10 kV on a holey C TEM grid.¹²

Following the positive results of positioning the aperture below the TEM grid (Figure 4.3 (c)), the effect of the acceleration voltage, tilt angle, and aperture size was analyzed in Figure 4.5. When using the 300 μm aperture the maximum PD achievable was approximately 84% at 20 kV. Upon increasing the aperture size to 800 μm , an increase in the PD was achieved when directly comparing equivalent acceleration voltages of 10 kV and 20 kV, respectively. More importantly, when operating at 20 kV with a Pt aperture of 800 μm below the TEM grid, a PD ranging from approximately 98% to 99% was achieved with a tilt angle of 50° to 0°, respectively. It can be hypothesized that the PD increased when increasing the aperture size because the Pt may have been acting as a source of background electrons; therefore, an increase in the aperture size could result in the reduction of the background signal when working in the center of the aperture. It should be noted that an acceleration voltage of 10 kV would be ideal as the quantification

¹² Error bars are missing, as only one point spectra was acquired for each data point.

standards are collected under these conditions; however, the poor PD at 10 kV prevents its use, thus the 20 kV acceleration voltage should be utilized. This suggests that the quantification results may not be exact, but it can be assumed that the effect of the different voltage on the N quantification will equally affect each measurement, thus the values can be relatively compared.

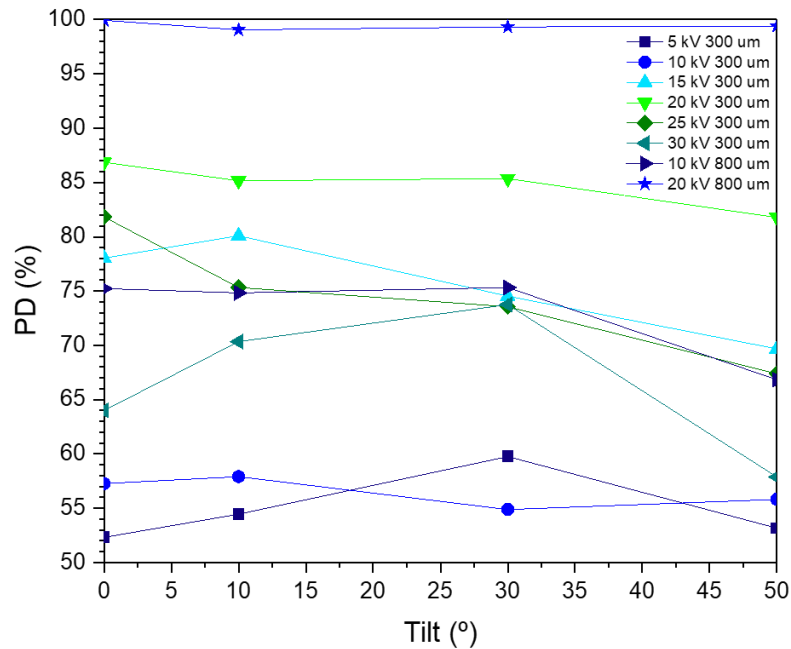


Figure 4.5 Effect of accelerating voltage, tilt angle, and aperture size on the PD from a holey C TEM grid.¹²

To reduce the source of electrons originating from below the sample, based on Figure 4.5, it is suggested to complete the quantification of the N-doped graphene TEM grids at an acceleration voltage of 20 kV with an aperture of 800 μm placed below the TEM grid at a tilt angle of 0° . However, when operating at 0° with the TEMH it was determined that the contrast in the SE image was reversed (Figure 4.6 (a)) in comparison to the conventional operating conditions (Figure 4.3 (d)). It is possible that at this tilt angle electrons (secondary and backscattered) are being excited through the hole of the TEMH, resulting in the increased brightness at 0° . Due to the unusual contrast encountered at this

tilt angle and the relatively stable PD when operating at 20 kV with an 800 μm aperture below the TEM grid, a tilt angle of 30° (standard operating angle) will be utilized for the quantification in the following sections (Figure 4.6 (b)). When comparing the Auger spectra on the Pt aperture and hole (Figure 4.6 (e)), it is clear that the signal greatly decreased within the hole, resulting in a PD of 98%. An Al-KLL peak was found in the hole, originating from the Al TEMH. Both C-KLL and O-KLL are found on the aperture and hole from surface contamination. The examination of the low intensity spectra originating from the hole illustrates that the TEMH was successful in removing the electron source from below the sample, thus resulting in the collection of Auger electrons primarily from the suspended sample on the TEM grid.

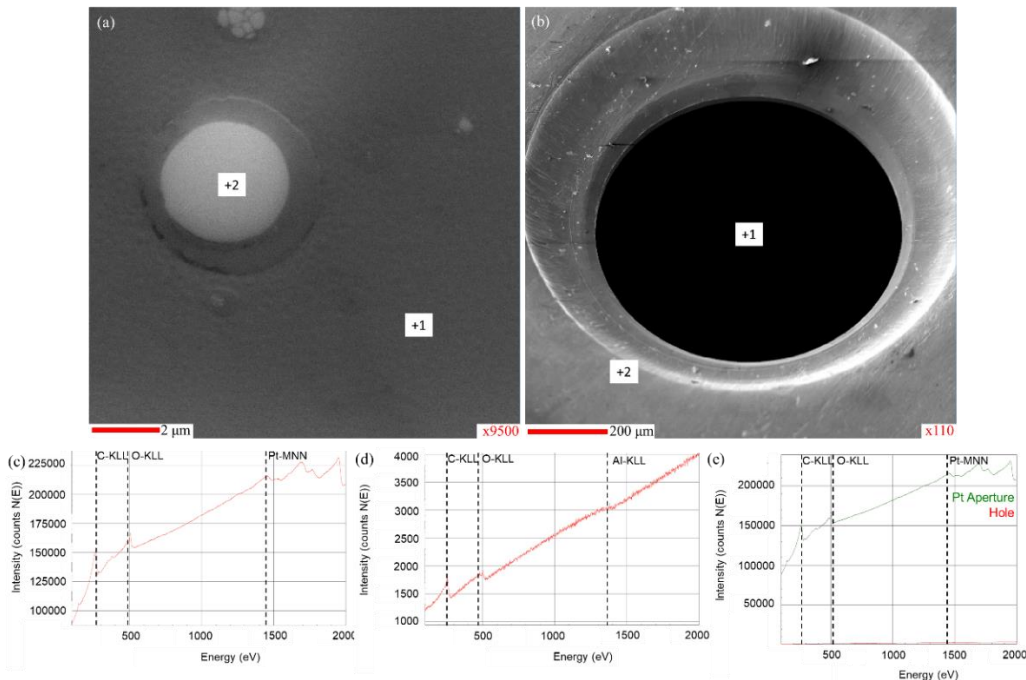


Figure 4.6 SEM image of a hole in the C film with various tilt angles and the comparison of the Auger spectra acquired over a hole and over an aperture. (a) SEM image acquired with the TEMH at 20 kV and a tilt angle of 0° . (b) SEM image of Auger quantification set-up without a TEM grid. Full scan Auger spectra were acquired over (c) the Pt aperture (+2) and (d) the hole (+1), which are then compared in (e) when acquired with a 20 kV acceleration voltage, 800 μm aperture, and 30° tilt.

It should be noted that it was qualitatively determined through multiple examinations during Auger quantification of N-doped graphene, that smaller holes resulted in lower PDs between the sample and the hole. This suggests that there is a minimum diameter at which the Auger spectrometer collects signal, but this was not investigated further and may be a source of error in the Auger quantification. For conciseness and accuracy, in the future, the effect of the size of the hole diameter on the PD should be measured and compared to prevent signal overlap during individual spot quantification. Furthermore, the effect of the diameter size should be re-examined with regards to Figure 4.5 to ensure the PDs were not artificially affected by the diameter of the hole. For the sake of the thesis, the fact that the 20 kV source results in the highest PD suggests that it is sufficient for the Auger quantification. To ensure the hole diameter does not greatly affect the quantification results, the measurements presented in the following section were only acquired from quantification in which the PD is greater than 80%. Moreover, during future analysis, multiple data points should be collected with respect to each experimental condition in Figure 4.5 to determine the accuracy of the measurements.

4.2 Production of N-Doped Graphene TEM Grids Using In-House Techniques

Three in-house electron microscopy instruments were examined as N sources to produce single sheet N-doped graphene: Solarus plasma cleanerTM, Technoorg Linda Model IV5 Gentle MillTM, and a Fischione NanoMill®. Graphene Supermarket© TEM grids [202] were purchased as the graphene source. Varying experimental conditions were examined and the concentration of N was quantified first using EELS, followed by a more accurate measurement technique for low N concentration, as outlined in Section 4.1, using Auger spectroscopy. The NanoMill® results were the most promising for the production of the

single-sheet N-doped graphene, which are discussed in this section. For more details concerning the plasma cleaner, and Gentle Mill™, *Appendix 1: N-doping Graphene TEM Grids using a Plasma Cleaner and Gentle Mill™* should be consulted.

4.2.1 Characterization of N-Doped Graphene Using High Resolution STEM

The aberration correctors allow the acquisition of high resolution images in both TEM and STEM. STEM imaging was performed using ADF (detector semi-angles of 31.4 mrad to 191.9 mrad, as measured by FEI) conditions with an FEI Titan 80-300 Cubed TEM equipped with hexapole-based aberration corrector (Corrected Electron Optical Systems GmbH) for the probe lens, and a high brightness field emission gun (XFEG). The aberration corrector was tuned to minimize spherical aberration in the probe lens. An imaging current of 40 to 100 pA was used (maximum dose of $1.7 \times 10^7 \text{ e}^- \text{nm}^{-2}$ and dose rate of $1.9 \times 10^{11} \text{ e}^- \text{nm}^{-2} \text{s}^{-1}$) to increase the signal to noise ratio. Based on the discussion in *Chapter 2.2 Using TEM to Study Graphene and Heavy Atoms* defects were observed in the graphene lattice at this high of a dose, thus the lower dose discussed in that chapter was utilized for the subsequent images. It has been suggested in literature to increase the signal to noise ratio by over-sampling the graphene lattice through the collection of more pixels, while working at a lower dose [122]. This method to increase the signal is suggested for future experiments to limit the beam damage imposed on the sample. Figure 4.7 illustrates images of Graphene Supermarket© TEM grids [202] before N-doping, acquired with an 80 kV ((a) low and (b) high magnification) and (c) 40 kV electron source. As expected, the images acquired using the higher acceleration voltage resulted in a better spatial resolution; however, the correctors could be optimized such that graphene imaging was possible at an acceleration voltage as low as 40 kV. Due to time constraints and ease of operation, 80 kV was used to

examine the structure of the graphene lattice after the various in-house doping techniques and conditions were trialed.

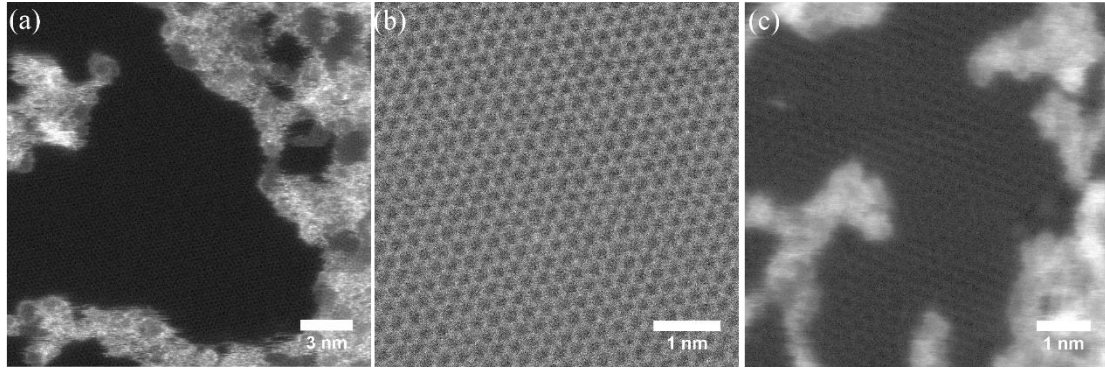


Figure 4.7 HR-STEM images of Graphene Supermarket© TEM grids using an ((a) (gamma adjusted) and (b)) 80 kV and (c) 40 kV electron source (gamma adjusted).

4.2.2 NanoMill®: Nitrogen Ion Source

The Fischione Instruments Inc. Model 1040 NanoMill® was considered as the most favourable potential source, due to the fact that it can produce a low energy ion beam (minimum 50 eV) that also operates with a low current (pA adjustments available), providing more control of the source energy and overall fluence exposed to the sample. During these experiments the ion energy, overall fluence, and impact angle were examined.

4.2.2.1 Experimental Conditions

The Fischione Instruments Inc. Model 1040 NanoMill® (Figure 4.8 (a)) equipped with an electron impact source using an N₂ gas supply was operated at 50 and 100 eV. A magnification of 100x was used to increase the exposure area of the TEM grid in the fast

scan imaging mode. A base vacuum of 2×10^{-6} torr was achieved with a specimen operating under vacuum upon exposure to the N_2 gas of 4×10^{-4} torr. All experiments were performed at room temperature and a maximum tilt angle of 90° was examined. To complete the tilt experiments the supplied sample holder (Figure 4.8 (b)) was used up to 30° , and a new holder was made in-house¹³ (Figure 4.8 (c)) to rotate 360° , allowing the maximum 90° angle to be achieved. The fluence (ions \cdot cm $^{-2}$) was approximated using

$$fluence = \frac{(Current \times Time \times 6.241 \times 10^{18} / C)}{Area} \quad (4.3)$$

in which the current is measured in amps, time in seconds, and area in cm 2 . The beam size is unknown at a beam energy as low as 50 eV and a N_2 gas source, therefore it was assumed that the area in equation (4.3) is the area scanned by the beam at 100x magnification (1.7 mm by 1.7 mm resulting in an area of 0.0289 cm 2). The beam size is likely smaller than the scanned area, thus the fluences reported may be underestimated. Additionally, the exact nature of the ionic charge within the plasma is unknown (assumed to be 1^+), which could alter equation (4.3) by a division of the charge; however, this would then increase the current by the same amount, thus cancelling the effect.

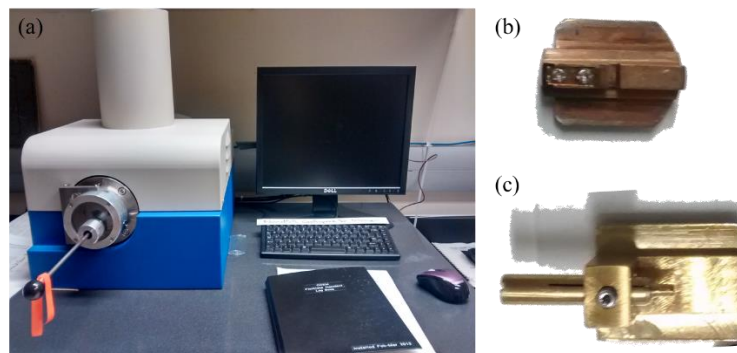


Figure 4.8 NanoMill® experimental set-up. (a) Fischione Instruments Inc. Model 1040 NanoMill® (b) conventional holder and (c) in-house 360° holder.

¹³ 360° holder machined by Andy Duft.

The ion beam current was measured prior to sample loading and was adjusted using the NanoMill® controls. A specific time and current was selected to provide the desired fluence to the sample in a single experiment. The current could vary within approximately 10 pA during a single exposure, therefore the approximate mean current was used during the calculation of equation (4.3) and the reported fluences are not exact. It is suggested that for future experiments the current be monitored for an entire TEM grid exposure to better characterize the current fluctuations and determine if the current is consistent throughout the entire ion exposure. Examining the current will ensure a more accurate calculation of the ion fluence. When operating at 50 eV the image cannot be focused, therefore care must be taken to ensure the sample is centered in the ion beam without exposing the sample to a high energy beam source. A dummy sample was first placed in the NanoMill® and focused at a high ion energy (200 eV) and centered in the screen. The energy was gradually decreased until 50 eV, when the sample was no longer visible. The dummy sample was then removed and the pristine Graphene Supermarket© TEM grid was placed in approximately the same location. The grid was then inserted in the NanoMill® and exposed to the N⁺ ion source for the indicated time based on the desired fluence. The samples were rotated from 10° to 90° with respect to the ion beam (Figure 4.8 (c)).

Image analysis was performed using monochromated negative spherical aberration imaging with HRTEM at 80 kV on the Titan 80-300 Cubed. EELS experiments were carried out with an FEI 80-300 Cryo-Twin TEM equipped with a monochromator and an XFEI. The EELS acquisition was performed in STEM mode with the spectrum imaging technique implemented by the GATAN Digital Micrograph software, using the monochromator to achieve an energy resolution of 0.08 eV as measured from the full width at half maximum of the zero-loss peak. Prior to performing EELS experiments the sample was baked at 150°C for 17 hours to prevent beam contamination that had previously been problematic when the sample was not baked or baked at 100°C. A dispersion of 0.1 eV/pixel was used for EELS acquisition of the C-K and the N-K edges. The spectra in the spectrum image were aligned and calibrated in energy to the C-K edge pi* peak (285 eV)

using built-in functions in GATAN Digital Micrograph. The spectra presented in this section were summed based on the intensity in the DF image which is related to the thickness of the graphene sheets. Python code written by Isobel Bicket (PhD student in the group) was used to sum spectra from a polygonal area [203].

Auger quantification was used to determine the average N content as outlined in *Chapter 4.1 Nitrogen Quantification on TEM Grids Using Auger Spectroscopy*. The values reported for quantification have been normalized for C and N content; however, beam contamination could not be avoided so it should be noted that the N content may be slightly underestimated. For quantification purposes, six to nine locations were examined and averaged for each experiment. The signal and background on the holes were measured for reference to ensure a clean source signal was obtained, and all signals included in this examination contained a PD greater than 80%.

4.2.2.2 Results and Discussion

Multiple experiments were conducted to examine the effects of ion energy, fluence, and tilt angle on the average N % in graphene. Figure 4.9 (a) shows the results obtained from the various doping conditions, where the average N % (normalized to C and N) is plotted with the error bars obtained by the two-tailed one-sample Student's t-test with a probability of 0.05. The large error bars indicate the wide data spread acquired from the Auger quantification. It is believed that this spread may originate from the sample not being fully centered in the ion beam during doping due to the lack of spatial resolution when operating at 50 eV, the sample drifting during the doping experiment, and the instability in the current. For conciseness, the exposure time and current are supplied in the legend for each data point. A colour coding was utilized to more easily examine the plot, such that all orange points were acquired at a beam energy of 50 eV and a tilt angle of 30°, and the pink data points were acquired at a beam energy of 50 eV and a fluence of approximately 2 x

10^{15} ions·cm⁻². Direct observation of Figure 4.9 (a) (orange points) indicates that increasing the fluence when operating at a fixed energy and tilt angle results in an increased N concentration; however, the maximum concentration of approximately $0.86 \pm 0.20\%$ (normalized to C and N) occurs at 50 eV and a tilt angle of 90°, which agrees well with literature [189], [191], [196]. It appears that the concentration plateaus at a fluence between approximately 1.2×10^{15} ions·cm⁻² and 1.5×10^{15} ions·cm⁻². The exact reason for the plateau is unknown, but it can be hypothesized that it may be related to the contamination production observed by Pan *et al.* [192] at 3.0×10^{15} ions·cm⁻² when operating at 30 keV. When examining the series of pink data points, it is evident that as the tilt angle increases the N concentration also tends to increase. This phenomenon has been predicted in literature for O ions by Bai *et al.*, in which a maximum probability of O substitution at 50 eV occurs at 90° [204]. It should be noted that at a tilt angle greater than 30°, the precision in the angle is quite poor due to the 360° rotation of the new holder. While a rough approximation of the angle was completed with a 10° scale marked on the holder with permanent marker, the exact angle is unknown, which could account for the overlap of the data points ranging from 40-50° and 70-90°, respectively. However, this trend can also be observed at a fluence of 5×10^{14} ions·cm⁻², wherein the mechanical adjuster within the NanoMill® was used to set the angle. In this case, as the tilt angle increased, the N concentration also increased, thereby corroborating the trend observed at the higher dose. There is a violation of this trend when comparing the low dose (yellow star) and high dose (pink star) analysis for a 90° tilt, wherein the low dose doping resulted in a lower concentration than the 30° tilt samples at a similar dose. This may be an artifact of the angle adjustment or the data points may be influenced by the instability of the current, centering of the sample, or sample drift during doping. Furthermore, as the energy is increased when maintaining the dose, an increase in the average N % is observed to reach approximately $1.6 \pm 0.5\%$ (normalized to C and N) at 100 eV. This effect cannot be explained based on the DFT calculations performed in literature that predict a higher probability of N substitution as opposed to vacancy formation at 50 eV versus 100 eV [193], [204]. Because

50 eV is the minimum operating condition of the NanoMill®, it is possible that the beam energy is more stable at 100 eV, which may account for the higher N content.

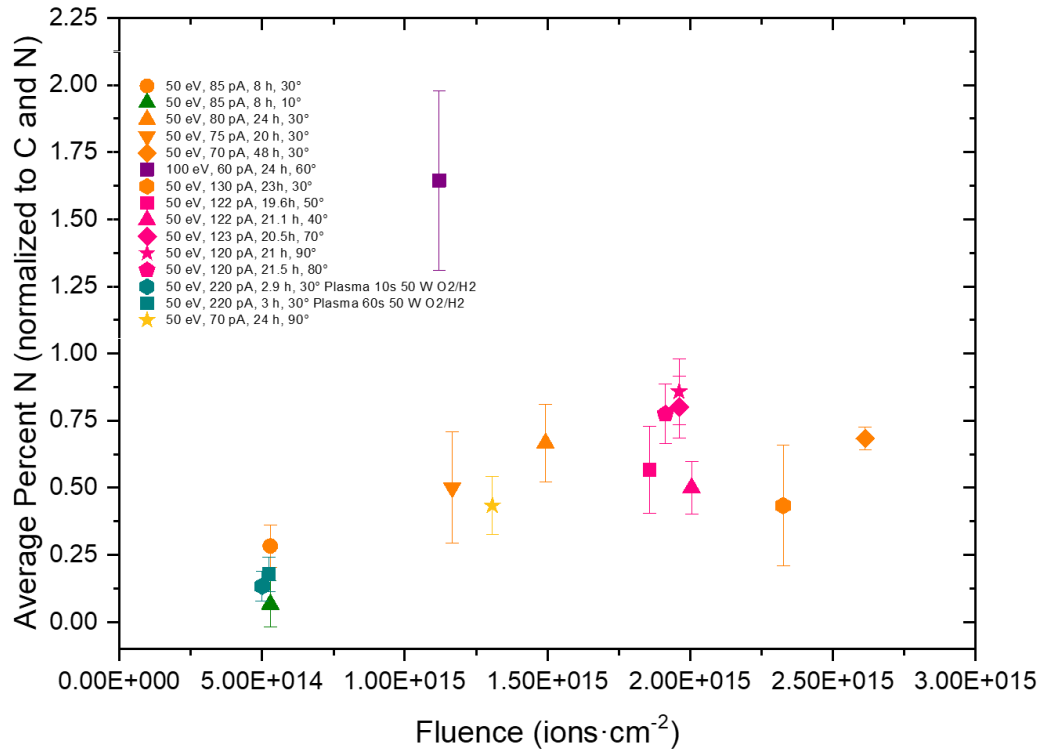


Figure 4.9 Auger quantification of various NanoMill® experiment configurations. The data points represent the mean values acquired from six to twelve measurements and the error bars show the sample error as calculated by the two-tailed one-sample Student's t-test with a probability of 0.05.

In order to further increase the N concentration, experiments were performed in which the graphene was first exposed to an oxidizing environment using a 10 s and 60 s exposure to a 50 W O₂/H₂ plasma source. This method was used to induce defects with the O plasma source which could then be occupied with a N-dopant. Unfortunately, an O₂ feed gas could not be used in the NanoMill® as it could damage the ion gun, therefore a two step-experiment with the plasma cleaner was utilized. According to Figure 4.9 (a) (green points) the O plasma exposure had little effect on the N concentration when normalized to

C. The reason for this may simply be due to the fact that the damaged sites from the plasma cleaner acquired an O-species when exposed to air during the transfer from the plasma cleaner to the NanoMill®. The O content was not examined during Auger quantification of the N-doped graphene without the exposure to the O plasma; however, comparison of the SEM images during Auger examinations (Figure 4.10 (a), (b), (c)) shows the damage induced by the plasma cleaner as pitting after 10 s and 60 s, respectively.

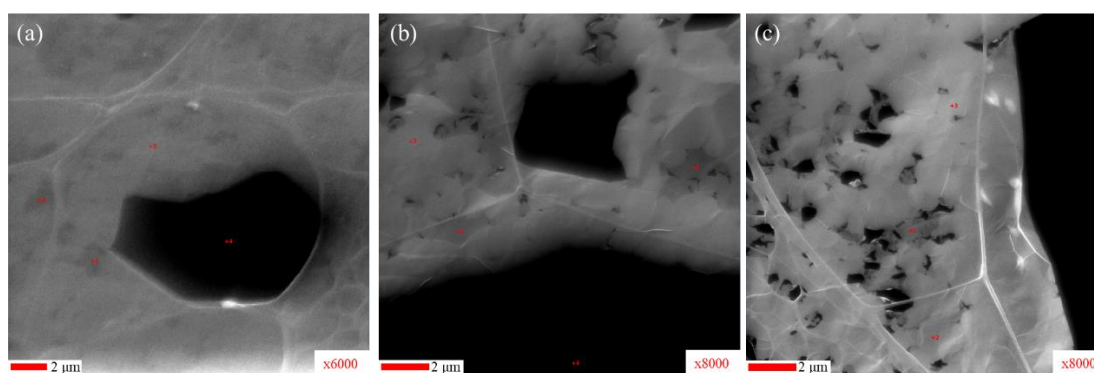


Figure 4.10 SEM SE images comparing N-doped graphene to N-doped graphene with O₂/H₂ plasma exposure. (a) N-doped graphene (NanoMill® 50 eV, 85 pA, 8 hours, 30° tilt), (b) N-doped graphene with 10 second plasma pre-exposure (NanoMill® 50 eV, 220 pA, 2.9 hours, 30° tilt, 10 s O₂/H₂ 50 W plasma), and (c) N-doped graphene with 60 second plasma pre-exposure (NanoMill® 50 eV, 220 pA, 3 hours, 30° tilt, 60 s O₂/H₂ 50 W plasma).

HRTEM imaging (Figure 4.11 (a) and (b)) and EELS spectra (Figure 4.11 (e) and (f)) were utilized to examine the structure after N-doping without exposure to an O plasma source. Following a doping level of approximately 0.50 ± 0.21 % (normalized to C and N), the graphene structure is still intact, which can be observed in a window of amorphous C contaminants. The amorphous C likely originates from the TEM grids, as Graphene Supermarket® grids tend to have high surface coverage of hydrocarbons; however, increased coverage may have developed due to ion exposure [192]. The FFT acquired from the entire image displays the characteristic hexagonal pattern acquired from graphene sample, wherein multiple grains can be observed in the FFT of the low magnification image (Figure 4.11 (b)). However, care must be taken when examining this sample, due to the

fact that the grid is not in focus upon doping. Although unlikely, it is possible that the area examined with HRTEM was not exposed to the N^+ ions. To conduct further evaluation of the doping process, EELS was completed on a sample produced using the NanoMill® with a beam energy of 50 eV, a fluence of approximately 2.0×10^{15} ions·cm⁻², and a tilt of 90°. By employing Auger spectroscopy, it was determined that the sample was N-doped to 0.5 ± 0.6 % (normalized to C and N). This low N content in comparison to the equivalent sample in Figure 4.9 (a) (pink star) may indicate that the current was not maintained throughout the duration of the doping process, the sample was not centered in the ion beam or the sample drifted during ion exposure; further emphasizing the approximation of the total fluence the graphene receives. EELS spectra from this sample were separated based on the thickness of the local graphene sheets, as observed in the dark field (DF) image (Figure 4.11 (c)). The shaded areas in Figure 4.11 (d) show the areas in which the spectra were summed to form the final spectra appearing in Figure 4.11 (e). The purple region is the thinnest, followed by the red region, with the blue area being the thickest, respectively. Upon examination of the three spectra it is apparent that an N-K edge exists in the thinnest area. The fact that the N-K edge was observed in the thin area and not the thick area was not surprising, as the concentration of N in this sample is quite low, and a deconvolution was not performed to remove plural scattering effects from the sample. Due to the weak N-K edge observed in the thin specimen and the lack of the N-K edge in the thick regions, the fine structure of the C-K edge can be utilized to examine the effect of the NanoMill®. The thicker regions in red and blue appear to have a sharp π^* and σ^* peak at 285 eV and 292 eV, respectively, which is characteristic of graphene. More interestingly, when examining the ELNES of the thin region (purple), the shape of the fine structure of the C-K edge is modified. The π^* and σ^* peaks are still present, but they have weakened and broadened with respect to the thick graphene regions. Moreover, the fine structure at higher energies after the σ^* peak in the thin region is lost and a broad onset to the σ^* peak is observed. These spectra did not undergo low-loss deconvolution to remove multiple scattering effects. This suggests that within the thin region the long-range order of the

graphene lattice has been lost, or the sheet has a thin layer of amorphous C, while the graphene lattice is maintained with short-range order. This has been observed in the N-doped graphene in *Chapter 3.2.1 Graphene* and in graphene oxide in literature [205]. Furthermore, a shoulder on the σ^* peak has been observed in atomic resolution EELS of N-doped graphene, as reported by Nicholls *et al.* [140]. The broadening of the σ^* peak could be related to the formation of this shoulder from the presence of the N-dopants. Because atomic EELS was not performed for this sample the reason for the broadening cannot be directly specified, but based on the Auger results and loss of fine-structure in the C-K edge, it can be speculated that the N^+ ions doped the graphene lattice. However, the loss of fine structure could be attributed to damage from the N-doping process and/or a thin layer of surface contamination. The broadening effects of the π^* and σ^* peaks were not observable in EELS when examining the thicker regions, likely due to the fact that only the top-most sheets exposed to the beam were damaged, and the fine structure of the undamaged lower graphene sheets overwhelms the C-K signal in these regions. Upon normalizing the thick and thin regions using a 5 eV window at 300 eV, it is evident that the π^* and σ^* peaks are of similar intensity, further confirming the fact that the graphene lattice is present after the doping process; however, the lack of fine structure after the σ^* peak is indicative of a defective graphene lattice.

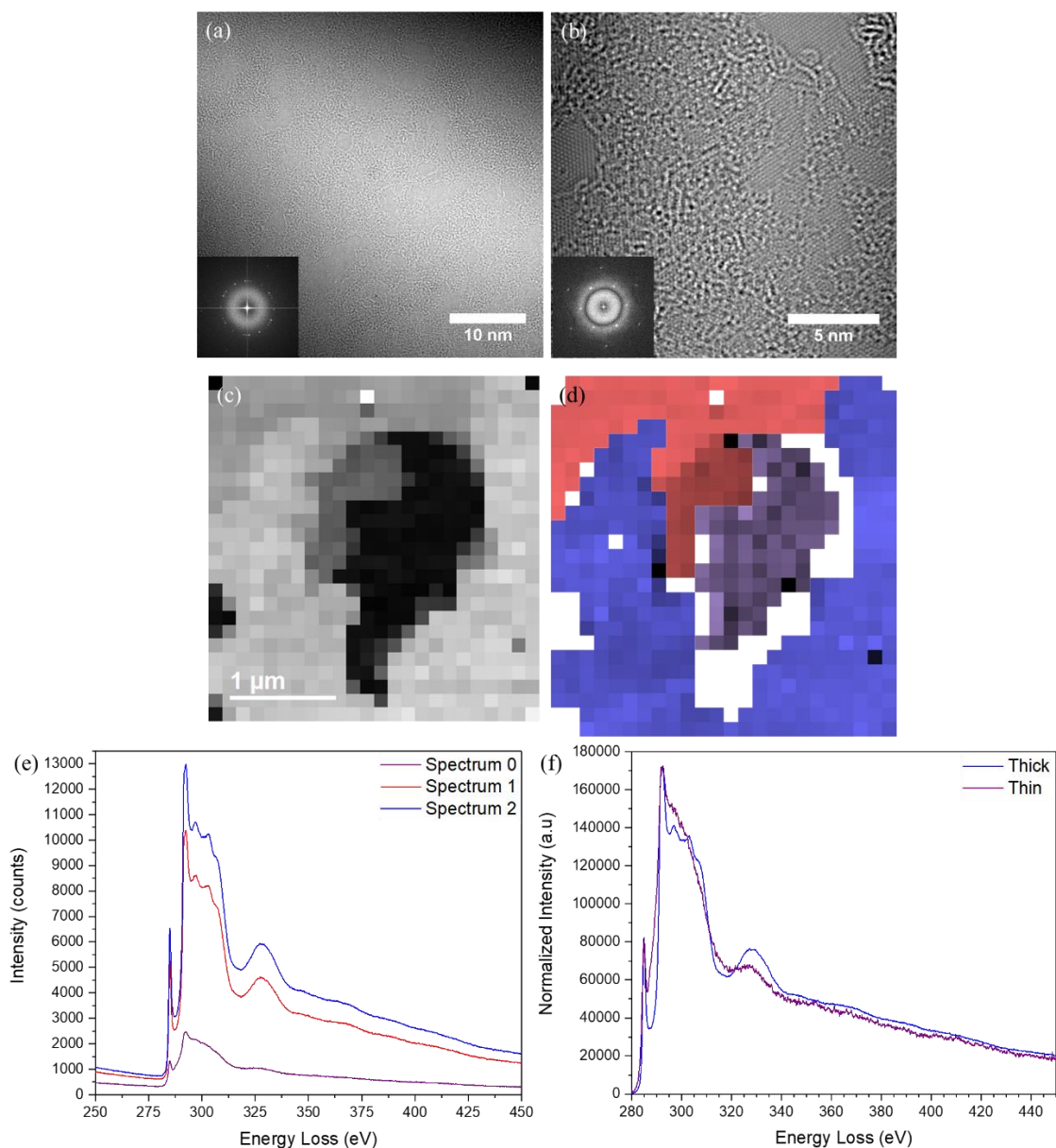


Figure 4.11 HRTEM and EELS analysis of NanoMill® N-doped graphene sample. HRTEM images at (a) low and (b) high magnifications were acquired after N-doping of approximately 0.50 ± 0.21 % (normalized to C and N, error calculated from the two-tailed one-sample Student's t-test with a probability of 0.05) (NanoMill® 50 eV, 75 pA, 20 h, 30°). An EELS spectrum image was collected from a multi-layered region as observed in the (c) DF image and the EELS spectrum image was summed into (d) three polygonal regions based on the graphene thickness, resulting in (e) three separate EELS spectra. (f) Normalized EELS spectra acquired from the thinnest and thickest regions of the spectrum image.

4.3 Pd Deposition on Pristine Graphene TEM grids

As a proof of concept, Pd was deposited on a pristine Graphene Supermarket© TEM grid to determine if ALD could lead to a successful deposition. Pd was used rather than Pt, in effort to reduce the cost of the samples that will not be used for electrocatalytic cycling. Commonly Pd is deposited with the first half cycle of Pd(II) hexafluoroacetylacetonate and a second half cycle of formalin, glyoxylic acid, molecular H₂, or plasma sources¹⁴ [206], [207], [208]. After 20 ALD cycles, high resolution STEM images were acquired using ADF imaging conditions. The sample was highly contaminating under the electron beam, thus a beam shower in TEM mode with a current of 3.51 nA for approximately 15 minutes was applied before high magnification ADF imaging. In Figure 4.12 (a) and (b) surface hydrocarbons (grey level intensity) can be seen covering the graphene surface (black) and Pd particles can be found (white) decorating the surface contamination. The specific area imaged is multilayered graphene, as determined through the Moiré pattern in the darker areas of Figure 4.12 (b). The location of the Pd with respect to the surface contamination is not unexpected based on many examples in literature. Zan *et al.* summarizes the results from a few sources, illustrating the preferential deposition on Au, Fe, Co, Ni, Pd, Ti, and Al on the surface hydrocarbons rather than graphene [165]. This reference illustrates that in most cases the metals sit on the center of the contamination, but can be dragged to edge sites with the assistance of the beam and can result in graphene etching under ultra-high vacuum [165]. Interestingly, in Figure 4.12 (b) the Pd particles tend to sit in the center of the surface contamination with some atoms located at the edge of the hydrocarbons, as labelled with white arrows. It is uncertain if this is the preferred location of those individual atoms deposited by ALD, or if they were dragged to those locations under the excitation of the electron beam. The area of 185 particles and atoms were manually measured from

¹⁴ ALD was completed by members of Dr. X. Sun's group at Western University.

ADF images using built in functions in ImageJ [209]. The results are contained in the histograms in Figure 4.12 (b), in which the area of the particles was converted to an equivalent diameter. It was determined that the average particle size in the high magnification regime $0.8 \pm 0.9 \text{ nm}^{15}$ (Figure 4.12 (a)) with a maximum particle size measured at $8.35 \pm 1.03 \text{ nm}$ in the low magnification regime (Figure 4.12 (b)). From the histogram and low magnification images, it is evident that there is a large spread in the size of the Pd particles on the Graphene Supermarket© TEM grid. During future examination, the TEM graphene grid must first be cleaned from surface hydrocarbons and fewer than 20 ALD cycles should be utilized during the deposition to examine the bonding location of Pt or Pd atoms with respect to the N-dopants.

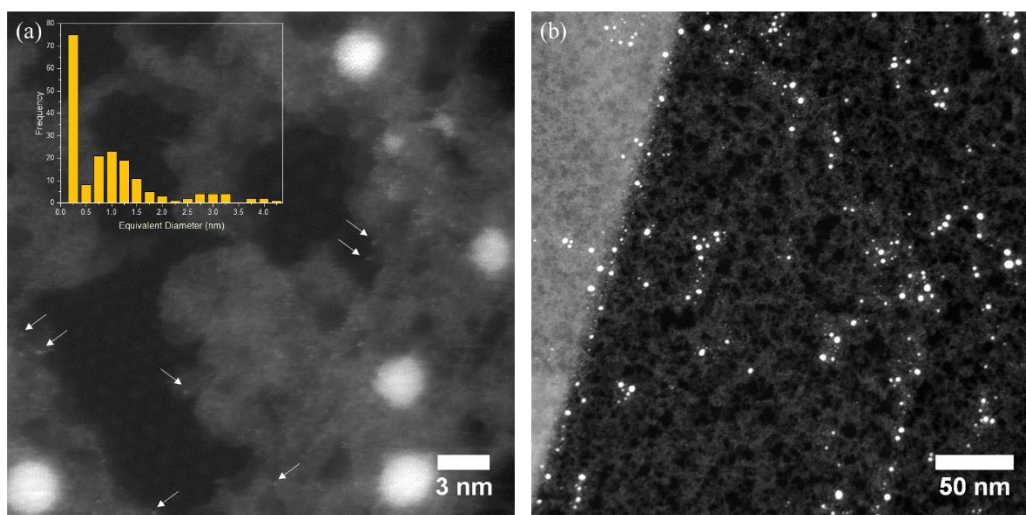


Figure 4.12 ALD Pd on Graphene Supermarket© TEM grid at (a) high (gamma adjusted) and (b) low magnifications (brightness adjusted) with white arrows pointing to Pd atoms sitting on the edge of surface contaminants in (a). The inset shows the histogram acquired from the equivalent diameter (nm) of the Pd particles and atoms taken from various ADF images.

EELS was used to examine the binding location of Pd on the TEM grid. The ADF image in Figure 4.13 (a) shows that the Pd is located on the surface contaminants, as observed in Figure 4.12. The ICA components can be observed in Figure 4.13 (b) with the

¹⁵ Error acquired from measured sample standard deviation.

respective loadings in Figure 4.13 (c), (d), and (e). Based on the spectral signatures, loading 0 is assigned to Pd with a small amount of C, loading 1 has graphitic C and O, and loading 2 is composed of disordered C and O. Loading 1 shows a shell-like structure surrounding the Pd structures, which could be originating from the C and O containing ligand from the first half-cycle in the deposition process. It should be noted that the source of the graphitic nature of the C-K edge surrounding the Pd particle is unaccounted for in this explanation. It is expected that the graphene component should be more uniform, thus it is not clear if loading 1 is in fact an isolated component or it is undergoing cross-talk between other components. Alternatively, loading 2, which is associated with a disordered C-K edge and an O-K edge, likely derives from the surface contamination observed in the DF image (Figure 4.13 (a)). By simply adjusting the opacity of the loadings, overlay images can be observed in Figure 4.13 (f) and (g). These images more easily illustrate the method in which the Pd interacts with the different C sources. Figure 4.13 (f) clearly shows that the graphitic C-K signal (loading 1) is coating the Pd particles, while the particles are sitting on what is assumed to be the surface hydrocarbons (loading 2). It is unlikely in this case that the Pd particles would be active as a catalyst due to the surface coating observed in loading 1, thus care should be taken in the future to ensure the ligands are fully reduced, if this is indeed the source of the C in loading 1.

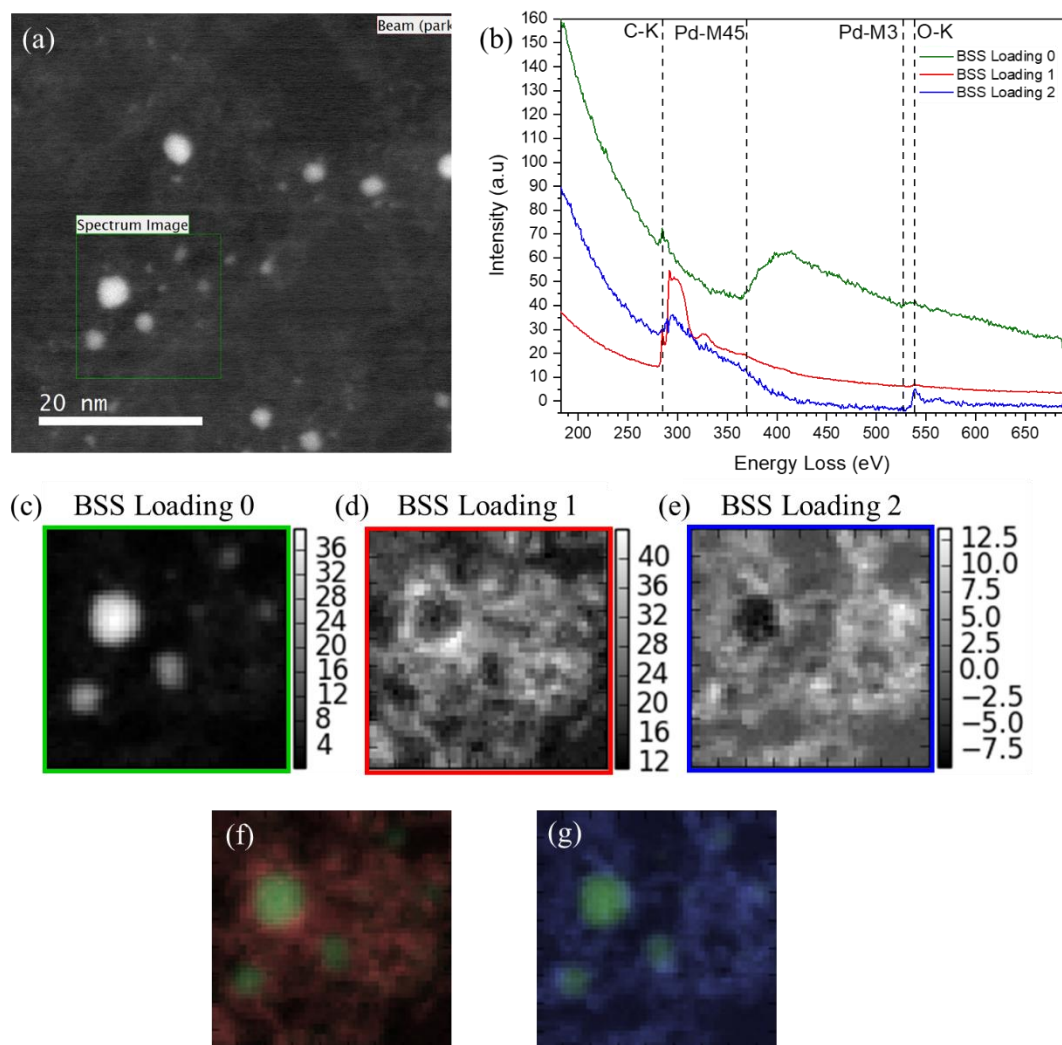


Figure 4.13 EELS spectrum images acquired from ALD Pd on a Graphene Supermarket grid.

The green box in (a) shows the DF image (gamma adjusted) of the area examined. ICA decomposed (b) spectra and respective loadings for (c) Pd, (d) graphitic C-K and O-K edges, and (e) disordered C-K and O-K edges. Overlay images were produced for (f) loading 0 and loading 1 and (g) loading 0 and loading 2 by adjusting the opacity the images in (d) and (e).

4.4 Summary

In summary, Auger spectroscopy was used to quantify the N content of various in-house doping conditions of thin-suspended graphene sheets on TEM grids. The Auger conditions were optimized to reduce background signals originating from electrons below the TEM grid. The conditions for N quantification included an acceleration voltage of 20 kV, at a tilt angle of 30° with respect to the electron source, and with an 800 µm Pt aperture located below the TEM grid when using a specially design holder, resulted in a 98% reduction of the background signal.

Three in-house sample preparation instruments were used to N-doped graphene containing TEM grids. The NanoMill® had proven useful for N-doping the graphene lattice. As quantified by Auger spectroscopy a maximum average N concentration of $0.86 \pm 0.20\%$ (normalized to C and N) when operating at 50 eV with a tilt angle of 90° and a fluence of approximately 2.0×10^{15} ions·cm⁻² can be achieved. Using HRTEM and EELS, the structure of the graphene was determined to be intact with short-range order, but the sheets were covered in a thick layer of amorphous C that likely originated from the TEM grids and the ion exposure. ELNES of thicker regions clearly indicated that the graphene sheets were present after N-doping; however, when examining the thin area, the fine structure was weakened and the π^* and σ^* peaks broadened. This can be attributed to three potential factors: N-dopants disturbing the graphene lattice, damage from the ion beam, and/or contributions from the surface C layer. Because the NanoMill® shows positive results for the N-doping in a controlled manner, it is a viable source for N-doping thin graphene sheets; however, the exact concentration will need to be examined after each doping process, as the concentration was not observed to be consistent when using the same energy and fluence. The difference in concentration between samples at the same operating conditions could be related to the fact that the current in the NanoMill® fluctuates during use since the minimum operating energy was utilized, thus the exact fluence and exposure location on the TEM grid cannot be fully identified. As previously mentioned, the current

should be monitored throughout the entire exposure of a TEM grid to better understand the effects of the current fluctuations, and to determine if the current is stable throughout the long exposure times or if it decreases. It is also suggested that a measurement of the beam size is completed for future experiments to more accurately determine the ion fluence and the diameter of exposure for TEM investigations. Moreover, a holder with a more precise angle positioning should be machined to remove the ambiguity of the tilt angle.

Lastly, ALD was used to deposit Pd on the graphene containing TEM grid, as a proof-of-concept for future experiments. It was determined that with 20 ALD cycles, a distribution of Pd entities ranging from atoms, clusters, and nanoparticles were deposited on the graphene TEM grid. The Pd was found to be preferentially located on the surface hydrocarbons, and contained a C shell, likely originating from incomplete oxidation of the ALD precursor ligands. For future, experiments it is suggested that the graphene be thoroughly cleaned to reduce the source of surface hydrocarbons, and care be taken during ALD to eliminate the C containing shell on the Pd particles.

Chapter Five

NCNT Characterization and ALD Fine Tuning

Multi-wall carbon nanotubes (MWCNTs) consist of concentric cylinders of rolled graphene sheets. They were first produced by Iijima *et.al* as a by-product of fullerene synthesis in 1991; however, at that time, they were called graphitic microtubules [210]. Since the first creation of MWCNTs, many synthesis routes have been examined to solely produce the CNTs in which control of size, length, and number of layers has been a priority to explore their effects on different physical properties. The most common synthesis routes and physical properties are outlined in numerous review papers and textbooks, as listed here, but these are outside the scope of this report [211], [212], [213], [214]. Within this chapter NCNTs will be examined as media for gas containers, and as a substrate material used to optimize the ALD parameters for Pt deposition. Using quantitative EELS, the pressure within the NCNTs will be examined with respect to the size of the NCNT to determine if a correlation exists. Furthermore, the effects of specific ALD deposition conditions such as temperature, dosing time, and substrate (NCNT and CNT) will be examined with respect to the first deposition cycle, in an effort to increase the control over the size of the deposited Pt clusters.

5.1 Gas Filled NCNTs with ALD Pd

Gas containing materials have been examined in the TEM for many years with samples varying from He bubbles in nuclear reactor materials [215] to N₂ containing CNTs [216], [217], [218], [219], [220], [221], [222], [223]. Trasobares *et al.* completed an extensive investigation into the chemistry and morphology of NCNTs, illustrating the vast dependence of gas-filling on catalyst selection, precursor gas, and reaction temperature [224]. Various growth mechanisms have been proposed for gas incorporation, in which the CN_x precursor species or N₂ carrier gas are absorbed in the catalyst, thus leading to N production during the precipitation of the CNT. The gas had been reportedly trapped as a by-product of the wall formation [216], [224], or had been absorbed within the Fe catalysts and subsequently released/encapsulated upon saturation within the growth catalyst [217], [221]. Currently, the encapsulation methods are hypothesized and seem to be system dependent, as not all N containing precursors produce a N₂ gas within the CNT.

In the following sections, the presence of the gas using an ultrasonic spray pyrolysis synthesis technique [218] will be determined with emphasis on the relationship between the pressure of the trapped gas and the size of the tubes. The growth mechanism of this technique is outside the scope of this report; however, a discussion outlining necessary steps to determine the growth will be presented. It should be noted that during the synthesis technique both the C, N, and Fe catalysts are introduced into the reaction chamber as a single solution [218], thus CNT growth and N-doping occur simultaneously.

5.1.1 Experimental Conditions

5.1.1.1 Material Preparation

All samples were prepared by Dr. Sun's group at Western University. The NCNTs and ALD were produced in-house using the technique outlined in ref. [218]. During the ALD process a precursor of Pd(II) hexafluoroacetylacetonate was used in the first half cycle, and the second half cycle consisted of formalin, glyoxylic acid, molecular H₂, or plasma sources [206], [207], [208]. TEM samples were prepared by drop casting an ultrasonicated solution of dilute HPLC grade methanol with the sample of interest onto a lacey C grid.

5.1.1.2 High Resolution Imaging

High resolution images were acquired using an FEI Titan 80-300 Cubed TEM equipped with hexapole-based aberration correctors (Corrected Electron Optical Systems GmbH) for the probe and imaging lenses, and a high brightness field emission gun (*XFEG*). The acceleration voltage was set to 80 kV to minimize knock-on damage to the CNT, while still maintaining an energy that allows relatively easy image acquisition. STEM imaging was performed using HAADF (detector semi-angles of 63.8 mrad to 200 mrad, as measured by FEI) conditions with a C2 aperture of 50 μm and a spot size of 9. The aberration corrector was tuned to minimize spherical aberration in the probe lens. Monochromated negative spherical aberration corrected HRTEM was performed, in which the image corrector was used to adjust the C₃ in combination with the C₁ to compensate for the intrinsic C₅.

5.1.1.3 Auger Quantification

Auger spectroscopy was also utilized to quantify the N content in the NCNTs. The spectroscopy was completed using a JEOL JAMP-9500F field emission-Auger at an energy of 10 kV, a current of 30 nA, a tilt of 30°, and M5 mode. Beam contamination could not be avoided during spectral acquisition; thus, it should be noted that the elemental content other than C may be slightly underestimated. Quantification was completed using an in-house HOPG standard from a freshly cleaved surface, and Cr₂N, Pd, ZnS, and SiO₂ JEOL supplied standards for the C-KLL, N-KLL, Pd-MNN, S-LVV, O-KLL, and Si-KLL Auger electrons, respectively.

5.1.1.4 EELS Quantification and ICA Conditions

Using the Titan 80-300 Cubed, EELS spectra were acquired to examine the elemental content and species within the NCNTs. EELS spectra were acquired in EFSTEM mode with a dispersion of 0.4 eV/pixel, and a convergence and collection semi-angle of 19 mrad and 58 mrad (as measured by FEI), respectively (as measured by FEI), resulting in an energy resolution of 1.2 eV, as measured by the FWHM of the zero-loss peak. DualEELS™ was used to collect both the zero-loss peak and core-loss spectrum using the GATAN image filter (GIF) Quantum® [225]. To reduce the NCNT exposure to the beam and reduce the sample drift, a current of approximately 40 pA with relatively quick exposure times of 4×10^{-5} s/pixel and 0.01 s/pixel were used for the zero-loss and core-loss spectra, respectively. Core-loss edges were collected for ICA with an exposure time of 0.1 s/pixel. Using DualEELS™ the zero-loss peak was used to align and calibrate the low-loss spectrum image, and the high-loss spectrum image was aligned and calibrated using the π^*

peak (285 eV) in the C-K edge. Using GATAN Digital Micrograph software, X-ray spikes were removed from the spectra prior to quantification and ICA.

The N₂ pressure within the NCNTs was quantified by following procedures outlined by Egerton [125], Walsh *et al.* [226], and Lacroix *et al.* [227]. The N volumetric density (atoms/nm³) within the NCNTs was determined using,

$$n_N = \frac{I_N}{I_Z \sigma_N d} \quad (5.1) \text{ [226], [227]},$$

in which I_N (counts) is the integrated intensity of the N-K edge, I_Z (counts) is the integrated intensity of the unscattered beam (deconvolved zero-loss peak), σ_N (barns) is the integrated cross-section, and d (nm) is the inner diameter of the nanotube. Digital Micrograph software was utilized to acquire the N density from equation (5.1), as will be detailed in the following text.

Spectrum images were acquired with a magnification of 160 Kx and 320 Kx (Figure 5.1 (a)), which were calibrated using a linear extrapolation from a gold cross-grating at 10 Kx. The spectra within a spectrum image were aligned and the energy was calibrated using the zero-loss peak. The spectra used for quantification were summed (Figure 5.1 (b),(d) and (c),(e)) from the center-most regions of the inner diameter for each NCNT, and for each individual compartment within the NCNT under examination (region of interest (ROI) in Figure 5.1 (a), (b), (c)). Following the alignment and calibration, X-ray spikes were removed using Digital Micrograph's built-in function. The low-loss and core-loss spectra were then spliced together using 100 overlapping channels to calculate the new scale (Figure 5.1 (f)). Multiple scattering events were then removed from the spectra through a deconvolution of the zero-loss peak performed in Digital Micrograph using a Fourier-log deconvolution with the reflected-tails model (Figure 5.1 (g)). The zero-loss modifier was used during the deconvolution; however, this method occasionally resulted in a periodic noise, in which case the Gaussian modifier was used with the width set to the FWHM of the zero-loss peak. During deconvolution, Digital Micrograph stores the integrated intensity of the zero-loss peak which it later uses for the calculation of the areal density (atoms/nm²), as shown in equation (5.1). The N areal density was then calculated within

Digital Micrograph from the deconvoluted core-loss spectra (Figure 5.1 (h)) and the “Quantification” routine in Digital Micrograph. To calculate the absolute areal density the background fit was individually set for each N-K edge to ensure an adequate background was set for each quantification. Further parameters for quantification included, the signal integration window which was set at 50 eV with the window ranging from approximately 395.9 to 445.9 eV with the partial cross-section modeled using the hydrogenic model. Using the equation outlined in *Chapter 2.2.3.1 Elemental Quantification using EELS*, and the stored integrated zero-loss intensity, the “Quantification” routine calculated the areal density. The areal density (atoms/nm²) was then converted to the density (atoms/nm³) through means of dividing by the inner diameter, as shown in equation (5.1). The density was then converted to pressure using the ideal gas law:

Equations used:
$$\left(\frac{n_N}{V}\right) = \frac{I_N}{I_Z \sigma_N d}, P = \left(\frac{N_{N_2}}{V}\right) \times RT$$

Example of Numerical Input:

$$20 \frac{N \text{ atoms}}{\text{nm}^3} = 10 \frac{N_2 \text{ molecules}}{\text{nm}^3} \times \frac{1}{6.022 \times 10^{23} \frac{\text{molecules}}{\text{mol}}} = 1.7 \times 10^{-23} \frac{\text{mol}}{\text{nm}^3} \times \frac{1 \text{ nm}^3}{1 \times 10^{-27} \text{ m}^3} =$$

$$168777 \frac{\text{mol}}{\text{m}^3} \times 8.314 \frac{\text{J}}{\text{mol K}} \times 298 \text{ K} \times \frac{9.86923 \times 10^{-6} \text{ atm}}{1 \text{ Pa}} = 412 \text{ atm} \quad (5.2).$$

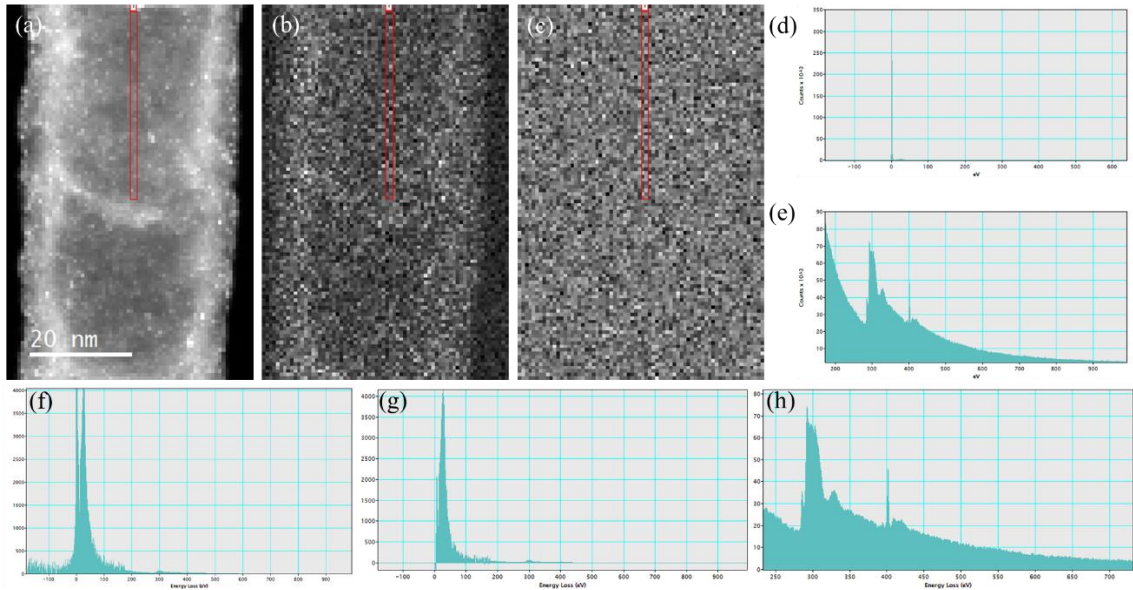


Figure 5.1 Various steps used in the quantification of the N_2 pressure within the NCNT. For each NCNT and compartment in the NCNT the (a) ADF, (b) core-loss spectrum image, and (c) low-loss spectrum image were acquired. The spectra were then summed from the inner most region of the NCNT for the (d) low-loss and the (e) core-loss spectra. These summed spectra are then (f) spliced together to form one spectrum and the zero-loss peak is removed using a (g) spectrum deconvolution to remove the effects of multiple scattering. The spectra (h) after deconvolution of the C-K and N-K edges can be used for quantification.

In order to determine the diameter of the nanotubes, specific steps were utilized to ensure the most accurate calculation. The ADF image (Figure 5.2 (a)) of the NCNT analyzed was first calibrated using a linear extrapolation at 14 Kx and 20 Kx of the Au cross-grating which contains a period of 463 nm. An error analysis was performed by examining the percent difference between the maximum and minimum calibration scale (pixels/nm) from eight measurements, which resulted in 3% error. Using previously analyzed data for the FEI HAADF detector, the linear extrapolation resulted in a percent error of approximately 4.4%, as compared to a standard magnification calibration sample, which suggests an adequate approximation for the NCNT size. The diameter of the NCNTs was then determined using the line profile tool (Figure 5.2 (b)) in Digital Micrograph, wherein multiple measurements were acquired on a single NCNT (labelled boxes in Figure

5.2 (a)). The line profile was converted to an EELS spectrum and the first derivative of the spectrum was obtained (Figure 5.2 (c)). When considering the walls of the NCNT, the inflection points result in the inner and outer diameter, which can be seen as a peak in the first derivative plot (Figure 5.2 (d)). This method of analysis is better suited to measure the inner and outer diameter of the NCNTs, rather than strictly using the line profile plot, as the inflection points are easier to identify than the noisy summed line profile. Areas where Pd was located at the inner or outer diameter were excluded from the measurement, as this resulted in intensity shifts in the line profile that distorted the diameter measurement. The diameter used in equation (5.1) to calculate the areal density of the N_2 molecules was the average inner diameter measured from single NCNT compartments the error calculated by the two-tailed one-sample Student's t-test with a probability of 0.05.

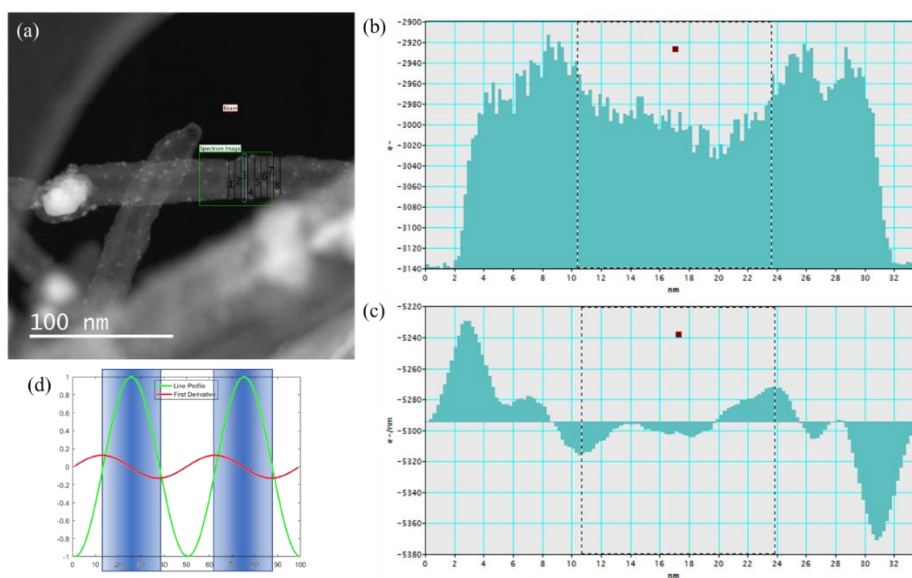


Figure 5.2 Experimental measurement of the diameter of the NCNTs. The diameter of the NCNTs was measured using (a) ADF images (gamma adjusted), wherein the annotated areas were used for the measurements along the NCNT. The (b) summed profile and (c) first derivative were acquired for each of the annotated areas in (a), wherein they were used to measure the inner diameter from the dashed lines outlined in (c). A (d) schematic of the line profile (green) and first derivative (red) with respect to the intensity of the two-dimensional projection of the NCNTs side walls (blue) shows that peaks in the first derivative (with a positive and negative value) can be used to determine the edge of the CNT.

Lastly, ICA was completed on the EELS spectra from the NCNTs to determine the different elemental composition of the Pd catalysts on the surface of the NCNTs, and the catalysts used to grow the NCNTs (Fe). HyperSpy [127] was used to produce the ICA loadings and respective factors. In order to produce physically significant factors, the EELS spectra were cropped, such that the C-K and N-K edges were examined separately. Prior to performing the ICA, Digital Micrograph was used to align the spectra in the spectrum image using the π^* and σ^* peaks in the C-K edge. The spectra were then calibrated to the π^* edge at 285 eV and the X-rays were removed using Digital Micrograph's internal function.

5.1.2 Identification of Gas and Elemental Components

The NCNTs with Pd were examined using various imaging conditions, including SEM, ADF, and HRTEM (Figure 5.3). The SEM shows the small Pd particles through the bright contrast that were also visible in the ADF (bright particles) and HRTEM images (dark particles). According to the ADF images, the Pd nanoparticles resulted in an average size of approximately 2.15 ± 0.05 nm¹⁶ (excluding the quantification of Pd single atoms). Using the ADF and HRTEM images, it can be concluded that the NCNTs are multiwalled of varying thicknesses. More specific structural examination of the NCNTs can be completed with HRTEM images, wherein defects can be observed on the surface of the NCNT and on the walls, especially in the walls separating the compartments in the NCNTs due to its bamboo structure. It should be noted that this can be due to both the synthesis technique, and potential beam induced damage. Importantly, these NCNTs are relatively clean, as most areas of the CNT wall contain only a thin (< 2 nm) layer of disordered C. Looking at the interior of the tubes in the HRTEM images, crystalline material is observed, suggesting

¹⁶ Sample errors were calculated using the two-tailed one-sample Student's t-test with a probability of 0.05.

the walls maintain the graphene structure after N-doping with defects potentially arising from the N-doping, the synthesis technique, the disordered C contamination, and possible electron beam interactions.

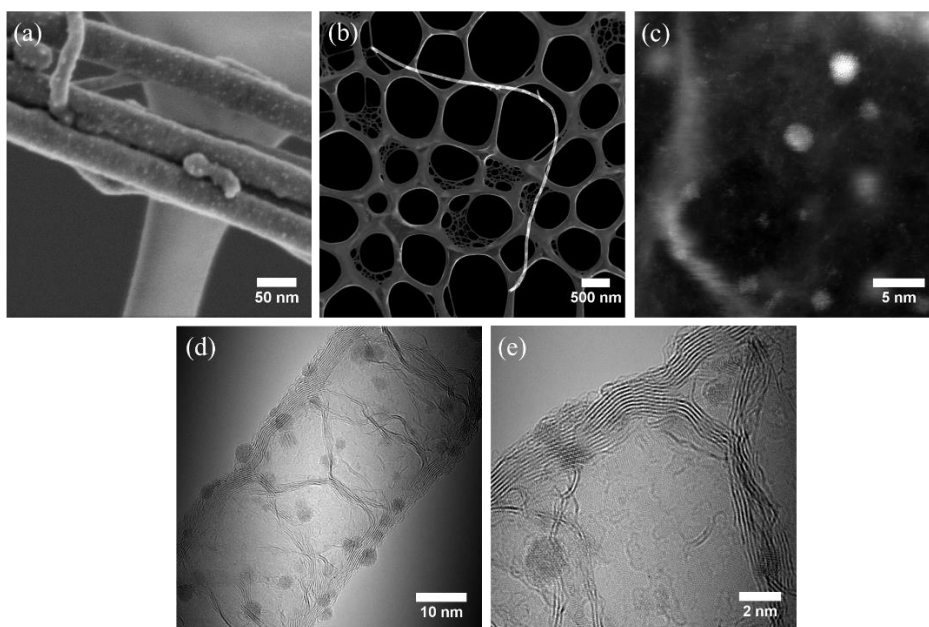


Figure 5.3 NCNT images acquired by (a) SEM¹⁷ (b,c) ADF, and (d,e) HRTEM.

The elemental composition of the NCNTs was analyzed using Auger quantification, as outline in Table 5.1. It can be observed that the tubes contain both N and O, which are likely introduced through N-doping, and surface hydrocarbons or N-oxides [218], respectively. A small amount of S contamination was found on this sample, the source of which is unknown. Interestingly, the O content is larger than the N content; however, the significance of these values for the stabilization of Pd is unknown without the use of spectrum imaging. It is expected that the N content originates from the walls of the tubes, and not the N encapsulated within the tubes as the average wall thickness

¹⁷ Image acquired by Travis Casagrande, CCEM research associate.

measured from 18 CNTs is approximately 12.1 ± 1.0 nm, which is greater than the escape depth of the Auger electrons.

Table 5.1 Auger quantification of NCNTs after Pd deposition. The reported values are averages, and the sample errors were calculated using the two-tailed one-sample Student's t-test with a probability of 0.05.

Signal (standard)	Average Atomic Percent
C	93.2 ± 1.6
Pd	1.3 ± 0.5
N (Cr ₂ N)	1.6 ± 0.4
O (SiO ₂)	3.0 ± 1.1
S (ZnS)	0.9 ± 0.4

Upon EELS examination, a sharp peak was identified in the N-K region for some NCNTs. At the time of collection, it was proposed to produce a hole in the NCNT to determine if the peak was related to a gaseous species. Figure 5.4 (a) illustrates the ADF image of a filled NCNT before the hole was produced. The spectrum image in Figure 5.4 (b) and the summed spectra in Figure 5.4 (e) shows the intense peak at 401 eV with the source originating from within the CNT. A hole was produced by placing the electron beam on the NCNT for one minute with a 40 pA current. As can be shown in Figure 5.4 (b) and (e), after the beam exposure a small hole was produced; however, the tube was still filled. In order to produce a larger hole, the beam was defocused and exposed to the NCNT for two minutes with a current of 250 pA. Following the production of the larger hole, the EELS spectra was modified such that the intensity of the peak greatly decreased and shifted to a lower energy (~399 eV). Because the N-K edge changed after the production of a larger hole, it is believed that the NCNT was filled with a gas prior to puncture. It is expected that gas is still present within the tube after the creation of the hole, based on the evidence from the high intensity in the spectrum image located at the hole and along the interior walls of the NCNT. The presence of the gas after puncturing the NCNT could be caused by incomplete release of the gas before spectrum acquisition and/or physisorption of the gas

to the inner side walls. The shift in energy of the N-K edge EELS spectrum observed after the production of the hole may suggest the presence of N-dopants in the graphene wall of the NCNT. Similar spectra have been observed by Trasobares *et.al* [216], who noted that after puncturing a NCNT that contained N₂, a N-K peak related to a graphitic-type dopant was found. They proposed the N-K peak originated from the incorporation of N₂ gas into an amorphous C layer created at the puncture site due to the electron beam interaction. When considering the findings from this paper [216], it is unclear if the N-K peak at 399 eV in Figure 5.4 (e) originates from the hole or a graphitic-type N-dopant in the NCNT walls.

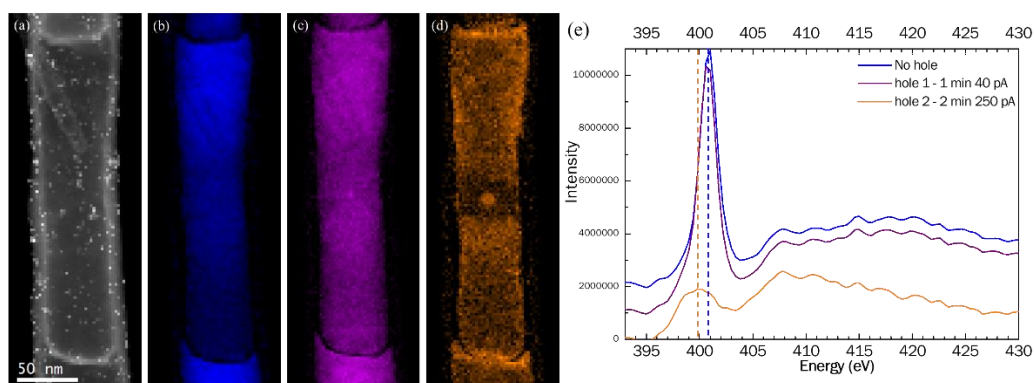


Figure 5.4 EELS N-K maps and edges from NCNTs. (a) ADF image of the NCNT with Pd, (b) N-K edge composite map from (a), (c) N-K edge composite map after a hole was created from a 1 min exposure to a 40 pA electron beam, and (d) N-K edge composite map after a second consecutive hole created from a two minute exposure to a 250 pA electron beam. (e) The summed N-K edge from the composite maps.

To determine the source of the N gas within the NCNTs, a comparison of the fine structure was performed for the N-K edge in Figure 5.4 (e) with literature reference spectra (*Appendix 2: N-K Edge Reference Spectra*) acquired by gas phase EELS. In this investigation, it was determined that a sharp peak located at 401 eV was evidence for both N₂ and acetonitrile. Because the fine structure is so similar for N₂ and acetonitrile, in which the sharp peak is only separated by 1 eV, strictly using the reference spectra cannot be

utilized to discern the gas held within the NCNTs. However, when referring to the production method of the NCNTs as outlined by Liu *et al.* [218], it can be observed that an N₂ XPS peak only arises when imidazole is added to the acetonitrile solvent, thus suggesting that a reaction occurring with the imidazole is responsible for the N₂ production. Due to the fact that the reference used to produce the NCNTs [218] observes an N₂ XPS peak, and the peak is only visible when imidazole is used during the production method, the peak we are observing in EELS is likely originating from N₂, as opposed to acetonitrile. This is also supported by other work [216], [220], [217], which has identified N₂ gas filled CNTs as a by-product of the production methods. Furthermore, STXM spectra from this sample, acquired by Dr. Adam Hitchcock, confirmed the origin of the gas to be N₂, as opposed to acetonitrile.

While observing the gas peak within the N-K edge, other edges were evident within the EELS spectrum image, including the C-K, O-K, Pd-M, and Fe-L edges. Unfortunately, the Pd-M edge overlaps the N-K edge, thus making spectral separation very difficult. In order to separate the spectral features and better understand the nature of different components within the spectrum images, ICA was performed on an NCNT containing N₂ gas, Pd nanoparticles, and a growth catalyst. The spectra examined were divided such that the C-K edge and higher energy edges were cropped to result in physically meaningful data. Figure 5.5 shows the components acquired from the higher order core-loss edges in which different spectral features are identified: (a) spectrum of the background, (b) O-K edge with a weak Pd-M edge, (c) Pd-M edge, (d) Fe-L and O-K edge, (e) N-K edge, and (f) Fe-L edge, respectively. Examination of the maps can provide some interesting information concerning the growth catalyst and Pd nanoparticles. Loading 1 indicated that an oxide exists within the sample through the large catalyst located on the right-hand side of the NCNT and on some Pd particles; however, comparison of loading 2 indicates that not all of the Pd particles are oxidized. The oxidation observed on the Pd particles may have manifested from the incomplete reduction of the Pd(II) hexafluoroacetylacetonate precursor used in the ALD process. Furthermore, the large oxide observed in loading 1 can

be attributed to an iron oxide particle observed in loading 3. Interestingly, loading 5 indicated that there are two Fe particles, which are introduced during the production method as the growth catalyst. Shown in Figure 5.5, the Fe particle located within the NCNT walls remains in pure Fe form, while the Fe particle outside of the NCNT is oxidized due to its exposure to the atmosphere. During the spray pyrolysis production method, it is possible for the catalysts to deposit on the outside of an already formed tube, as the catalyst is being introduced simultaneously with the C and N reactants. Lastly, the N₂ gas peak can be observed in loading 4, wherein it is contained within the NCNT, as previously observed. Once again, a higher density of the N₂ gas is observed on the interior walls of the NCNT, which may be an indication of physisorption.

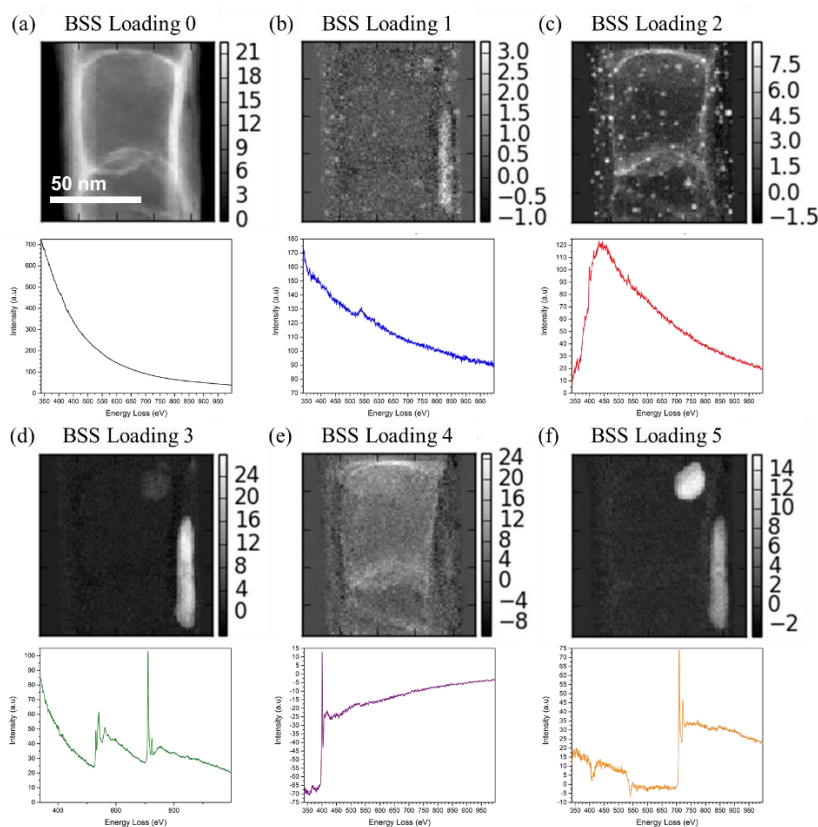


Figure 5.5 Higher energy NCNT ICA results showing different spectral components: (a) background, (b) weak Pd-M edge with an O-K edge, (c) Pd-M edge, (d) O-K and Fe-L edge, (e) N-K edge, and (f) Fe-L edge, respectively.

Further examination of the same NCNT was completed for the C-K edge in an effort to examine the cleanliness of the NCNTs through spectral separation of the disordered and graphitic C. Due to the uncertainty in the decomposition, spectral fingerprinting was not completed on the disordered C; however, through direct analysis of the spectrum image, the disorder C resembles the amorphous C observed in Figure 3.3, but it could originate from a number of surface hydrocarbons. Figure 5.6 shows the spectral components identified for the C-K edge. Loading 1 was assigned to the disordered C in which the highest intensity is located on the outer walls of the NCNT. The exact cause is unknown, but potential sources include surface hydrocarbons from the production method,

surface contaminants from the Pd deposition, hydrocarbons from the TEM production method, and potential beam contamination. Lastly, the individual graphitic spectral components are removed as the σ^* and π^* peaks in loading 2 and loading 3, respectively. Through minor image processing, by overlapping loading 2 in Figure 5.5 and loading 1 in Figure 5.6, it can be shown that the Pd is located on the outside of the disordered C signal (Figure 5.6 (e)), thus the contamination likely originates from the NCNT production method.

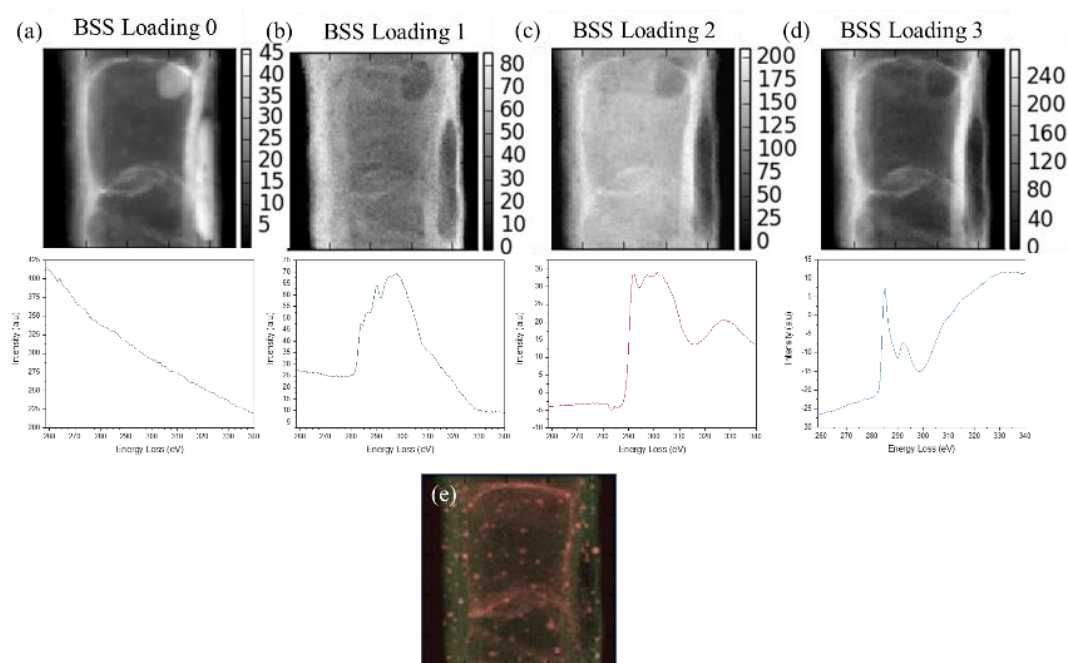


Figure 5.6 NCNT ICA C-K results showing different spectral components: (a) background, (b) disordered C, (c) graphite σ^* , and (d) graphite π^* peaks, respectively. (e) Overlapped images of loading 2 (red) from Figure 5.5 and (b) loading 1 (green).

To further investigate the graphitic N-K peak observed after the gas escaped from the nanotube, ICA was performed on the spectrum image from Figure 5.4 (c) as shown in Figure 5.7. A series of loadings were decomposed related to the background, amorphous C contamination, Pd nanoparticles, the C-K and N-K edges, disordered C oxide originating from surface hydrocarbons and/or beam contamination, and the graphene π^* and σ^* peaks,

respectively. Interestingly, the C-K edge fine structure in loading 3 (Figure 5.7 (d)) is different than the disordered C and graphene fine structure in loadings 1, 5 and 6. Based on factor 3, the N-K signal from loading 3 originates from the interior of the NCNT, wherein the tube walls are excluded from the measurement. This suggests that the walls of the NCNT do not contain substitutional N, or in other words are not N-doped; however, the presence of an N-KLL signal from Auger spectroscopy suggests the presence of substitutional N within the tube walls (N-doping), thus the concentration may be below the detection limit of EELS. Furthermore, it should be noted that the negative loading in the NCNT walls from loading 3 may suggest an issue with the decomposition, thus the substitutional N-doping cannot be ruled out. It is possible the N-K edge resembles substitutional N because it has doped the amorphous C created at the site of the hole, as suggested by Trasobares *et al.* [216]. Through observation of loading 3, it is also evident that the source of the signal arises from the hole and interior walls of the NCNT. The intensity observed at the hole may be present from the substitutional N-doping of the amorphous C, and the intensity at the walls may be from the incomplete release of the gas due to physisorption. Because only one hole was produced within these tubes, it is not possible to observe if the C-K signal is consistent among many samples, thus the fine structure of the C-K edge could be an artifact of the ICA decomposition. However, poor decompositions were obtained from other tubes, not shown herein, which relate the N₂ gas to a σ^* -like graphitic C-K peak, due to the location of the gas along the interior walls of the NCNT. Therefore, the C-K edge observed in loading 3 may in fact be a weak C-K edge σ^* peak. This is further supported by loading 6, wherein the strong σ^* peak arises with a weak N-K edge, thus point towards physisorption of the remaining gas within the NCNT after the hole formation.

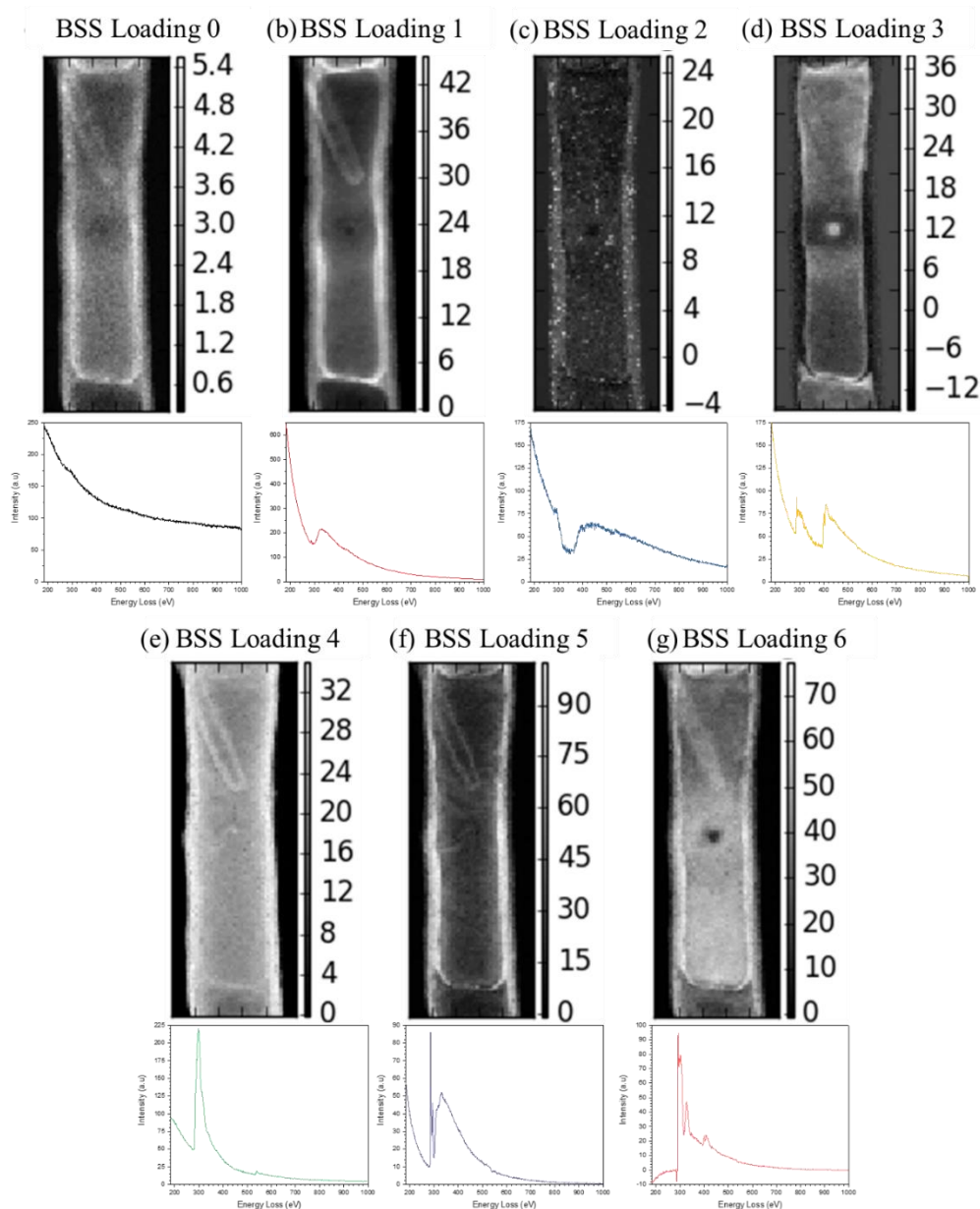


Figure 5.7 ICA results from Figure 5.4 (d) showing different spectral components: (a) background, (b) disordered C, (c) Pd-M edge, (d) C-K and N-K edge, (e) disordered C-K and O-K edge, and (f) C-K edge π^* peak and (g) σ^* peak, respectively.

Following experiments completed in literature for various materials containing gas bubbles [226], [227], [216] and N₂ filled CNTs, pressure quantification was performed on

the NCNTs. In the literature, a correlation has been observed between the radii of bubbles [226], [227], [228] and the pressure of the gas which is contained within them. Furthermore, the beam has been seen to affect the quantification process through interactions with the gas [216] and detrapping [229]. These effects will be discussed in context to the pressure quantification performed here, with a brief examination of potential beam effects on the quantification accuracy.

5.1.3 Pressure Quantification

In order to draw correlations between the diameter of the NCNTs, and the pressure of the gas within the NCNTs, quantification was performed following steps outlined in *Chapter 5.1.1.4 EELS Quantification and ICA Conditions*. The accumulated results can be observed in Figure 5.8. Experimentally, 18 tubes were analyzed in detail, in which 8 of 13 randomly selected NCNTs contained N₂ gas with an additional 5 NCNTs specifically selected for their gas containment. Quantification was performed on individual compartments for each NCNT (Figure 5.8 (a) and (b)), and as an average measurement for each individual tube using the compartments from Figure 5.8 (a) and (b) (Figure 5.8 (c)). Of the randomly selected 13 NCNTs, 3 individual NCNTs contained one empty and one gas filled compartment. In a single case, a hole was produced during the spectrum image acquisition, which caused the gas to escape, and in the other two cases, the signal to noise ratio was too low and it was questionable if the gas was present in the measurements. These two cases were excluded from the data analysis in Figure 5.8. Of the 5 empty NCNTs, there appeared to be no visible signs of damage in the ADF image after spectrum image acquisition that could have caused the release of the gas; however, this cannot be ruled out, as a low magnification was utilized (160 and 320 Kx), thus a small hole may go unnoticed in the ADF image. Furthermore, there are no physically significant features or similar diameters that relate the empty tubes to each other. Assuming the empty NCNTs did not undergo

damage during the signal acquisition, it can be suggested that it may be possible to produce a distribution of gas filled and empty tubes during the production method. This could be caused by the local environment during the growth process; however, the exact conditions cannot be known or predicted as the empty tubes do not contain any physical resemblances. Of the tubes that were empty, half contained an N-K edge with an average concentration of 7.4 ± 0.7 % (normalized to C and N), while the other half lacked an N-K edge. Interestingly, the N concentration measured by EELS is significantly higher than that measured by Auger spectroscopy (Table 5.1). Following data presented in *Appendix 1.1.2 Results and Discussion*, Auger spectroscopy is a better quantification tool to determine the concentration of N in graphitic C materials. This suggests that the NCNTs lacking an N-K edge either had a low N concentration (below the signal to noise ratio), or completely lacked N within the NCNT walls. Under these pretenses, no comment is made on the possibility of the tubes observed in Figure 5.4 being N-doped, as the NCNTs can be doped with varying concentrations.

It is suggested that for further investigation and understanding of the growth mechanism of these NCNTs, an *in situ* experiment with an environmental TEM (ETEM) or liquid-cell holder is performed, wherein the growth process with and without imidazole/acetonitrile is monitored. Literature has pointed to the use of ETEM to examine the growth mode for both single-walled CNTs (SWCNTs) and MWCNTs by replicating CVD growth conditions within the TEM [230], [231], [232]. In both references, elongation and a dynamic restructuring of the catalyst particles were observed before CNT growth commenced. Hofmann *et al.* [231] noted the incorporation of N during the growth of C nanofibers, but did not report if it appeared as a dopant or as a gas. Yoshida *et al.* [230] were interested in the state of the Fe catalyst during MWCNT growth, and they suggest three major findings: (1) the catalyst is in a solid state of fluctuating crystal structure during growth, (2) the Fe is in a carbide form during CNT growth, and (3) C undergoes volume diffusion through the Fe catalyst to form the CNT. Within the EELS maps observed with ICA (and from the raw data) in Figure 5.5 and Figure 5.6, C appears to be absent in the Fe

catalysts in our NCNTs. This suggests a different growth mechanism may be occurring during the spray pyrolysis, possibly due to the growth method itself, or the selected solvents used in the growth process. Using an ETEM or a liquid-cell, the growth mechanism of the ferrocene/imidazole/acetonitrile precursor can be determined. This is a rather difficult experiment due to the potential for the beam to interact with the solution. To further complicate the results, the ELNES of the acetonitrile and N₂ gas are very similar in shape and energy, thus the quantification of the development of the gas must be normalized to the acetonitrile background. In addition, the small confines of the liquid will limit the experiment to the flow of the precursors, rather than the droplet form found in the spray pyrolysis. In this case, the true experimental conditions will not be completely replicated but approximated, which could lead to different results than those obtained using spray pyrolysis.

Examination of the *ex situ* NCNTs leads to the production of various plots in Figure 5.8, describing the quantitative information derived from the NCNTs. Based on the various NCNTs examined, it was determined that the density of N atoms within a compartment of the NCNTs can vary from approximately 4 to 55 atoms/nm³ (2 to 27 molecules/nm³) (Figure 5.8 (a) and (c)). This agrees with literature which indicate an approximate density of 11 molecules/nm³ in an NCNT [216], and 40 to 72 atoms/nm³ within an SiO_xN_y nanobubble [227]. Using the ideal gas law at room temperature, a pressure ranging from 87 to 1123 atm (9 to 113 MPa) can be achieved within the gas filled NCNTs (Figure 5.8 (b)). The ideal gas law underestimates very high pressures through its assumed simplifications. Thus, using a calculated pressure-volume equation of state at 300 K for N₂ [233], the pressures in the NCNTs are approximately 150 atm to 14800 atm (approximately 15 MPa to greater than approximately 1.5 GPa). While these pressures are quite high, they are not outside of the realm of possibility, as the radial Young's modulus for a MWCNT is 30 GPa for external radii greater than 5 nm [234]. Within these pressures and at room temperature the N₂ is still in a fluid state according to the phase temperature diagram [235], [236], which agrees with the N₂ gas signal observed through the EELS fine structure.

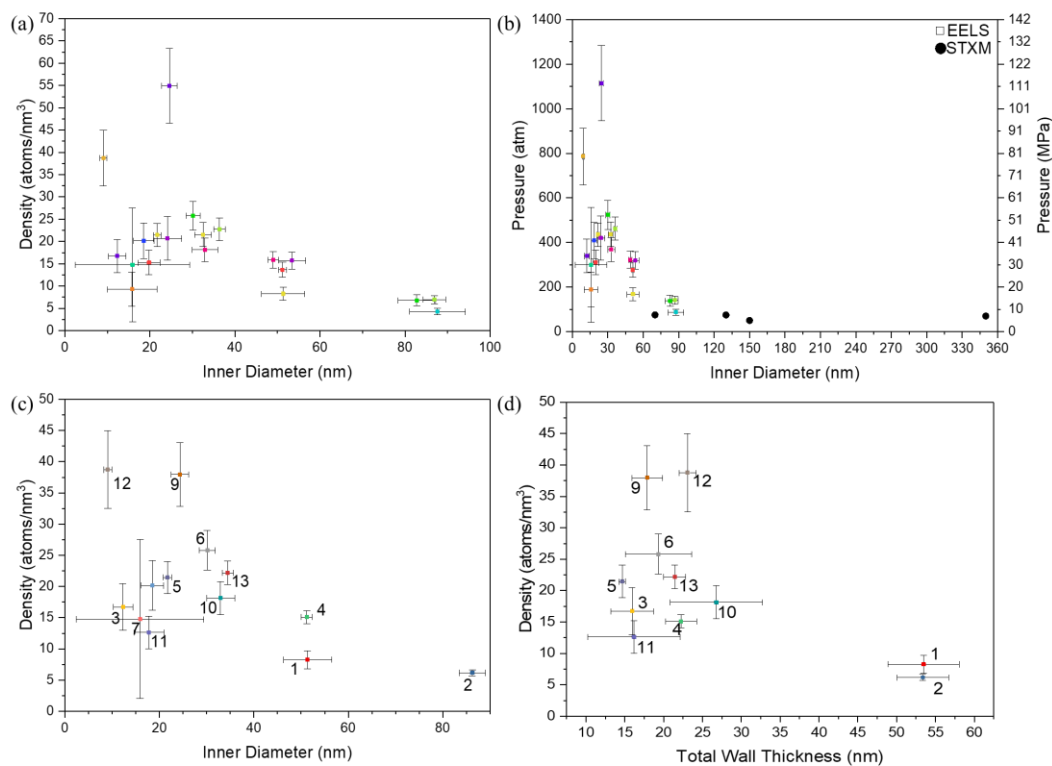


Figure 5.8 EELS N_2 gas quantification results. Quantitative analysis of (a) the density (atoms/nm³) and (b) pressure (atm and MPa) for each compartment within the NCNTs containing N_2 as a function of the NCNTs inner diameter. The average density (atoms/nm³) for each NCNT containing N_2 as a function of the NCNTs (c) inner diameter and (d) total wall thickness (considering the upper and lower wall of the 2D projection). The error bars shown for the density and pressure were acquired from the quantification routine in Digital Micrograph, and the error bars for the diameters were measured using the two-tailed one-sample Student's t-test with a probability of 0.05 from the measurements performed based on Figure 5.2. The numbers next to the data points in (c) and (d) correspond to the NCNT analyzed. Number 8 and 7 are missing from (d) as an accurate thickness measurement was not possible due to the high density of Pd obscuring the outer edge of the NCNT during the measurement process.

Notably, within Figure 5.8 a decrease in the density and pressure of the N_2 is observed with an increase in the inner diameter of the tube. To determine if the decrease

was legitimate, the N₂ pressure was quantified using STXM¹⁸, wherein a pressure of approximately 50 atm was quantified for a nanotube of 150 nm in outer diameter, and approximately 70 atm for nanotubes with outer diameters ranging from 75 nm to 350 nm. Furthermore, the stability of the gas was remarkable considering the initial experiments were performed in January 2015, and the STXM experiments were completed using the same TEM grid stored in atmosphere in May and September 2017. Based on the STXM data, the decrease in the pressure observed with an increase in the inner diameter is considered real; however, the variability in the data points from the EELS quantification indicate inconsistency and errors associated with the quantification method. While the error associated with the diameter measurement was discussed in *Chapter 5.1.1.4 EELS Quantification and ICA Conditions*, other errors likely occurred while collecting the EELS data. It was first thought that potential knock-on damage could result in the slow release of gas through a small puncture in the tubes that would not be visible in the ADF image. Under this assumption gas would release during acquisition, thus possibly reducing the pressure measured through the EELS quantification. To determine if this was an issue the N density was plotted as a function of the NCNTs wall thickness (Figure 5.8 (d)). The rate of knock-on damage has been calculated to increase in the center of the CNT, and would be more pronounced in NCNTs with thinner walls. Thus, if knock-on damage was affecting the quantification, it is expected that the thinner walls would have a lower N₂ density. Based on Figure 5.8 (d), there appears to be no correlation between the wall thickness and the density, thus knock-on damage is likely not the cause for the variability in the data. Other possible issues that may arise during the data acquisition include the electron beam interacting with the gas which could lead to local increases in pressure through Coulombic attraction with ionized gas [216], or local decreases in the pressure through detrapping due to specific experimental conditions [229]. Following David *et al.* [229], N density maps that are normalized to the maximum N density were produced and can be observed in

¹⁸ An acknowledgement to Dr. Adam Hitchcock and his student Juan Wu, for collecting the STXM data and performing the data processing and quantification.

Appendix 3: N-K EELS Maps Gas Filled NCNTs. Detrapping can be observed as a linearly decreasing gradient towards the bottom of the spectrum image (based on the beam scan direction) of the N density maps. For the maps obtained by the NCNTs, a relatively constant N density within the NCNTs was observed. An increase in the N density can be seen along the interior walls, thus indicating that detrapping was not an error associated with our experimental conditions, but the N₂ gas is likely experiencing physisorption on the walls of the NCNT. Moreover, the N density maps can be utilized to examine the Coulombic attractions of the gas to the electron beam. It is expected that if the gas was ionized and attracted to the beam, an increase in the gas density would be observed at the bottom of the N density map, as the ionized molecules would follow the electron beam scan from the top of the NCNT to the bottom. The relatively constant N density maps indicate the Coulombic attraction likely did not affect the quantification results. Issues may have been generated during the spectrum image acquisition from sample drift and the quantification process from the presence of Pd. Each NCNT underwent a different drift rate and direction based on the time allowed for stabilization and the alignment of the tube, respectively. Furthermore, the Pd-M edge, which overlaps the N-K edge, may have resulted in variability with the background subtraction for each NCNT, which could affect the final quantification. A multiple linear least square (MLLS) fit was considered for the Pd and N₂ gas; however, due to the small amount of Pd, it was determined that the MLLS fit could result in a larger error in the measurement. Thus, it is suggested that both the drift and Pd may have played a role in the variability of the observed data. In the future, for best quantification results, it is advisable to perform the N₂ quantification with NCNTs containing no catalysts or surface functionalization, and that sufficient time is provided between EELS measurements to allow the tubes to completely stabilize.

The trend of decreasing density with an increase in the inner diameter of the NCNTs observed in Figure 5.8 is not completely understood, but the mechanism can be hypothesized. Experiments by Reyes-Reyes *et al.* [217] suggested that the N₂ is produced within the NCNTs as a result of supersaturation within the Fe catalyst from the reactor

environment. Once the Fe is supersaturated, the N₂ will be released as the NCNT walls are forming, thus causing it to be captured within the interior walls of the NCNT. Therefore, as the inner diameter decreases, the growth time potentially increases, resulting in an increased concentration of N₂. This also agrees with Trasobares *et al.* [216] and Liu *et al.* [218], who proposed that the N₂ is a by-product of the chemical reactions occurring to produce the NCNT. As the C containing molecules are absorbed in the Fe catalyst and precipitate upon saturation, they react to form N₂ which is then captured in the newly formed NCNT walls. Alternatively, it can be theorized that if a constant concentration of N₂ is produced during the growth process, capturing it in a smaller volume (smaller diameter) could result in a higher density assuming the height of the bamboo structures are relatively constant (Figure 5.9). However, this hypothesis was proved incorrect when the density was plotted against the volume of the compartments and no correlation was observed. This suggests that the gas may continuously evolve, while the NCNT is growing. As previously mentioned, these are all hypotheses and would potentially require in-depth ETEM analysis for further understanding.

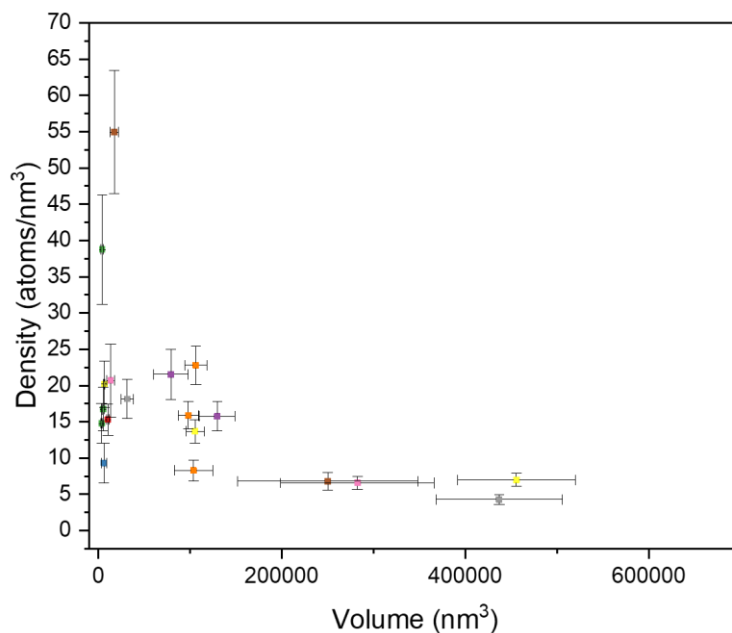


Figure 5.9 Quantitative analysis of the N density (atoms/nm³) for each compartment within the NCNTs containing N₂ as a function of the NCNTs' compartment volume. The error bars shown for the density and pressure were acquired from the quantification routine in Digital Micrograph, and the error bars for the volume were measured by the two-tailed one-sample Student's t-test with a probability of 0.05 from the measurements performed based on Figure 5.2. In cases in which only one measurement was made for the diameter and height of the NCNT compartment the error was determined through the uncertainty in the number of pixels in the measurement and the pixel size.

5.2 ALD Fine Tuning to Consistently Produce Single Atom Catalysts with NCNTs

As previously determined in *Chapter Three*, producing a range of particle sizes from single Pt atoms to nanoparticles when dealing with ALD on graphene substrates is most common. Ideally, we could better control the size of the Pt to ensure a more homogenous size when depositing on graphene substrates, which would allow us to truly determine the cause of

the enhanced activity observed for the materials containing a mix of single Pt atoms, Pt clusters, and nanoparticles.

A significant amount of research has been completed in literature to examine the effects of different ALD operating conditions on the size of the deposited material. A range of substrate materials from insulators [237], [178], metal oxides [238], [239], [240], [241], pure metals [179], [242], and C structures (C cloth [38], C aerogels [243], CNTs [167], [34], HOPG [244], graphene [245], [162], [138], and ozone treated graphene [177]) have been examined. From these experiments and calculations general trends have been observed concerning the effects of the experimental parameters on the ALD Pt deposition and growth. Generally, it has been agreed that the thickness of the Pt film or size of the nanoparticles can be controlled by the number of ALD cycles, in which a linear increase in size is observed with the number of cycles after an initial nucleation delay [238], [239], [244], [245]. Mackus *et al.* examined the effect of the ALD O₂ pulse based on duration and pressure [239]. They determined that prolonged exposures to O₂ encouraged Pt ripening, but interestingly resulted in an increased particle density [239]. This suggests that the O atom acts as a nucleation site for Pt deposition, upon which subsequent exposure to O₂ was observed to cause enhanced rates of Pt atom diffusion and agglomeration, causing the increased density and growth rate, respectively [239]. Setthapun *et al.* proposed the idea that the Pt precursor first reacts with available hydroxyl sites on metal oxide supports and only once there are few nucleation sites available will the Pt deposit on the previous nucleation Pt-O sites [240]. Through this mechanism, Pt metal is deposited after the first half reaction through the combustion of precursor ligands with the hydroxyl group [240]. Furthermore, they suggested that the Pt loading can be directly related to the surface area of the substrate [240]. This was corroborated using nanoparticles on C cloth, in which increased acid treatment time resulted in increased Pt nanoparticle density and loading [38]. Mackus *et al.* [179] and Kessels *et al.* [242] also examined the Pt growth from ALD on metal oxide supports and determined that Pt prefers to deposit at Pt-O sites through combustion, producing CO₂, H₂, and H₂O. Yan *et al.* similarly showed that Pd prefers to

bond to OH sites on graphene, wherein single Pd particles were stabilized on graphene nanosheets containing O functional groups [246]. When O sites are not available, Mackus *et al.* and Kessels *et al.* determined that the Pt will adsorb on the substrate, which results in a dehydrogenation reaction, and subsequently the production of H₂, CO, CH₄, and a carbonaceous layer over the Pt film that can only be removed with O₂ exposure [179], [242]. Meanwhile, Kim *et al.* showed that Ru films can readily adsorb on metallic surfaces without the presence of O containing groups [247]. Nevertheless, the differences in the nucleation and growth rate of the ALD deposited material on varying substrates illustrates the importance the substrate plays in the ALD process, and the complex nucleation and growth reactions occurring.

While growth is a major source of interest for many groups, as thin films are generally desired with ALD, nucleation has been studied to a lesser extent. Liang *et al.* examined the effect of precursor dosing time, and found that an increased dosing time resulted in an increased Pt particle size and loading, and a decreased dispersion [178]. Furthermore, deposition on HOPG illustrated that the Pt prefers to nucleate at edge locations, wherein Pt nanowires were formed at the HOPG edge and nucleation was not observed on the basal plane [244]. It was suggested by Lee *et al.* [244] that the edge sites are more chemically active due to the dangling bonds, thus they are easily oxidized during the O₂ exposure resulting in many preferred nucleation sites, as discussed in previous literature [179], [242]. This was also observed in *Chapter Three* with the N-doped graphene, wherein the Pt atoms and clusters were found preferentially located at edge sites; however, some Pt atoms were found on the basal plane, as suggested to be stable from point defects. This was also found by Kim *et al.* from CVD grown graphene, in which Pt nanoparticles and nanowires were observed to nucleate at point defects and grain boundaries in graphene, respectively [245]. Interestingly, they showed through DFT calculations that defects from the grain boundary resulted in a chemically reactive species from the induced strain, resulting in relaxation with Pt nucleation; suggesting that O adsorbents are not necessary for Pt nucleation [245].

Pt films or nanoparticles growth is commonly studied by examining the change in the Pt size, density, and loading with ALD cycles. Mackus *et al.* have made progress towards understanding the nucleation stage of ALD on oxide surfaces [248], [249]. They indicated that the nucleation stage is quite complex in the sense that it involves Pt diffusion and particle ripening [248], which are temperature and surface dependent [249]. Furthermore, the adsorption and desorption rate of the Pt precursor on the substrate must also be considered, which is also dependent on the temperature and the substrate [250]. Grillo *et al.* performed experimental and computational studies that showed that nanoparticle diffusion and coalescence is the main source of growth when considering thermal Pt growth with O₂ exposure [177]. They suggested that local heat and pressure from the subsequent combustion reactions between Pt and O results in the unpinning of the Pt nanoparticles, thus enabling their mobility [177]. Additionally, upon saturation of the nucleation sites, the growth process of the Pt catalyst can significantly modify the growth rate due to the presence of the catalyst, thus further complicating the understanding of the initial nucleation process [249]. During ALD, in an effort to minimize costs of the overall process, the temperature is generally selected to be as low as possible to obtain the desirable results [250]. It is commonly believed that as the temperature increases, the distribution of the particle size broadens, due to the increased average diffusion distance of the adatom and nanoparticles [208], [177], [37]. Some theorize that cases in which the Pt size distribution does not change with temperature may be caused by diffusion limitations from surface contamination, such as ligand decomposition rather than combustion, thus suggesting a surface controlled diffusion process [208]. In further consideration of cost, the quickest deposition time is selected without compromise of the desired outcome. Long Pt precursor deposition times have been found to lead to steric hindrance between the adsorbed precursor molecules, thus preventing Pt agglomeration and decreasing the growth rate [250].

In order to better understand the production of Pt atoms using ALD, the nucleation of the Pt precursor within the first ALD cycle was examined. Specifically, we investigated

the effects of the Pt dosing time, substrate deposition temperature, and the substrate material. For this study NCNTs and pristine CNTs (PCNTs) were used as the substrate. Examination was completed using HAADF imaging to analyze the particle size, and EELS to determine the quality of the NCNTs.

5.2.1 Experimental Conditions

5.2.1.1 Material Preparation

All samples were prepared by Dr. Sun's group at Western University. The NCNTs and ALD were produced in-house and the PCNTs were bought from MER Corporation© [251]. These NCNTs were prepared in a similar manner to ref. [218]; however, the ferrocene and imidazole were injected separately rather than as a single solution. Prior to ALD, the NCNTs and PCNTs were suspended in ethanol to produce a slurry that was then wiped on an Al foil plate to ensure the substrate material was not free when entering the ALD chamber, which can cause vacuum damage. The NCNTs and PCNTs were then exposed to various deposition conditions to examine the effect of dosing time (1 minute, 30 minutes, and 60 minutes), and temperature (100°C, 175°C, and 250°C). After ALD, the powder was removed from the Al foil using a razor blade.

5.2.1.2 HAADF Imaging

TEM samples were prepared by drop casting an ultrasonicated solution of dilute HPLC grade methanol solution with the sample of interest onto a lacey C grid. Generally, two samples were prepared, in which one was baked at 100°C overnight and the other was left to dry in air. Whenever possible the non-baked sample was used, and only in cases of high

beam contamination that prevented the ability to image the Pt atoms was the baked sample used for imaging. High resolution images were acquired using an FEI Titan 80-300 Cubed TEM. The aberration corrector was tuned to minimize spherical aberration in the probe forming lens and the acceleration voltage was set to 80 kV. STEM imaging was performed using HAADF (detector semi-angles of 63.8 mrad to 200 mrad, as measured by FEI) conditions with a C2 aperture of 50 μm . Varying exposure times were used for each given sample with a beam current of approximately 50 pA.

5.2.1.3 Image Quantification

To examine the effect of the ALD conditions on the Pt size, the acquired HAADF images required quantification. For each sample, the Pt size was examined for six individual CNTs. Selection of the CNTs was random based on size (diameter); however, CNTs that appeared to be the cleanest were preferred. Generally, the CNTs appeared to have a layer of residue surrounding them, which added background contrast, making the CNTs more difficult to image. Furthermore, some tubes were filled with either a liquid or gas (as to be discussed later) that would move when imaged and cause the tube to become more easily damaged. Therefore, to ensure better quality images, tubes that were highly covered in residue or seemed to be filled were avoided. Additionally, when possible, during quantification, images that showed signs of beam damage to the CNTs and/or beam contamination were avoided. Based on the nature of knock-on damage to CNTs [91], [252] and beam contamination issues when using solvents, it was not always possible to avoid these effects, as these images occasionally offered the best resolution, such that the Pt was in focus, thus in these cases the images were selected. For openness and clarity to the reader, all raw and

processed images used for quantification can be observed in *Appendix 4: Images Used for ALD Pt Quantification*.

The steps used for image quantification are as follows (quantification was performed on “tiff” image types). First, each HAADF image was calibrated using a MAG*I*CAL® reference standard from Electron Microscopy Sciences© (Figure 5.10 (a)). Second, ImageJ [253] was utilized to perform a background subtraction using the “subtract background” built-in function with the smoothing function enabled (Figure 5.10 (b) and (c)). Third, using the polygon selection tool and consulting the original image, the Pt atoms and particles that appeared to be in focus were manually encircled and deleted from the image (Figure 5.10 (d)). Fourth, the “Simple Math” built-in function in GATAN Digital Micrograph software was used to subtract the image with the deleted Pt particles (Figure 5.10 (d)) from the original background subtracted image (Figure 5.10 (c)) to produce an image wherein the particles were of varying greyscale and all other areas in the image were black (Figure 5.10 (e)). Fifth, the threshold of the subtracted image was adjusted using ImageJ to accept all grey levels except pure black (background) (Figure 5.10 (f)).

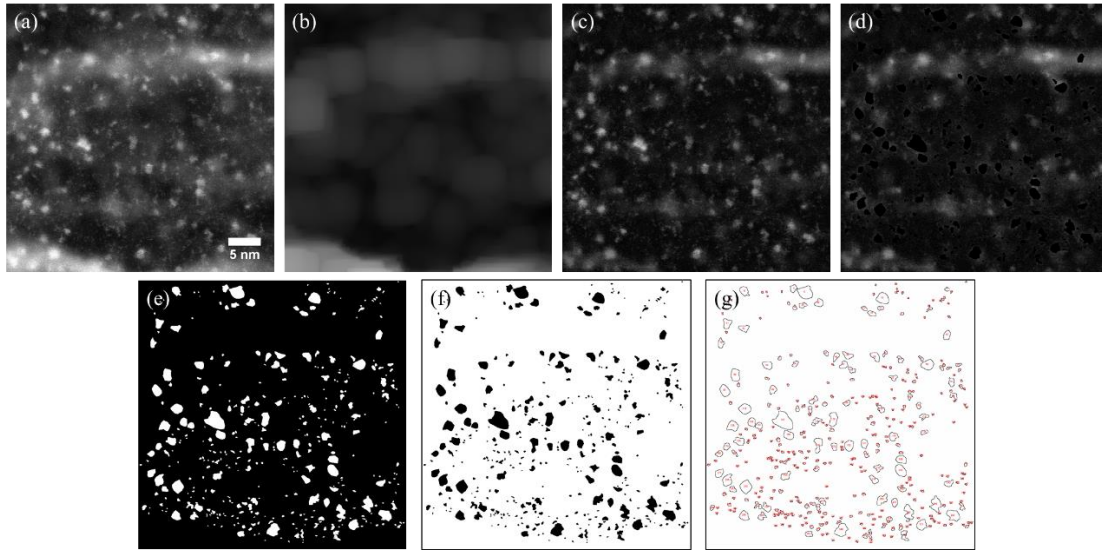


Figure 5.10 Experimental steps used for the quantification of the Pt equivalent diameter. 60 minute Pt dosing time at 250°C (a) calibrated raw HAADF image (“tiff” image type was used). ImageJ was used to subtract the (b) background from (a), thus forming the (c) background subtracted image. Pt was then (d) manually removed using the polygon selection tool in ImageJ. Digital Micrograph software was used to subtract image (d) from (c) to produce image (e), wherein the (f) threshold was adjusted, and the image was (g) analyzed with ImageJ.

The particles from Figure 5.10 (f) were then analyzed in ImageJ using the “Analyze Particles” function with the particles on the edge excluded. Specifically, the “Analyze Particles” function was used to determine the area of each individual particle, the number of particles, and the total area of the particles (Figure 5.10 (g)). Prior to constructing the histograms shown in *Chapter 5.2.3 Effect of ALD Conditions*, the measurements were analyzed and particles of one-pixel area were removed, which likely originated from noise in the image. ImageJ provided a value of the area (A) measured for each particle based on the number of pixels encircled per particle and the calibrated scale. This value was then converted into an equivalent diameter (d_{eq}) by assuming the Pt particles have a spherical shape or a circular shape when projected in the two-dimensional image $\left(d_{eq} = 2 \times \sqrt{\frac{A}{\pi}}\right)$.

5.2.1.4 Error Analysis and Histogram Formation

Errors were introduced into the measurements through intrinsic mechanisms related to the image collection process from STEM and from manual error during data processing. According to Browning *et al.* the resolution of STEM images can be affected by the object under investigation, the probe size, vibrations experienced at the sample and from the scanning coils, and the image being out of focus [254]. Other effects may also include sample drift, atom movement from beam excitation, and beam damage. Following error analysis completed for manual measurements of biological samples [255] and after discussion with group/department members¹⁹, an error analysis was completed using a single image in which the Pt size was measured on five separate days. This information was used to determine the binning width and the error associated with each bin. The image was selected based on its magnification and particle size range. The images analyzed in this report most commonly had a magnification of 1.8 Mx or 2.55 Mx (with exception of one image with a magnification of 1.3 Mx and two images with a magnification of 3.6 Mx). The selected image for the error analysis was acquired at 1.8 Mx, which would be more susceptible to error based on the image resolution. Furthermore, the selected image had the broadest range of particle sizes based on the original data analysis, thus allowing the error characterization over more Pt sizes. After performing the image quantification process described in Figure 5.10 for the same image on five separate days, the total error and intra-observer error was then estimated.

The data was compiled for the five days, and a histogram was created wherein each bin represents as a single pixel, and the counts per bin were acquired based on the number of pixels measured in each particle. The bins were then summed over the five days to compile the total number of counts for each bin into a single histogram, as shown in Figure

¹⁹ Thank you to PhD students in Dr. Botton's group, Isobel Bicket and Alexandre Pofelski, and Mukesh Sharma (PhD student in Material Science and Engineering department) for discussion on methods of performing error analysis.

5.11 (a). Two peaks were observed in a low and high pixel number regime (Figure 5.11 (a)), at approximately 25 and 650 pixels, respectively. The error associated with Pt particles containing a lower number of pixels will be greater, as the deviation of one pixel will have a greater effect on the total area of the Pt particle examined. Following this rationale, a Gaussian fit was performed on the peak in the low pixel number regime from 0 to 174 pixels using OriginPro software (Figure 5.11 (b)). While the model did not entirely fit the data, likely due to the high noise, the FWHM (w) was used to estimate the total error of the measurement. Therefore, with a w equal to 20 pixels, the error equates to an area of 0.032 nm² (image calibration of 24.8412 pixels/nm) and an equivalent diameter of 0.20 nm.

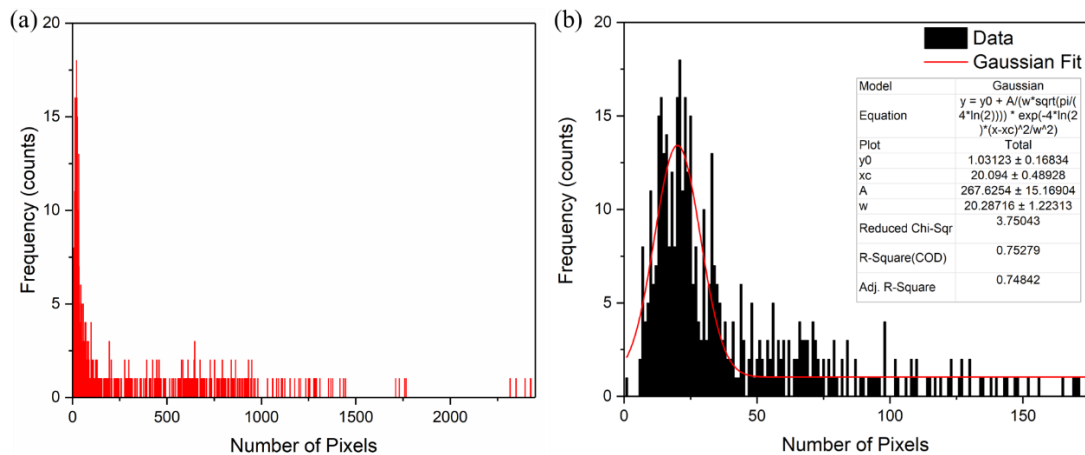


Figure 5.11 Error analysis for the Pt quantification process. Histogram showing the (a) total counts for the Pt entities as a function of the number of pixels, summed from five days of data analysis on a single image. (b) Fitted Gaussian model and parameters from the low range peak in (a).

Using the error as the bin width, the data collected over the five days is presented in Figure 5.12 (a) as individual components, and (b) as the mean value per bin with the error bars calculated by the standard deviation for each bin. These error bars represent the error introduced by the manual measurement (intra-observer error) and are individually calculated for each bin. The data presented in the remaining histograms has been

normalized to the total number of Pt particles for each individual CNT, such that over a single measurement the frequency of all bins sums to 1.

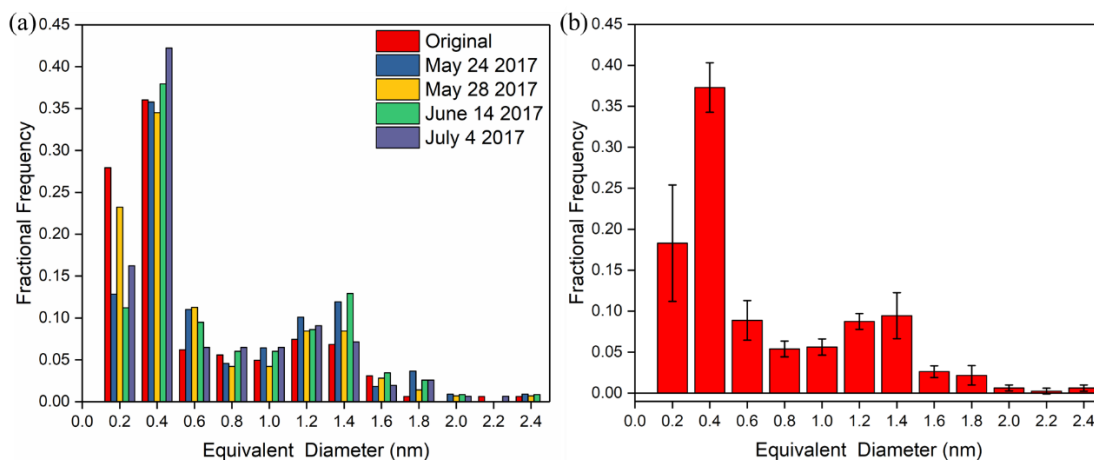


Figure 5.12 Error analysis results from five days of study on a single HAADF image with bins showing the experimental error. Data analysis from a single image showing (a) each individual analysis over five days and (b) the mean and standard deviation for each bin from the five days of measurement. The errors in (b) represent the error introduced into the measurement from the manual process.

Following the error analysis, all histograms were produced with a bin width of 0.2 nm. The histograms were constructed by examining the size of the Pt entities on six different tubes, in which a minimum of 59 atoms were counted per nanotube. If a single image did not contain 59 atoms, multiple images of the same tube were analyzed from different areas along the tube (see Table 5.2 for details). It should be noted that in a single location, only one side of the tube was examined to limit the electron exposure to the CNT and hence decrease the possible beam damage. In some cases, out of curiosity, both sides of the tubes were imaged, and it was found that a higher loading was preferentially deposited on one side of the tube. This was not further examined for the extent of this report, but could be a future area of research, possibly using electron tomography to get a better representation of the Pt homogeneity on a single tube. The individual density of Pt varied between the CNTs within the same sample. Individual CNT, histograms showing

the frequency of the equivalent diameter between the individual CNTs under the same experimental conditions can be observed in *Appendix 5: Individual Histograms from Each Tube Analyzed in Appendix 4*. The histograms are presented in frequency, rather than fractional frequency, to provide the reader with the number of Pt entities analyzed per CNT. The numbers located on top of the bins in the histograms are the standard deviations that are greater than the standard deviation related to the error in the measurements (Figure 5.12), thus indicating the variability between the Pt size on different CNTs within the same preparation conditions. The exact cause for the difference in the histograms from the same batch cannot be completely known; however, it is possible it is due to local variabilities in the Pt density, which could be affected by the local binding locations, and the CNTs potential location in the ALD chamber during deposition. This indicates that, while ALD can produce ultra-small clusters and atoms, variability will still exist within a single sample batch. The histograms produced in the remainder of this chapter are produced from the summed counts of all the CNTs presented in *Appendix 5: Individual Histograms from Each Tube Analyzed in Appendix 4* and are represented in fractional frequency to account for the normalization to the number of Pt entities analyzed per sample preparation conditions. A secondary method of normalization is presented in *Appendix 5: Individual Histograms from Each Tube Analyzed in Appendix 4*, wherein the fractional frequency has been normalized to each CNT analyzed per sample. Generally, the high frequency bins have been observed to have a similar fractional frequency to those normalized by the overall number of Pt entities per sample preparation technique. A maximum of 9.7% difference of the two measurement techniques is observed for the high frequency bins. The exact fractional frequencies for each normalization method can be found in *Appendix 5: Individual Histograms from Each Tube Analyzed in Appendix 4*.

Table 5.2 Number of images analyzed, and the number of Pt entities counted per image.

Time (min)	Temp (°C)/Substrate	Number of Images Analyzed	Number of Pt Entities
1	250/NCNT	12	1034
	250/PCNT	15	613
	175/NCNT	8	825
	100/NCNT	10	934
30	250/NCNT	6	3534
	250/PCNT	11	863
	100/NCNT	9	927
60	250/NCNT	6	2490

Using the threshold images produced from the quantification routine, the density of the Pt was measured. In order to perform the measurement, it was necessary to have the Pt in focus across the entire area examined. Due to the curvature of CNTs, the area under examination cannot be easily measured. Therefore, images from the center most region of the tubes (one quarter of the inner diameter of the tube) were analyzed. These values should be considered strictly approximations, as not all tubes could be analyzed, due to the fact that some images were acquired at the edge on the CNT. In cases in which the edge of the tubes could not be seen in the image, it was assumed that the image was centered on the CNT, and those images were used in the density quantification. All errors presented in density measurements were acquired from the two-tailed one-sample Student's t-test with a probability of 0.05.

5.2.1.5 EELS Analysis

Using the Titan 80-300 Cubed, EELS spectra were acquired to examine the quality of the NCNTs. EELS spectra were acquired in EFSTEM mode with a dispersion of 0.4 eV/pixel and a convergence and collection semi-angle of 19 mrad and 58 mrad (as measured by FEI), respectively. Relatively fast acquisition times are preferred to decrease the amount of sample drift and beam interaction with the Pt atoms. The Pt spectrum image was

acquired using an exposure time of 0.1 s/pixel. The C-K and N-K edges were acquired with an exposure time of 0.05 s/pix and 0.01 s/pix. The spectra in each C-K spectrum image were aligned and calibrated in energy using the C-K π^* (285 eV) peak.

5.2.1.6 Auger Analysis

Auger spectroscopy was also utilized to quantify the elemental content in the NCNTs. The spectroscopy was completed using a JEOL JAMP-9500F field emission-Auger microprobe with an energy of 10 kV, a current of 40 nA, a tilt of 30°, and M4 mode. The reported values from the quantification were normalized with respect to the total elemental content; however, beam contamination was an issue, therefore the concentrations of all elements with exception to C may be slightly underestimated. Quantification was completed using an in-house HOPG standard from a freshly cleaved surface, and Cr₂N, SiO₂, NaCl, ZnS, CaF₂ JEOL supplied standards for the C-KLL, N-KLL, O-KLL, Cl-LVV, S-LLV, Ca-LMM Auger electrons, respectively. The values reported are averages acquired from a minimum of nine measurements on NCNT bundles. The sample was prepared by drop casting suspended samples in HPLC methanol onto an SiO₂ wafer with a Au sputter coated surface.

5.2.2 Elemental Quantification and Examination of NCNTs

Using Auger spectroscopy, the surface of the NCNTs were examined for their elemental content, as this would dictate the potential available surface sites for Pt adsorption. Table 5.3 indicated that the N content of these tubes was 3.2 ± 0.4 at. %²⁰ and the O content was

²⁰ Sample errors were calculated using the two-tailed one-sample Student's t-test with a probability of 0.05.

approximately 5.4 ± 0.7 at. %. Trace amounts of contaminants (Cl and S) were found on the NCNTs during a full spectrum acquisition; however, the elemental concentration was low, therefore these trace elements are expected to have little effect on the surface sites of the NCNTs. The O content may be originating from a few potential sources: hydrocarbon contamination, and O or N-oxide adsorbents. Through a separate examination on the Au substrate without NCNTs, the contamination caused by the methanol solvent and beam contamination is evident by the 30 at. % C content, suggesting that the values acquired from the NCNTs were also affected by the C contamination, which could lead to the underestimation of the doping levels. In an effort to examine the effect of the C contamination, after all measurements were completed, the sample was exposed to a 3 kV Ar^+ beam at 30 nA for 20 s to remove the surface contamination. When comparing the Au substrate before and after sputtering, it is apparent that the Ar^+ cleaned the surface, resulting in a C concentration of 5.9 at. % after sputtering. A single area on the NCNT was then compared before and after sputtering (Table 5.3) to see if it greatly affected the N concentration. Surprisingly the N concentration decreased after sputtering. While the reason for this phenomenon is not known, it can be postulated that the tube under examination was gas filled, and upon Ar^+ exposure was damaged and released the gas thus decreasing the overall N content. The decrease in the N signal after Ar^+ exposure could also indicate that the N is contained in a C contamination layer and was removed with cleaning, or the Ar^+ preferentially etched the N-dopants versus the C sites. Conversely, a decrease in the O content was expected due to the fact that the sputtering would remove the surface hydrocarbons. Lastly, Au was found on the NCNT after sputtering, which can be attributed to re-deposition from the Au surface after the sputtering process. Based on these results sputtering is not recommended for NCNT quantification, due to the drastic decrease in the N concentration and the contamination caused by the re-deposition of the substrate material on the sample of interest.

Table 5.3 Auger Spectroscopy elemental quantification of NCNTs. Reported at. % were acquired from the average value of nine measurements with the error calculated using the two-tailed one-sample Student's t-test with a probability of 0.05. Measurements without an error were acquired from a single measurement.

C (%)	N (%)	O (%)	Cl (%)	S (%)	Au (%)
NCNT Before Pt Deposition					
90.0 ± 1.5	3.2 ± 0.4	5.4 ± 0.7	0.8 ± 0.6	0.51 ± 0.19	0
Au Substrate without NCNT					
30	0	3.9	0	0	66
Au Substrate After Ar⁺ Sputtering without NCNT					
5.9	0	1.4	0	0	92.8
NCNT Area 9 Before Ar⁺ Sputtering					
89	2.8	5.6	1.5	0.7	0
NCNT Area 9 After Ar⁺ Sputtering					
91	1.2	1.8	0.7	0.4	4.4

EELS was also used to examine the quality of the NCNTs before Pt deposition. Based on the ADF image in Figure 5.13 (a), bright spots can be seen covering the NCNT and lacey C support. A spectrum was collected through the summed spectra in the ROI (red box) over the bright areas in Figure 5.13 (a), in which a C, Ca, and O peak can be assigned (Figure 5.13 (b)). Through fingerprinting the ELNES structure, the Ca containing contamination is likely calcium carbonate [256]. Using the Ca-L edge, the location of the signal was mapped in the spectrum image (Figure 5.13 (c) acquired from the green box in (a)), wherein the Ca can be seen covering the NCNT and acting as the bright contrast observed on the lacey C grid. Furthermore, polymer-like material, which was highly beam sensitive was also apparent in high quantities on this sample. The source of the Ca and the C contamination is unknown. These bright spots remain on the TEM grid for the Pt deposited samples, but to a lesser extent, and a weaker Ca edge (if at all) can be found on the grids after Pt deposition. Through further investigation, it is possible that the Ca source and C contamination may have originated during the TEM sample preparation, as a quick HAADF investigation of a newly prepared sample showed cleaner NCNTs. Auger results from the newly prepared sample showed lower N content and higher O content than Table 5.3, likely due to the fact that the Si substrate was collected in the signal. More importantly,

a Ca source of 0.54 ± 0.14 at. % was found, thus indicating that some Ca was located on the NCNTs, but Cl and S were not observed on these samples. Hence, the NCNTs likely contain an approximate N content of 3 at. % with trace amounts of Ca, Cl, and S.

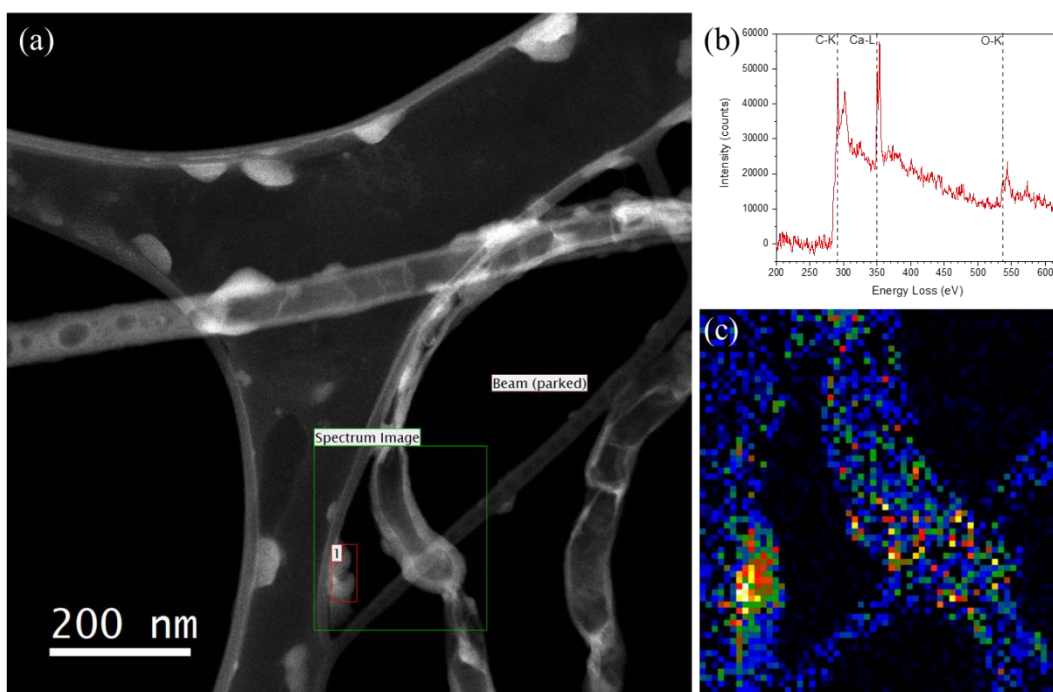


Figure 5.13 EELS analysis of NCNT before Pt deposition. (a) ADF image of a NCNT before Pt deposition. The red box in (a) was the ROI in which spectrum (b) was extracted, showing a material containing a C-K, Ca-L, and an O-K edge. Using the spectrum image from the green box in (a), the Ca-L edge was mapped in (c).

Multiple NCNTs were further examined after Pt deposition using a dosing time of 30 minutes and a temperature of 250°C. Under these conditions, different elemental compositions were observed through ELNES examinations. First, some NCNTs were observed to have a bright intensity region located on the interior of the tube (Figure 5.14 (a)). Upon imaging, it was found that the substance moved when exposed to the beam (Figure 5.14 (b)) and caused the NCNT to become easily damaged by the rapid creation of a hole. Through EELS analysis, a C-K edge resembling graphite and a strong O-K was

observed (Figure 5.14 (e)). As expected, mapping the C-K edge resulted in the signal originating from the NCNT structure (Figure 5.14 (c)), but the O-K edge was clearly located within the compartments of the NCNT (Figure 5.14 (d)). The source of this O is unknown, as a Ca-L edge is not present in the spectrum (Figure 5.14 (e)), as previously observed in Figure 5.13 (b). Based on the high intensity in the ADF image, and movement when exposed to the electron beam, it is expected that the substance within the tube is quite dense, thus it is likely a liquid.

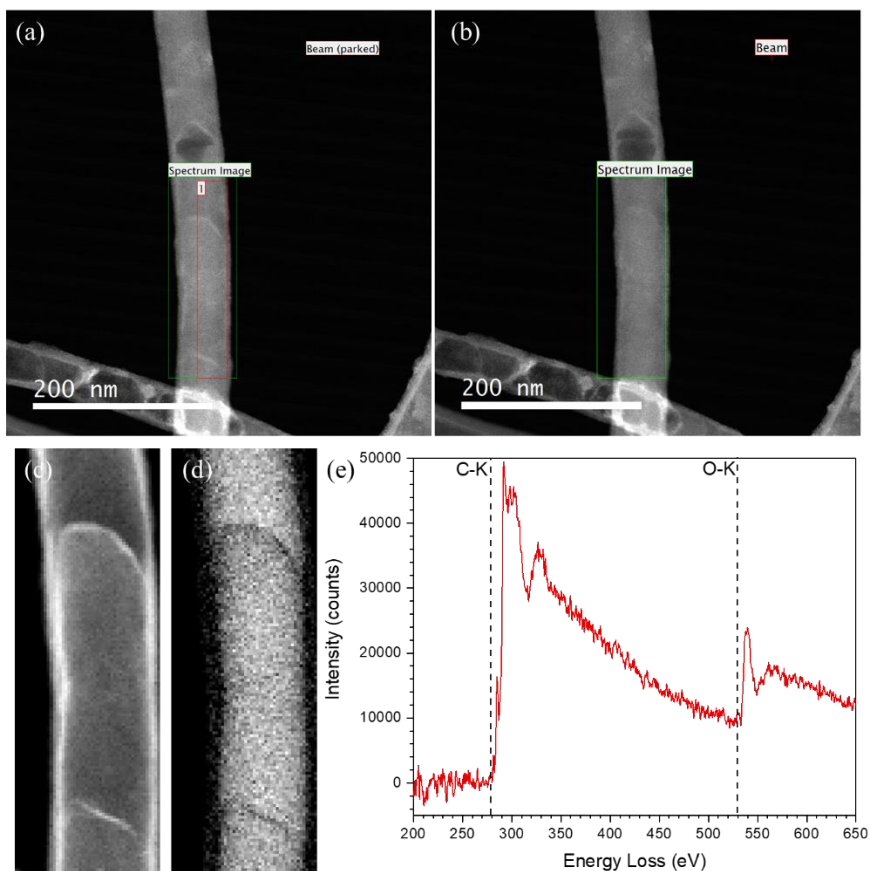


Figure 5.14 EELS analysis of Pt deposited on NCNTs for 30 minutes at a temperature of 250°C. Three NCNTs were analyzed with EELS. The first NCNT contained a bright intensity region in the ADF image (a) before and (b) after the EELS acquisition. From the first NCNT the (c) C-K and (d) O-K edges were mapped from the (e) summed spectra from the region of interest (red box) in (a).

A second and third NCNT were analyzed with EELS, each having a unique chemical distribution that can be observed in Figure 5.15. A tube containing N₂ gas (Figure 5.15 (a) and (b)) was found in this batch of samples; however, on a qualitative basis, the frequency with which the tubes are gas-filled was less frequently observed than in *Chapter 5.1 Gas Filled NCNTs with ALD Pd*. It was more common to find tubes with the bright contrast observed in Figure 5.14, as seen in the NCNT in the bottom left corner of Figure 5.15 (a). Additionally, the third NCNT was found to be composed of C, Ca, N, and O (Figure 5.15 (c) and (d)). The Ca source is likely originating from the Ca carbonate observed on the as-made NCNTs. Correlation of the Pt (bright spots in the ADF image) with the N and Ca is difficult as the Pt is mobile under the electron beam; however, based on image simulations (*Appendix 6: STEM Image Simulation*), it is expected that the Ca would not appear as bright as the Pt in the ADF image, thus its contrast should blend into the C background for both thick and thin regions. It is possible that the Pt is sitting on a Ca site, since the Ca carbonate was found on the NCNT sample prior to Pt deposition, and EELS maps correlate the location of Ca with the bright intensity of the Pt in the ADF image. This suggests that at 250°C, the Ca carbonate is still present on the NCNT, thus in the future the samples should be cleaned by heating the NCNTs to a higher temperature.

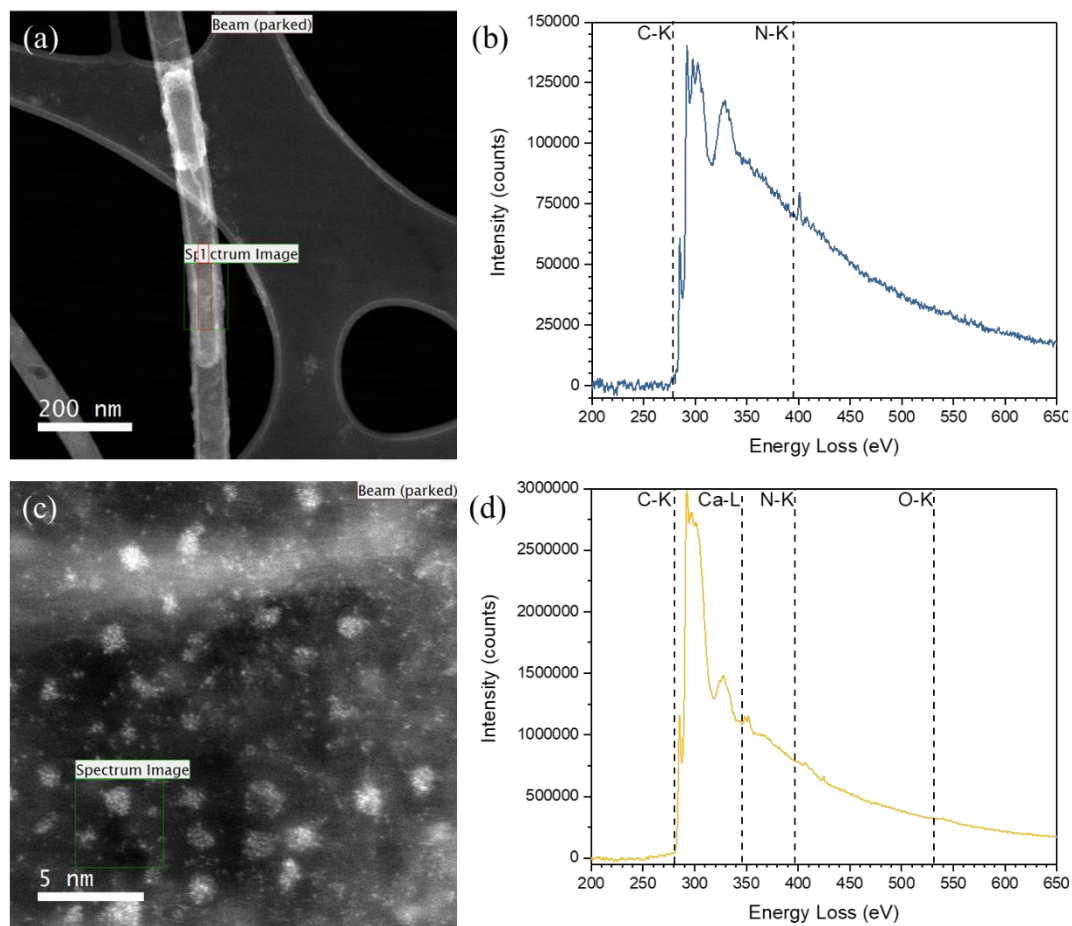


Figure 5.15 Second and third, EELS analysis of Pt deposited on NCNTs for 30 minutes at a temperature of 250°C. The (a) ADF image of the second NCNT shows N₂ gas in the (b) summed spectra acquired from the center of the NCNT marked by the red box in (a). Lastly, the (c) ADF image of the third NCNT contains C, Ca, N, and O, as determined by the (d) summed spectra from the entire spectrum image in (c).

Low magnification ADF images and EELS maps were acquired for Pt deposited with a deposition time of 60 minutes and a temperature of 250°C (Figure 5.16). Within the ADF image (Figure 5.16 (a) and (b)) large bright particles were observed on the interior of the tubes, and two low contrast less defined particles were observed on either side of the tube located below the other particles. Using EELS spectrum imaging, elemental maps (Figure 5.16 (c)-(e)) were acquired from the ROI in Figure 5.16 (a). It was determined that the bright particles are Fe oxide (Figure 5.16 (d) and (e)), which likely originate from the

catalyst used for the NCNT growth, as observed in *Chapter 5.1 Gas Filled NCNTs with ALD Pd*. Furthermore, the other particles can be identified as the Ca oxide observed on the NCNTs (Figure 5.16 (c) and (d)). Interestingly, the Fe that is contained within the NCNT is oxidized, which is in contrast to the Fe particle found in Figure 5.5. Based on the contrast in the ADF image of the NCNT, it is possible that it is storing the O containing liquid observed in Figure 5.14, which may have caused the Fe to oxidize. Because the larger particles in these low magnification images were determined to be growth catalysts and contaminants, during image quantification low magnification images were excluded, such that only the Pt atoms and particles were examined.

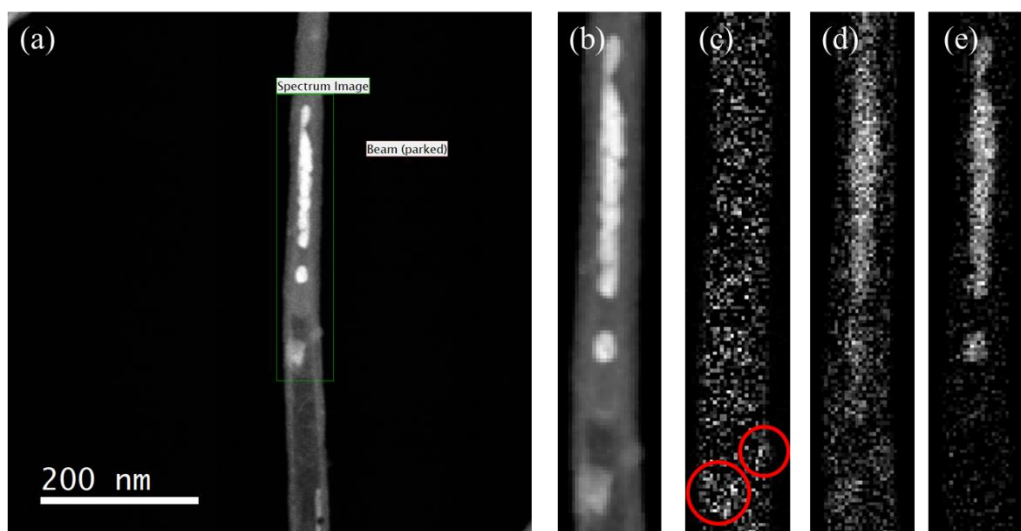


Figure 5.16 EELS analysis of Pt deposited on NCNTs for 60 minutes at a temperature of 250°C. (a) ADF image of the NCNT. The (b) DF image can be used to examine the presence of the large nanoparticles from the ROI in (a) using extracted EELS maps of (c) Ca-L (red circles highlighting areas of higher density above the noise), (d) O-K, and (e) Fe-L edges, respectively.

Examination of high magnification ADF images acquired in GATAN Digital Micrograph (Figure 5.17 (a) and (b)) shows many bright spots decorating the NCNT. It is expected through the z-contrast imaging, that the bright spots are related to Pt. For confirmation, EELS was used to determine the origin of the bright spots. Through

inspection of the ADF image (Figure 5.17 (c)) and the spectrum image (Figure 5.17 (d)) a Pt-M edge at 2122 eV (Figure 5.17 (e)) is evident from the ROI over the bright region found in the ADF image, thus confirming that the origin of the bright spots in the HAADF images used for quantification are the ALD deposited Pt catalysts. The beam effects on the Pt atoms are observed when comparing the ROI (green box) in the ADF image before (Figure 5.17 (a)) and after (Figure 5.17 (b)) the EELS acquisition. Due to beam excitation, the atoms tend to migrate on the surface of the NCNT, thus acting as a source of error on the size of the Pt atoms (as mentioned in *Chapter 5.2.1.4 Error Analysis and Histogram Formation*). Using the high magnifications mentioned in the experimental conditions of this chapter, the following section will examine the Pt quantification and the effects of the different deposition conditions on the Pt size and density.

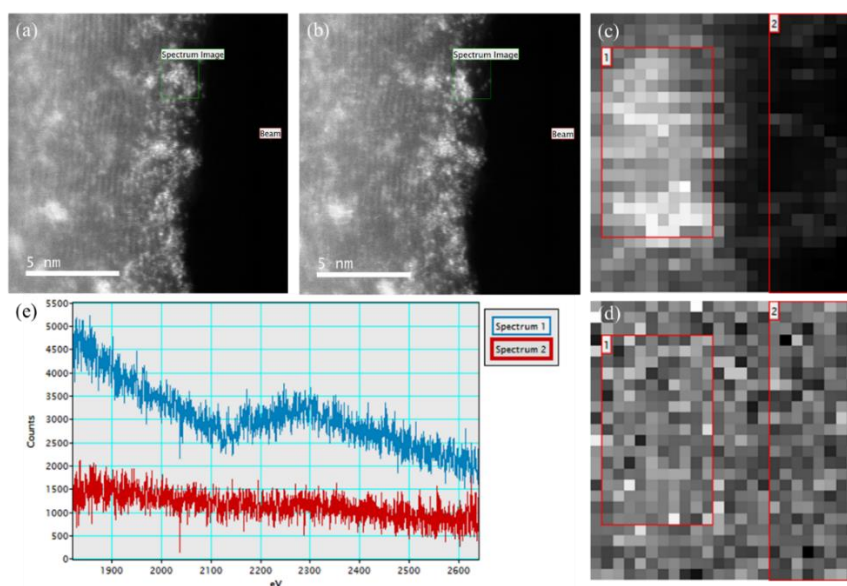


Figure 5.17 High energy EELS analysis of Pt deposited on NCNTs for 60 minutes at a temperature of 250°C was imaged using ADF (a) before and (b) after the EELS acquisition. The (c) ADF image corresponding to the (d) spectrum image shows that the bright spots correlate to a Pt-L edge, as shown in the (e) extracted spectra from the areas outlined in (c) and (d).

5.2.3 Effect of ALD Conditions

Ideally, homogenous single Pt atoms could be produced on any substrate using the ALD deposition technique. Experience working with ALD has led to the belief that a better understanding of the deposition parameters is required to ensure homogenous Pt deposition is possible, such that single atoms and nanoparticles do not exist simultaneously. In reality, due to the difference in substrates and potential inhomogeneity of a single substrate powder, it is expected that the ALD may not be able to produce solely single Pt atoms; thus, we strive to understand how the deposition parameters affect the particle size distribution (PSD) and particle density on real substrate materials. Table 5.4 illustrates the Pt density from the various experiments performed and the following chapters show collected histograms to understand the effects on the first ALD cycle (Pt precursor). The individual effects of the dosing time, temperature, and substrate will be examined in the section below with reference to Table 5.4.

Table 5.4 Average measurement values from various deposition parameters of the first ALD cycle for Pt on NCNTs and PCNTs are shown with the error calculated using the two-tailed one-sample Student's t-test with a probability of 0.05. The density measurements were measured by counts and area, which refer to the number of Pt atoms and the area of Pt atoms as measured from the center of the NCNTs during image analysis, respectively.

Time (mins)	Temp (°C)	Number of CNT Measured for the Density	Density	
			Counts/nm ²	Area/nm ²
1	250	3	0.08 ± 0.09	0.0121 ± 0.0005
		3	0.05 ± 0.07 (PCNT)	0.012 ± 0.012 (PCNT)
	175	0.09 ± 0.05	0.005 ± 0.001	
	100	0.08 ± 0.11	0.0062 ± 0.0024	
30	250	6	0.44 ± 0.25	0.05 ± 0.03
		2	0.19 ± 0.04 (PCNT)	0.05 ± 0.18 (PCNT)
	100	0.13 ± 0.18	0.015 ± 0.008	
60	250	4	0.3 ± 0.4	0.074 ± 0.028

5.2.3.1 Effect of Dosing Time

The first cycle in the ALD procedure is the introduction of the Pt precursor into the reaction chamber. To understand the effect of the dosing time, NCNTs were exposed to the precursor for 1 minute (Figure 5.18 (a)), 30 minutes (Figure 5.18 (b)), and 60 minutes (Figure 5.18 (c)) when held at a temperature of 250°C. Through image processing and analysis of the HAADF images, PSDs (Figure 5.18 (d)) were constructed using the six NCNTs examined for each sample. Figure 5.18 demonstrates that as the dosing time increased, the distribution of the particle size increased, leading to the eventual production of Pt atoms mixed with clusters and nanoparticles after 30 minutes of exposure. Interestingly, after 1 minute of dosing, mostly single atoms and small clusters were

observed; however, large clusters and nanoparticles of 1 nm were formed for the longer dosing times, with a single nanoparticle arising in the 2.8 nm bin for the 1 minute exposure. It was also determined from the PSDs that the distribution of the equivalent diameters increased as the dosing time increased, due to agglomeration of Pt. This agrees with Liang *et al.*, who also observed an increase in Pt particle size with an increased Pt dosing time [178]. The trend in particle growth is clearly evident when comparing the dosing time PSD histograms. As the time increased the fractional frequency within the bins corresponding to atoms and small clusters (0.2 and 0.4 nm) began to decrease and shift to larger clusters and nanoparticles, resulting in the broadening of the PSDs for the increased dosing times (Figure 5.18 (d)). Remarkably, nanoparticles were able to form without an O₂ exposure. This suggests that the Pt precursor is undergoing ligand decomposition; otherwise, steric hindrance from the ligands on the MeCpPtMe₃ precursor would prevent the formation of nanoparticles. This decomposition could potentially occur from the dehydrogenation reaction found by Mackus *et al.* [179] and Kessels *et al.* [242]. This requires further investigation, as the production of the surface carbonaceous layer produced through the dehydrogenation reaction would be detrimental for catalysis reactions, and may suggest the need for a final O₂ exposure to remove the carbon layer. Furthermore, as evidenced in the HAADF images, the density of Pt also increased with dosing time; however, careful inspection of the individual densities can provide significant details concerning the nucleation of the Pt on the NCNTs (Table 5.4). When comparing both the counts/nm² and area/nm² between the 1 minute and 30 minute samples, it is apparent that each density measurement increased with dosing time. This suggests that as the dosing time increased, more nucleation sites were formed, while former Pt sites grew in size, respectively. As the dosing time was increased to 60 minutes, the counts/nm² slightly decreased while the area/nm² increased. This suggests that after 30 minutes, or even potentially before 30 minutes of deposition, the nucleation sites were fully saturated, and the remaining Pt deposition resulted in growth. This growth may have occurred through multiple venues, as outlined by Grillo *et al.*, such as atom diffusion and deposition, nanoparticle coalescence,

and Ostwald ripening [177]; however, the true nature cannot be known without detailed calculations on similar substrates to the NCNTs.

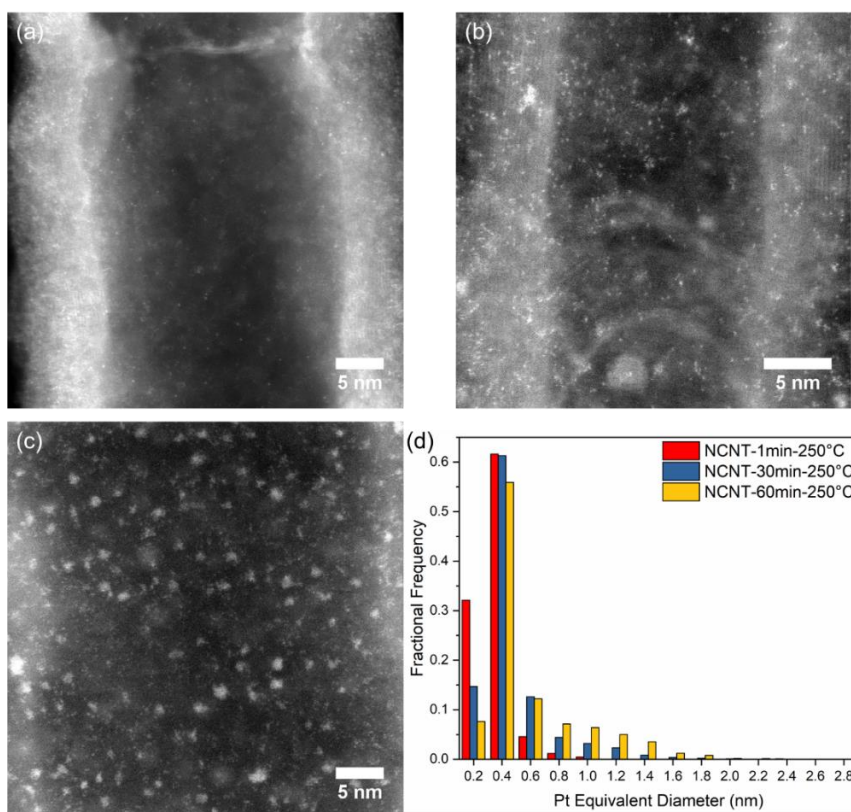


Figure 5.18 Effect of dosing time on the equivalent diameter of Pt with NCNTs and a temperature of 250°C. HAADF images of Pt with a dosing time of (a) 1 minute, (b) 30 minutes, (c) 60 minutes, and the respective experimentally measured (d) PSD histograms.

Similar experiments were completed for the PCNT samples using a dosing time of 1 minute and 30 minutes (Figure 5.19 (a)). Following the same trend as the NCNTs, as the dosing time increased the PSD histogram broadened (Figure 5.19 (b)), tending to a higher density of large (>1 nm) clusters and nanoparticles. It was noted that after 30 minutes of dosing time, a second peak in the histogram began to form at bin sizes 1.0 and 1.2 nm, indicating the production of a secondary preferred Pt size. Furthermore, like the density observed for the NCNTs the counts/nm² and area/nm² both increased with an increase in dosing time (Table 5.4). This finding suggests that there is not only an increase in the

number of Pt particles, but also their size, thus the number of nucleation sites increased, and growth took place between the two dosing times, respectively.

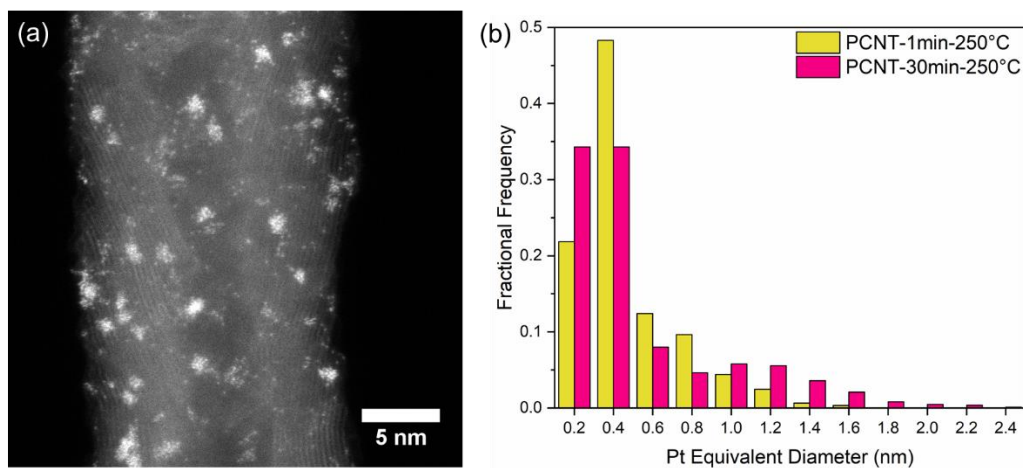


Figure 5.19 Effect of dosing time on the equivalent diameter of Pt with PCNTs and a temperature of 250°C. HAADF image of Pt with a dosing time of (a) 30 minutes and the respective experimentally measured (b) PSD histogram for dosing time of 1 minute and 30 minutes.

As a final confirmation, the effect of dosing time can also be established at a lower deposition temperature of 100°C. As shown in Figure 5.20, as the dosing time increases, the width of the PSD histogram also increases, leading to the production of single Pt atoms, Pt clusters, and nanoparticles. Furthermore, as expected from the previous samples, the density increased for both the counts/nm² and area/nm² when increasing the dosing time (Table 5.4) even at a substrate temperature of 100°C.

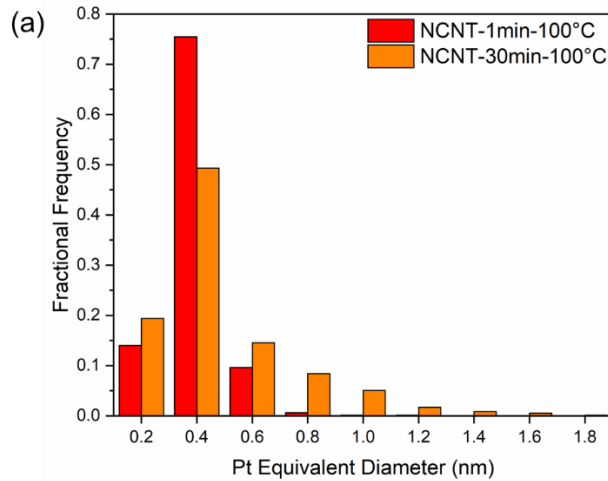


Figure 5.20 Effect of dosing time on the equivalent diameter of Pt with NCNTs and a temperature of 100°C. Cumulative PSD histograms of Pt deposition on NCNTs a dosing time of 1 minute and 30 minutes.

5.2.3.2 Effect of Temperature

Using a dosing time of 1 minute, the effect of temperature on the particle size and distribution was examined using temperatures of 100°C, 175°C, and 250°C. The HAADF images and PSD histograms in Figure 5.21 indicate that very little change occurred in the Pt size observed for varying deposition temperatures. For each deposition temperature, a narrow size distribution is observed with most of the fractional frequency originating between the 0.2 and 0.4 nm bins. This suggests that when operating at the varying temperatures and a deposition time of 1 minute, Pt single atoms and small clusters dominate. As suspected by the HAADF images, the deposition temperature also has little effect on the density of the Pt coverage, which was calculated to be virtually equivalent at all deposition temperatures (Table 5.4).

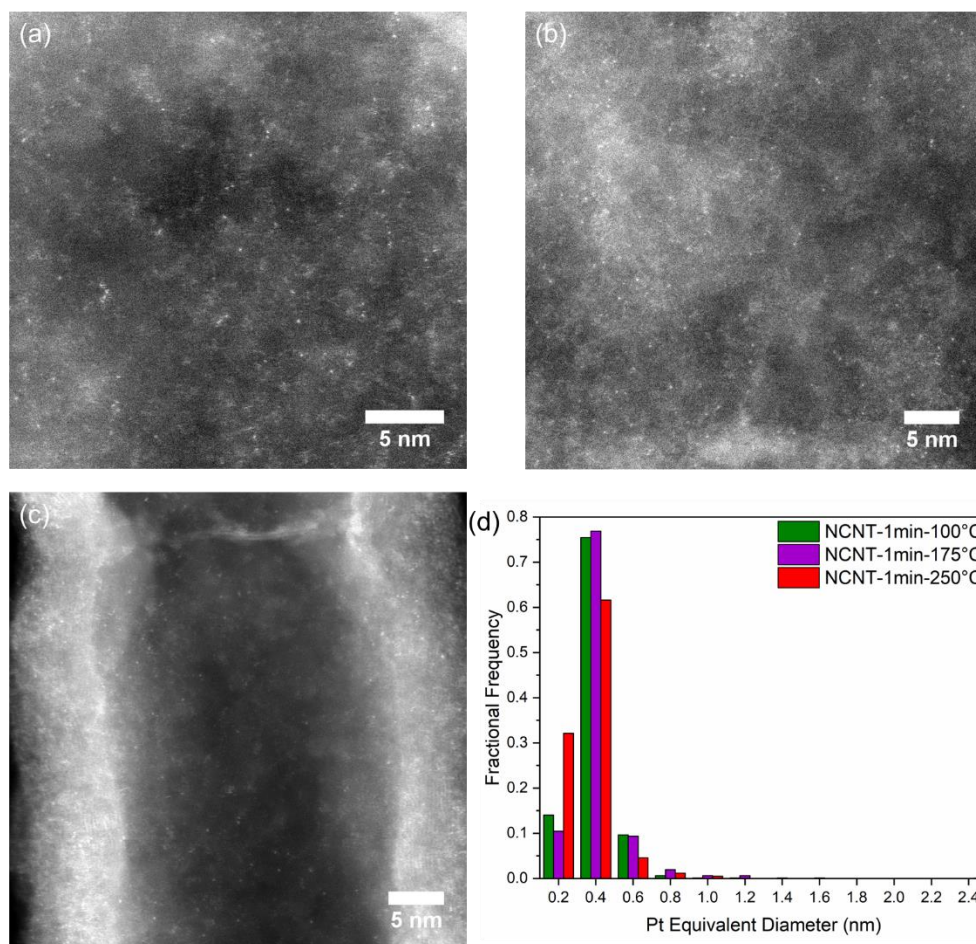


Figure 5.21 Effect of temperature on the equivalent diameter of Pt with NCNTs and a constant dosing time of 1 minute. HAADF images of Pt deposited on NCNTs with a temperature of (a) 100°C, (b) 175°C, (c) 250°C, and the respective experimentally measured (d) PSD histograms.

To ensure the effect of temperature was not an anomaly for a dosing time of 1 minute, a dosing time of 30 minutes was examined at deposition temperatures of 100°C and 250°C. Figure 5.22 (a) and (b) shows little variability between the width of the PSDs with the deposition temperature. According to literature, as the temperature is decreased it can be expected that the particle size will decrease, and a narrower size distribution will ensue, due to a decreased Pt diffusion rate [37], [177]. In situations where temperature had little effect on the particle size, it was theorized that the diffusion of the Pt was not limited

by the temperature, but the substrate [208]. This suggests that surface contaminants, ligand steric hinderance, or ligand decomposition from the dehydrogenation reaction could be limiting the Pt diffusion [208], [250]. However, unlike the 1 minute samples, as the deposition temperature increased, the density of the Pt increased for the 30 minute sample (Table 5.4). Various results have been found in literature outlining the effect of temperature. Feng *et al.* determined that the Pt loading generally increases when the temperature decreases, due to a decreased desorption rate of the Pt [37]. Meanwhile, Grillo *et al.* found almost no effect from the temperature on the Pt loading when examining differing number of ALD cycles [177]. In contrast, Setthapun *et al.* noted that at higher deposition temperatures (300°C in air) the particle size and loading increased, due to the decomposition of the precursor at the high temperature. While this may be unlikely at a temperature of 250°C, it is a possible explanation for the increased loading at higher temperatures. Rose *et al.* examined the effect of the temperature of the sticking coefficient for various Ti and Hf precursors through experimentation and calculation [257]. It was determined that different precursor ligands and their respective adsorption sites (assuming free movement) can affect the sticking coefficient, but in general higher temperatures likely result in higher sticking coefficients [257]. This however, is not universal for all precursors and substrates, thus possibly resulting in the variability observed in literature. Through the sticking coefficient explanation, it is possible that the higher temperature deposition conditions resulted in preferred adsorption versus desorption of the Pt precursor, thus leading to the observed increased Pt loading from the 30 minute dosing time. To be certain, specific calculations for the Pt precursor and NCNT substrate should be conducted. Similarly, the slight increase in the area/nm² with temperature can be explained by the increased loading of the Pt particles.

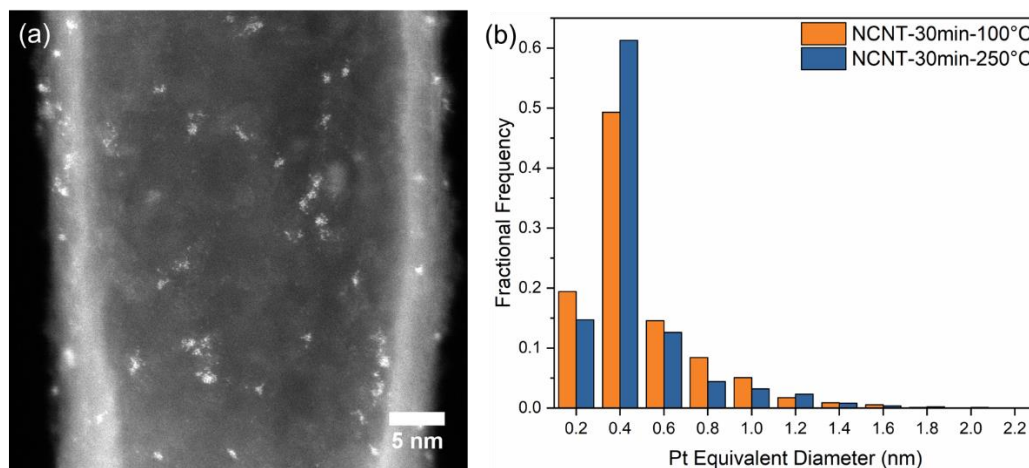


Figure 5.22 Effect of temperature on the equivalent diameter of Pt with NCNTs and a constant dosing time of 30 minutes. HAADF image of Pt deposited with a deposition temperature of (a) 100°C and the respective experimentally measured (b) PSD histogram for 100°C and 250°C deposition temperatures.

5.2.3.3 Effect of Substrate

The effect of the substrate can be examined by comparing the Pt deposition on NCNTs and PCNTs with varying dosing times. It should be noted that while it is expected that the N-dopants act as potential nucleation sites on the NCNTs, the Ca, Cl, and S contamination and presence of O likely contribute to nucleation sites, thus specific nucleation sites will not be discussed with respect to the N-dopants. In some cases, the PCNTs have a much cleaner surface in comparison to the NCNTs in which the C edges of the CNTs can be observed in contact with a Pt particle (*Appendix 4: Images Used for ALD Pt Quantification*). It is expected that the cleanliness of the PCNT surface and lack of doping will reduce the number of surface sites available for Pt adsorption, thus limiting deposition to defects in the lattice, facets in the nanotube walls, and adsorbed hydrocarbons. With this

being said, it is likely that the surface area for Pt adsorption is decreased on the PCNTs with respect to the NCNTs.

Using the HAADF images (Figure 5.23 (a)), PSD histograms were produced to compare deposition dosing times of 1 minute (Figure 5.23 (b)) and 30 minutes (Figure 5.23 (c)) at 250°C on NCNTs and PCNTs. As expected for both deposition times due to the decreased adsorption sites on the PCNTs, the PSD histograms for the PCNTs revealed a much broader size distribution in comparison to the NCNTs. This suggests that as the number of nucleation sites decreases, the average particle size increases, as can be expected from an increased growth regime. This was also observed by Settapan *et.al* on metal oxide surfaces, such that higher surface area substrates resulted in higher Pt loadings and smaller nanoparticles [240]. The Pt densities also confirm this story, as the counts/nm² are larger for the NCNTs, but the area/nm² is lower (Table 5.4). This indicates the presences of more, but smaller Pt particles on the NCNTs as compared to the PCNTs, due to fact that there likely exists a higher surface area for Pt nucleation, as a result of the high level of contamination on the NCNTs.

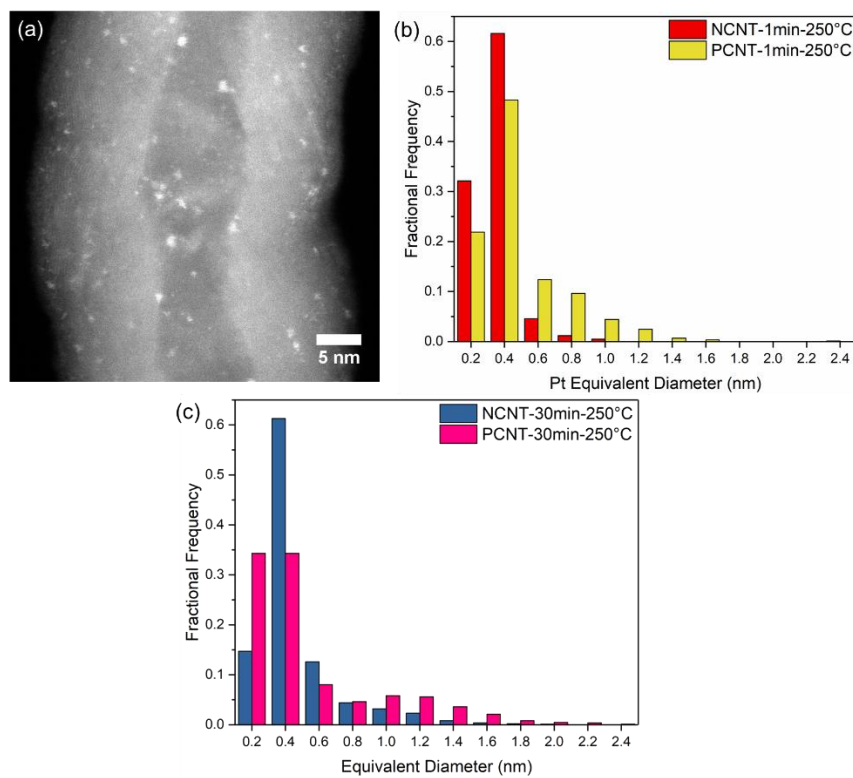


Figure 5.23 Effect of substrate on the equivalent diameter of Pt with a constant dosing time of 1 minute and a temperature of 250°C. HAADF image of Pt on (a) a PCNT and the respective experimentally measured (b) PSD histogram for deposition on NCNTs and PCNTs. (c) PSD histogram for NCNTs and PCNTs with a dosing time of 30 minutes and a deposition temperature of 250°C.

5.3 Summary

In summary, NCNTs containing N₂ gas were examined using EELS. It was determined that the gas is likely undergoing physisorption with the tube walls, leading to a higher concentration of the gas at the interior walls of each NCNT compartment. Using Auger quantification, it was determined that the NCNTs are N-doped with a concentration of approximately 1.6 ± 0.4 at. %. Through EELS analysis, this N-doping was confirmed in tubes that did not contain N₂ gas; however, separation of the N₂ gas and substitutional

signal, proved difficult and thus it was not conclusively determined that the tubes that contained the N_2 gas were also N-doped. Furthermore, an N-K edge was not observed in all tubes examined, thus suggesting varying N concentrations within the batch sample. Upon examination of the N_2 gas it was determined that the NCNT inner diameter is related to the pressure through a decreasing function. To decrease the variability in the data, it is suggested in the future that the quantification be completed on NCNTs that do not contain a Pd catalyst, and more time is given for the sample to stabilize from drift before the EEL spectra are acquired. While, trends were observed concerning the growth mechanisms of the NCNTs, the mechanism itself cannot not be fully understood now, and it is suggested that in-depth ETEM or *in situ* liquid cell experiments be completed in effort to determine the origin of this relationship between the inner diameter of the NCNTs and the gas pressure.

Using NCNTs and PCNTs as a substrate for Pt ALD deposition, the effect of the first ALD cycle was examined through varying the dosing time, temperature, and substrate. The aim of this investigation was to examine the effect of these parameters on the nucleation of Pt, such that the size of the Pt could be better controlled for future experiments concerning the catalytic efficiency of single Pt atoms. For each deposition condition analyzed, none solely produced single Pt atoms. It was observed that the temperature had little effect on the particle size, but caused an increase in the Pt density when working at higher temperatures. It was suggested that this could be related to substrate-limiting diffusion, through the potential decomposition of the Pt precursor upon deposition, steric hinderance of Pt ligands, and surface contaminants. Furthermore, an increase in dosing time and fewer nucleation sites on the PCNTs resulted in the broadening of the PSD and an average increase in the Pt equivalent diameters when compared to the NCNTs. Based on this study, it may be possible to produce single atoms and small clusters when working at low dosing times, and when the Pt density can be controlled with the temperature. In the ideal case, if a completely uniform substrate could be produced with many nucleation sites, it may be possible to deposit solely single Pt atoms using ALD. The

dosing time and temperature provide some degree of control over the particle size and density, respectively. Because the substrate influences the diffusion properties and the number of nucleation sites, it will always play a major role in the particle size, the size distribution, and the Pt density, thus individual studies of specific substrates is required. In the case of the substrates used in this study, single Pt atoms could be deposited on the NCNTs, if a faster deposition time was utilized, and the density was controlled by the deposition temperature. It may be possible to form single atoms on the PCNT with extremely short exposure times; however, the dispersion is likely to be poor due to the decreased degree in control over the exposure and the available nucleation sites.

Chapter Six

Synopsis and Future Work

In this thesis, experimental work was completed to fully characterize and understand N-doped C allotropes decorated with noble metal catalysts on the atomic scale. This work was completed using aberration-corrected TEMs, wherein multiple avenues of characterization were utilized to examine the morphological structure of the material and chemical bonding composing the C substrates. Specifically, negative spherical aberration corrected HRTEM was primarily used to physically examine the structure of the material, EELS was used to examine the chemical bonding and perform in-depth quantification of N-dopant species, and STEM was utilized to examine the structure of the noble metals. These techniques were used in the capacity to examine three specific C allotropes: FLG and N-doped FLG with single Pt atoms and clusters (*Chapter Three*), CVD produced graphene with N-doping from in-house techniques (*Chapter Four*), and NCNTs used as N₂ gas-conduits and as substrates for Pt deposition (*Chapter Five*). A summary from each group of results is detailed below, followed by considerations for new experiments and future work to be completed.

The work pertaining to the few-layer N-doped graphene was completed using thermally reduced N-doped graphene, which was found to be highly defective and multi-layered when examining the material on a large-scale basis. Upon examination with HRTEM imaging, nanoprobe diffraction, and EELS, it was determined that the graphene

maintained its structure on the short-range; however, the long-range order was lost due to defects originating from the production method, incomplete reduction, N-dopants in the graphene lattice, and grain misorientation between and within graphene sheets. The N-dopants were characterized through examination of the ELNES, where it was determined that three peaks originating from the various N-species existed within the π^* region of the N-K edge. Interestingly, the peaks varied between and within the N-doped graphene, suggesting local variability of the N-dopants. Additionally, some sheets were found to be lacking N, thus suggesting that the N-doping process is inhomogeneous, which in effect will contribute to the ALD deposition sites. DFT analysis was performed to determine the origin of the peaks in the π^* region of the N-K edge; however, due to the complexity of the material, the proposed structures did not enable an appropriate reproduction of the experimental spectra, and further work is required. Using HAADF imaging, the Pt catalysts were analyzed, and single Pt atoms and clusters were found on this sample in the absence of nanoparticles. It was shown through image processing that the Pt prefers to sit at edge locations with few atoms stabilized on the basal plane, likely originating from a defect in the lattice.

The few layer N-doped graphene was analyzed as a potential electrode material for the HER. Within this experiment, Pt atoms, clusters, and nanoparticles were observed on both N-doped graphene and graphene substrates, which were compared to Pt nanoparticles on C black. The samples containing the Pt atoms and clusters, out performed the Pt/C black samples for both mass and specific activity before and after accelerated degradation tests. While quantitative analysis was not performed for the material, it is expected that the Pt atoms and clusters resulted in the increased activity. Furthermore, the N-doped graphene showed higher specific activity before and after cycling in comparison to the graphene substrate, which may be an effect of the substrate, due to modifications to the electronic structure of the Pt catalysts. The graphene substrate also showed a larger decrease in its activity after cycling, when compared to the N-doped graphene. It may be suggested that the smaller activity decrease observed on the N-doped graphene substrate arises from a

potential increase in binding energy with the N-dopants, thus decreasing the possibility for catalyst growth or dissolution during cycling. Because a variability in the size of the Pt catalyst existed on the graphene and N-doped graphene, quantification was not completed, as the results would directly depend on the sheets examined, thus comparison before and after cycling would not be significant in this case. To address this issue, ILSTEM imaging was performed for the N-doped graphene and graphene samples with 50 ALD cycles. Through comparison of both samples, before and after cycling, growth and dissolution were observed. Most importantly, the Pt atoms appeared physically stable after cycling on both samples. Before quantification of these samples is performed, control experiments should be completed to understand the influence of the beam and sample handling.

Using CVD grown graphene on TEM grids, in-house N-doping experiments were completed to produce a single-sheet N-doped graphene for TEM analysis, such that Pt could be deposited on the grids to determine the theoretically preferred binding locations of Pt on graphene. Prior to N-doping, Auger analysis was performed to determine optimized conditions for TEM analysis, such that background electron signals were reduced. Using the determined conditions, N quantification was performed on the TEM grids. Three sample preparation techniques were used for N-doping, which include a plasma cleaner, Gentle Mill™, and a NanoMill®, each with a N source. The plasma cleaner successfully doped the graphene lattice; however, it had many sources of contamination and resulted in destructive doping. Furthermore, the Gentle Mill™ also was able to dope the graphene lattice; however, control over the deposition fluence was poor due to high ion currents. The NanoMill® is the preferred method of N-doping, due to its low contamination, and high degree of control over the ion fluence through pA current control. It was determined that the NanoMill® successfully doped the graphene lattice; however, damage was caused to the single to few layer graphene sheets, likely originating from the N-dopants, ion beam damage, or surface hydrocarbons covering much of the graphene surface. Additionally, the doping concentrations cannot be fully trusted, as concentration variability for similar doping conditions existed. The variability on the overall N

concentration likely originated from fluctuating current during sample exposure. Lastly, Pd was deposited using 50 ALD cycles on a TEM grid as a proof-of-concept, wherein nanoparticles were observed to be decorating the surface hydrocarbons. It is suggested for future experiments that proper cleaning methods are devised to remove the surface hydrocarbons before noble metal deposition to ensure metals bind to the graphene lattice.

As a final analysis material, NCNTs were examined. It was determined through ELNES analysis that the NCNTs were N₂ gas-containing, and through Auger analysis that the walls were N-doped. Based on in-depth quantification a decreasing trend of the N₂ pressure with an increase in the inner wall diameter was observed. It is possible that the gas is captured during the growth process as a by-product of the reacting species to form the NCNT walls, but this hypothesis requires further experimentation for confirmation. Moreover, NCNTs and PCNTs were used as substrate material to examine the effects of ALD parameters on Pt nucleation during the first ALD cycle, in effort to determine methods to produce solely single Pt atoms. Specifically, the effect of dosing time, deposition temperature, and substrate were examined. It was determined that as dosing time increased, the Pt density increased and the PSD broadened, due to the initiation of particle growth. It was determined that within the one minute regime, small clusters and Pt atoms dominated. The temperature seemed to have little effect on the Pt size, which was deemed to be due to substrate-diffusion limitations; however, the density was observed to increase with temperature, but this may be an effect of the approximation used for this specific quantification. Lastly, the PSD histograms appeared to broaden and result in a larger equivalent diameter of the Pt catalysts on the PCNTs compared to the NCNTs, likely deriving from the reduced number of nucleation sites. While in this study Pt atoms were not solely produced, it was determined that potentially working at dosing times less than 1 minute could result in the production of single atoms. Furthermore, the importance of the substrate was observed, as it imposed diffusion limitations with the deposition temperature and controlled the number of the nucleation sites. This suggests, that while generalities can be observed for dosing time, individual experiments may need to be completed for specific

substrates to individually understand how the surface effects the diffusion properties and nucleation sites.

6.1 Future Work and Considerations

Based on the work completed during this Ph.D. thesis, much has been learned about graphene and single atom imaging. This section will outline considerations during future experiments based on my experience with this material and some potentially interesting experiments which could provide answers to open questions.

To begin, experimental design will be addressed for future considerations during imaging. First, it is suggested that a 60 kV alignment should be completed and utilized on the Titan Cubed, as this will reduce knock-on damage to the graphene lattice without being limited by the C_C . This should allow for higher resolution images than the 40 kV electron source, and less knock-on damage than the 80 kV electron source [122]. To err on the side of caution, lower dose and dose rates could be utilized without a loss in signal by increasing the sampling of the image and working at a current lower than 40 pA. Additionally, others have reported the use of cleaning the graphene sample in the microscope and even imaging at temperatures as high as 500°C to reduce the beam contamination during imaging [154]. This should be used with caution and consideration of the material under examination, such that melting of supported nanoparticles or thermal excitation of atoms can occur at elevated temperatures.

The ILSTEM experiments are important for future material consisting of a range of catalysts sizes, such that it allows for the individual examination of different particle size ranges, and also shows the stability of individual atoms with cycling. In this thesis, the atoms appear to be stable after electrochemical cycling; however, it should be noted that these were preliminary experiments. Important ILSTEM imaging experiments are required for the future to understand the origins of the observed changes in the TEM sample before

and after cycling. It has been shown in literature that atoms are affected by the electron beam [120], therefore the effect of the beam on the Pt atoms must be understood before quantification of the Pt size and location can be determined in ILSTEM. Utilizing STEM imaging, the average atomic movement with the electron beam can be monitored through sequential image acquisition, wherein the dose should be monitored and maintained once the examination is complete. Conditions that minimize atomic movement should be utilized, to ensure the imaging does not affect the atom location. Furthermore, as expressed by Mayrhofer *et al.* [134] and explained in detail in *Chapter 3.2.5.2 ILSTEM of Pt on Graphene and N-Doped Graphene*, the effect of sample handling should also be examined to ensure the observed changes on the TEM grid are related to the electrochemical cycling and not external factors, such as personal handling and sample storage.

Furthermore, the production of single Pt atoms and controlled Pt cluster sizes are paramount to understand the effects of these small catalysts on various reactions. In effort to remove the overlapping effects of the Pt atoms, clusters, and nanoparticles from electrochemical experiments, it is desired to have better control over the deposition parameters. While headway was made in this thesis to understand the nucleation parameters of the ALD conditions on NCNTs, other substrates specific to electrodes under consideration should be utilized, due to the control of the substrate on the Pt size, distribution, and density. It would be beneficial to have high throughput quantification of various substrate material using HAADF imaging. The challenge of quantification of single Pt atoms arise from the poor contrast of the atom on a thick substrate, due to the contrast mechanisms in HAADF images. For this thesis, manual individual image analysis was completed to account for the identification of the Pt atoms. It would be better to have the Pt atoms automatically identified, as the manual process accounted for a majority of the time for analysis. To increase the throughput of the analysis and allow more samples to be examined, it is suggested to produce a script that can perform the image quantification. With the advent of machine learning this processing may be possible. Machine learning has been used to examine images on the medical community [258] to agricultural

landscapes [259]. Currently, a trainable method is available through ImageJ [260] that can be used as a starting point for the automated image analysis; however, due to the complexity of the images, a code may need to be written. Nevertheless, final inspection of the image should be performed to ensure all selected atoms are in focus and indeed atoms. Additionally, neural networks have been seen to successfully segment cells in low contrast biological light micrographs [261], thus they may be useful for the suggested application. In this case, many²¹ input images produced through manual identification will be required to train the network, thus this approach may be impractical. The use of automated image analysis could be beneficial as it would remove the time required for image analysis, thus more time could be put towards image acquisition, thus increasing the experimental throughput. This method may also be used in conjunction with electron tomography [135], in order to observe and quantify the distribution of Pt atoms around a NCNT. It was noted in the thesis in a couple of instances that an uneven distribution of Pt was observed on a single NCNT, such that one side had a higher Pt density than the other. Through tomography and machine learning, it may be possible to map the location of the Pt atoms on a single NCNTs, thus indicating how evenly distributed the Pt atoms are on a single nanotube. It should be noted that this is experimentally very challenging due to the small size of the Pt atoms, thus a large convergence angle should be used in combination with fine-tuning of the corrector.

While necessary, but on a less important note, the ELNES of the N-K edge should continue to be modelled in WIEN2k. For future consideration, multilayered sheets should be utilized, first with single noninteracting dopants. Should a spectral match not exist, then varying concentrations and species of N-dopants should be examined in a single structure. These calculations will be very time consuming, and without having an idea of the individual dopant concentrations, very difficult; it is suggested that the structural

²¹ According to Masters student Michael Chatzidakis, whom has experience working with neural networks, it may take up to 1000 images for the training to result in a successful segmentation process.

complexity of the N-doped FLG may be too high to get a spectral match in a reasonable amount of time.

Lastly, *in situ* liquid cell experiments or ETEM experiments should be completed on the growth kinetics of the ferrocene/imidazole/acetonitrile solution used to grow the NCNTs in this thesis. The specific experimental design with reference to other experiments is discussed in *Chapter 5.1.3 Pressure Quantification*, but in short it will require careful examination of the ELNES structure with CNT growth. While the evolution of the gas may not be obvious, due to spectral overlap with the acetonitrile N-K edge, it may be possible to monitor the gas evolution through normalization of the local acetonitrile concentration. However, the gas evolution may be apparent in the ELNES structure through the broadening of the sharp peak in the N-K region due to the 1 eV separation of the N₂ gas and acetonitrile peak. As the gas concentration increases this could be observed as a shoulder on the right-hand side of the acetonitrile peak followed by peak broadening with increased N₂ concentration. While quantification of the gas may not be possible, due to the spectral overlap, the evolution should be apparent through peak broadening. Through observation of the gas evolution during the growth process, the origin of the gas and growth process may be made apparent.

References

- [1] Canada, Environment Canada, "National Inventory Report 1990-2013: Greenhouse Gas Sources and Sinks in Canada," Environment Canada, Ottawa, 2013.
- [2] Ontario, Ministry of the Environment and Climate Change, "Ontario's Climate Change Discussion Paper 2015," Ministry of the Environment and Climate Change, Toronto, 2015.
- [3] L. Chapman, "Transport and Climate Change: A Review," *Journal of Transport Geography*, vol. 15, pp. 354-367, 2007.
- [4] N. Stern, *The economy of climate change: The Stern Review*, Cambridge, UK: Cambridge Press, 2007.
- [5] J. Y. C. N. M. F. L. Ogden, "NextSTEPS White Paper: The hydrogen transition," Davis Institute of Transportation Studies, UC Davis, 2014.
- [6] California Fuel Cell Partnership, "A California Road Map: Bringing Hydrogen Fuel Cell Electric Vehicles to the Golden State," California Fuel Cell Partnership, West Sacramento, 2012.
- [7] W. Grove, "On a Gaseous Voltaic Battery," *The London, Edinburgh and Dublin Philosophical Magazine and Journal of Science*, vol. 21, pp. 417-420, 1842.

- [8] J. D. A. Larminie, *Fuel Cell Systems Explained*, vol. 2nd, West Sussex, England: John Wiley & Sons Ltd, 2003.
- [9] US Department of Energy: Energy Efficiency and Renewable, "Fuel Cell Technologies Office Multi-Year Research, Development, and Demonstration Plan (2011-2020)," 2003.
- [10] T. G. F. Barbir, "Efficiency and economics of proton exchange membrane (PEM) fuel cells," *International Journal of Hydrogen Energy*, vol. 22, no. 10-11, pp. 1027-1037, 1997.
- [11] V. Mehta and J. Cooper, "Review and analysis of PEM fuel cell design and manufacturing," *Journal of Power Sources*, vol. 114, no. 1, pp. 32-53, 2003.
- [12] J. Wu, X. Yuan, M. J. J., H. Wang, J. Zhang, J. Shen, S. Wu and W. Merida, "A review of PEM fuel cell durability: Degradation mechanisms and mitigation strategies," *Journal of Power Sources*, vol. 14, no. 1, pp. 104-119, 2008.
- [13] S. Z. M. Thomas, "Fuel Cells: Green Power," Los Alamos National Laboratory, Los Alamos.
- [14] M. Debe, "Electrocatalyst approaches and challenges for automotive fuel cells," *Nature*, vol. 486, pp. 43-51, 2012.
- [15] H. Gasteiger, S. S. Kocha, B. Sompalli and F. Wagner, "Activity benchmarks and requirements for Pt, Pt-alloy, and non-Pt oxygen reduction catalysts for PEMFCs," *Applied Catalysis B: Environment*, vol. 56, no. 1-2, pp. 9-35, 2005.
- [16] J. Holladay, J. Ju, D. King and Y. Wang, "An overview of hydrogen production technologies," *Catalysis Today*, vol. 139, pp. 244-260, 2009.

- [17] J. Ogden, "Prospects for building a hydrogen energy infrastructure," *Annual review energy environment and resources*, vol. 24, pp. 227-279, 1999.
- [18] Y. Shao, G. Yin and Y. Gao, "Understanding and approaches for the durability issues of Pt-Based catalysts for the PEM fuel cell," *Journal of Power Sources*, vol. 171, no. 2, pp. 558-566, 2007.
- [19] Y. Shao, J. Liu, Y. Wang and Y. Lin, "Novel catalyst support materials for PEM fuel cells: current status and future prospects," *Journal of Material Chemistry*, vol. 19, no. 1, p. 46, 2009.
- [20] G. Acres, J. Frost, G. Hards, R. Potter, T. Ralph, D. Thompsett, G. Burstein and G. Hutchings, "Electrocatalysts for fuel cells," *Catalysts Today*, vol. 38, no. 8, pp. 393-400, 1997.
- [21] J. Keith, G. Jerkiewicz and T. Jacob, "Theoretical investigations of the oxygen reduction reaction on Pt(111)," *ChemPhysChem*, vol. 11, no. 13, pp. 2779-2794, 2010.
- [22] B. Hammer and J. Norskov, "Theoretical Surface Science and Catalysis - Calculations and Concepts," *Advances in Catalysis*, vol. 45, pp. 71-129, 2000.
- [23] J. Norskov, J. Rossmeisl, A. Logadottir, L. Lindqvist, J. Kitchin, T. Bligaard and H. Jonsson, "Origin of the Overpotential for Oxygen Reduction at a Fuel-Cell Cathode," *Journal of Physical Chemistry B*, vol. 108, pp. 17886-17892, 2004.
- [24] H. Kim, K. Lee, S. L. Woo and Y. Jung, "On the mechanism of enhanced oxygen reduction reaction in nitrogen-doped graphene nanoribbons," *Physical Chemistry Chemical Physics*, vol. 13, no. 39, pp. 17505-17510, 2011.

- [25] T. Jacob, "The mechanism of forming H₂O from H₂ and O₂ over a Pt catalyst via direct oxygen reduction," *Fuel Cells*, vol. 6, no. 3-4, pp. 159-181, 2006.
- [26] K. Kolasinski, *Surface Science Foundations of Catalysis and Nanoscience*, 2nd ed., West Sussex, England: Wiley, 2008.
- [27] J. Aarons, L. Jones, A. Varambhia, K. MacArthur, D. Ozkaya, M. Sarwar, C. Skylaris and P. Nellist, "Predicting the Oxygen-Binding Properties of Platinum Nanoparticle Ensembles by Combining High-Precision Electron Microscopy and Density Functional Theory," *Nano Letters*, vol. 17, pp. 4003-4012, 2017.
- [28] Y. Zhuo, K. Neyerlin, T. S. Olson, S. Pylypenko, J. Bult, H. Dinh, T. Gennett, Z. Shao and R. O'Hayre, "Enhancement of Pt and Pt-alloy fuel cell catalyst and durability via nitrogen-modified carbon supports," *Energy Environmental Science*, vol. 3, no. 10, pp. 1437-1446, 2010.
- [29] S. St. John, L. Dutta and A. P. Angelopoulos, "Synthesis and characterization of electrocatalytically active platinum atom clusters and monodisperse single crystals," *Journal of Physical Chemistry C*, vol. 114, no. 32, pp. 13515-13525, 2010.
- [30] E. Toyoda, R. Jinnouchi, T. Hatanaka, Y. Morimoto, K. Mitsuhashi, A. Visikovskiy and Y. Kido, "The d-band structure of Pt nanoclusters correlated with the catalytic activity for an oxygen reduction reaction," *Journal of Physical Chemistry C*, vol. 115, no. 43, pp. 21236-21240, 2011.
- [31] C. Marichy, M. Bechelany and N. Pinna, "Atomic layer deposition of nanostructured materials for energy and environmental applications," *Advanced Materials*, vol. 24, no. 8, pp. 1017-1032, 2012.
- [32] N. Cheng, S. Stambula, D. Wang, M. Norouzi Banis, J. Liu, A. Riese, B. Xiao, R. Li, T.-K. Sham, Liu, L-M, G. A. Botton and X. Sun, "Platinum single-atom and

- cluster catalysis of the hydrogen evolution reaction," *Nature Communications*, vol. 7, p. 13638, 2016.
- [33] S. M. George, "Atomic layer deposition: an overview," *Chemical Reviews*, vol. 110, no. 1, pp. 111-131, 2010.
- [34] Y. -C. Hsueh, C. -C. Wang, C. Liu, C. -C. Kei and T. -P. Perng, "Deposition of platinum on oxygen plasma treated carbon nanotubes by atomic layer deposition," *Nanotechnology*, vol. 23, no. 40, p. 405603, 2012.
- [35] J. Li, X. Liang, D. King, Y.-B. Jiang and A. W. Weimer, "Highly dispersed Pt nanoparticle catalyst prepared by atomic layer deposition," *Applied Catalysis B: Environmental*, vol. 91, no. 1-2, pp. 220-226, 2010.
- [36] T. Shu, S.-J. Liao, C.-T. Hsieh, A. K. Roy, L. Y.-Y, D.-Y. Tzou and W.-Y. Chen, "Fabrication of platinum electrocatalysts on carbon nanotubes using atomic layer deposition for proton exchange membrane fuel cells," *Electrochimica Acta*, vol. 75, no. 30, pp. 101-107, 2012.
- [37] H. Feng, J. A. Libera, P. C. Stair, J. T. Miller and J. W. Elam, "Subnanometer palladium particles synthesized by atomic layer deposition," *ACS Catalysis*, vol. 1, no. 6, pp. 665-673, 2011.
- [38] C. Liu, C. -C. Wang, C. -C. Kei, Y. -C. Hsueh and T. -P. Perng, "Atomic layer deposition of platinum nanoparticles on carbon nanotubes for application in proton-exchange membrane fuel cells," *Small*, vol. 5, no. 13, pp. 1535-1538, 2009.
- [39] R. Puurunen, "Surface chemistry of atomic layer deposition: A case study for the trimethylaluminum/water process," *Journal of Applied Physics*, vol. 97, p. 121301, 2005.

- [40] C. Zhou, J. Wu, A. Nie, F. R. C. A. Tachibana and H. Cheng, "On the sequential hydrogen dissociative chemisorption on small platinum clusters: A density functional theory study," *Journal of Physical Chemistry C*, vol. 111, no. 34, pp. 12773-12778, 2007.
- [41] T. Holme, Y. Zhou, R. Pasquarelli and R. O'Hayre, "First principles study of doped carbon supports for enhanced platinum catalysts," *Physical Chemistry Chemical Physics*, vol. 12, no. 32, pp. 9461-9468, 2010.
- [42] J. Bai, Q. Zhu, Z. Lv, H. Dong, J. Yu and L. Dong, "Nitrogen-doped graphene as catalysts and catalyst supports for oxygen reduction in both acidic and alkaline solutions," *International Journal of Hydrogen Energy*, vol. 38, no. 3, pp. 1413-1418, 2013.
- [43] B. Qiao, A. Wang, X. Yang, L. F. Allard, Z. Jiang, Y. Cui, J. Liu, J. Li and T. Zhang, "Single-atom catalysis of CO oxidation using Pt1/FeOx," *Nature Chemistry*, vol. 3, no. 8, pp. 634-641, 2011.
- [44] H. Zhang, G. Liu, L. Shi and J. Ye, "Single-Atom Catalysts: Emerging Multifunctional Materials in Heterogeneous Catalysis," *Advanced Energy Materials*, p. 1701343, 2017.
- [45] C. Zhu, S. Fu, Q. Shi, D. Du and Y. Lin, "Single Atom Electrocatalysts," *Angewandte Chemie International Edition*, vol. 56, pp. 13944-13960, 2017.
- [46] J. Liu, "Catalysis by Supported Single Metal Atoms," *ACS Catalysis*, vol. 7, pp. 34-59, 2017.
- [47] J. M. Andujar and F. Segura, "Fuel cells: History and updating. A walk along to centuries," *Renewable and Sustainable Energy Reviews*, vol. 13, no. 9, pp. 2309-2322, 2009.

- [48] S. Srinivasan, E. A. Ticianelli, C. R. Derouin and A. Redondo, "Advances in solid polymer electrolyte technology and low platinum loading," *Journal of Power Sources*, vol. 22, pp. 359-375, 1988.
- [49] D. A. Stevens, M. T. Hicks, H. G. M and J. R. Dahn, "Ex situ and in situ stability studies of PEMFC catalysts: Effect of carbon type and humidification on degradation of the carbon," *Journal of the Electrochemical Society*, vol. 152, no. 12, pp. A2309-A2315, 2005.
- [50] K. Novoselov, A. Geim, S. Morozov, D. Jiang, Y. Zhang, S. Dubonos, I. Grigorieva and A. Firsov, "Electric field effect in atomically thin carbon films," *Science*, vol. 306, no. 5696, pp. 666-669, 2004.
- [51] A. K. Geim and K. S. Novoselov, "The rise of graphene," *Nature Materials*, vol. 6, no. 3, pp. 183-191, 2007.
- [52] J. H. Warner, "The influence of the number of graphene layers on the atomic resolution images obtained from aberration-corrected high resolution transmission electron microscopy," *Nanotechnology*, vol. 21, no. 25, p. 255707, 2010.
- [53] M. Yi and Z. Shen, "A review on mechanical exfoliation for the scalable production of graphene," *Journal of Material Chemistry A*, vol. 3, pp. 11700-11715, 2015.
- [54] C. Soldano, A. Mahmood and E. Dujardin, "Production, properties and potential of graphene," *Carbon*, vol. 48, pp. 2127-2150, 2010.
- [55] T. A. Land, T. Michelay, R. J. Behm, J. C. Hemminger and G. Comsa, "STM investigation of single layer graphite structures produced on Pt (111) by hydrocarbon decomposition," *Surface Science*, vol. 264, pp. 261-270, 1992.

- [56] A. Nagashima, K. Nuka, H. Itoh, T. Ichinokawa and C. Oshima, "Electronic states of monolayer graphite formed on TiC(111) surface," *Surface Science*, vol. 291, pp. 93-98, 1993.
- [57] A. Reina, X. Jia, J. N. D. Ho, H. Son, V. Bulovic, M. S. Dresselhaus and J. Kong, "Large area, few layer graphene films on arbitrary substrates by chemical vapour deposition," *Nano Letters*, vol. 9, no. 1, pp. 30-35, 2009.
- [58] S. Stankovich, D. A. Dikin, R. D. Piner, K. A. Kohlhaas, A. Kleinhammes, Y. Jia, Y. Wu, S. T. Nguyen and R. S. Ruoff, "Synthesis of graphene-based nanosheets via chemical reduction of exfoliated graphite oxide," *Carbon*, vol. 45, no. 7, pp. 1558-1565, 2007.
- [59] D. R. Dreyer, S. Park, C. W. Bielawski and R. S. Ruoff, "The chemistry of graphene oxide," *Chemical Society Reviews*, vol. 39, no. 1, pp. 228-240, 2010.
- [60] H. C. Schniepp, J.-L. Li, M. J. McAllister, H. Sai, M. Herrera-Alonso, D. H. Adamson, R. K. Prud'homme, R. Car, D. A. Saville and I. A. Aksay, "Functionalized single graphene sheets derived from splitting graphite oxide," *Journal of Physical Chemistry B*, vol. 110, no. 17, pp. 8535-8539, 2006.
- [61] M. S. Moldovan, H. Bulou, Y. J. Dappe, I. Janowska, D. Begin, C. Pham-Huu and O. Ersen, "On the evolution of Pt nanoparticles on few-layer graphene supports in the high-temperature range," *Journal of Physical Chemistry C*, vol. 116, no. 16, pp. 9274-9282, 2012.
- [62] K. Kong, Y. Choi, B.-H. Ryu, J.-O. Lee and H. Chang, "Investigation of metal/carbon-related materials for fuel cell applications by electronic structure calculations," *Material Science and Engineering C*, vol. 26, no. 5-7, pp. 1207-1210, 2006.

- [63] H. Wang, Q. Wang, Y. Cheng, K. Li, Y. Yao, Q. Zhang, C. Dong, P. Wang, U. Schwingenschlogl, W. Yang and X. X. Zhang, "Doping monolayer graphene with single atom substitutions," *Nano Letters*, vol. 12, no. 1, pp. 141-144, 2012.
- [64] J. A. Rodriguez-Manzo, O. Cretu and F. Banhart, "Trapping of metal atoms in vacancies of carbon nanotubes and graphene," *ACS Nano*, vol. 4, no. 6, pp. 3422-3428, 2010.
- [65] Y. Shao, S. Zhang, C. Wang, Z. Nie, J. Liu, Y. Wang and Y. Lin, "Highly durable graphene nanoplatelets supported Pt nanocatalysts for oxygen reduction," *Journal of Power Sources*, vol. 195, no. 15, pp. 4600-4605, 2010.
- [66] D. Luo, G. Zhang, J. Liu and X. Sun, "Evaluation criteria for reduced graphene oxide," *Journal of Physical Chemistry C*, vol. 115, no. 23, pp. 11327-11335, 2011.
- [67] Z. Xu, Y. Bando, L. Liu, W. Wang, X. Bai and D. Golberg, "Electrical conductivity, chemistry, and bonding alternations under graphene oxide to graphene transitions as revealed by in situ TEM," *ACS Nano*, vol. 5, no. 6, pp. 4401-4406, 2011.
- [68] D. Pacile, J. C. Meyer, A. F. Rodriguez, M. Papagno, C. Gomez-Navarro, R. S. Sundaram, M. Burghard, K. Kern, C. Carbone and U. Kaiser, "Electronic properties and atomic structure of graphene oxide membranes," *Carbon*, vol. 49, no. 3, pp. 966-972, 2011.
- [69] L.-S. Zhang, X.-Q. Liang, W.-G. Song and Z.-Y. Wu, "Identification of the nitrogen species on N-doped graphene layers and Pt/NG composite catalyst for direct methanol fuel cell," *Physical Chemistry Chemical Physics*, vol. 12, no. 38, pp. 12055-12059, 2010.

- [70] D. Wei, Y. Liu, Y. Wang, H. Zhang, L. Huang and G. Yu, "Synthesis of N-doped graphene by chemical vapour deposition and its electrical properties," *Nano Letters*, vol. 9, no. 5, pp. 1752-1758, 2009.
- [71] Z.-H. Sheng, L. Shao, J.-J. Chen, W.-J. Bao, F.-B. Wang and X.-H. Xia, "Catalyst-free synthesis of nitrogen-doped graphene via thermal annealing graphite oxide with melamine and its excellent electrocatalysis," *ACS Nano*, vol. 5, no. 6, pp. 4350-4358, 2011.
- [72] P. Wang, Z. Wang, L. Jia and Z. Xiao, "Origin of the catalytic activity of graphite nitride for the electrochemical reduction of oxygen: geometric factors vs. electronic factors," *Physical Chemistry Chemical Physics*, vol. 11, no. 15, pp. 2730-2740, 2009.
- [73] N. Alexeyeva, E. Shulga, V. Kisand, I. Kink and K. Tammeveski, "Electroreduction of oxygen on nitrogen-doped carbon nanotube modified glassy carbon electrodes in acid and alkaline solutions," *Journal of Electroanalytical Chemistry*, vol. 648, no. 2, pp. 169-175, 2010.
- [74] K. Momma and F. Izumi, "VESTA 3 for three-dimensional visualization of crystal, volumetric and morphology data," *Journal of Applied Crystallography*, vol. 44, no. 6, pp. 1272-1276, 2011.
- [75] L. Qu, Y. Liu, J.-B. Baek and L. Dai, "Nitrogen-Doped Graphene as Efficient Metal-Free Electrocatalyst for Oxygen Reduction in Fuel Cells," *ACS Nano*, vol. 4, no. 3, pp. 1321-1326, 2010.
- [76] L. Zhang, J. Niu, L. Dai and Z. Xia, "Effect of microstructure of nitrogen-doped graphene on oxygen reduction activity in fuel cells," *Langmuir*, vol. 28, no. 19, pp. 7542-7550, 2012.

- [77] J. Zhong, J.-J. Deng, B.-H. Mao, T. Xie, X.-H. Sun, Z.-G. Mou, C.-H. Hong, Y. P. and S.-D. Wang, "Probing solid state N-doping in graphene by X-ray absorption near-edge structure spectroscopy," *Carbon*, vol. 50, no. 1, pp. 335-338, 2012.
- [78] D. Deng, X. Pan, L. Yu, Y. Cui, Y. Jiang, J. Qi, W.-X. Li, Q. Fu, X. Ma, Q. Xue, G. Sun and X. Bao, "Toward N-doped graphene via solvothermal synthesis," *Chemistry of Materials*, vol. 23, no. 5, pp. 1188-1193, 2011.
- [79] T. Xing, Y. L. L. Zheng, B. Cowie, D. Gunzelmann, S. Qiao, S. Huang and Y. Chen, "Observation of Active Sites for Oxygen Reduction Reaction on Nitrogen-Doped Multilayer Graphene," *ACS Nano*, vol. 8, no. 7, pp. 6856-6862, 2014.
- [80] S. Ni, Z. Li and J. Yang, "Oxygen molecule dissociation on carbon nanostructures with different types of nitrogen doping," *Nanoscale*, vol. 4, no. 4, pp. 1184-1189, 2012.
- [81] Y. Shao, J. Sui, G. Yin and Y. Gao, "Nitrogen-doped carbon nanostructures and their composites as catalytic materials for proton exchange membrane fuel cell," *Applied Catalysis B: Environmental*, vol. 79, no. 1, pp. 89-99, 2008.
- [82] M. N. Groves, C. Malardier-Jugroot and M. Jugroot, "Improving platinum catalyst durability with a doped graphene support," *Journal of Physical Chemistry C*, vol. 116, no. 19, pp. 10548-10556, 2012.
- [83] Y.-C. Lin, P.-Y. Teng, P.-W. Chui and K. Suenaga, "Exploring the Single Atom Spin State by Electron Spectroscopy," *Physical Review Letters*, vol. 115, p. 206803, 2015.
- [84] C. Galeano, J. Meier, M. Soorholtz, H. Bongard, C. Baldizzone, K. Mayrhofer and F. Schuth, "Nitrogen-Doped Hollow Carbon Spheres as a Support for Platinum-Based Electrocatalysts," *ACS Catalysis*, vol. 4, pp. 3856-3868, 2014.

- [85] X. Li, H. Wang, J. T. Robinson, H. Sanchez, G. Diankov and H. Dai, "Simultaneous nitrogen doping and reduction of graphene oxides," *Journal of American Chemical Societies*, vol. 131, no. 43, pp. 15939-15944, 2009.
- [86] C.-C. Liu, W. A. B and M. A. Vannice, "Measurement of electrical properties of a carbon black," *Carbon*, vol. 33, no. 12, pp. 1699-1708, 1995.
- [87] T. Schiros, D. Nordlund, L. Palova, D. Prezzi, L. Zhao, K. Kim, U. Wurstbauer, C. Gutierrez, D. Delongchamp, C. Jaye, D. Fischer, H. Ogasawara, L. G. M. Pettersson, D. R. Reichman, P. Kim, M. S. Hybertsen and A. N. Pasupathy, "Connecting dopant bond type with electronic structure on N-doped graphene," *Nano Letters*, vol. 12, no. 8, pp. 4025-4031, 2012.
- [88] E. Najafi, A. P. Hitchcock, D. Rossouw and G. A. Botton, "Mapping defects in a carbon nanotube by momentum transfer electron energy loss spectromicroscopy," *Ultramicroscopy*, vol. 113, pp. 158-164, 2012.
- [89] J. Goldstein, D. Newbury, D. Joy, C. Lyman, P. Echlin, E. Lifshin, L. Sawyer and J. Micheal, *Scanning Electron Microscopy and X-Ray Microanalysis*, 3rd ed., New York, NY: Springer, 2003.
- [90] R. Erni, *Aberation-corrected imaging in transmission electron microscopy: An introduction*, Covent Garden, London: Imperial College Press, 2010.
- [91] R. Egerton, R. McLeod, F. Wang and M. Malac, "Basic questions related to electron-induced sputtering in the TEM," *Ultramicroscopy*, vol. 110, pp. 991-997, 2010.
- [92] A. Zobelli, A. Gloter, C. P. Ewels, G. Seifert and C. Colliex, "Electron knock-on cross section of carbon and boron nitride nanotubes," *Physical Review B*, vol. 75, no. 24, p. 245402, 2007.

- [93] J. C. Meyer, F. K. S. Eder, V. Skakalova, J. Kotakoski, H. J. Park, S. Roth, A. Chuvilin, S. Eychus, G. Benner, A. V. Krasheninnikov and U. Kaiser, "Accurate measurement of electron beam induced displacement cross sections for single-layer graphene," *Physical Review Letters*, vol. 108, no. 19, p. 196102, 2012.
- [94] A. W. Robertson, C. Allen, Y. A. Wu, K. He, J. Olivier, J. Neethling, A. I. Kirkland and J. H. Warner, "Spatial control of defect creation in graphene at the nanoscale," *Nature Communications*, vol. 3, pp. 1144-1147, 2012.
- [95] K. Suenaga, Y. Iizumi and T. Okazaki, "Single atom spectroscopy with reduced delocalization effect using a 30 kV-STEM," *The European Physical Journal of Applied Physics*, vol. 54, no. 3, p. 33508, 2011.
- [96] J. Kotakoski, D. Santos-Cottin and A. Krasheninnikov, "Stability of Graphene Edges under Electron Beam: Equilibrium Energetics versus Dynamic Effects," *ACS Nano*, vol. 6, no. 7, pp. 671-676, 2012.
- [97] K. Suenaga and M. Koshino, "Atom-by-atom spectroscopy at graphene edge," *Nature*, vol. 468, no. 7327, pp. 1088-1090, 2010.
- [98] O. Scherzer, "The theoretical resolution limit of the electron microscope," *Journal of Applied Physics*, vol. 20, pp. 20-29, 1949.
- [99] P. Stadelmann, "JEMS-SAAS," 2014. [Online]. Available: <http://www.jems-saas.ch/>. [Accessed 26 June 2017].
- [100] O. Scherzer, *Optik*, vol. 2, pp. 114-132, 1947.
- [101] M. Haider, S. Uhlemann, E. Schwan, H. Rose, B. Kabius and K. Urban, "Electron microscopy image enhanced," *Nature*, vol. 392, pp. 768-769, 1998.

- [102] E. Yucelen, "Characterization of low-dimensional structures by advanced transmission electron microscopy," PhD of Science, Delft University of Technology, Delft Neatherlands, 2011.
- [103] J. Meyer, C. Kisielowski, R. Erni, M. Rossel, M. Crommie and A. Zettl, "Direct imaging of lattice atoms and topological defects in graphene membranes," *Nano Letters*, vol. 8, no. 11, pp. 3582-3586, 2008.
- [104] M. Otten and W. Coene, "High-resolution imaging on a field emission TEM," *Ultramicroscopy*, vol. 48, pp. 77-91, 1993.
- [105] M. Linck, P. Hartel, S. Uhlemann, F. Kahl, H. Muller, J. Zach, M. Haider, M. Neistadt, M. Bischoff, J. Biskupek, Z. Lee, T. Lehnert, F. Bornert, H. Rose and U. Kaiser, "Chromatic Aberration Correction for Atomic Resolution TEM Imaging from 20 to 80 kV," *Physical Review Letters*, vol. 117, p. 076101, 2016.
- [106] W. Coene, G. Janssen, M. Op de Beeck and D. Van Dyck, "Phase retrieval through focus variation for ultra-resolution in field-emission transmission electron microscopy," *Physical Review Letters*, vol. 69, no. 26, pp. 3743-4376, 1992.
- [107] B. Freitag, S. Kujawa, P. Mul, J. Ringnalda and P. Tiemeijer, "Breaking the spherical and chromatic aberration barrier in transmission electron microscopy," *Ultramicroscopy*, vol. 102, no. 3, pp. 209-214, 2005.
- [108] T. Walther, E. Quandt, H. Stegmann, A. Thesen and G. Benner, "First experimental test of a new monochromated and aberration-corrected 200 kV field-emission scanning transmission electron microscope," *Ultramicroscopy*, vol. 106, pp. 963-969, 2006.
- [109] P. Tiemeijer, "Measurement of coulomb interactions in an electron beam monochromator," *Ultramicroscopy*, vol. 78, pp. 53-62, 1999.

- [110] P. Tiemeijer, "Advanced EELS and the Monochromator," in *CCEM Summer School*, McMaster University, Hamilton, ON, 2012.
- [111] E. Kirkland, *Advanced computing in electron microscopy*, 2nd ed., Ithica, New York: Springer, 2010.
- [112] J. Meyer, A. Gaim, M. Katnelson, K. Novoselov, T. Booth and S. Roth, "The structure of suspended graphene sheets," *Nature*, vol. 446, no. 7131, pp. 60-63, 2007.
- [113] P. Huang, C. Ruiz-Vargas, A. van der Zande, W. Whitney, M. Levendorf, J. Kevek, S. Garg, J. Alden, C. Huestedt, Y. Zhu, J. Park, O. McEuen and D. Muller, "Grains and grain boundaries in single-layer graphene atomic patchwork quilts," *Nature*, vol. 469, no. 7330, pp. 389-393, 2011.
- [114] K. Kim, Z. Lee, W. Regan, C. Kisielowski, M. Crommie and A. Zettl, "Grain boundary mapping in polycrystalline graphene," *ACS Nano*, vol. 5, no. 3, pp. 2142-2146, 2011.
- [115] D. Long, W. Li, L. Ling, J. Miyawaki, I. Mochida and S. Yoon, "Preparation of nitrogen-doped graphene sheets by a combined chemical and hydrothermal reduction of graphene oxide," *Langmuir*, vol. 26, no. 20, pp. 16096-16102, 2010.
- [116] L. Qu, Y. Liu, J.-B. Baek and L. Dai, "Nitrogen-doped graphene as efficient metal-free electrocatalyst for oxygen reduction in fuel cells," *ACS Nano*, vol. 4, no. 3, pp. 1321-1326, 2010.
- [117] P. Nellist, "The Principles of STEM Imaging," in *Scanning Transmission Electron Microscope Imaging and Analysis*, S. Pennycook and P. Nellist, Eds., New York, NY, Springer, 2011, pp. 91-115.

- [118] O. Krivanek, M. Chrisholm, N. Dellby and M. Murfitt, "Atomic-Resolution STEM and Low Primary Energies," in *Scanning Transmission Electron Microscopy Imaging and Analysis*, S. Pennycook and P. Nellist, Eds., New York, NY, Springer, 2011, pp. 615-658.
- [119] Q. Ramasse, R. Zan, U. Bangert, D. Boukhvalov, Y.-W. Son and K. Novoselov, "Direct Experimental Evidence of Metal-Mediated Etching of Suspended Graphene," *ACS Nano*, vol. 6, no. 5, pp. 4063-4071, 2012.
- [120] R. Zan, U. Bangert, Q. Ramasse and K. Novoselov, "Metal-graphene interaction studied via atomic resolution scanning transmission electron microscopy," *Nano Letters*, vol. 11, no. 3, pp. 1087-1092, 2011.
- [121] G. Ilari, F. Hage, Y. Zhang, M. Rossell, Q. Ramasse, M. Niederberger and E. R., "Carbon–metal interfaces analyzed by aberration-corrected TEM: How copper and nickel nanoparticles interact with MWCNTs," *Micron*, vol. 72, pp. 52-58, 2015.
- [122] O. Krivanek, N. Dellby, M. C. M. Murfitt, T. Pennycook, K. Suenaga and V. Nicolosi, "Gentle STEM: ADF imaging and EELS at low primary energies," *Ultramicroscopy*, vol. 110, pp. 935-945, 2010.
- [123] G. Botton, "Analytical electron microscopy," in *Science of Microscopy*, New York, Springer, 2007, pp. 273-406.
- [124] C. Jeanguillaume and C. Colliex, "Spectrum-image: the next step in EELS digital acquisition and processing," *Ultramicroscopy*, vol. 28, no. 1-4, pp. 252-257, 1989.
- [125] R. Egerton, *Electron Energy-Loss Spectroscopy in the Electron Microscope*, 3rd ed., New York: Springer, 2011.

- [126] A. Hyvarinen and E. Oja, "Independent component analysis: algorithms and applications," *Neural Networks*, vol. 13, pp. 411-430, 2000.
- [127] F. de la Pena, T. Ostasevicius, V. Fauske, P. Burdet, P. Jokubauskas, M. Nord, ... and H.-W. Chang, "hyperspy/hyperspy: HyperSpy 1.3. Zenodo.," 2017.
- [128] L. Shimoyama, G. Wu, T. Sekiguchi and Y. Baba, "Evidence for the existence of nitrogen-substituted graphite structure by polarization dependence of near-edge x-ray adsorption fine structure," *Physical Review B: Condensed Matter Material Physics*, vol. 62, no. 10, pp. 6053-6056, 2000.
- [129] G. Abbas, P. Papakonstantinou, G. Iyer, I. Kirkman and L. Chen, "Substitutional nitrogen incorporation through rf glow discharge treatment and subsequent oxygen uptake on vertically aligned carbon nanotubes," *Physical Review B*, vol. 75, no. 19, p. 195429, 2007.
- [130] X. Li, W. Hua, J. Guo and Y. Luo, "Electronic Structure of Nitrogen-Doped Graphene in the Ground and Core-Excited States from First-Principles Simulations," *The Journal of Physical Chemistry C*, vol. 119, pp. 16660-16666, 2015.
- [131] R. Arenal, K. March, C. Ewels, X. Rocquefelte, M. Kociak, A. Loiseau and O. Stephan, "Atomic Configuration of Nitrogen-Doped Single-Walled Carbon Nanotubes," *Nano Letters*, vol. 14, pp. 5509-5516, 2014.
- [132] Y.-C. Lin, P.-Y. Teng, C.-H. Yeh, M. Koshino, P.-W. Chiu and K. Suenaga, "Structural and Chemical Dynamics of Pyridinic-Nitrogen Defects in Graphene," *Nano Letters*, vol. 15, pp. 7408-7413, 2015.

- [133] Y. Li, W. Zhou, H. Wang, L. Xie, Y. Liang, F. Wei, J.-C. Idrobo, S. Pennycook and H. Dai, "An oxygen reduction electrocatalyst based on carbon nanotube-graphene complexes," *Nature Nanotechnology*, vol. 7, no. 6, pp. 394-400, 2012.
- [134] K. Mayrhofer, S. M. J. Ashton, G. Wiberg, M. Hanzlik and M. Arenz, "Non-destructive transmission electron microscopy study of catalyst degradation under electrochemical treatment," *Journal of Power Sources*, vol. 185, pp. 734-739, 2008.
- [135] D. Rossouw, L. Chinchilla, N. Kremliakova and G. Botton, "The 3D Nanoscale Evolution of Platinum–Niobium Oxide Fuel Cell Catalysts via Identical Location Electron Tomography," *Particle and Particle Synthesis Characterization*, vol. 34, p. 1700051, 2017.
- [136] L. Chinchilla, D. Rossouw, T. Trefz, D. Susac, N. Kremliakova and G. Botton, "Nanoscale analysis of structural and chemical changes in aged hybrid Pt/NbO_x/C fuel cell catalysts," *Journal of Power Sources*, vol. 356, pp. 140-152, 2017.
- [137] S. Hofmann, Auger- and X-ray- Photoelectron Spectroscopy in Material Science: A User Oriented Guide, Verlag Berlin Heidelberg: Springer, 2013.
- [138] S. Stambula, N. Gauquelin, M. Bugnet, S. Gorantla, S. Turner, S. Sun, J. Liu, G. Zhang, X. Sun and G. Botton, "Chemical Structure of Nitrogen-Doped Graphene with Single Platinum Atoms and Atomic Clusters as a Platform for the PEMFC Electrode," *Journal of Physical Chemistry C*, vol. 118, pp. 3890-3990, 2014.
- [139] J. Jinschek, E. Yucelec, H. Calderon and B. Freitag, "Quantitative atomic 3-D imaging of single/double sheet graphene structure," *Carbon*, vol. 49, pp. 556-562, 2011.

- [140] R. Nicholls, A. Murdock, J. Tsang, J. Britton, T. Pennycook, A. Koos, P. Nellist, N. Grobert and J. Yates, "Probing the bonding in nitrogen-doped graphene using electron energy loss spectroscopy," *ACS Nano*, vol. 7, pp. 7145-7150, 2013.
- [141] R. Egerton, *Electron energy-loss spectroscopy in the electron microscope*, Boston, USA: Springer, 2011.
- [142] W. Hummers and R. Offerman, "Preparation of graphite oxide," *Journal of American Chemical Society*, vol. 80, pp. 1339-1339, 1958.
- [143] J. Warner, M. Rummeli, L. Ge, T. Gemming, B. Montanari, N. Harrison, B. Buchner and G. Briggs, "Structural transformations in graphene studied with high spatial and temporal resolution," *Nature Nanotechnology*, vol. 4, pp. 500-504, 2009.
- [144] C. Gomez-Navarro, J. Meyer, R. Sundaram, A. Chuvilin, S. Kurasch, M. Burghard, K. Kern and U. Kaiser, "Atomic structure of reduced graphene oxide," *Nano Letters*, vol. 10, pp. 1144-1148, 2010.
- [145] J. Meyer, S. Kurasch, H. Park, V. Skakalova, D. Kunzel, A. GroB, A. Chuvilin, G. Algara-Siller, S. Roth, T. Iwasaki, U. Starke, J. Smet and U. Kaiser, "Experimental analysis of charge redistribution due to chemical bonding by high-resolution transmission electron microscopy," *Nature Material*, vol. 10, pp. 209-215, 2011.
- [146] H.-K. Jeong, H.-J. Noh, J.-Y. Kim, M.-H. Jin, C. Park and Y. Lee, "X-ray adsorption spectroscopy of graphite oxide," *Europhysics Letters*, vol. 82, pp. 67004 1-5, 2008.
- [147] A. Gunguly, S. Sharma, P. Papkonstantinou and J. Hamilton, "Probing the thermal deoxygenation of graphene oxide using high-resolution in-situ X-ray based spectroscopies," *Journal of Physical Chemistry C*, vol. 115, pp. 17009-17019, 2011.

- [148] T. Van Khai, H. Na, D. Kwak, Y. Kwon, H. Ham, K. Shim and H. Kim, "Significant enhancement of blue emission and electrical conductivity of N-doped graphene," *Journal of Material Chemistry*, vol. 22, pp. 17992-18003, 2012.
- [149] D. Kepaptsoglou, T. Hardcastle, C. Seabourne, U. Bangert, R. Zan, J. Amani, H. Hofsass, R. Nicholls, R. Brydson, A. Scott and Q. Ramasse, "Electronic Structure Modification of Ion Implanted Graphene: The Spectroscopic Signatures of p- and n-Type Doping," *ACS Nano*, vol. 9, no. 11, pp. 11398-11407, 2015.
- [150] J. Casanovas, J. Ricart, J. Rubio, F. Illas and J. Jimenez-Mateis, "Origin of the large N1s binding energy in X-ray photoelectron spectra of calcined carbonaceous materials," *Journal of American Chemical Society*, vol. 118, no. 34, pp. 8071-8076, 1996.
- [151] D. Geng, S. Yang, Y. Zhang, J. Yang, J. Liu, R. Li, T.-K. Sham, X. Sun, S. Ye and S. Knights, "Nitrogen doping effects on the structure of graphene," *Applied Surface Science*, vol. 257, pp. 9193-9198, 2011.
- [152] P. Blaha, K. Schwarz, G. Madsen, D. Kvasnicka and J. Luitz, "WIEN2k, An Augmented Plane Wave + Local Orbitals Program for Calculating Crystal Properties," ISBN 3-9501031-1-2, Karlheinz Schwarz, Techn. Universität Wien, Austria, 2001.
- [153] P. Blaha, K. Schwarz, G. Madsen, D. Kvasnicka and J. Luitz, "WIEN2k An Augmented Plane Wave Plus Local Orbitals Program for Calculating Crystal Properties User's Guide," ISBN 3-9501031-1-2, Vienna, Austria, 2016.
- [154] J. Warner, Lin, Y-C, K. He, M. Koshino and K. Suenaga, "Stability and Spectroscopy of Single Nitrogen Dopants in Graphene at Elevated Temperatures," *ACS Nano*, vol. 8, no. 11, pp. 11806-11815, 2014.

- [155] P. Blaha, K. Schwarz, G. Madsen, D. Kvasnicka and J. Luitz, WIEN2k An Augmented Plane Wave Plus Local Orbitals Program for Calculating Crystal Properties, User's Guide, WIEN2k_14.2 ed., Vienna, Austria, 2014.
- [156] S. Cottenier, "Density Functional Theory and the Family of (L)APW-methods: a step-by-step introduction," (2nd edition), ISBN 978-90-807215-1-7, (freely available at http://www.wien2k.at/reg_user/textbooks), 2002-2013.
- [157] C. Hebert, "Practical aspects of running the WIEN2k code for electron spectroscopy," *Micron*, vol. 38, pp. 12-28, 2007.
- [158] P. Blaha, K. Schwarz, G. Madsen, D. Kvasnicka and J. Luitz, "WIEN2k An Augmented Plane Wave Plus Local Orbitals Program User's Guide, WIEN2k 17.1 (Release 07/03/2017)," Vienna University of Technology Institute of Materials Chemistry, Vienna, 2017.
- [159] P. Blockl, O. Jepsen and O. Andersen, "Improved tetrahedron method for Brillouin-zone integrations," *Physical Review B*, vol. 49, p. 16223, 1994.
- [160] J. Warner, Y.-C. Lin, K. He, M. Koshino and K. Suenaga, "Atomic Level Spatial Variations of Energy States along Graphene Edges," *Nano Letters*, vol. 14, pp. 6155-6159, 2014.
- [161] W. Zhuo, M. Kapetanakis, M. Prange, S. Pantelides, S. Pennycook and J.-C. Idrobo, "Direct determination of the chemical bonding of individual impurities in graphene," *Physical Review Letters*, vol. 109, p. 206803, 2012.
- [162] S. Sun, G. Zhang, N. Gauquelin, N. Chen, J. Zhuo, S. Yang, W. Chen, X. Meng, D. Geng, M. Banis, R. Li, S. Ye, S. Knights, B. G.A, S. T-K and X. Sun, "Single-atom catalysis under Pt/Graphene achieved through atomic layer deposition," *Scientific Reports*, vol. 3, pp. 1-9, 2013.

- [163] O. Cretu, A. Krashennikov, J. Rodriguez-Manzo, L. Sun, R. Nieminen and F. Banhart, "Migration and localization of metal atoms on strained graphene," *Physical Review Letters*, vol. 105, p. 196102, 2010.
- [164] Y. Gan, L. Sun and F. Banhart, "One and two-dimensional diffusion of metal atoms in graphene," *Small*, vol. 4, pp. 587-591, 2008.
- [165] R. Zan, Q. Ramasse, R. Jalil and U. Bangert, "Atomic Structure of Graphene and h-BN Layers and Their Interactions with Metals," in *Advances in Graphene Science*, M. Aliofkhazraei, Ed., InTech, 2013, pp. 3-30.
- [166] W. L. Wang, E. Santos, B. Jiang, E. Cubuk, C. Ophus, A. Centeno, A. Pesquera, A. Zurutuza, J. Ciston, R. Westervelt and E. Kaxiras, "Direct Observation of a Long-Lived Single-Atom Catalyst Chiseling Atomic Structures in Graphene," *Nano Letters*, vol. 14, pp. 450-455, 2014.
- [167] T. Shu, S.-J. Liao, C.-T. Hsieh, A. Roy, Y.-Y. Liu, D.-Y. Tzou and W.-Y. Chen, "Fabrication of platinum electrocatalysts on carbon nanotubes using atomic layer deposition for proton exchange membrane fuel cells," *Electrochimica Acta*, vol. 75, pp. 101-107, 2012.
- [168] T. Imaoka, H. Kitazawa, C. W-J, S. Omura, K. Albrecht and K. Yamamoto, "Magic Number Pt₁₃ and Misshapen Pt₁₂ Clusters: Which One is the Better Catalyst?," *Journal of the American Chemical Society*, vol. 135, pp. 13089-13095, 2013.
- [169] K. Yamamoto, T. Imaoka, C. W-J, O. Enoki, H. Katoh, M. Takenaga and A. Sonoi, "Size-Specific Catalytic Activity of Platinum Clusters Enhances Oxygen Reduction Reaction," *Nature Chemistry*, vol. 1, pp. 397-402, 2009.

- [170] T. Imaoka, H. Kitazawa, W.-J. Chen and K. Yamamoto, "Finding the Most Catalytically Active Platinum Clusters Low Atomicity," *Angewandte Communications*, vol. 54, pp. 9810-9815, 2015.
- [171] X. Zhang, J. Guo, P. Guan, C. Liu, H. Huang, F. Xue, X. Dong, S. Pennycook and M. Chrisholm, "Catalytically active single-atom niobium in graphitic layers," *Nature Communications*, vol. 4, p. 1924, 2013.
- [172] C. Zhang, J. Sha, H. Fei, M. Liu, S. Yazdi, J. Zhang, Q. Zhong, X. Zou, N. Zhao, H. Yu, Z. Jiang, E. Ringe, B. Yakobson, J. Dong, D. Chen and J. Tour, "Single-Atomic Ruthenium Catalytic Sites on Nitrogen-Doped Graphene for Oxygen Reduction Reaction in Acidic Medium," *ACS Nano*, vol. 11, pp. 6930-6941, 2017.
- [173] Q. Jia, N. Ramaswamy, H. Hafiz, U. Tylus, K. Strickland, G. Wu, B. Barbellini, A. Bansil, E. Holby, P. Zelany and S. Mukerjee, *ACS Nano*, vol. 9, no. 12, pp. 12496-12505, 2015.
- [174] A. Zitolo, V. A. V. Goellner, M.-T. Sougrati, T. Mineva, L. Stievano, E. Fonda and F. Jaouen, "Identification of catalytic sites for oxygen reduction in iron- and nitrogen-doped graphene materials," *Nature Materials*, vol. 14, pp. 937-944, 2015.
- [175] P. Yin, T. Yao, Y. Wu, L. Zheng, Y. Lin, W. Liu, H. Ju, J. Zhu, X. Hong, Z. Deng, G. Zhou, S. Wei and Y. Li, "Single Cobalt Atoms with Precise N-Coordination as Superior Oxygen Reduction Reaction Catalysts," *Angewandte Chemie International Edition*, vol. 55, pp. 10800-10805, 2016.
- [176] C. Choi, M. Kim, H. Kwon, S. Cho, S. Yun, H.-T. Kim, K. Mayrhofer, H. Kim and M. Choi, "Tuning selectivity of electrochemical reactions by atomically dispersed platinum catalyst," *Nature Communications*, vol. 7, p. 10922, 2016.

- [177] F. Grillo, H. Bui, J. Moulijin, M. Kreutzer and J. van Ommen, "Understanding and Controlling the Aggregative Growth of Platinum Nanoparticles in Atomic Layer Deposition: An Avenue to Size Selections," *The Journal of Physical Chemistry Letters*, vol. 8, pp. 975-983, 2017.
- [178] X. Liang, Y. Zhuo, J. Li and A. Weimer, "Reaction mechanism studies for platinum nanoparticle growth by atomic layer deposition," *Journal of Nanoparticle Research*, vol. 13, pp. 3781-3788, 2011.
- [179] A. Mackus, N. Leick, L. Baker and W. Kessels, "Catalytic Combustion and Dehydrogenation Reactions during Atomic Layer Deposition of Platinum," *Chemistry of Materials*, vol. 24, pp. 1752-1761, 2012.
- [180] J. Norskov, T. Bligaard, A. Logadottir, J. Kitchin, J. Chen, S. Pandelov and U. Stimming, "Trends in the Exchange Current for Hydrogen Evolution," *Journal of the Electrochemical Society*, vol. 152, no. 3, pp. J23-J26, 2005.
- [181] M. Zeng and Y. Li, "Recent advances in heterogeneous electrocatalysts for the hydrogen evolution reaction," *Journal of Materials Chemistry A*, vol. 3, pp. 14942-14962, 2015.
- [182] Y. Jiao, Y. Zheng, M. Jaroniec and S. Qiao, "Design of electrocatalysts for oxygen- and hydrogen-involving energy conversion reactions," *Chemical Society Reviews*, vol. 44, pp. 2060-2086, 2015.
- [183] T. Jaramillo, K. Jorgensen, J. Bonde, J. Nielsen, S. Horch and I. Chorkendorff, "Identification of Active Edge Sites for Electrochemical H₂ Evolution from MoS₂ Nanocatalysts," *Science*, vol. 317, pp. 100-102, 2007.

- [184] Y. Zheng, Y. Jiao, Y. Zhu, L. Li, Y. Han, Y. Chen, A. Du, M. Jaroniec and S. Qiao, "Hydrogen evolution by a metal-free electrocatalyst," *Nature Communications*, vol. 5, p. 3783, 2014.
- [185] J. Deng, H. Li, J. Xiao, Y. Tu, D. Deng, H. Yang, H. Tian, J. Li, P. Ren and X. Bao, "Triggering the electrocatalytic hydrogen evolution activity of the inert two-dimensional MoS₂ surface via single-atom metal doping," *Energy and Environmental Science*, vol. 8, pp. 1594-1601, 2015.
- [186] D. Bulushev, M. Zacharska, A. Lisitsyn, O. Podyacheva, F. Hage, Q. Ramasse, U. Bangert and L. Bulusheva, "Single Atoms of Pt-Group Metals Stabilized by N-Doped Carbon Nanofibers for Efficient Hydrogen Production from Formic Acid," *ACS Catalysis*, vol. 6, pp. 3442-3451, 2016.
- [187] H. Fei, J. Dong, M. Arellano-Jimenez, G. Ye, N. Kim, E. Samuel, Z. Peng, Z. Zhu, F. Qin, J. Bao, M. Yacaman, P. Ajayan, D. Chen and J. Tour, "Atomic cobalt on nitrogen-doped graphene for hydrogen generation," *Nature Communications*, vol. 6, p. 8668, 2015.
- [188] R. Egerton, "Beam-Induced Motion of Adatoms in the Transmission Electron Microscope," *Microscopy and Microanalysis*, vol. 19, pp. 479-486, 2013.
- [189] Y. Wang, Y. Shao, D. Matson, J. Li and Y. Lin, "Nitrogen-Doped Graphene and Its Application in Electrochemical Biosensing," *ACS Nano*, vol. 4, no. 4, pp. 1790-1798, 2010.
- [190] Y. Shao, S. Zhang, M. Engelhard, G. Li, G. Shao, Y. Wang, J. Liu, I. Aksay and Y. Lin, "Nitrogen-doped graphene and its electrochemical applications," *Journal of Material Chemistry*, vol. 20, pp. 7491-7496, 2010.

- [191] B. Guo, Q. Liu, E. Chen, H. Zhu, L. Fang and J. Gong, "Controllable N-Doping of Graphene," *Nano Letters*, vol. 10, pp. 4975-4980, 2010.
- [192] C.-T. Pan, J. Hinks, Q. Ramasse, G. Greaves, U. Bangert, S. Donnelly and S. Haigh, "In-situ observation and atomic resolution of the ion irradiation induced amorphisation of graphene," *Scientific Reports*, vol. 4, p. 6334, 2014.
- [193] E. Ahlgren, J. Kotakoski and A. V. Krashennnikov, "Atomistic simulations of the implantation of low-energy boron and nitrogen ions into graphene," *Physical Review B*, vol. 83, p. 115424, 2011.
- [194] K.-J. Kim, H. Lee, J. Choi, H. Lee, M. Jung, H. Shin, T.-H. Kang, B. Kim and S. Kim, "Surface property change of graphene using nitrogen ion," *Journal of Physics: Condensed Matter*, vol. 22, p. 045005, 2010.
- [195] Y. Xu, K. Zhang, C. Brusewitz, X. Wu and H.-C. Hofsass, "Investigation of the effect of low energy ion beam irradiation on mono-layer graphene," *AIP Advances*, vol. 3, p. 072120, 2013.
- [196] U. Bangert, W. Pierce, D. Kepaptsoglou, Q. Ramasse, R. Zan, M. Gass, V. d. Berg, J.A. Boothroyd, J. Amani and H. Hofsass, "Ion Implantation of Graphene-Toward IC Compatible Technologies," *Nano Letters*, vol. 13, pp. 4902-4907, 2013.
- [197] K.-J. Kim, S. Yang, Y. Park, M. Lee, B. Kim and H. Lee, "Annealing Effects after Nitrogen Ion Casting on Monolayer and Multilayer Graphene," *Journal of Physical Chemistry C*, vol. 117, pp. 2129-2134, 2013.
- [198] M. Telychko, P. Mutombo, M. Ondracek, P. Hapala, F. Bocquet, J. Kolorenc, M. Vondracek, P. Jelinek and M. Svec, "Achieving High-Quality Single-Atom Nitrogen Doping of Graphene/SiC(0001) by Ion Implantation and Subsequent Thermal Stabilization," *ACS Nano*, vol. 8, no. 7, pp. 7318-7324, 2014.

- [199] W. Zhao, O. Hofert, K. Gotterbarm, J. Zhu, C. Papp and H.-P. Steinruck, "Production of Nitrogen-Doped Graphene by Low-Energy Nitrogen Implantation," *Journal of Physical Chemistry C*, vol. 116, pp. 5062-5066, 2012.
- [200] S. Hofmann, *Auger- and X-Ray Photoelectron Spectroscopy in Material Science: A User Oriented Guide*, Heidelberg: Springer, 2013.
- [201] M. Xu, D. Fujita, J. Gao, Hanagata and N, "Auger Electron Spectroscopy: A Rational Method for Determining Thickness of Graphene Films," *ACS Nano*, vol. 4, no. 5, pp. 2937-2945, 2010.
- [202] "Graphene Transmission Electron Microscopy Support Films," Graphene Supermarket, [Online]. Available: http://www.graphene-supermarket.com/images/XC/TEM/GrapheneTEMgrids-General_info.pdf. [Accessed 18 February 2013].
- [203] I. Bicket, "Data Analysis," GitHub, Inc, [Online]. Available: <https://github.com/icbicket/DataAnalysis>. [Accessed 13 June 2017].
- [204] Z. Bai, L. Zhang and L. Liu, "Bombarding Graphene with Oxygen Ions: Combining Effects of Incident Angle and Ion Energy To Control Defect Generation," *The Journal of Physical Chemistry C*, vol. 119, pp. 26793-26802, 2015.
- [205] A. Mkhoyan, A. Contryman, J. Silcox, D. Stewart, G. Eda, M. C. S. Miller and M. Chhowalla, "Atomic and electronic structure of graphene oxide," *Nano Letters*, vol. 9, no. 3, pp. 1058-1063, 2009.
- [206] J. Elam, A. Zinovev, C. Han, H. Wang, U. Welp, J. Hryn and M. Pellin, "Atomic layer deposition of palladium films on Al₂O₃ surfaces," *Thin Solid Films*, vol. 515, pp. 1664-1673, 2006.

- [207] J. Hamalainen, M. Ritala and M. Leskela, "Atomic Layer Deposition of Noble Metals and Their Oxides," *Chemistry of Materials*, vol. 26, no. 1, pp. 786-801, 2014.
- [208] A. Mackus, M. Weber, N. Thissen, D. Garcia-Alonso, R. Vervuurt, S. Assali, A. Bol, M. Verheijen and W. Kessels, "Atomic layer deposition of Pd and Pt nanoparticles for catalysis: on the mechanisms of nanoparticle formation," *Nanotechnology*, vol. 27, p. 034001, 2016.
- [209] C. Schnieder, W. Rasband and K. Eliceiri, "NIH Image to ImageJ: 25 years of image analysis," *Nature methods*, vol. 9, no. 7, pp. 671-675, 2012.
- [210] S. Iijima, "Helical microtubules of graphitic carbon," *Nature*, vol. 354, pp. 56-58, 1991.
- [211] R. Andrews, D. Jacques, D. Qian and T. Rantell, "Multi-walled carbon nanotubes, synthesis and application," *Accounts of Chemical Research*, vol. 35, no. 12, pp. 1008-1017, 2002.
- [212] J. Lehman, M. Terrones, E. Mansfield, K. Hurst and V. Meunier, "Evaluating the characteristics of multiwalled carbon nanotubes," *Carbon*, vol. 49, no. 8, pp. 2581-2602, 2011.
- [213] A. Kukovecz, G. Kozma and Z. Konya, "Multiwalled Carbon Nanotubes," in *Springer Handbook of Nanomaterials*, Houston, TX, Springer, 2013, pp. 147-188.
- [214] L. Forro and C. Schonenberger, "Physical properties of multi-walled nanotubes," *Carbon Nanotubes*, vol. 80, pp. 329-390, 2001.
- [215] C. Judge, N. Gauquelin, L. Walters, M. Wright, J. Cole, J. Madden, G. Botton and M. Griffiths, "Intergranular fracture in irradiated Inconel X-750 containing very

- high concentrations of helium and hydrogen," *Journal of Nuclear Materials*, vol. 457, pp. 165-172, 2015.
- [216] S. Trasobares, O. Stephan, C. Colliex, G. Hug, W. Hsu, H. Kroto and D. Walton, "Electron beam puncturing of carbon nanotube containers for release of stored N₂ gas," *The European Physical Journal B*, vol. 22, pp. 117-122, 2001.
- [217] M. Reyes-Reyes, N. Gobert, R. Kamalakaran, T. Seeger, D. Golberg, M. Ruhle, Y. Bando, H. Terrone and M. Terrones, "Efficient encapsulation of gaseous nitrogen inside carbon nanotubes with bamboo-like structure using aerosol thermolysis," *Chemical Physics Letters*, vol. 396, pp. 167-173, 2004.
- [218] J. Liu, Y. Zhang, M. Ionescu, R. Li and X. Sun, "Nitrogen-doped carbon nanotubes with tunable structure and high yield produced by ultrasonic spray pyrolysis," *Applied Surface Science*, vol. 257, pp. 7837-7844, 2011.
- [219] H. Choi, S. Bae, W.-S. Jang, J. Park, H. Song, H.-J. Shin, H. Jung and J.-P. Ahn, "Release of N₂ from the Carbon Nanotubes via High-Temperature Annealing," *Journal of Physical Chemistry B*, vol. 109, pp. 1683-1688, 2005.
- [220] M. Terrones, R. Kamalakaran, T. Seeger and M. Ruhle, "Novel nanoscale gas containers: encapsulation of N₂ in CN_x nanotubes," *Chemical Communications*, vol. 0, pp. 2335-2336, 2000.
- [221] J. Su, Y. Yu and R. Che, "Aligned array of N₂-encapsulated multilevel branched carbon nanotubes," *Applied Physics A*, vol. 90, pp. 135-139, 2008.
- [222] S. Enouz, J. Bantignies, M. Babaa, L. Alvarez, P. Parent, P. Le Normand, O. Stephan, P. Poncharal, A. Loiseau and B. Doyle, "Spectroscopic Study of Nitrogen Doping of Multi-Walled Carbon Nanotubes," *Journal of Nanoscience and Nanotechnology*, vol. 7, pp. 3524-3527, 2007.

- [223] J. Zhuo, J. Wang, H. Liu, M. Banis, X. Sun and T.-K. Sham, "Imaging Nitrogen in Individual Carbon Nanotubes," *The Journal of Physical Chemistry Letters*, vol. 1, pp. 1709-1713, 2010.
- [224] S. Trasobares, O. Stephan, C. Colliex, W. Hsu, H. Kroto and D. Walton, "Compartmentalized CNx nanotubes: Chemistry, morphology, and growth," *Journal of Chemical Physics*, vol. 116, no. 20, pp. 8966-8972, 2002.
- [225] "GIF Quantum Energy Filters," Gatan, Inc, 2017. [Online]. Available: <http://www.gatan.com/products/tem-imaging-spectroscopy/gif-quantum-energy-filters>. [Accessed 27 October 2017].
- [226] C. Walsh, J. Yuan and L. Brown, "A procedure for measuring the helium density and pressure in nanometre-sized bubbles in irradiated materials using electron-energy-loss spectroscopy," *Philosophical Magazine A*, vol. 80, no. 7, pp. 1507-1543, 2000.
- [227] B. Lacroix, V. Godinho and A. Fernandez, "Nitrogen nanobubbles in a-SiOxNy Coatings: Evaluation of its physical properties and chemical bonding state by spatially resolved electron energy-loss spectroscopy," *The Journal of Physical Chemistry C*, vol. 120, no. 10, pp. 5651-5658, 2016.
- [228] D. Taverna, M. Kociak, O. Stephan, A. Fabre, E. Finot, B. Decamps and C. Colliex, "Probing physical properties of confined fluids within individual nanobubbles," *Physical Review Letters*, vol. 100, no. 3, p. 035301, 2008.
- [229] M.-L. David, K. Alix, F. Pailloux, V. Mauchamp, M. Couillard and G. P. L. Botton, "In situ controlled modification of the helium density in single helium-filled nanobubbles," *Journal of Applied Physics*, vol. 115, p. 123508, 2014.

- [230] H. Yoshida, S. Takeda, T. Uchiyama, H. Kohno and Y. Homma, "Atomic-Scale In-situ Observation of Carbon Nanotube Growth from Solid State Iron Carbide Nanoparticles," *Nano Letters*, vol. 8, no. 7, pp. 2082-2086, 2008.
- [231] S. Hofmann, R. Sharma, C. Ducati, G. Du, C. Mattevi, C. Cepek, M. Cantoro, S. Pisana, A. Parvez, F. Cervantes-Sodi, A. Ferrari, R. Dunin-Borkowski, S. Lizzit, L. Petaccia, A. Goldoni and J. Robertson, "In situ Observations of Catalyst Dynamics during Surface-Bound C Nanotube Nucleation," *Nano Letters*, vol. 7, no. 3, pp. 602-608, 2007.
- [232] J. Jinschek, "Advances in the environmental transmission electron microscope (ETEM) for nanoscale in situ studies of gas-solid interactions," *Chemical Communications*, vol. 50, pp. 2696-2706, 2014.
- [233] P. Strak and S. Krukowski, "Molecular N₂ properties: The intermolecular potential and equation of state," *The Journal of Chemical Physics*, vol. 126, p. 194501, 2007.
- [234] I. Palaci, S. Fedrigo, H. Brune, C. Klinke, M. Chen and E. Riedo, "Radial Elasticity of Multiwalled Carbon Nanotubes," *Physical Review Letters*, vol. 94, no. 17, p. 175502, 2005.
- [235] R. Mills, B. Olinger and D. Cromer, "Structures and phase diagrams of N₂ and CO to 13 GPa by x-ray diffraction," *Journal of Chemical Physics*, vol. 84, no. 5, pp. 2837-2845, 1986.
- [236] E. Gregoranz, A. Goncharov, R. Hemley and H. Mao, "High-pressure amorphous nitrogen," *Physical Review B*, vol. 64, p. 052103, 2001.

- [237] J. Li, X. Liang, D. King, Y.-B. Jiang and A. Weimer, "Highly dispersed Pt nanoparticle catalyst prepared by atomic layer deposition," *Applied Catalysis B: Environmental*, vol. 97, pp. 220-226, 2010.
- [238] T. Aaltonen, M. Ritala, T. Sajavaara, J. Keinonen and M. Leskela, "Atomic Layer Deposition of Platinum Thin Films," *Chemistry of Materials*, vol. 15, pp. 1924-1928, 2003.
- [239] A. Mackus, M. Verheijen, N. Leick, A. Bol and W. Kessels, "Influence of Oxygen Exposure on the Nucleation of Platinum Atomic Layer Deposition: Consequences for Film Growth, Nanopatterning, and Nanoparticle Synthesis," *Chemistry of Materials*, vol. 25, no. 9, pp. 1905-1911, 2013.
- [240] W. Setthapun, W. Williams, S. Kim, H. Feng, J. Elam, F. Rabuffetti, K. Poepelmeier, P. Stair, E. Stach, F. Ribeiro, J. Miller and C. Marshall, "Genesis and Evolution of Surface Species during Pt Atomic Layer Deposition on Oxide Supports Characterized by in Situ XAFS Analysis and Water-Gas Shift Reaction," *Journal of Physical Chemistry C*, vol. 114, pp. 9758-9771, 2010.
- [241] S. Takakusagi, K.-I. Fukui, R. Tero, F. Nariyuki and Y. Iwasawa, "Self-Limiting Growth of Pt Nanoparticles from MeCpPtMe₃ Adsorbed on TiO₂ (110) Studied by Scanning Tunneling Microscopy," *Physical Review Letters*, vol. 91, no. 6, p. 066102, 2003.
- [242] W. Kessels, H. Knoops, S. Dielissen, A. Mackus and M. van de Sanden, "Surface reactions during atomic layer deposition of Pt derived from gas phase infrared spectroscopy," *Applied Physics Letters*, vol. 95, p. 013114, 2009.
- [243] J. King, A. Wittstock, J. Beiner, S. Kucheyev, Y. Wang, T. Baumann, S. Giri, A. Hamza, M. Baeumer and S. Bent, "Ultralow Loading Pt Nanocatalysts Prepared by

- Atomic Layer Deposition on Carbon Aerogels," *Nano Letters*, vol. 8, no. 8, pp. 2405-2409, 2008.
- [244] H. Lee, S. Baeck, T. Jaramillo and S. Bent, "Growth of Pt Nanowires by Atomic Layer Deposition on Highly Ordered Pyrolytic Graphite," *Nano Letters*, vol. 13, pp. 457-463, 2013.
- [245] K. Kim, H.-B.-R. Lee, R. Johnson, J. Tanskanen, N. Liu, M.-G. Kim, C. Pang, C. Ahn, S. Bent and Z. Bao, "Selective metal deposition at graphene line defects by atomic layer deposition," *Nature Communications*, vol. 5, p. 4781, 2014.
- [246] H. Yan, H. Cheng, H. Yi, Y. Lin, T. Yao, C. Wang, J. Li, S. Wei and J. Lu, "Single-Atom Pd1/Graphene Catalyst Achieved by Atomic Layer Deposition: Remarkable Performance in Selective Hydrogenation of 1,3-Butadiene," *Journal of the American Chemical Society*, vol. 137, pp. 10484-10487, 2015.
- [247] S. Kim, J. Han, G. Kim and C. Hwang, "Investigation on the Growth Initiation of Ru Thin Films by Atomic Layer Deposition," *Chemistry of Materials*, vol. 22, pp. 2850-2856, 2010.
- [248] A. Mackus, A. Bol and W. Kessels, "Catalytic Surface Reactions during Nucleation and Growth of Atomic Layer Deposition of Noble Metals: a Case Study for Platinum," *ECS Transactions*, vol. 58, no. 10, pp. 183-193, 2013.
- [249] A. Mackus, M. Weber, N. Thissen, D. Garcia-Alonso, R. Vervuurt, S. Assali, A. Bol, M. Verheijen and W. Kessels, "Atomic layer deposition of Pd and Pt nanoparticles for catalysis: on the mechanisms of nanoparticle formation," *Nanotechnology*, vol. 27, p. 034001, 2016.
- [250] H. Van Bui, F. Grillo and J. van Ommen, "Atomic and molecular layer deposition: off the beaten track," *Chemical Communications*, vol. 53, pp. 45-71, 2017.

- [251] M. Corporation, Materials and Electrochemical Research Corporation, [Online]. Available: <http://www.mercorp.com/>. [Accessed August 2017].
- [252] B. Smith and D. Luzzi, "Electron irradiation effects in single wall carbon nanotubes," *Journal of Applied Physics*, vol. 90, no. 7, pp. 3509-3515, 2001.
- [253] C. A. Schneider, W. S. Rasband and K. Eliceiri, "NIH Image to ImageJ: 25 years of image analysis," *Nature Methods*, vol. 9, pp. 671-675, 2012.
- [254] N. Okamoto, B. Reed, S. Mehraeen, A. Kulkarni, D. Morgan, B. Gates and N. Browning, "Determination of Nanocluster Sizes from Dark-Field Scanning Transmission Electron Microscopy Images," *The Journal of Physical Chemistry C Letters*, vol. 112, pp. 1759-1763, 2008.
- [255] C. Soderman, A. Johnsson, J. Vikgren, R. Morrlund, D. Molnar, A. Svalkvist, L. Mansson and M. Bath, "Evaluation of Accuracy and Precision of Manual Size Measurements in Chest Tomosynthesis using Simulated Pulmonary Nodules," *Academic Radiology*, vol. 22, no. 4, pp. 496-504, 2015.
- [256] J.-W. Kim, T. Kogure, K. Yang, S.-T. Kim, Y.-N. Jang, H.-S. Baik and G. Geesey, "The Characterization of CaCO₃ in a Geothermal Environment: A SEM/TEM Study," *Clay and Clay Minerals*, vol. 60, no. 5, pp. 484-495, 2012.
- [257] M. Rose, J. Bartha and I. Endler, "Temperature dependence of the sticking coefficient in atomic layer deposition," *Applied Surface Science*, vol. 256, pp. 3778-3782, 2010.
- [258] M. de Bruijne, "Machine learning approaches in medical image analysis: From detection to diagnosis," *Medical Image Analysis*, vol. 33, pp. 94-97, 2016.

- [259] A. c. o. p.-b. a. o.-b. i. a. w. s. m. l. a. f. t. c. o. a. l. u. S.-5. H. imagery, "Duro, D.C; Franklin, S.E; Dube, M.G," *Remote Sensing of Environment*, vol. 118, pp. 259-272, 2012.
- [260] I. Arganda-Carreras, V. Kaynig, C. Rueden, K. Eliceiri, J. Schindelin, A. Cardona and H. Seung, "Trainable Weka Segmentation: a machine learning tool for microscopy pixel classification," *Bioinformatics*, vol. 33, no. 15, pp. 2424-2426, 2017.
- [261] O. Ronneberger, P. Fischer and T. Brox, "U-Net: Convolutional Networks for Biomedical Image Segmentation," in *Medical Image Computing and Computer-Assisted Intervention – MICCAI 2015. Lecture Notes in Computer Science*, vol. 9351, N. Navab, J. Hornegger, W. Wells and A. Frangi, Eds., Springer, Cham, 2015.
- [262] K. Novoselov, D. Jiang, F. Schedin, T. Booth, V. Khotkevich, S. Morozov and A. Geim, "Two-dimensional atomic crystals," *Proceedings of the National Academy of Sciences*, vol. 102, no. 30, pp. 10451-10453, 2005.
- [263] M. Scardamaglia, B. Aleman, M. Amati, C. Ewels, P. Pochet, N. Reckinger, J.-F. Colomer, T. Skaltas, N. Tagmatarchis, R. Snyders, L. Gregoratti and C. Bittencourt, "Nitrogen implantation of suspended graphene flakes: Annealing effects and selectivity of sp² nitrogen species," *Carbon*, vol. 73, pp. 371-381, 2014.
- [264] T. Linda, *Gentle Mill Ion Mill Model IV5 Technical Manual*.
- [265] "25 pack: CVD Graphene TEM Grid on Lacey Carbon Support," Graphene Supermarket, [Online]. Available: <https://graphene-supermarket.com/25-pack-CVDGraphene-TEM-Grid-on-Lacey-Carbon-Support.html>. [Accessed 2017].
- [266] A. Hitchcock, "Gas Phase Core Excitation Database," [Online]. Available: <http://unicorn.mcmaster.ca/corex/cedb-title.html>. [Accessed August 2017].

- [267] A. Hitchcock, M. Tronc and A. Modelli, "Electron transmission and inner-shell electron energy loss spectroscopy of acetonitrile, isocyanomethane, methyl thiocyanate, and isothiocyanatomethane," *Journal of Physical Chemistry*, vol. 93, no. 8, pp. 3068-3077, 1989.
- [268] E. Apen, A. Hitchcock and J. Gland, "Experimental studies of the core excitation of imidazole, 4,5-dicyanoimidazole, and s-triazine," *The Journal of Physical Chemistry*, vol. 97, no. 26, pp. 6859-6866, 1993.
- [269] R. McLaren, S. Clark, I. Ishii and A. Hitchcock, "Absolute oscillator strengths from K-shell electron-energy-loss spectra of the fluoroethenes and 1,3-perfluorobutadiene," *Physical Review A*, vol. 36, p. 1683, 1987.
- [270] S. Urquhart, A. Hitchcock, R. Priester and E. Rightor, "Analysis of polyurethanes using core excitation spectroscopy. Part II: Inner shell spectra of ether, urea and carbamate model compounds," *Journal of Polymer Science Part B: Polymer Physics*, vol. 33, pp. 1603-1620, 1995.

Appendix

Appendix 1: N-doping Graphene TEM Grids using a Plasma Cleaner and Gentle Mill™

Appendix 1.1 Plasma Cleaner: Nitrogen Plasma Source

The Solarus 950 Gatan Advanced Plasma System with an RF power supply (13.56 Hz) and a maximum operating power of 65 W is commonly used with an O₂/H₂ gas source to remove surface C contaminants before TEM imaging or spectroscopy, as a so-called “plasma cleaner.” For N-doping, the feed gas was replaced with an N₂/H₂ source operated with a gas flow of 27.5 standard cubic centimeter per minute (sccm) and 6.4 sccm, respectively. The effect of plasma power, exposure time, and sample distance from the direct source on the N concentration were investigated.

Appendix 1.1.1 Experimental Conditions

N-doping was performed using the Solarus 950 Gatan Advanced Plasma System with a feed gas mixture of N₂/H₂, resulting in a bright purple plasma (Figure A.1.1). For EELS quantification, the plasma source power was adjusted to 10, 20, 25, and 30 W for exposure times reaching up to 30 minutes. A Graphene Supermarket© TEM grid was inserted and exposed to the N⁺ plasma in five to ten minute intervals, in which the total exposure time

was determined by the total duration of plasma exposure. The graphene examined for Auger quantification was not supplied from Graphene Supermarket©, but was mechanically exfoliated using the scotch tape method from highly-ordered pyrolytic graphite (HOPG) and placed on an SiO₂ wafer with a 300 nm oxide thickness [50], [262]. This process was performed by Kevin A. Villegas, a summer student assisting with graphene production and doping. N-doping proceeded by exposing the graphene sheets to the N⁺ plasma in 5 minute intervals, in which the N quantification was completed between each exposure.



Figure A.1.1 N₂/H₂ plasma activated in the Solarus 950 Gatan Advanced Plasma System. The central window shows the pink colour of the plasma inside the chamber.

EELS experiments were performed on the FEI 80-300 Cryo-Twin TEM equipped with a Schottky field emission gun (*SFEG*). The EELS acquisition for the N-K edge was performed in TEM mode using GATAN Digital Micrograph software, in which three to seven measurements were performed for each sample condition. The same areas were analyzed before and after each doping exposure when using EELS, as the sample was not removed from the holder during plasma cleaning. A broad beam without the use of an objective aperture was used as a rough estimate for the N concentration. Because the fine structure was not of concern for this specific experiment, the monochromator was not excited. EELS acquisition times were varied depending on the thickness of the local area

examined to acquire a N-K edge with a high signal to noise ratio. A dispersion of 0.1 eV/pixel was used to acquire the C-K and the N-K edges simultaneously. GATAN Digital Micrograph was used to quantify the relative N % for each operating condition by considering a convergence semi-angle of 3 mrad and a collection semi-angle greater than 100 mrad. In the future, when performing this experiment, the objective aperture should be used to better control the collection angle. High resolution ADF imaging was completed using details listed in *Chapter 4.2.1 Characterization of N-Doped Graphene Using High Resolution STEM*. Using the Titan 80-300 Cubed, high-resolution EELS spectra were acquired to examine the source of surface contamination with a dispersion of 0.4 eV/pixel and a convergence and collection semi-angle of 26 mrad and 58 mrad, respectively (as measured by FEI). The spectra in the spectrum image were aligned and calibrated in energy to the C-K edge π^* peak (285 eV) using built-in functions in GATAN Digital Micrograph.

Auger spectroscopy was also utilized to quantify the N content in graphene after plasma exposure. The spectroscopy was completed using an energy of 10 kV, a current of 20 nA, a tilt of 30°, and M5 mode. The reported values from the quantification of the N % were normalized with respect to the C content (relative %); however, because beam contamination could not be avoided it should be noted that the N content may be slightly underestimated. Quantification was completed using an in-house HOPG standard from a freshly cleaved surface, and supplied internal standards from JEOL of Cr₂N, and SiO₂ for the C-KLL, N-KLL, O-KLL, and Si-KLL Auger electrons, respectively.

Appendix 1.1.2 Results and Discussion

The effect of the plasma power, and exposure time to the N plasma are of interest to understand the potential for N-doping graphene using a TEM plasma cleaner. Figure A.1.2 (a) summarize these effects. Observation of the average N at.% (normalized to C and N) in the graphene samples with respect to the power reveals that over time, the concentration of

N remains relatively stable excluding the increase observed at 30 W. According to the EELS quantification acquired from GATAN Digital Micrograph an average maximum N concentration of approximately 4 at. % (normalized to C and N) can be achieved when the graphene is directly exposed to a 30 W N plasma source for 20 minutes. This value disagrees with the literature [189], [191], [196], which reports an average N concentration of 1%. Higher concentrations have been reported with plasma doping [190], [263] as opposed to ion doping, and for N-dopants other than graphitic-type [132]. However, in the case of the experiments from this report, the source of high N content is postulated to arise from the quantification procedure from the EELS spectra. It can be suggested that the extended fine-structure modulations from the C-K edge interfere with the background subtraction during the quantification of the N-K edge, thus causing a systematic error in the signal detection when N is not present, and a large variation in the detected concentration. The effect is confirmed when a concentration greater than three percent can be apparently detected from a sample that has not been exposed to the plasma source, which is an indication that the background was not removed appropriately.

To more accurately characterize the N concentration, Auger spectroscopy was utilized for the 30 W power source, as this condition showed a positive increase in the N concentration with time when performing EELS quantification. Figure A.1.2 (b) shows an approximate linear increase in the N concentration with time. Consistent with other literature references [189], [191], [196] an average N concentration of approximately 1.3 ± 0.7 at. %²² (normalized to C and N) was observed after a 25 minute exposure to the 30 W plasma. A maximum exposure time of 25 minutes at 30 W was utilized, due to the adverse graphene structure observed after a 20 minute exposure.

²² Sample error calculated using the two-tailed one-sample Student's t-test with a probability of 0.05.

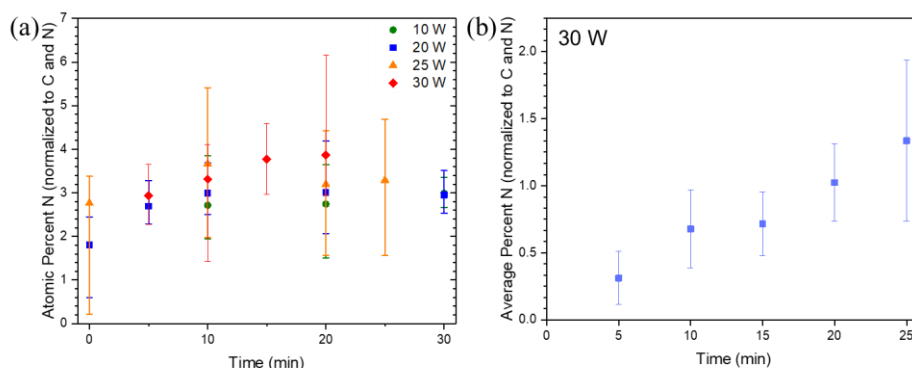


Figure A.1.2 Quantification results from N plasma exposure. (a) Effect of power and time on the N concentration after plasma exposure (error showing the minimum and maximum quantification values) as quantified with EELS. (b) Auger quantification from exfoliated graphene on SiO₂ exposed with 5 minute intervals of N⁺ plasma (error calculated using the two-tailed one-sample Student's t-test with a probability of 0.05).

High-resolution images were acquired for graphene exposed to the 30 W plasma source for 20 minutes. Following the exposure to the plasma source, ALD was used to deposit Pt on the TEM grid with hopes of finding the Pt binding location. Upon low magnification imaging (Figure A.1.3 (a)), it was determined that the graphene was damaged after doping. Higher magnification images show two possible outcomes from a single TEM grid after exposure to the N⁺ plasma and 50 ALD cycles: the complete removal of graphene (Figure A.1.3 (b)) with the structurally sound contamination layer remaining, or the presence of the graphene lattice (Figure A.1.3 (c)). The remaining graphene layers in Figure A.1.3 (c) appear to be decorated with bright atoms (yellow arrows) and darker atomic clusters (red arrows). Following EELS examination of this material (Figure A.1.3 (d), (e), (f)) many contaminants were identified: Cu, O, F, and Gd. It should be noted that beam contamination was an issue during the collection of these EELS spectrum images; however, through ELNES analysis, pertinent information was still obtained. Comparing the intensity from the ADF image (Figure A.1.3 (c)) to STEM simulations (*Appendix 6: STEM Image Simulation*) it is expected that the bright atoms are Pt (Z=78) and/or Gd (Z=64) and the larger clusters are Cu (Z=29). It is unclear if the Gd source is from the

plasma cleaner or the ALD process, as high energy core-loss EELS spectra were not acquired prior to ALD. However, it should be noted that samples containing low concentrations of Gd were plasma cleaned in the Solarus around the time of the N-doping experiments, thus it is suspected that the Gd contaminant originates from the plasma cleaner. Moreover, it is suspected that the Cu source originates from a sputtering process of the TEM grid during the doping process. Using separate spectrum images of the same area (Figure A.1.3 (d) and (e)) the presence O and F were detected on the substrate. The O may arise from surface hydrocarbon contaminants or the plasma doping process, but the source of F is unknown. Furthermore, examination of the C-K edge reveals a sharp π^* and σ^* peak, thus suggesting the presence of graphene in the area examined. Lastly, it was noted that a N-K edge was not present in this area of examination after N-doping, likely due to the N concentration being below the detection limit of EELS.

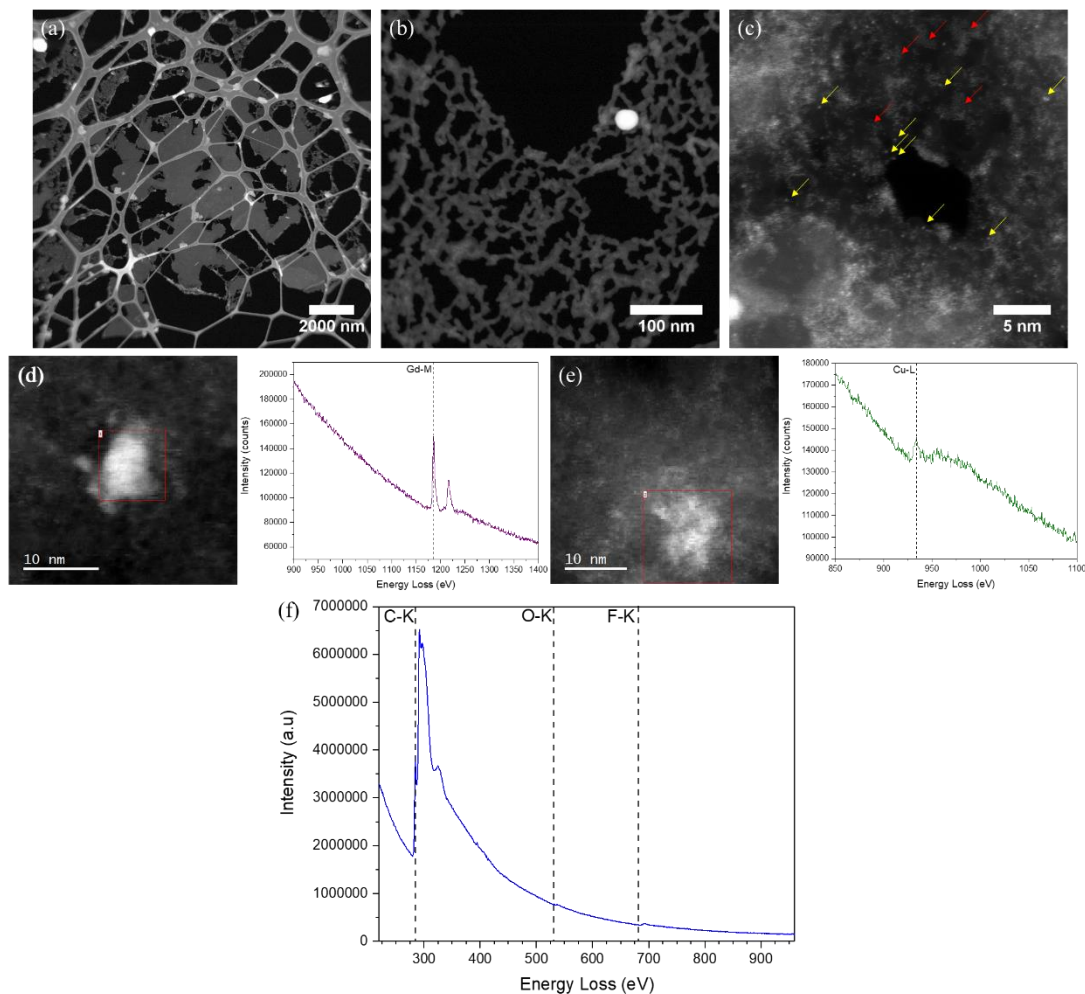


Figure A.1.3 STEM images and EELS analysis from N-doped graphene after exposure to the Solarus plasma cleaner at 30 W for 20 minutes with direct N plasma exposure and Pt deposited using 50 ALD cycles. ADF images were acquired at (a) low magnification (gamma adjusted), and (b) (gamma adjusted) and (c) high magnifications. (d) DF image and EELS spectra of Gd particle found in the same spectral area as (f) summed spectra containing C, O, and F. (e) DF image and EELS spectra of Cu contaminant.

In summary, using the Solarus plasma cleaner as a potential N source successfully resulted in the doping of approximately 1% N (normalized to C and N). Through ADF images and EELS it was shown that the graphene lattice was maintained in some regions; however, the sample had various sources of contamination, regions with low N concentrations, and the complete absence of the graphene lattice in other areas. Due to the

high degree of damage upon achieving a 1 at. % N-doping concentration and the multiple contamination sources, a different N-doping method should be used.

Appendix 1.2 Gentle Mill: Nitrogen Ion Source

The Gentle Mill Ion Miller Technoorg Linda Model IV5 [264] is primarily utilized during final thinning steps when producing TEM samples using an Ar⁺ source. It operates at relatively low angles and low energy, thus allowing the removal of potential amorphous layers created during other sample preparation techniques. For the purpose of N-doping, the source was replaced with N⁺, and other instrument modifications such as tilt angle and beam energy were personalized for the doping process. The effect of the beam energy and exposure time using the Gentle Mill will be examined as a source for N-doped graphene.

Appendix 4.2.1 Experimental Conditions

N-doping was performed using a Gentle Mill Ion Miller Technoorg Linda Model IV5 [264] (Figure A.1.4 (a)) with an N₂ gas source at room temperature on Graphene Supermarket© TEM grids [265]. Traditionally, this instrument is operated with a beam energy ranging from 100 V to 2000 V, a minimum vacuum of 10⁻⁴ Pa, and Ar⁺ ions. Modifications were made to the Gentle Mill to decrease the energy to a minimum of 25 V by applying a positive bias to the sample stage. When applying the bias, the current could not be continually monitored, thus the current was set prior to the application of the bias. The minimum achievable current of 1-2 μA, was utilized in these experiments. A maximum tilt angle of 40° to the surface normal with respect to the ion gun was possible using the internal rotating mechanism of the Gentle Mill. In order to achieve higher angles, the rotation mechanism

was disconnected, and the angle was measured by eye to 90° , Figure A.1.4 (b)). The ion energies examined included 25 V, 50 V, and 300 V at different exposure times.

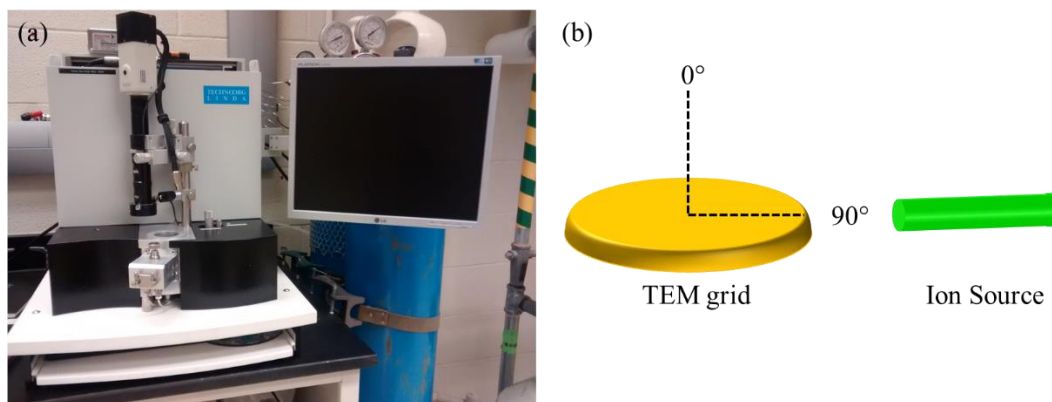


Figure A.1.4 Gentle Mill experimental set-up. (a) Gentle Mill Ion Miller Technoorg Linda Model IV5 under regular operating conditions. (b) The TEM grid orientation with respect to the ion beam.

N-doping concentrations were measured using Auger spectroscopy, as outlined in *Chapter 4.1 Nitrogen Quantification on TEM Grids Using Auger Spectroscopy*. During quantification JEOL supplied reference spectra were utilized and Si and O contaminants could be found in some locations. The N concentrations reported have been normalized to C; however, beam contamination could not be avoided, thus it should be noted that the N content may be slightly underestimated. The PD was monitored for each area analyzed and all signals included in this examination contained a PD greater than 80%. One area for the 50 V sample was excluded from the data analysis as it had a relatively low PD. It was qualitatively determined through multiple examinations that smaller holes resulted in lower PDs between the sample and the hole. This suggests that there is a minimum diameter at which the Auger spectrometer collects signal, but this was not investigated further and may be a source of error in the Auger quantification. For conciseness and accuracy, in the future, the effect of the size of the hole diameter on the PD should be measured and compared to prevent signal overlap during individual spot quantification.

High resolution ADF imaging was completed using details listed in Chapter 4.2.1 *Characterization of N-Doped Graphene Using High Resolution STEM*. Using the Titan 80-300 Cubed, EELS spectra were used to examine the C-K, N-K, and O-K edges with a 0.25 eV/pixel dispersion and a convergence and collection semi-angle of 26 mrad and 58 mrad, respectively (as measured by FEI). The spectra in the spectrum image were aligned and calibrated in energy to the C-K edge π^* peak (285 eV) using built-in functions in GATAN Digital Micrograph. To minimize beam contamination, the sample underwent a beam shower using a low magnification in TEM mode.

Appendix 4.2.2 Results and Discussion

Using the Auger quantification, the effect of the ion source energy and exposure time can be examined in Figure A.1.5. It can be observed that as the exposure time increases from 3 to 30 seconds at 25 V, the average N concentration increases to 0.36 ± 0.06 %²³ (normalized to C and N). Furthermore, as the energy increases to 300 V at 30 seconds the average N concentration increases to 2.81 ± 0.12 % (normalized to C and N). This suggests that both the exposure time and beam energy can increase the N loading in the graphene lattice. Another sample was examined at 50 V for 60 seconds resulting in an average N concentration of 2.1 ± 0.6 % (normalized to C and N). While this cannot be directly compared to the other samples as it has a different beam energy and exposure time, it is interesting to note that the average N % is quite similar to the 300 V sample. The Gentle Mill operates by optimizing the negative bias applied at the sample to increase the ion beam current, such that it attracts the positive N^+ ions and repels any generated secondary electrons [264]. However, to decrease the overall fluence and to maintain better control on the exposure time, the current was minimized to 1-2 μA , thus potentially resulting in an

²³ Sample errors calculated using the two-tailed one-sample Student's t-test with a probability of 0.05.

increased concentration of electrons interacting with the sample. In addition, to decrease the energy down to 25 V and 50 V, a positive bias was applied to the sample, which likely further increased the sample exposure to electrons. Therefore, it is not surprising that the 300 V sample has a higher N % than the 25 V and 50 V samples, such that the Gentle Mill could be operated in conditions closer to the optimum. It should be noted that the N-doping in the samples from a 50 V and 300 V ion source, is still higher than some literature values. A potential explanation for the increased level of doping is that the graphene has been partially amorphized [192] leading to the doping of amorphous C, or the introduction of defects other than the graphitic-type dopant occurred, due to damage to the graphene lattice, thus enabling higher doping levels to be achieved [132].

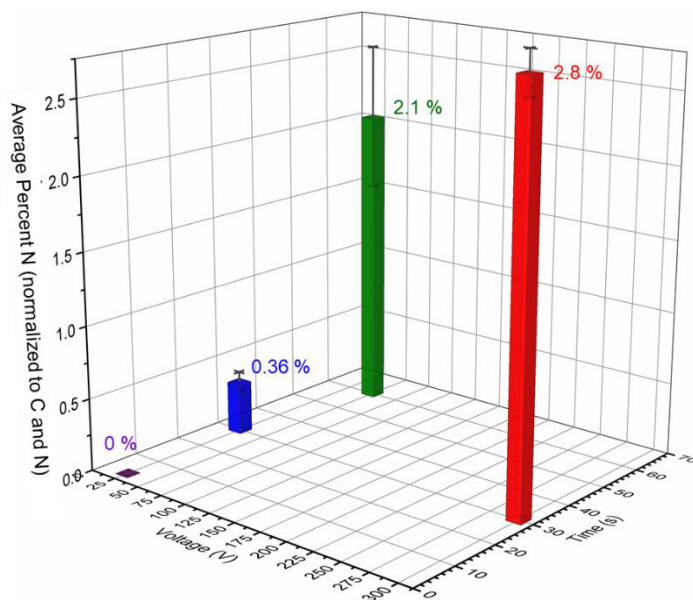


Figure A.1.5 Average N % (normalized to C and N) in Graphene Supermarket© TEM grids, as characterized by Auger spectroscopy (errors calculated using the two-tailed one-sample Student's t-test with a probability of 0.05).

To examine the effect of the ion beam, the sample was imaged using ADF conditions and the C-K edge was acquired with EELS to examine the fine structure. Figure A.1.6 (a), (b), and (c) show different areas of the graphene lattice. Each area appears

disordered and multilayered, which may be an effect of the milling process. Furthermore, bright atomic contaminants were observed in both ADF images; however, their origin is unknown. An Si-KLL Auger peak could be observed in a few locations examined during Auger quantification, which possibly originate from the TEM grid; however, the Si-K edge was outside of the acquired EELS spectra (Figure A.1.6 (d)), thus direct analysis of the atomic contaminants is not possible. The EELS spectra (Figure A.1.6 (d)) contain both a C-K and N-K edge, suggesting a successful doping process. When examining the C-K edge the fine structure resembles a graphene edge, accordingly confirming the presence of the graphene lattice observed in the ADF images.

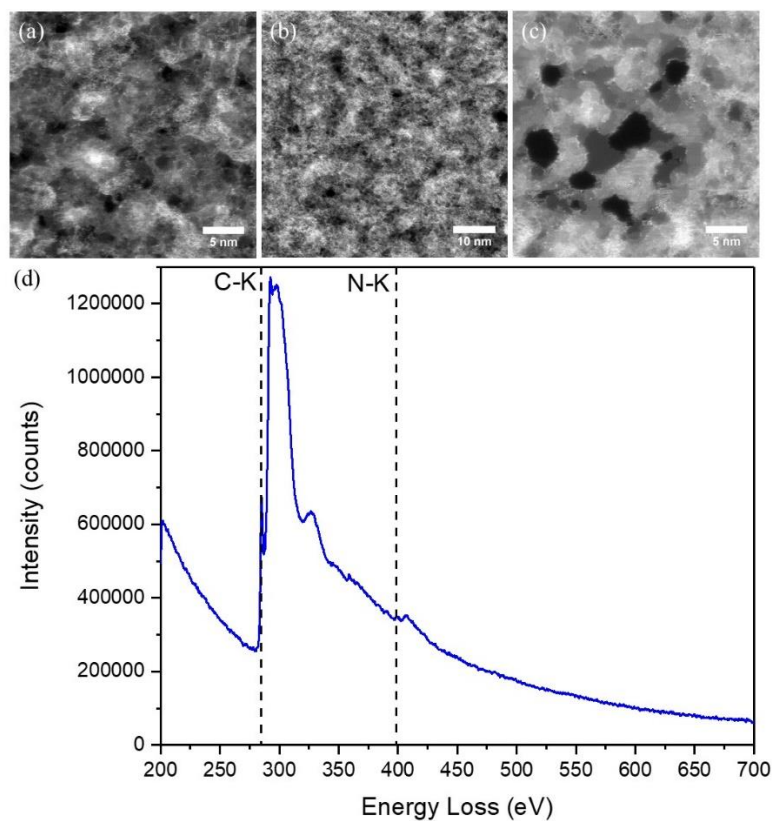


Figure A.1.6 STEM images and EELS analysis of Gentle Mill sample acquired at 50 V for three minutes using a current of nine to ten μA . High magnification ADF images (a), (b), and (c) (gamma corrected), and an EELS spectrum (d) were acquired.

To conclude, while this doping method was partially successful due to the fact that it was able to N-dope the graphene lattice, it still resulted in local structural changes as observed by ADF imaging. Moreover, this is not an ideal doping method due to the poor control over ion fluence from the relatively high beam currents (1-2 μA minimum). A more restricted doping method is preferred that allows the ion fluence to be controlled by time.

Appendix 2: N-K Edge Reference Spectra

All reference spectra were acquired from a database compiled by Prof. Adam Hitchcock. [266]. The NCNT production method contains N sources from acetonitrile and imidazole [218].

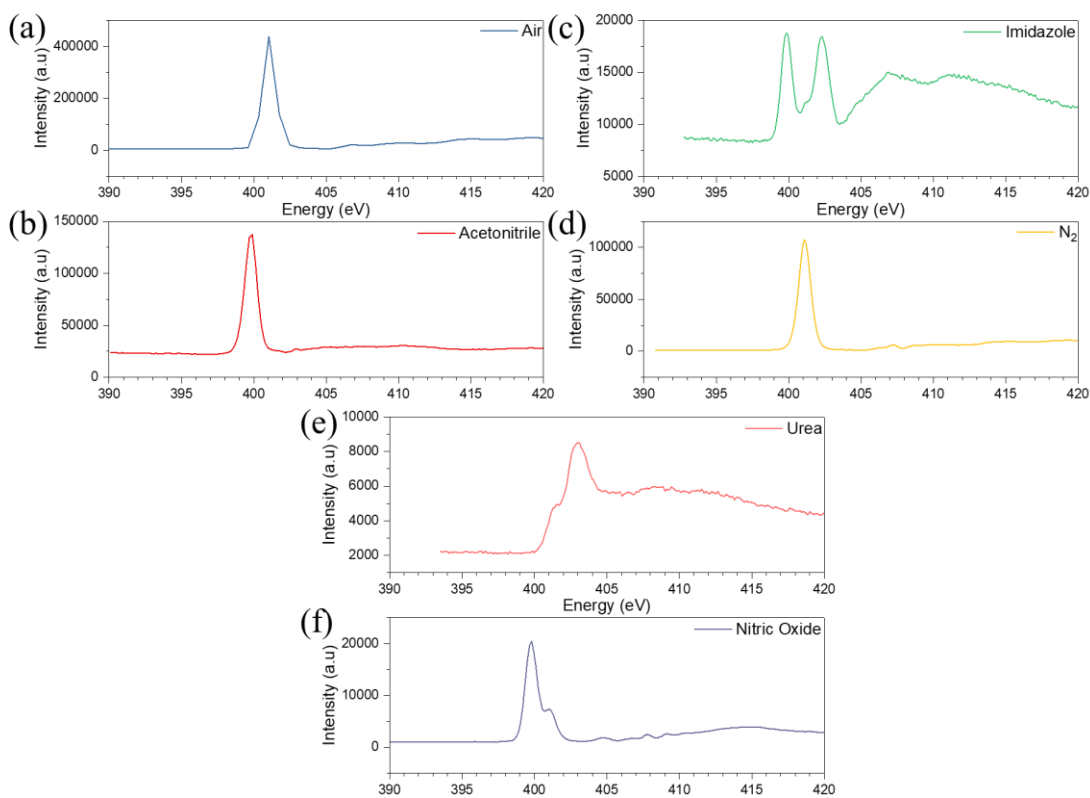


Figure A.2.1 EELS N-K reference spectra acquired from gaseous species from (a) air, (b) acetonitrile [267], (c) imidazole [268], (d) N₂ [269], (e) urea [270], and (f) nitric oxide.

Appendix 3: N-K EELS Maps Gas Filled NCNTs

Using GATAN Digital Micrograph software and the spectrum images used to quantify the gas, N-K areal density maps were produced using a power law background subtraction, collection window of 50 eV, and the hydrogenic model. Each map was normalized to the maximum areal density quantified per spectrum image, as follows from [229] (black has an intensity value of 0 and white an intensity value of 1). The N-K areal density maps acquired from the quantification can be found in Figure A.3.1 **Error! Reference source not found.** The N areal density is relatively uniform within each NCNT, which may be an indication that the beam is not greatly affecting the N pressure during acquisition. There are cases in which the N density seems higher within the walls of the NCNTs, which may be a cause of a poor background subtraction, gas physisorption on the walls, and/or N-doping within the NCNTs.

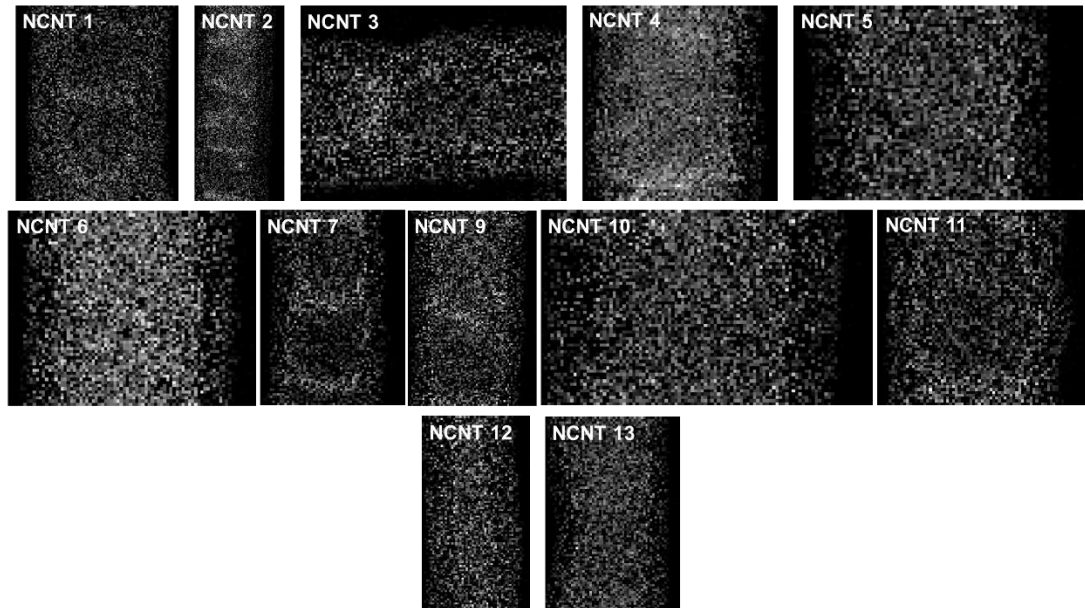


Figure A.3.1 N-K areal density maps normalized to the maximum areal density for each individual NCNT.

Appendix 4: Images Used for ALD Pt Quantification

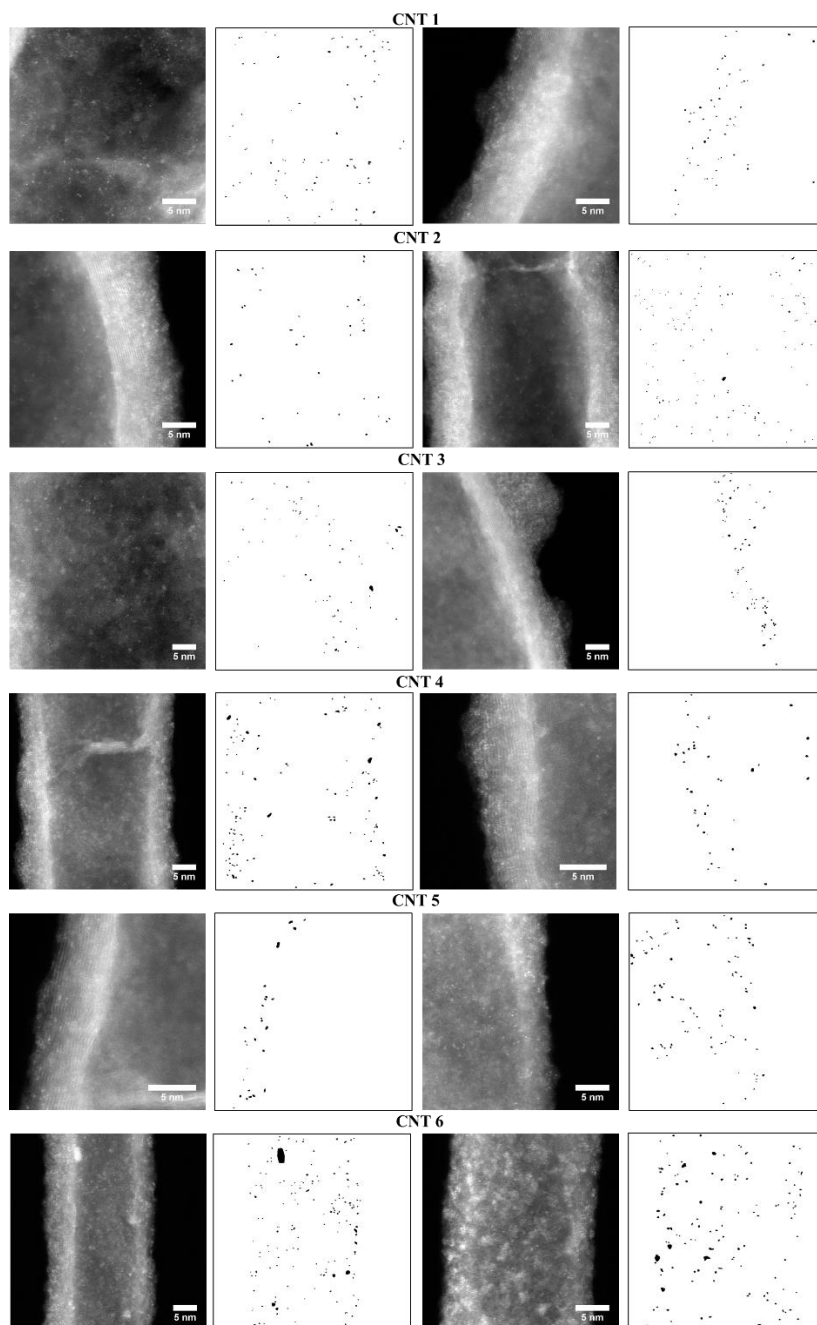


Figure A.4.1 250°C NCNT 1minute

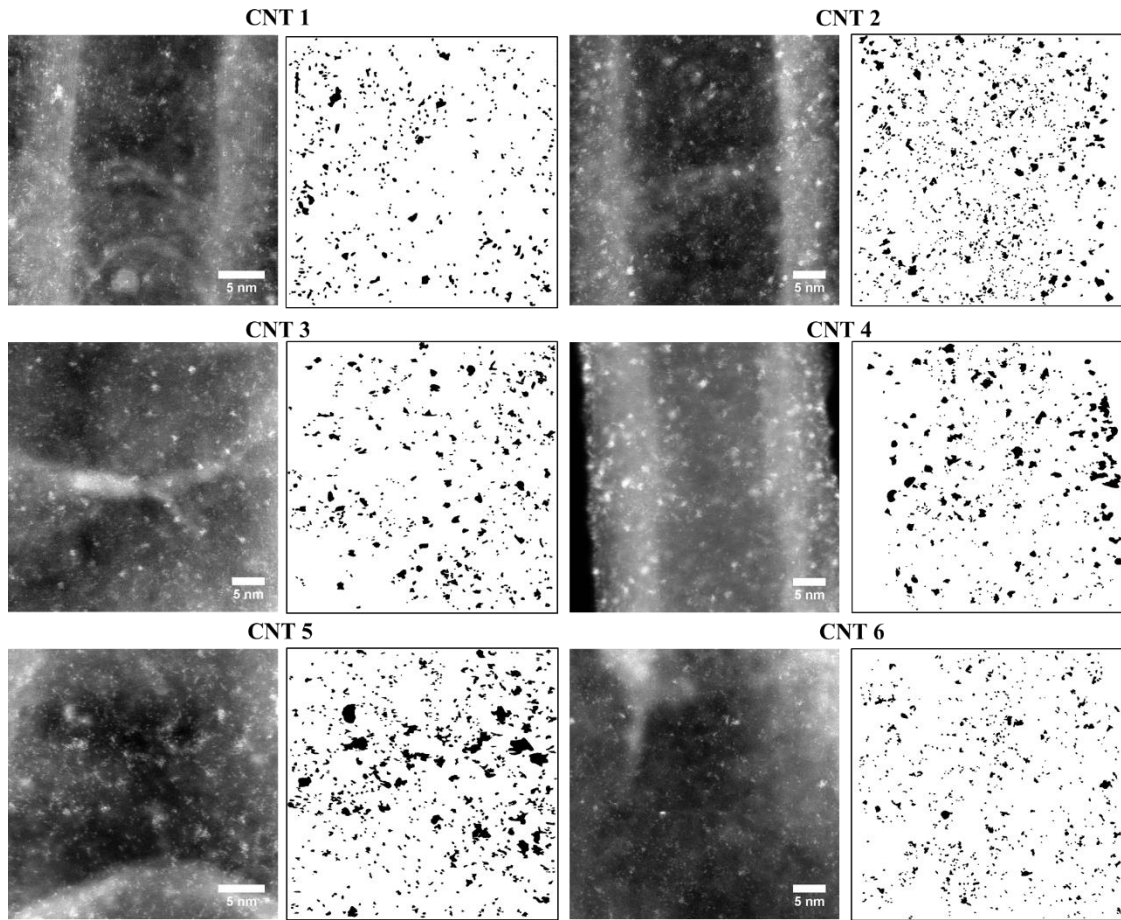


Figure A.4.2 250°C NCNT 30 minutes

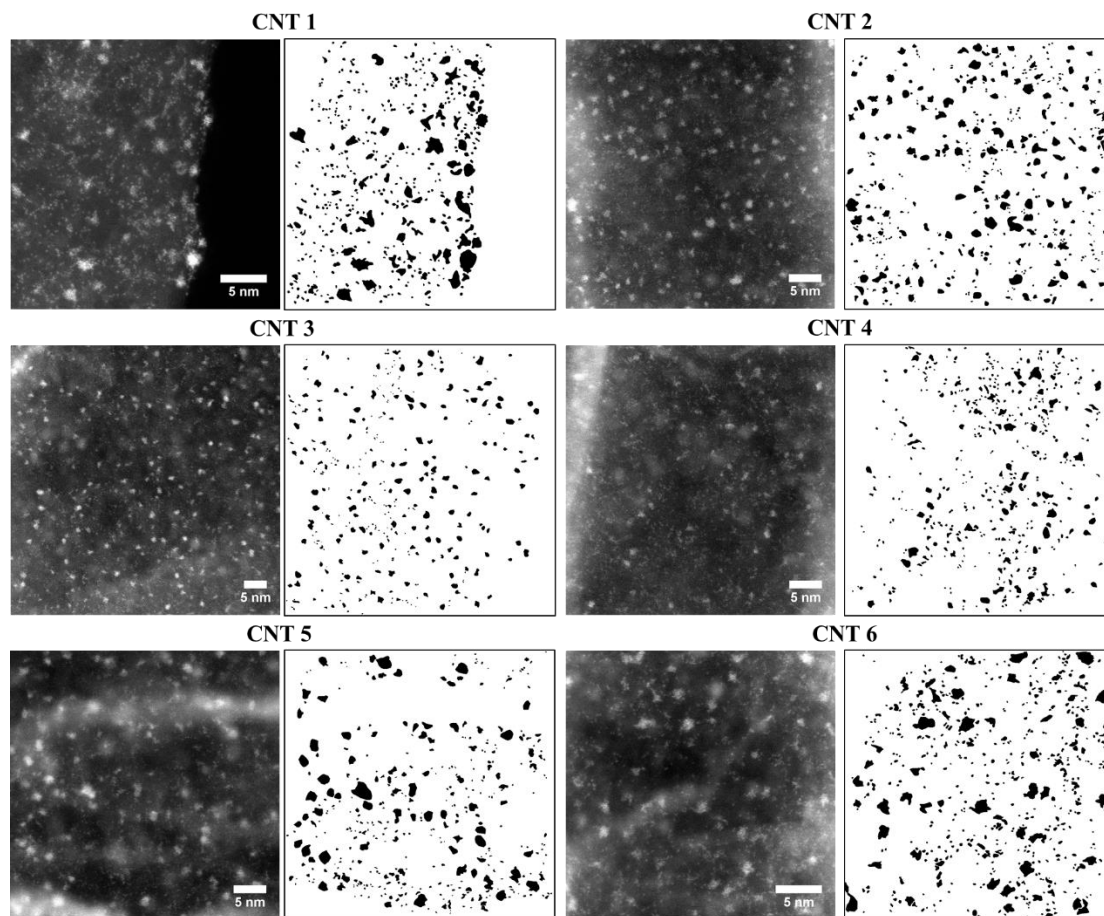


Figure A.4.3 250°C NCNT 60 minutes

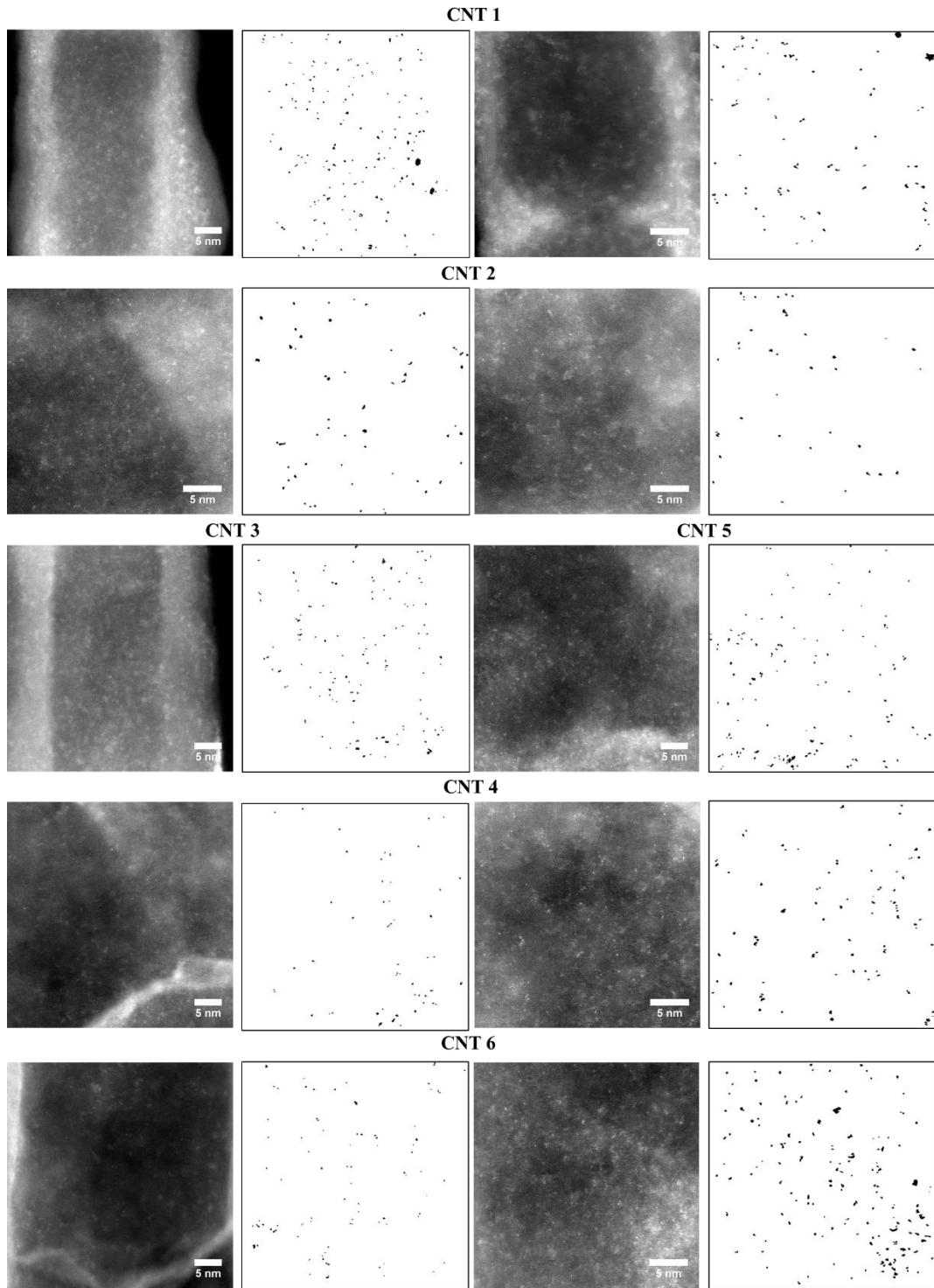


Figure A.4.4 100°C NCNT 1 minute

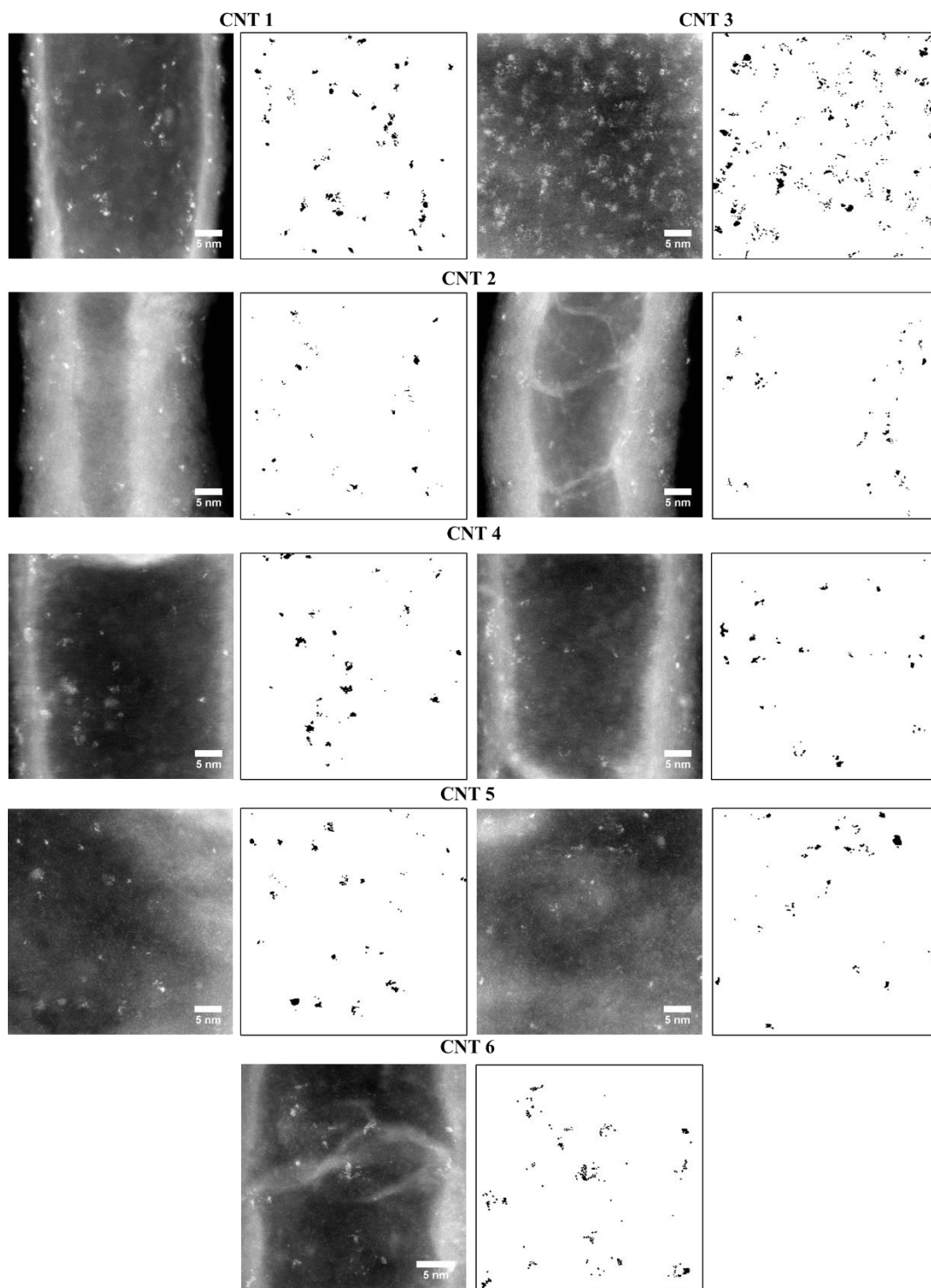


Figure A.4.5 100°C NCNT 30 minutes

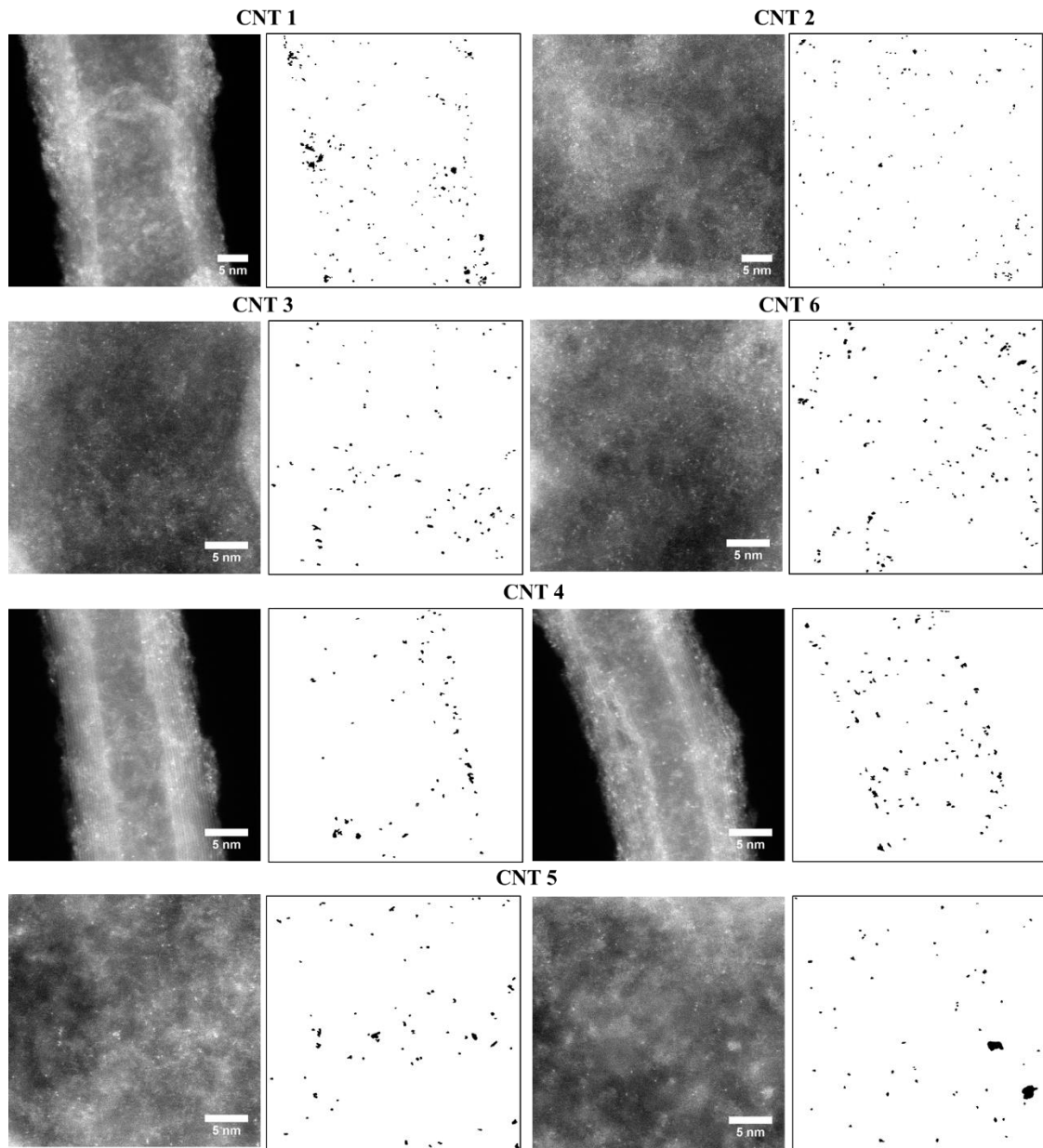


Figure A.4.6 175°C NCNT 1 minute

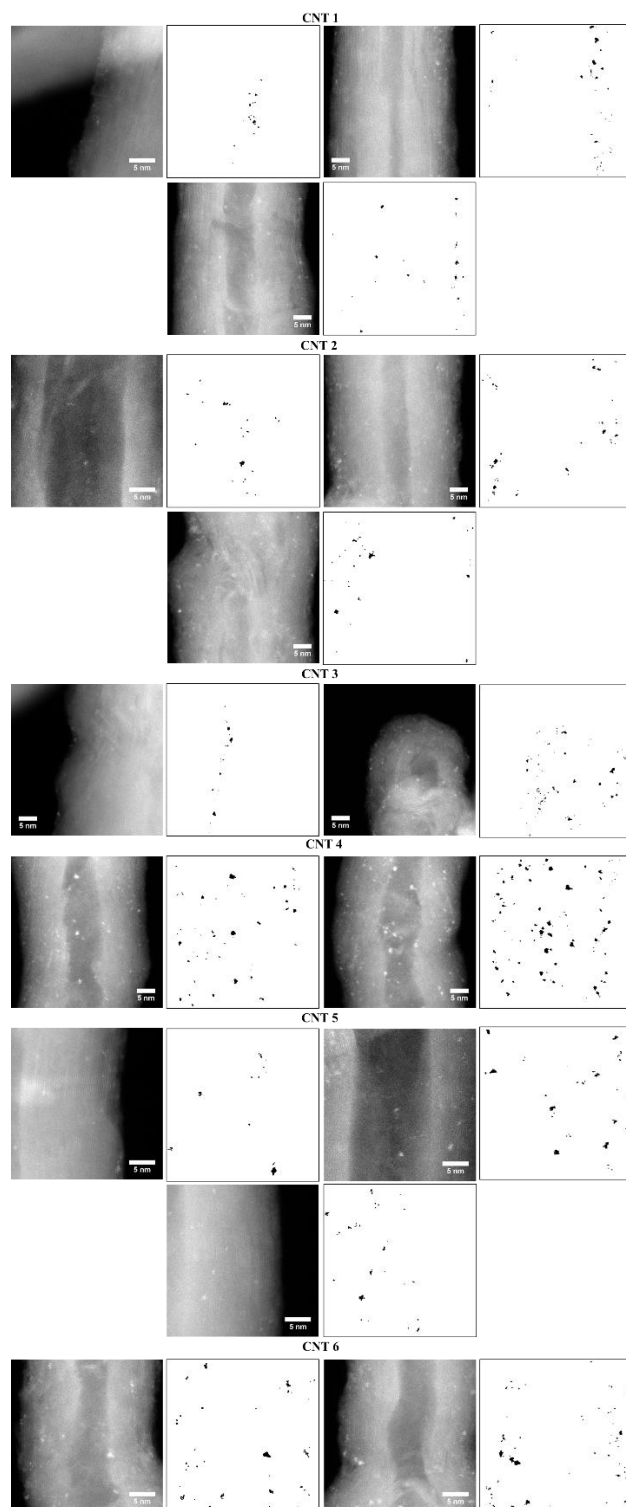


Figure A.4.7 250°C PCNT 1 minute

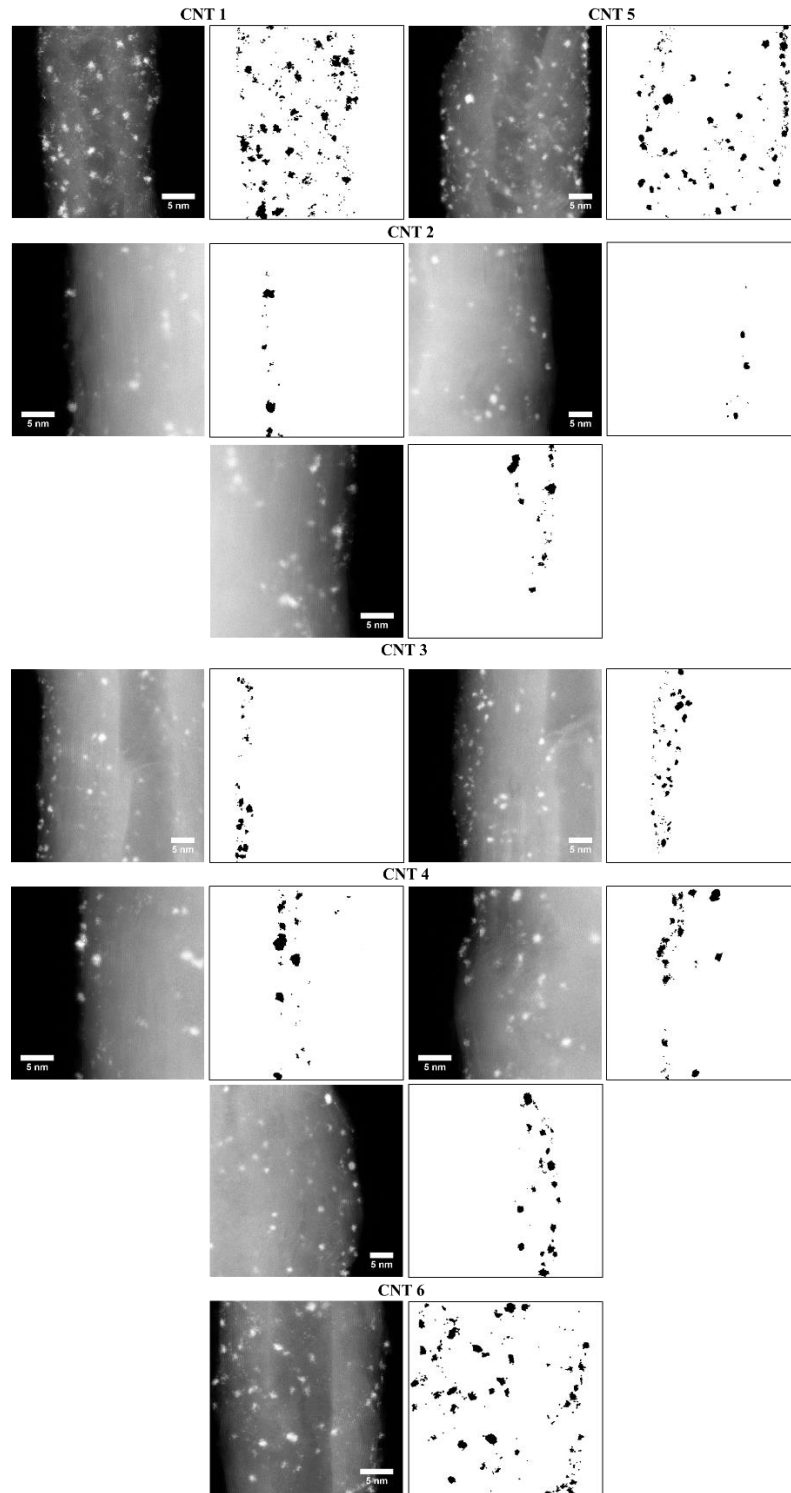
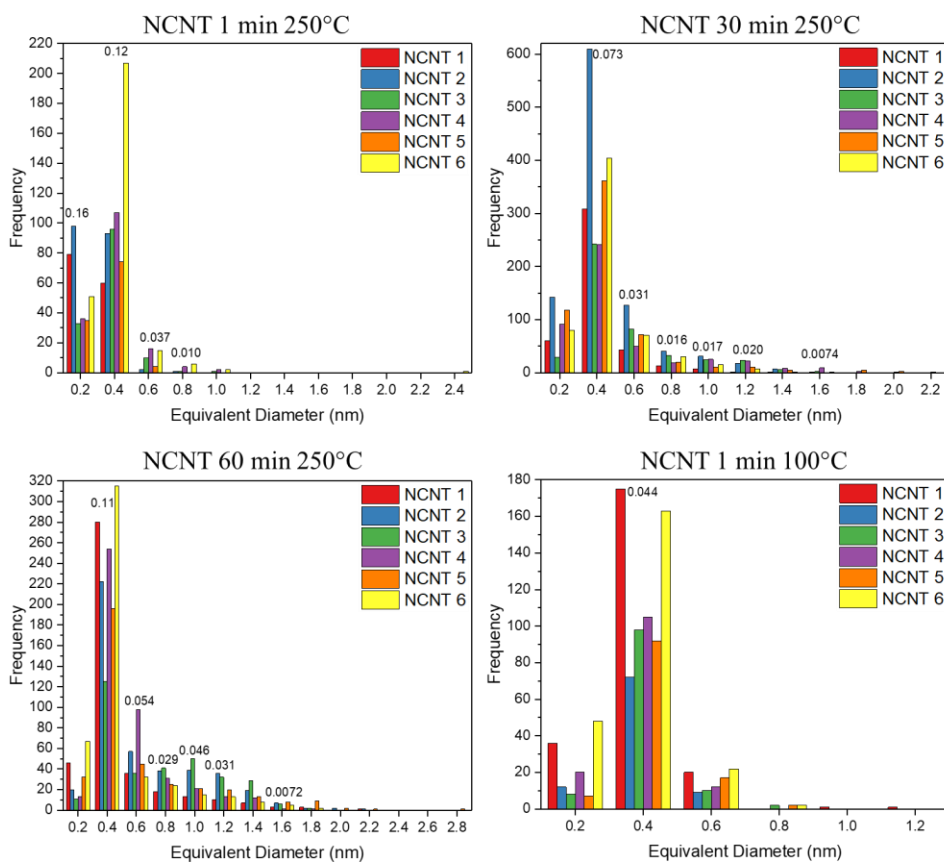
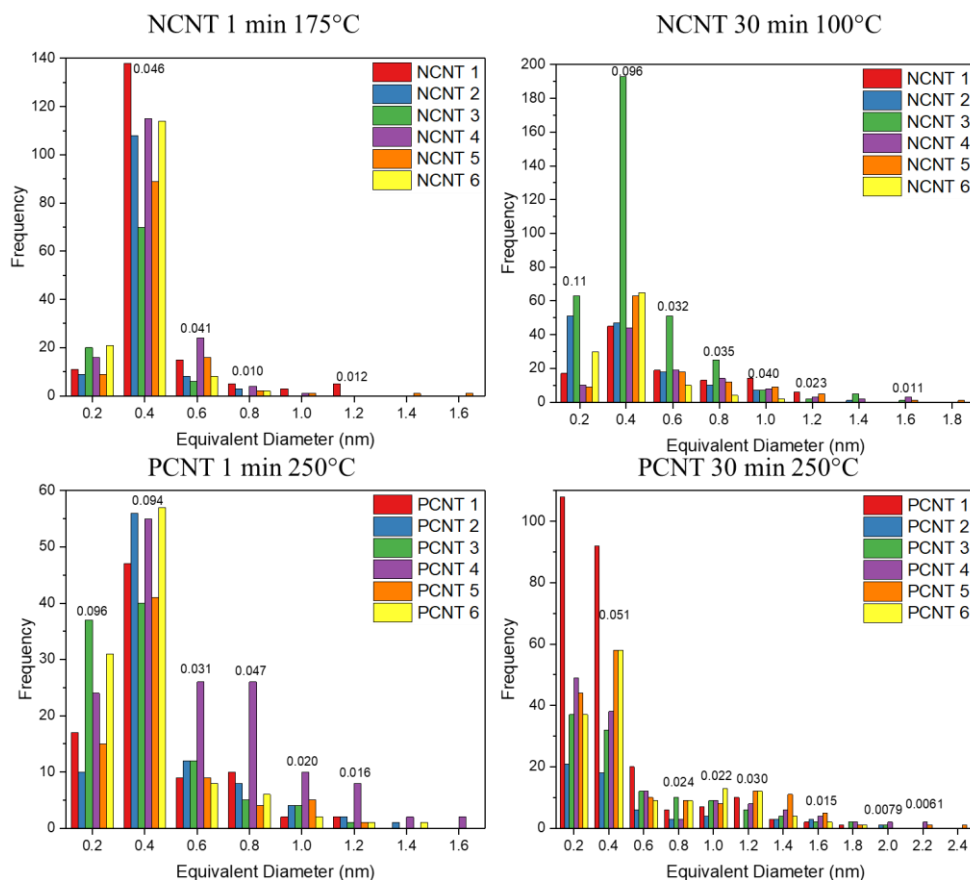


Figure A.4.8 250°C PCNT 30 minutes

Appendix 5: Individual Histograms from Each Tube Analyzed in Appendix 4

Histograms were produced from each individual CNT analyzed in *Appendix 4: Images Used for ALD Pt Quantification* and grouped based on each sample preparation conditions. The histograms were left in frequency, rather than fractional frequency, to provide the reader with the number of Pt entities analyzed for each CNT. The numbers on top of each of the bins are the standard deviations from the fractional frequency of the measurements that were greater than the standard deviation from the error in the measurement (Figure 5.12).





In order to examine the effects of the varying number of Pt entities counted per CNT on the final fractional frequency for each sample preparation technique, an unconventional method was used to determine the normalized fractional frequency per CNT, rather than the normalized fraction frequency per Pt entity presented in *Chapter Five*. The fractional frequency of each CNT was normalized to the number of Pt entities on the single CNT. The fractional frequency for each sample preparation method was then determined by summing the fractional frequencies per bin for each CNT and dividing by the number of CNTs analyzed (six). The results for the new normalization and a comparison to the method used in *Chapter Five* can be observed in the tables below. Large percent differences are observed when low fractional frequencies are present, due to low statistical counts, as can be observed in the figures above. Colour coding was used to

highlight the percent difference for CNTs with a fractional frequency per CNT bin greater than 0.05 (five percent, blue) and 0.01 (one percent, green). A maximum percent difference of 9.6% and 20.7% are calculated for a fractional frequency per bin greater than five percent and one percent, respectively. This suggests that for high frequency bins, there is a small effect of the individual CNTs on the overall fractional frequency, thus ensuring the histograms presented in *Chapter Five* are sufficient. The tables presented below can be used for the readers, who desire to examine the data based on a per CNT basis, rather than normalized to the number of Pt entities, as presented in *Chapter Five*.

NCNT 1 min 250C									
CNT	1	2	3	4	5	6	Normalized to CNT	Normalized to Pt	% change
0.2	0.568345	0.505155	0.234043	0.218182	0.309735	0.180851	0.336052	0.321083	4.7
0.4	0.431655	0.479381	0.680851	0.648485	0.654867	0.734043	0.60488	0.616054	-1.8
0.6	0	0.010309	0.070922	0.09697	0.035398	0.053191	0.044465	0.045455	-2.2
0.8	0	0.005155	0.007092	0.024242	0	0.021277	0.009628	0.011605	-17
1	0	0	0.007092	0.012121	0	0.007092	0.004384	0.004836	-9.3
1.2	0	0	0	0	0	0	0	0	#DIV/0!
1.4	0	0	0	0	0	0	0	0	#DIV/0!
1.6	0	0	0	0	0	0	0	0	#DIV/0!
1.8	0	0	0	0	0	0	0	0	#DIV/0!
2	0	0	0	0	0	0	0	0	#DIV/0!
2.2	0	0	0	0	0	0	0	0	#DIV/0!
2.4	0	0	0	0	0	0.003546	0.000591	0.000967	-39

NCNT 30 min 250C									
CNT	1	2	3	4	5	6	Normalized to CNT	Normalized to Pt	% change
0.2	0.138568	0.145492	0.06576	0.19403	0.194719	0.131363	0.144989	0.147142	-1.5
0.4	0.711316	0.625	0.548753	0.513859	0.59571	0.663383	0.60967	0.612903	-0.53
0.6	0.099307	0.130123	0.185941	0.10661	0.118812	0.116585	0.12623	0.12592	0.25
0.8	0.030023	0.042008	0.07483	0.03838	0.033003	0.049261	0.044584	0.04386	1.6
1	0.016166	0.031762	0.054422	0.053305	0.018152	0.024631	0.033073	0.031975	3.4
1.2	0.002309	0.017418	0.052154	0.046908	0.018152	0.011494	0.024739	0.02292	7.9
1.4	0.002309	0.007172	0.013605	0.017058	0.008251	0.001642	0.00834	0.007923	5.2
1.6	0	0.001025	0.004535	0.01919	0	0.001642	0.004399	0.003679	20
1.8	0	0	0	0.006397	0.008251	0	0.002441	0.002264	7.8
2	0	0	0	0.002132	0.00495	0	0.00118	0.001132	4.3
2.2	0	0	0	0.002132	0	0	0.000355	0.000283	26

NCNT 60 min 250C									
CNT	1	2	3	4	5	6	Normalized to CNT	Normalized to Pt	% change
0.2	0.110312	0.045147	0.033133	0.029279	0.085791	0.139293	0.073826	0.075904	-2.7
0.4	0.671463	0.501129	0.376506	0.572072	0.525469	0.654886	0.550254	0.559036	-1.6
0.6	0.086331	0.128668	0.108434	0.220721	0.120643	0.066528	0.121888	0.122088	-0.16
0.8	0.043165	0.085779	0.123494	0.06982	0.067024	0.049896	0.073196	0.071084	3.0
1	0.031175	0.088036	0.150602	0.047297	0.0563	0.031185	0.067433	0.063855	5.6
1.2	0.023981	0.081264	0.096386	0.029279	0.053619	0.027027	0.051926	0.049799	4.3
1.4	0.016787	0.042889	0.087349	0.027027	0.034853	0.016632	0.037589	0.035341	6.4
1.6	0.007194	0.015801	0.018072	0.002252	0.021448	0.010395	0.012527	0.012048	4.0
1.8	0.007194	0.004515	0.006024	0.002252	0.024129	0.004158	0.008045	0.007631	5.4
2	0	0.004515	0	0	0.005362	0	0.001646	0.001606	2.5
2.2	0.002398	0.002257	0	0	0.002681	0	0.001223	0.001205	1.5
2.4	0	0	0	0	0	0	0	0	#DIV/0!
2.6	0	0	0	0	0	0	0	0	#DIV/0!
2.8	0	0	0	0	0.002681	0	0.000447	0.000402	11

NCNT 1 min 100C									
CNT	1	2	3	4	5	6	Normalized to CNT	Normalized to Pt	% change
0.2	0.154506	0.129032	0.067797	0.145985	0.059322	0.204255	0.126816	0.140257	-9.6
0.4	0.751073	0.774194	0.830508	0.766423	0.779661	0.693617	0.765913	0.754818	1.5
0.6	0.085837	0.096774	0.084746	0.087591	0.144068	0.093617	0.098772	0.09636	2.5
0.8	0	0	0.016949	0	0.016949	0.008511	0.007068	0.006424	10
1	0.004292	0	0	0	0	0	0.000715	0.001071	-33
1.2	0.004292	0	0	0	0	0	0.000715	0.001071	-33

NCNT 1 min 175C									
CNT	1	2	3	4	5	6	Normalized to CNT	Normalized to Pt	% change
0.2	0.062147	0.070313	0.208333	0.1	0.07563	0.144828	0.110208	0.104242	5.7
0.4	0.779661	0.84375	0.729167	0.71875	0.747899	0.786207	0.767572	0.768485	-0.12
0.6	0.084746	0.0625	0.0625	0.15	0.134454	0.055172	0.091562	0.093333	-1.9
0.8	0.028249	0.023438	0	0.025	0.016807	0.013793	0.017881	0.019394	-7.8
1	0.016949	0	0	0.00625	0.008403	0	0.005267	0.006061	-13
1.2	0.028249	0	0	0	0	0	0.004708	0.006061	-22
1.4	0	0	0	0	0.008403	0	0.001401	0.001212	16
1.6	0	0	0	0	0.008403	0	0.001401	0.001212	16

NCNT 30min 100C									
CNT	1	2	3	4	5	6	Normalized to CNT	Normalized to Pt	% change
0.2	0.149123	0.380597	0.181556	0.097087	0.076271	0.27027	0.192484	0.194175	-0.87
0.4	0.394737	0.350746	0.556196	0.427184	0.533898	0.585586	0.474725	0.492988	-3.7
0.6	0.166667	0.134328	0.146974	0.184466	0.152542	0.09009	0.145845	0.145631	0.15
0.8	0.114035	0.074627	0.072046	0.135922	0.101695	0.036036	0.08906	0.084142	5.8
1	0.122807	0.052239	0.020173	0.07767	0.076271	0.018018	0.061196	0.050701	21
1.2	0.052632	0	0.005764	0.029126	0.042373	0	0.021649	0.01726	25
1.4	0	0.007463	0.014409	0.019417	0	0	0.006882	0.00863	-20
1.6	0	0	0.002882	0.029126	0.008475	0	0.006747	0.005394	25
1.8	0	0	0	0	0.008475	0	0.001412	0.001079	31

PCNT 1min 250C									
CNT	1	2	3	4	5	6	Normalized to CNT	Normalized to Pt	% change
0.2	0.195402	0.107527	0.373737	0.156863	0.2	0.292453	0.220997	0.218597	1.1
0.4	0.54023	0.602151	0.40404	0.359477	0.546667	0.537736	0.498383	0.482871	3.2
0.6	0.103448	0.129032	0.121212	0.169935	0.12	0.075472	0.11985	0.12398	-3.3
0.8	0.114943	0.086022	0.050505	0.169935	0.053333	0.056604	0.088557	0.096248	-8.0
1	0.022989	0.043011	0.040404	0.065359	0.066667	0.018868	0.042883	0.044046	-2.6
1.2	0.022989	0.021505	0.010101	0.052288	0.013333	0.009434	0.021608	0.02447	-12
1.4	0	0.010753	0	0.013072	0	0.009434	0.005543	0.006525	-15
1.6	0	0	0	0.013072	0	0	0.002179	0.003263	-33

PCNT 30min 250									
CNT	1	2	3	4	5	6	Normalized to CNT	Normalized to Pt	% change
0.2	0.433735	0.355932	0.321739	0.362963	0.275	0.255172	0.33409	0.34299	-2.6
0.4	0.369478	0.305085	0.278261	0.281481	0.3625	0.4	0.332801	0.34299	-3.0
0.6	0.080321	0.101695	0.104348	0.088889	0.0625	0.062069	0.083304	0.079954	4.2
0.8	0.024096	0.050847	0.086957	0.022222	0.05625	0.062069	0.050407	0.04635	8.8
1	0.028112	0.067797	0.078261	0.066667	0.05	0.089655	0.063415	0.057937	9.4
1.2	0.040161	0	0.052174	0.059259	0.075	0.082759	0.051559	0.05562	-7.3
1.4	0.012048	0.050847	0.034783	0.044444	0.06875	0.027586	0.039743	0.035921	11
1.6	0.008032	0.050847	0.017391	0.02963	0.03125	0.013793	0.025157	0.020857	21
1.8	0.004016	0	0.017391	0.014815	0.00625	0.006897	0.008228	0.008111	1.4
2	0	0.016949	0.008696	0.014815	0	0	0.006743	0.004635	45
2.2	0	0	0	0.014815	0.00625	0	0.003511	0.003476	0.99
2.4	0	0	0	0	0.00625	0	0.001042	0.001159	-10

Appendix 6: STEM Image Simulation

Multislice STEM simulations were utilized in JEMS to calculate the relative intensity profiles of Pt, Gd, and Cu on a six-layer graphene crystal, in which the metallic atom took a substitutional position. Six-layers were selected, as the Graphene Supermarket© grids are composed of one to six layer sheets, thus the least contrast would be generated from a six-layer sheet, due to the projected thickness. [265] A 3 x 3 x 6 supercell was developed using CrystalMaker and the substitutional atoms were placed at the bottom most layer. JEMS was developed in 2004 by P. Stadelmann through the use of java. [99] The multislice simulation was completed using a slice thickness of 0.34 nm, a Titan 80-300 microscope configuration with an 80 kV electron source, 70 μm C2 aperture, ADF conditions (detector semi-angle of 31 to 192 mrad), and minimal lens aberrations. The projection potentials were developed using the analytic option with a multislice approximation on the order of z^1 , and a temperature of 298 K. The Weickenmeier-Kohl atomic form factor was used with the frozen lattice approximation. Lastly a multislice and scan area size (pixels) of 256 x 256 was utilized with a scan step size of 2. Using these inputs Figure A.6.1 **Error!** **Reference source not found.** was generated for the three respective dopant atoms.

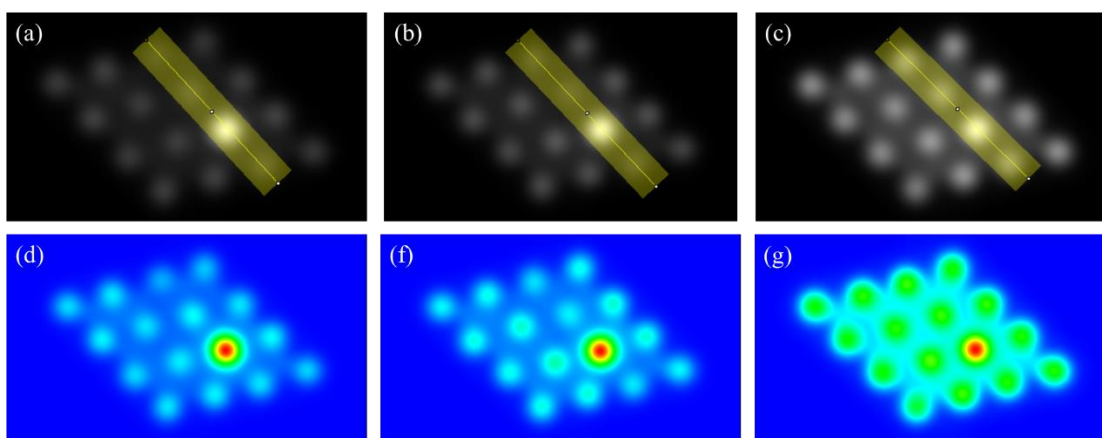


Figure A.6.1 JEMS multislice ADF image simulations of six graphene layers from (a,d) Pt, (b,f) Gd, and (c,g) Cu.

To further accentuate the difference and similarities of the intensity profiles of the dopant atoms a line profile averaged over the yellow squares in Figure A.6.2 (a), (b), and (c) was acquired, as shown in Figure A.6.2. Using the maximum peak and maximum next nearest-neighbour value, a ratio of 3.6, 3.7, and 1.7 were calculated for Pt, Gd, Cu, respectively. Using these relative intensity ratios, it can be suggested that the bright atoms in Figure A.1.3 (c) originate from Pt or Gd, and the dark clusters arise from Cu.

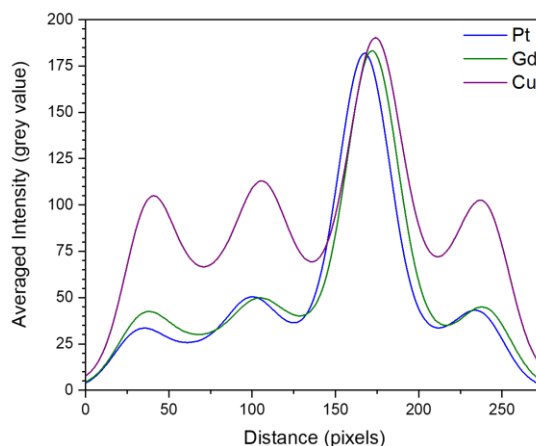


Figure A.6.2 Line profiles acquired from averaged intensities in the yellow rectangle in Figure A.6.1.

Utilizing the same simulation conditions in JEMS, 21 nm thick graphene slabs were compared for Pt and Ca substitutional atoms in the bottom-most graphene layer, to examine the contrast observed by the HAADF detector and the DF detector when performing EELS (Figure A.6.3). For each image simulation, experimental conditions were set to contain a C2 aperture of 50 μm and collections angles of 64-200 mrad and 61-139 mrad, respectively. Single sheet graphene was also modelled in (e) containing both Pt and Ca atoms, wherein the respective ADF image was simulated with collections angles of 64-200 mrad ((f) and (g)).

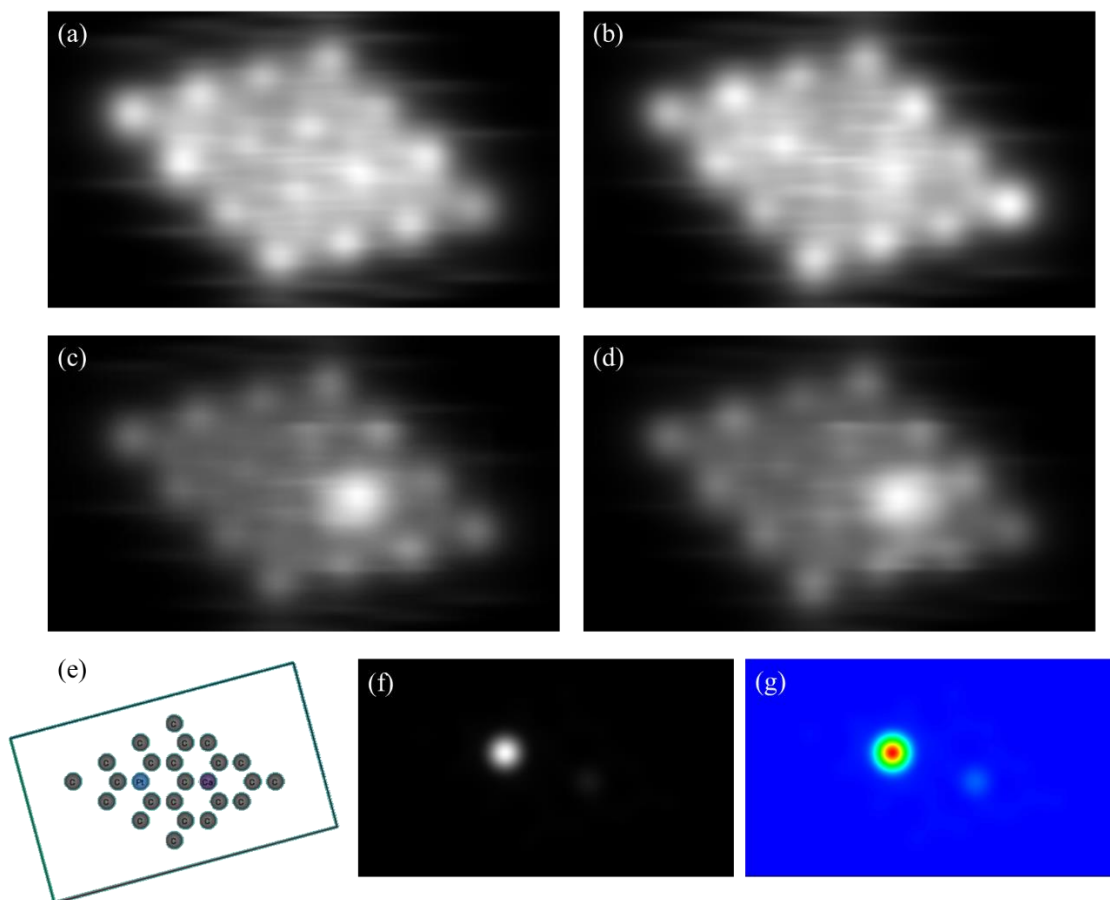
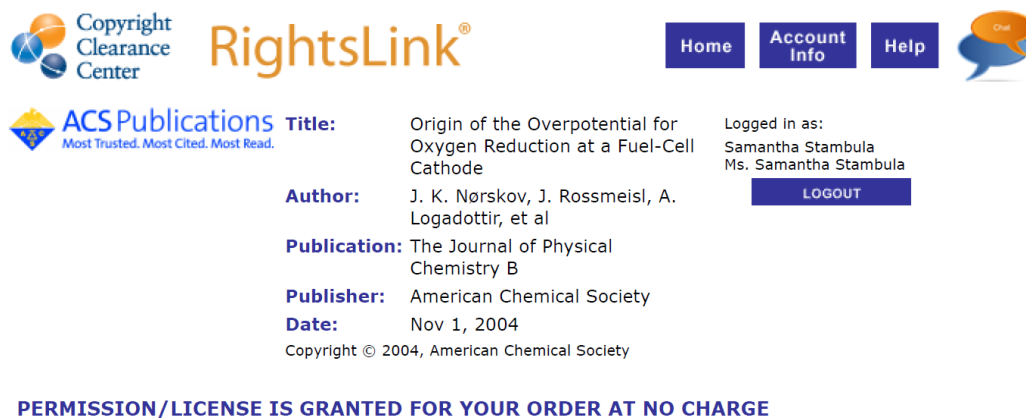


Figure A.6.3 JEMS multislice ADF image simulations from 21 nm thick graphene sheet (a,b) Ca and (c,d) Pt for collection angles of (a,c) 64-200 mrad and (b,d) 61-139 mrad. A single sheet of graphene was (a) modelled with both Pt and Ca atoms present (C=grey, Pt=blue, Ca=purple). (f) and (g) are the resulting ADF image for collection angles of 64-200 mrad.

Appendix 7: Copyright Permissions

Figure 1.3 (b)



Copyright Clearance Center RightsLink® Home Account Info Help Chat

ACS Publications Most Trusted. Most Cited. Most Read.

Title: Origin of the Overpotential for Oxygen Reduction at a Fuel-Cell Cathode

Author: J. K. Nørskov, J. Rossmeisl, A. Logadottir, et al

Publication: The Journal of Physical Chemistry B

Publisher: American Chemical Society

Date: Nov 1, 2004

Copyright © 2004, American Chemical Society

Logged in as:
Samantha Stambula
Ms. Samantha Stambula

LOGOUT

PERMISSION/LICENSE IS GRANTED FOR YOUR ORDER AT NO CHARGE

Figure 1.4



Copyright Clearance Center RightsLink® Home Create Account Help Chat

npg nature publishing group

Title: Platinum single-atom and cluster catalysis of the hydrogen evolution reaction

Author: Niancai Cheng, Samantha Stambula, Da Wang, Mohammad Norouzi Banis, Jian Liu et al.

Publication: Nature Communications

Publisher: Nature Publishing Group

Date: Nov 30, 2016

Copyright © 2016, Rights Managed by Nature Publishing Group

LOGIN

If you're a copyright.com user, you can login to RightsLink using your copyright.com credentials. Already a RightsLink user or want to [learn more?](#)

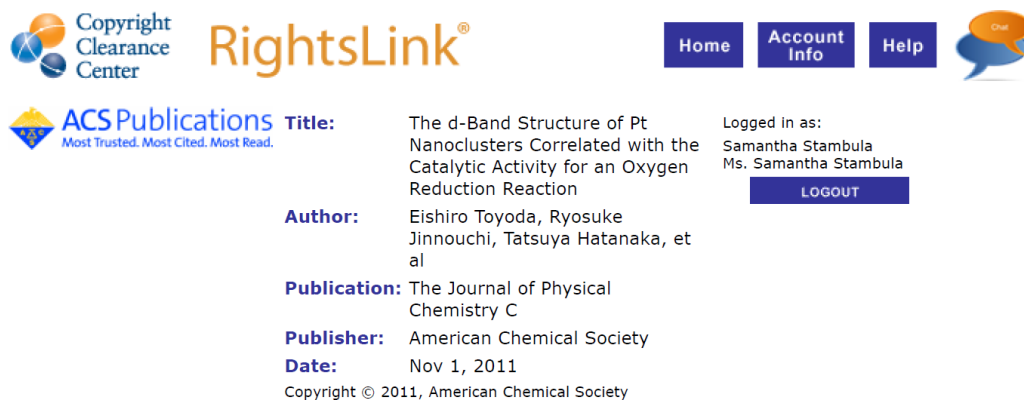
Creative Commons

The article for which you have requested permission has been distributed under a Creative Commons CC-BY license (please see the article itself for the license version number). You may reuse this material without obtaining permission from Nature Publishing Group, providing that the author and the original source of publication are fully acknowledged, as per the terms of the license. For license terms, please see <http://creativecommons.org/>

Figure 1.5

License Number	4220860029926
License date	Nov 02, 2017
Licensed Content Publisher	John Wiley and Sons
Licensed Content Publication	Small
Licensed Content Title	Atomic Layer Deposition of Platinum Nanoparticles on Carbon Nanotubes for Application in Proton-Exchange Membrane Fuel Cells
Licensed Content Author	Chueh Liu,Chih-Chieh Wang,Chi-Chung Kei,Yang-Chih Hsueh,Tsong-Pyng Perng
Licensed Content Date	Apr 20, 2009
Licensed Content Pages	4
Type of use	Dissertation/Thesis
Requestor type	University/Academic
Format	Print and electronic
Portion	Figure/table
Number of figures/tables	1
Original Wiley figure/table number(s)	4
Will you be translating?	No
Title of your thesis / dissertation	High-Resolution Characterization of Nitrogen-Doped Carbon Support Materials Decorated with Noble Metal Atom Catalysts
Expected completion date	Jan 2018
Expected size (number of pages)	310
Requestor Location	Ms. Samantha Stambula McMaster Univeristy 1280 Main St W Hamilton, ON L8S 4L8 Canada Attn: Ms. Samantha Stambula
Publisher Tax ID	EU826007151
Billing Type	Invoice
Billing address	Ms. Samantha Stambula McMaster Univeristy 1280 Main St W Hamilton, ON L8S 4L8 Canada Attn: Ms. Samantha Stambula
Total	0.00 CAD

Figure 1.6 (a) and (b)



Copyright Clearance Center RightsLink® Home Account Info Help Chat

ACS Publications Title: The d-Band Structure of Pt Nanoclusters Correlated with the Catalytic Activity for an Oxygen Reduction Reaction
 Most Trusted. Most Cited. Most Read.

Author: Eishiro Toyoda, Ryosuke Jinnouchi, Tatsuya Hatanaka, et al

Publication: The Journal of Physical Chemistry C

Publisher: American Chemical Society

Date: Nov 1, 2011

Copyright © 2011, American Chemical Society

Logged in as:
 Samantha Stambula
 Ms. Samantha Stambula
 LOGOUT

PERMISSION/LICENSE IS GRANTED FOR YOUR ORDER AT NO CHARGE

Figure 1.7

License Number	4220861086761
License date	Nov 02, 2017
Licensed Content Publisher	Nature Publishing Group
Licensed Content Publication	Nature Materials
Licensed Content Title	The rise of graphene
Licensed Content Author	A. K. Geim, K. S. Novoselov
Licensed Content Date	Mar 1, 2007
Licensed Content Volume	6
Licensed Content Issue	3
Type of Use	reuse in a dissertation / thesis
Requestor type	academic/educational
Format	print and electronic
Portion	figures/tables/illustrations
Number of figures/tables/illustrations	1
High-res required	no
Figures	Fig. 1
Author of this NPG article	no
Your reference number	
Title of your thesis / dissertation	High-Resolution Characterization of Nitrogen-Doped Carbon Support Materials Decorated with Noble Metal Atom Catalysts
Expected completion date	Jan 2018
Estimated size (number of 310 pages)	
Requestor Location	Ms. Samantha Stambula McMaster University 1280 Main St W Hamilton, ON L8S 4L8 Canada Attn: Ms. Samantha Stambula
Billing Type	Invoice
Billing address	Ms. Samantha Stambula McMaster University 1280 Main St W Hamilton, ON L8S 4L8 Canada Attn: Ms. Samantha Stambula
Total	0.00 CAD

Figure 1.8

Copyright Clearance Center RightsLink®

Home Account Info Help Chat

ACS Publications Most Trusted. Most Cited. Most Read.

Title: On the Evolution of Pt Nanoparticles on Few-Layer Graphene Supports in the High-Temperature Range

Author: M. Simona Moldovan, Hervé Bulou, Yannick J. Dappe, et al

Publication: The Journal of Physical Chemistry C

Publisher: American Chemical Society

Date: Apr 1, 2012

Copyright © 2012, American Chemical Society

Logged in as:
Samantha Stambula
Ms. Samantha Stambula

LOGOUT

PERMISSION/LICENSE IS GRANTED FOR YOUR ORDER AT NO CHARGE

Figure 1.10

Copyright Clearance Center RightsLink®

Home Account Info Help Chat

ACS Publications Most Trusted. Most Cited. Most Read.

Title: Improving Platinum Catalyst Durability with a Doped Graphene Support

Author: Michael N. Groves, Cecile Malardier-Jugroot, Manish Jugroot

Publication: The Journal of Physical Chemistry C

Publisher: American Chemical Society

Date: May 1, 2012

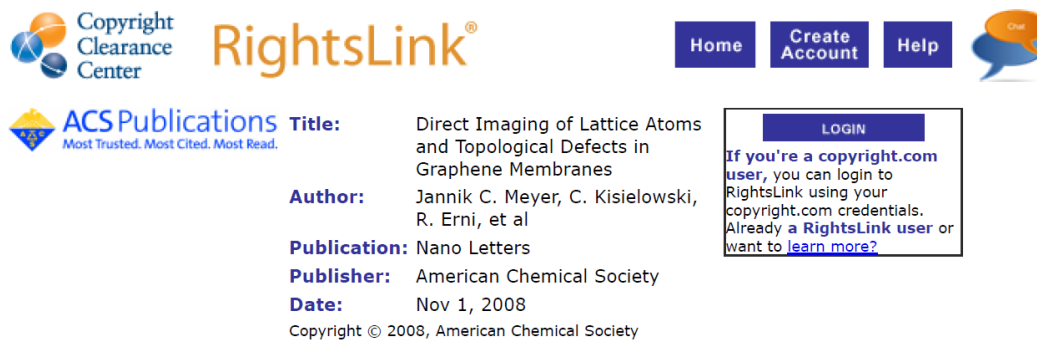
Copyright © 2012, American Chemical Society

Logged in as:
Samantha Stambula
Ms. Samantha Stambula

LOGOUT

PERMISSION/LICENSE IS GRANTED FOR YOUR ORDER AT NO CHARGE

Figure 2.3 (a) and (b)



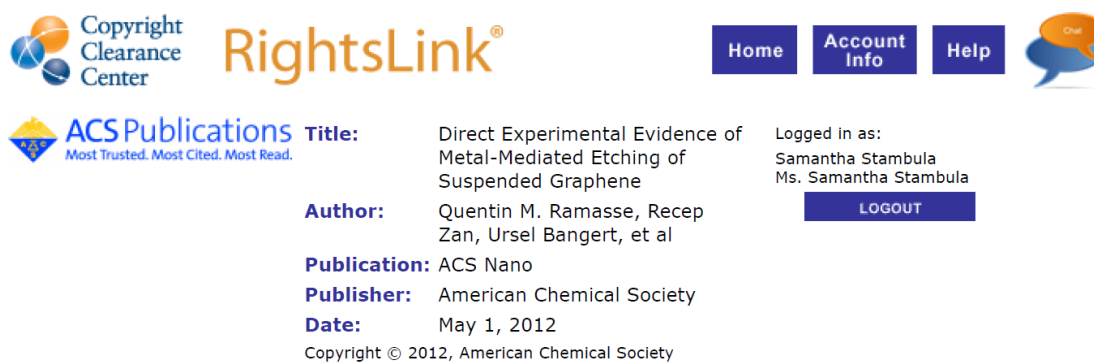
Copyright Clearance Center **RightsLink**[®] Home Create Account Help Chat

ACS Publications **Title:** Direct Imaging of Lattice Atoms and Topological Defects in Graphene Membranes
Author: Jannik C. Meyer, C. Kisielowski, R. Erni, et al
Publication: Nano Letters
Publisher: American Chemical Society
Date: Nov 1, 2008
 Copyright © 2008, American Chemical Society

LOGIN
 If you're a copyright.com user, you can login to RightsLink using your copyright.com credentials. Already a RightsLink user or want to [learn more?](#)

PERMISSION/LICENSE IS GRANTED FOR YOUR ORDER AT NO CHARGE

Figure 2.5 (a), (b), and (c)



Copyright Clearance Center **RightsLink**[®] Home Account Info Help Chat

ACS Publications **Title:** Direct Experimental Evidence of Metal-Mediated Etching of Suspended Graphene
Author: Quentin M. Ramasse, Recep Zan, Ursel Bangert, et al
Publication: ACS Nano
Publisher: American Chemical Society
Date: May 1, 2012
 Copyright © 2012, American Chemical Society

Logged in as:
 Samantha Stambula
 Ms. Samantha Stambula
LOGOUT

PERMISSION/LICENSE IS GRANTED FOR YOUR ORDER AT NO CHARGE

JPCC Article – author: S. Stambula, permission for print and electronic full copy



RightsLink®

[Home](#) [Create Account](#) [Help](#)



ACS Publications

Most Trusted. Most Cited. Most Read.

Title: Chemical Structure of Nitrogen-Doped Graphene with Single Platinum Atoms and Atomic Clusters as a Platform for the PEMFC Electrode

Author: Samantha Stambula, Nicolas Gauquelin, Matthieu Bugnet, et al

Publication: The Journal of Physical Chemistry C

Publisher: American Chemical Society

Date: Feb 1, 2014

Copyright © 2014, American Chemical Society

LOGIN

If you're a [copyright.com](#) user, you can login to RightsLink using your [copyright.com](#) credentials. Already a [RightsLink](#) user or want to [learn more?](#)

PERMISSION/LICENSE IS GRANTED FOR YOUR ORDER AT NO CHARGE

This type of permission/license, instead of the standard Terms & Conditions, is sent to you because no fee is being charged for your order. Please note the following:

- Permission is granted for your request in both print and electronic formats, and translations.
- If figures and/or tables were requested, they may be adapted or used in part.
- Please print this page for your records and send a copy of it to your publisher/graduate school.
- Appropriate credit for the requested material should be given as follows: "Reprinted (adapted) with permission from (COMPLETE REFERENCE CITATION). Copyright (YEAR) American Chemical Society." Insert appropriate information in place of the capitalized words.
- One-time permission is granted only for the use specified in your request. No additional uses are granted (such as derivative works or other editions). For any other uses, please submit a new request.